

**PROBING THE ELECTROSTATICS AND HYDRODYNAMICS IN
GAS-SOLID FLUIDIZED BEDS**

by

Chuan He

M.Sc., Nanjing University of Science and Technology, 2010

B.Eng., Nanjing University of Science and Technology, 2008

A THESIS SUBMITTED IN PARTIAL FULFILLMENT OF

THE REQUIREMENTS FOR THE DEGREE OF

DOCTOR OF PHILOSOPHY

in

THE FACULTY OF GRADUATE AND POSTDOCTORAL STUDIES

(Chemical and Biological Engineering)

THE UNIVERSITY OF BRITISH COLUMBIA

(Vancouver)

March 2015

© Chuan He, 2015

Abstract

Novel electrostatic dual-tip probes, combined with suitable signal analysis methods, were developed for *in-situ* measurement and monitoring of particle charge density levels and bubble properties inside gas-fluidized beds. The probes were calibrated in several particulate flow devices: ejector-funnel, motor-pulley, vertical tube and vibration tray setups, as well as a two-dimensional fluidized bed. The effects of particle charge density, solid flux, particle velocity and angle of impact on the transferred current received by the probe from charged particles were quantified. For dual-tip (two-material) probes, substantial differences were observed in the signals from the two tips made of different materials, arising mainly from charge transfer and depending on the hydrodynamics and charge density inside the bed.

The probes were deployed with glass beads and polyethylene particles for both single bubble injection and freely bubbling experiments in two- and three-dimensional fluidization columns of different scales. Statistical and Fast Fourier Transform analysis showed that current signals were strongly affected by the local hydrodynamics in the fluidized bed. The amplitudes of current signal peaks, peak frequencies, as well as mean and standard deviations of the current increased with increasing superficial gas velocity. Local particle charge density and bubble behaviour were estimated by a signal processing procedure with decoupling methods. The probes were tested in steady state experiments, as well as in dynamic experiments by abruptly changing the superficial gas velocity or adding antistatic agent. Both particle charge density and bubble rise velocity obtained from the probes were of the same order of magnitude and followed similar trends as those directly measured by a Faraday cup and video images, respectively. The electrostatic probe signal was found to not always be consistent with the charge polarity and charge density on the particles. The probe signals and particles charge densities may have different polarity and relative magnitudes for different operating conditions and particle properties: density, mean size and size range, dielectric constant, sphericity, roughness and hydrophobicity. Particles with narrow size distribution and larger mean size generated higher charge densities. The novel probe has potential for *in-situ* monitoring electrostatic charges and hydrodynamic behaviour in gas-solid fluidized beds.

Preface

At the time of writing this thesis, three research papers have been published, one in press and one under reviewed. The author carried out all stages of the research described in the published and submitted papers and also prepared manuscripts. The co-authors supervised the work, provided feedback and insight throughout this process, and edited the manuscripts.

- He C., Bi X. T., Grace J. R. Simultaneous measurements of particle charge density and bubble properties in gas-solid fluidized beds by dual-tip electrostatic probes. *Chemical Engineering Science*, 2015, 123, 11-21.
- He C., Bi, X. T., Grace J. R. Contact electrification of a novel dual-material probe with charged particulate flow in an ejector-funnel setup. *Powder Technology*, 2014, 253, 1-9.
- He C., Bi X. T., Grace J. R. A novel dual-material probe for in situ measurement of particle charge densities in gas-solid fluidized beds. *Particuology*, in press.
- He C., Bi X. T., Grace J. R. Decoupling electrostatic signals from gas-solid bubbling fluidized beds. under review.
- He C., Bi X. T., Grace J. R. Dual-material probe measurement of electrostatic charges and hydrodynamics in gas-solid fluidized beds. *Proceedings of 11th International Conference on Fluidized bed Technology*, Beijing, China, May 2014.

Above papers correspond to Chapters 2-4 of this thesis. A manuscript corresponds to Chapter 5, He C., Bi X. T., Grace J. R. “In-situ monitoring electrostatics and hydrodynamics in gas-solid bubbling fluidized beds” will be submitted to a journal for publication.

The author has also given several presentations at international, national and local conferences and scientific/technical forums:

- He C., Bi X. T., Grace J. R. Dual-material probe measurement of electrostatic charges and hydrodynamics in gas-solid fluidized beds. 11th International Conference on Fluidized bed Technology, Beijing, China, May 14-17, 2014. (*Keynote Presentation*)
- He C., Bi X. T., Grace J. R. Decoupling electrostatics signals from gas-solid bubbling fluidized beds. International workshop on Fluid-Particle Systems, Vancouver, Canada, June 26-27th, 2014.

- He C., Bi X. T., Grace J. R. Analysis of electrostatic signals from gas-solid fluidized bed. 62nd Canadian Chemical Engineering Conference, Vancouver, BC, Canada, October 14-17, 2012.

The authors also submitted one patent application titled “Method and apparatus for monitoring electrostatics in fluidized beds” to University-Industry Liaison Office (UILO) at UBC.

Table of Contents

Abstract.....	ii
Preface.....	iii
Table of Contents	v
List of Tables	ix
List of Figures.....	xi
List of Symbols and Abbreviations	xxiii
Acknowledgements	xxvii
Chapter 1 Introduction.....	1
1.1 Electrostatics in gas-solid fluidized beds.....	1
1.2 Problem definition	1
1.3 Thesis objectives	2
1.4 Thesis outline	3
1.5 Interaction between electrostatics and hydrodynamics in gas-solid fluidized beds	4
1.6 Electrostatic charge measurement techniques	5
1.6.1 Faraday cup and particle trajectory tracking methods	5
1.6.2 Probes.....	8
1.7 Particle charging models.....	14
1.7.1 Models for pneumatic transport	14
1.7.2 Models for fluidized beds	14
1.8 Electrostatic signal analysis	15
1.8.1 Electrostatic signals from pneumatic transportation.....	15
1.8.2 Electrostatic signals from fluidized beds	17
Chapter 2 Probes Design, Fabrication and Calibration.....	23
2.1 Introduction.....	23
2.2 Design and fabrication	23
2.2.1 Design	23
2.2.2 Fabrication	27
2.3 Calibration of probes outside fluidized bed	28
2.3.1 Ejector-funnel setup	28

2.3.2 Motor-pulley setup.....	32
2.3.3 Vertical tube setup and vibration tray setup.....	33
2.4 Calibration of probes inside fluidized bed	35
2.5 Results and discussion	37
2.5.1 Ejector-funnel setup	37
2.5.2 Motor-pulley setup.....	47
2.5.3 Vertical tube and vibration tray setups	49
2.5.4 Two-dimensional fluidized bed	51
2.5.5 Probes calibrations with particles of different properties	59
2.6 Summary.....	63
Chapter 3 Measurements in Gas-Solid Fluidized Beds.....	65
3.1 Introduction.....	65
3.2 Experimental equipment and methods.....	65
3.2.1 Two-dimensional fluidization column.....	65
3.2.2 Three-dimensional fluidization column of ID 0.10 m	65
3.2.3 Three-dimensional fluidization column of ID 0.30 m	66
3.3 Results and discussion	68
3.3.1 Results from two-dimensional fluidization column.....	68
3.3.2 Results from three-dimensional fluidization column of ID 0.10 m	77
3.3.3 Results from three-dimensional fluidization column of ID 0.30 m	82
3.4 Summary	87
Chapter 4 Decoupling Electrostatic Signals from Gas-Solid Fluidized Beds.....	89
4.1 Introduction.....	89
4.2 Signal analysis procedure	89
4.2.1 Peak (bubble) detection.....	89
4.2.2 Peak (bubble) selection	91
4.3 Decoupling methods	93
4.3.1 Charge transfer and induction model.....	93
4.3.2 Dual-tip (two-material) probe	94
4.3.3 Dual-tip (one-material) probe	96
4.4 Results and discussion	98

4.4.1 Signal processing	98
4.4.2 Results from two-dimensional fluidization column.....	105
4.4.3 Results from three-dimensional fluidization column of ID 0.10 m	117
4.4.4 Results from three-dimensional fluidization column of ID 0.30 m	118
4.4.5 Comparison of two types of dual-tip probes.....	123
4.4.6 Signals from conventional single-tip probes in pressurised column with original PE-II.....	124
4.4.7 Differences between polyethylene and glass beads	126
4.5 Summary	127
Chapter 5 In-situ Monitoring in Gas-Solid Fluidized Beds	129
5.1 Introduction.....	129
5.2 Experimental equipment and methods.....	130
5.3 Results and discussion	131
5.3.1 Effect of sampling parameters	131
5.3.2 Changing U_g in two-dimensional bed of 500-600 μm GB	133
5.3.3 Adding antistatic agent to two-dimensional bed of 500-600 μm GB	136
5.3.4 Changing U_g in two-dimensional bed of 100-1500 μm PE	138
5.3.5 Changing U_g in three-dimensional bed of 100-1500 μm PE	140
5.4 Summary	143
Chapter 6 Overall Conclusions and Recommendations for Future Work.....	144
6.1 Conclusions.....	144
6.1.1 Probes fabrication and calibration.....	144
6.1.2 Measurements in gas-solid fluidized beds of glass beads and polyethylene	145
6.1.3 Signal analysis and decoupling	146
6.1.4 In-situ monitoring in gas-solid fluidized beds	147
6.2 Recommendations for future work	148
References	149
Appendix A Photographs of experimental components	162
A.1 Fabricated probes	162
A.2 Ejector-funnel setup	163
A.3 Motor-pulley and vibration tray setups.....	164

A.4 Two-dimensional fluidization column	165
A.5 Three-dimensional Plexiglas fluidizaton columns	166
A.6 Pressurized three-dimensional stainless steel fluidization column	167
Appendix B Experimental details.....	168
B.1 Experimental data from calibration in two-dimensional fluidization column	168
B.2 X-ray Photoelectron Spectrometers characterization of Ni and TiN tips	173
B.3 Probe response time	174
B.4 Sensitivity test in 0.10 m ID three-dimensional fluidization column	175
B.5 Troubleshooting signal drift of custom-made probe	178
B.6 Determination of minimum fluidization velocity	179
B.7 Particle size distributions	183
B.8 Synchronization of camera and probe.....	185
B.9 Polarity of cumulative charge signals from probe	187
B.10 Further results from pressurized three-dimensional fluidization column	191
B.10.1 Sampling parameters and signal conditioning.....	192
B.10.2 Statistical and time-frequency analysis	198
B.10.3 Conclusions	201
Appendix C Details of modeling and signal processing.....	202
C.1 Simulation results from a charge transfer and induction model	202
C.2 Improvement of charge transfer model	206
C.3 MATLAB codes for charge transfer and induction model as well as signal processing and decoupling.....	211

List of Tables

Table 1.1 Charge density on particles by different powder operations [3, 29].....	5
Table 1.2 Summary of collision probes previously used in fluidized beds.	12
Table 1.3 Summary of charge density measurement techniques used in gas-solid fluidized beds.....	13
Table 2.1 Summary of tested probes in this work.	27
Table 2.2 Electrical properties and hardness of different materials used in the experiments [74, 106-115].	30
Table 2.3 Directly measured charge density (q_m), bubble size (D_B) and rise velocity (U_B) and current peaks (I_{peak}) from single bubble injection experiments.	53
Table 2.4 Directly measured charge density (q_m), bubble rise velocity (U_B) and current peaks (I_{peak}) from freely bubbling experiments with synchronization (see Section 2.4).	57
Table 2.5 Fitted parameters in Eq. (2.13) for different probe tips and particle size distributions of PE powders.....	62
Table 4.1 Decoupled charge densities and bubble rise velocities based on different decoupling methods for one segment of signals (~1 s duration) for two-dimensional bubbling fluidized bed at different superficial gas velocities, U_g	104
Table 4.2 Estimated charge densities and bubble rise velocities from 2t1m probe with different configurations by different decoupling methods at different U_g in freely bubbling two-dimensional fluidized bed of 500-600 μm GB.....	113
Table 4.3 Average charge densities (q_m) measured by Faraday cup (FC) and decoupled from 2t2ma probe, and bubble rise velocities (U_B) decoupled from probe at different U_g in 0.10 m ID three-dimensional bubbling bed of 500-600 μm GB.	117
Table 4.4 Decoupled q_m and U_B from 2t1m probes with different configurations and tips and Faraday cup (FC) at different U_g in freely bubbling 0.30 m ID three-dimensional fluidized bed of original PE-I particles.....	121
Table 4.5 Mean bubble rise velocity (U_B) decoupled from the 1t1m probe in pressurized stainless steel three-dimensional column with original PE-II particles at different operating conditions.....	125

Table B.1 Directly measured charge density (q_m), bubble rise velocity (U_B) and current peaks (I_{peak}) from synchronization experiments (see Section 2.4) with 2t2mb probe and 106-212 μm GB.....	168
Table B.2 Directly measured charge density (q_m), bubble rise velocity (U_B) and current peaks (I_{peak}) from synchronization experiments (see Section 2.4) for different cases corresponding to Table 2.5. (Fluidizing gas air: $T=22\pm2^\circ\text{C}$, $RH=6\pm2\%$)	169
Table B.3 Ratio of mean currents from Ni and TiN of 2t2ma probe when U_g was changed in 0.10 m ID freely bubbling fluidized bed. ($f_s= 100$ Hz, Fluidizing gas air: $T=22\pm2^\circ\text{C}$, $RH=10\pm2\%$.).....	177
Table B.4 Faraday cup measurements by scooping particles (static bed height: 0.30 m, $U_g= 0.30$ m/s).	188
Table B.5 Faraday cup measurements of particles discharged through sampling port within 6 s and 25 s (static bed height: 0.30 m, sampling port: 0.22 m above distributor, $U_g= 0.30$ m/s).....	188
Table B.6 Results from Faraday cup measurements of particles discharged through sampling port (Static bed height: 0.30 m, sampling port: 0.22 m above distributor).....	189
Table B.7 Minimum fluidization velocities of polyethylene particles (PE-II) at different pressures in pressurized three-dimensional column.	191
Table B.8 Sampling parameters for each run in pressurized three-dimensional column.	192
Table B.9 Summary of literature on sampling conditions and denoising of fluidized bed electrostatic signals.....	193
Table B.10 Values used in de-noising for different 1t1m probes and sampling frequencies.	199
Table C.1 Input parameters used in simulation.	203
Table C.2 Simulated minimum and maximum peaks and their relative differences in Figures C.2 and C.3.	204

List of Figures

Figure 1.1 Schematic of a Faraday cup (adapted from Cross [30]).	6
Figure 1.2 Faraday cup column with quick-opening distributor for measuring particle charging (adapted from Sowinski et al. [32]).	7
Figure 1.3 Experimental setup for particle trajectory tracking (1) fluidized bed (2) air-plate capacitor (3) high tension source (4) “pneumatic gun” (5) valves (6) motion-picture camera (adapted from Wolny [35]).	8
Figure 1.4 Capacitance probe (adapted from Guardiola et al. [36]).	9
Figure 1.5 (a) Induction probe (adapted from Chen et al. [22]) and (b) Copper ring probe (adapted from Armour-Chelu et al. [38]).	10
Figure 1.6 Schematics of (a) industrial and (b) laboratory collision probes (adapted from Park et al. [45] and Chen et al. [11]).	11
Figure 1.7 Sample real-time reactor electrostatic probe data (Marino [90]).	17
Figure 2.1 Schematic of dual-tip (two-material) probes: (a) design a; (b) design b.	24
Figure 2.2 Schematic of dual-tip (one-material) probe with different configuration and tip shape: F configuration (two tips protruding); Γ configuration (upper tip protruding, lower tip retracted); L configuration (upper tip retracted, lower tip protruding); flat and rod shape tips.....	26
Figure 2.3 Schematic of experimental apparatus for ejector setup: (a) overall setup; (b) elbow and pipe combinations. (PVC: polyvinyl chloride; SS: stainless steel) (not to scale)	29
Figure 2.4 Schematic of technique for measuring average particle velocity at different angles of inclination of probe.	32
Figure 2.5 Experimental setup of motor-pulley system and different positions of 2t2mb probe tip (not to scale).	33
Figure 2.6 Schematic of experimental apparatus for vertical tube setup (not to scale).	34
Figure 2.7 Schematic of experimental apparatus for vibration tray setup (not to scale).	34
Figure 2.8 Schematic of two-dimensional column, bubble injection system and charge measurement system (not to scale).	35

Figure 2.9 Charge carried by particles after passing through ejector setup shown in Figure 2.3b with different pipe materials; Average gas velocity =2.79 m/s (at outlet of vertical pipe with average pipe inner diameter is 25 mm).....	38
Figure 2.10 Charge carried by particles after passing through ejector setup with different gas velocities for PVC+PVC elbow and pipe combination (see Figure 2.3b).....	39
Figure 2.11 Measured charge densities on particles in dilute phase with different pipe materials and particle velocities.....	40
Figure 2.12 Typical cumulative charge signals measured by 2t2ma probe in dilute phase flow with different pipe materials; average particle velocity $V_p=4.42\text{m/s}$; collision angle $\theta=0$ degree.....	41
Figure 2.13 Characteristics of Ni and TiN tips at different particle velocities in dilute phase flow, collision angle $\theta=0$ degree; four pipe combinations as shown in Figure 2.14b.	42
Figure 2.15 Comparison of fitted and experimental data for (a) dilute phase flow ($\varepsilon > 0.99$), and (b) dense phase flow ($0.87 \geq \varepsilon \geq 0.72$).....	44
Figure 2.16 Relationship between $-I_{tran}/W_s$ and collision angle θ at different particle velocities for two tips in dilute phase flow: (a) Ni and (b) TiN.	45
Figure 2.17 Relationship between $-I_{tran}/W_s$ and collision angle θ for two tips at $V_p=4.42\text{ m/s}$ in dilute phase flow; pipe material combination: Al+Al.	46
Figure 2.18 Cumulative charge signal measured by 2t2mb probe (facing vertically downward) when negatively charged ball passed by in motor-pulley setup.....	47
Figure 2.19 Cumulative charge signal measured by covered tips of 2t2mb probe in two-dimensional fluidized bed: (a) single bubble; (b) free bubbling, $U_g =0.30\text{ m/s}$. .	48
Figure 2.20 Ratio ($C_{min,TiN} / C_{min,Ni}$) from 2t2mb probe (see Table 2.1) (a) in motor-pulley setup; (b) in two-dimensional fluidized bed.	49
Figure 2.21 Cumulative charge signals from 2t2ma probe at different locations in vertical tube setup, shown in Figure 2.6.	49
Figure 2.22 Comparison of cumulative charge signals from 2t2ma probe with both tips uncovered and one tip (Ni or TiN) covered in vertical tube setup (probe at bottom of tube with probe tip facing upward).	50
Figure 2.23 Cumulative charge signal from 2t2ma probe in vibration tray setup.	51

Figure 2.24 Charge (raw signal), current (derivative of charge) signal from 2t2mb probe and synchronized snapshots for single bubble injection in two-dimensional fluidized bed. (Back pressure for bubble injection: 345 kPa; solenoid valve opening time: 0.2 s; $\sim 2E-4$ m ³ pressurized air injected; centre of probe location: 0.17 m above bubble injector; bubble injector: 0.04 m above distributor)	52
Figure 2.25 Current signals from 2t1mfF probe for single bubble injection in two-dimensional fluidized bed containing glass beads (Pressure in bubble injector: 345 kPa; solenoid valve opening time: 0.2 s; $\sim 2E-4$ m ³ pressurized air injected; centre of probe port 0.17 m above bubble injection port; bubble injector: 0.04 m above distributor).....	54
Figure 2.26 Current signals from 2t1m probe with different configurations for multiple bubble injections in two-dimensional fluidized bed containing glass beads (Pressure in bubble injector: 345 kPa; solenoid valve opening time: 0.2 s and closing time: 3 s; centre of probe port 0.17 m above bubble injection port; bubble injector: 0.04 m above distributor).	55
Figure 2.27 Charge density decay curve after cutting off gas flow following free-bubbling with compressed air (RH=10%) and nitrogen (RH=2%).	56
Figure 2.28 Comparison of empirical correlation (Eqs. (2.13-2.15)) and experimental data for two probe materials.....	59
Figure 2.29 Contour plots of current peaks from Ni tip of 2t2mb probe as a function of bubble rise velocity and particle charge density from calibration experiments for 106-212 μ m and 500-600 μ m GB.....	60
Figure 2.30 Synchronized 2t1mr Γ probe (inserted 0.42 m above the distributor) and differential pressure signals across the bed in two-dimensional fluidization column of 710-850 μ m PE at $U_g = U_{mf} + 0.04$ m/s. (Fluidizing gas air: T=23.2°C, RH=4.2 %).....	62
Figure 2.31 Comparison of fitted data (from Eq. (2.13)) and experimental data for different probe tips and particle size ranges of PE powders.	63
Figure 3.1 Schematic of 0.10 m ID three-dimensional column and charge measurement system (not to scale).	66

Figure 3.2 Schematic of 0.30 m ID three-dimensional column and charge measurement system (not to scale).	67
Figure 3.3 Cumulative charge (a) and current (b) signals from 2t2mb probe in freely bubbling two-dimensional fluidized bed of 500-600 μm GB with static bed height of 0.30 m at $U_g=0.50$ m/s over duration of 5 s. (Fluidizing gas air: $T= \sim 22^\circ\text{C}$, $\text{RH}= \sim 10 \%$).....	69
Figure 3.4 Mean and standard deviation of current as a function of superficial gas velocity and particle charge density in freely bubbling two-dimensional fluidized bed with a static bed height of 0.30 m.....	70
Figure 3.5 Comparison of $(\bar{I}_{\max} + \bar{I}_{\min})/2$ and $(\bar{I}_{\min} - \bar{I}_{\max})/2$ for both materials at different superficial gas velocities in two-dimensional fluidized bed with static bed height of 0.30 m.....	71
Figure 3.6 Cumulative charges and current signals from 2t2mb probe at different superficial gas velocity in two-dimensional freely bubbling bed of 106-212 μm GB. (Fluidizing gas air: $T= \sim 22^\circ\text{C}$, $\text{RH}= \sim 10 \%$)	72
Figure 3.7 Mean currents as a function of superficial gas velocity and particle charge density for 106- 212 μm GB.	73
Figure 3.8 Cumulative charge and current signals from 2t1mfF probe in freely bubbling two-dimensional fluidized bed of 500-600 μm GB at different superficial gas velocities. (Fluidizing gas air: $T= \sim 23^\circ\text{C}$, $\text{RH}= \sim 3 \%$)	74
Figure 3.9 Cumulative charge and current signals from 2t1m probe with different configurations in freely bubbling two-dimensional fluidized bed of 500-600 μm GB at excess superficial gas velocities, $U_g-U_{\text{mf}}=0.02$ and 0.14 m/s. (Fluidizing gas air: $T= \sim 23^\circ\text{C}$, $\text{RH}= \sim 3 \%$)	75
Figure 3.10 Cumulative charge and current signals from 2t1mfF probe in freely bubbling two-dimensional fluidized bed of 710-850 μm PE at different U_g . (Fluidizing gas air: $T= \sim 23^\circ\text{C}$, $\text{RH}= \sim 7 \%$)	76
Figure 3.11 Cumulative charge signals from 2t2ma probe horizontally inserted to centre and near the wall in 0.10 m ID freely bubbling fluidized bed ($U_g=0.29$ m/s). (Fluidizing gas air: $T= \sim 22^\circ\text{C}$, $\text{RH}= \sim 10 \%$)	77

Figure 3.12 Mean and standard deviation of current signals from 2t2ma probe as a function of probe insertion distance.....	78
Figure 3.13 Comparison of cumulative charge signals from 2t2ma probe inserted: (a) horizontally and (b) vertically into 0.10 m ID freely bubbling fluidized bed ($U_g=0.33$ m/s). (Fluidizing gas air: $T= \sim 22^\circ\text{C}$, $\text{RH}= \sim 10\ %$)	79
Figure 3.14 Typical current signals from: (a) homogeneous particulate flow with particles dropped from funnel; (b) 0.10 m ID freely bubbling fluidized bed.....	79
Figure 3.15 Current signals from 2t2ma probe inserted vertically into 0.10 m ID freely bubbling fluidized bed at different superficial gas velocities. (Fluidizing gas air: $T= \sim 22^\circ\text{C}$, $\text{RH}= \sim 10\ %$).....	80
Figure 3.16 (a) Mean, (b) standard deviation and (c) normalized standard deviation of current signals from 2t2ma probe as function of superficial gas velocity in 0.10 m ID freely bubbling fluidized bed (probe inserted vertically). (Experiments for $U_g=0.22$, 0.25, 0.28 and 0.31 m/s were conducted on a different day as experiments for $U_g=0.33$, 0.36, 0.39 and 0.44 m/s).....	81
Figure 3.17 FFT of current signals from 2t2ma probe in 0.10 m ID freely bubbling fluidized bed at different superficial gas velocities.	82
Figure 3.18 Current signal from 2t2mb probe in 0.30 m ID freely bubbling fluidized bed of 420-590 μm GB at different superficial gas velocities. (Fluidizing gas air: $T=40\pm 5^\circ\text{C}$, $\text{RH}=15\pm 4\ %$).....	83
Figure 3.19 Cumulative charge and current signals from 2t1m probes at different U_g in freely bubbling 0.30 m ID three-dimensional fluidized bed of original PE-I particles. (Fluidizing gas air: $T=40\pm 5^\circ\text{C}$, $\text{RH}=15\pm 4\ %$)	84
Figure 3.20 Cumulative charge and current signals from 2t1mf Γ probe (insertion 0.25 m above distributor) at different U_g in 0.30 m ID fluidized bed of original PE-I particles. (Fluidizing gas air: $T=40\pm 5^\circ\text{C}$, $\text{RH}=15\pm 4\ %$).....	85
Figure 3.21 Current signals from 2t1mfF probes at different locations in 0.30 m ID fluidized bed of original PE. (probe 1: $z_1=0.25$ m, probe2: $z_2=0.70$ m and probe 3: $z_3=1.00$ m, $U_g-U_{mf}=0.24$ m/s) (Fluidizing gas air: $T=40\pm 5^\circ\text{C}$, $\text{RH}=15\pm 4\ %$)	86
Figure 3.22 Standard deviations of current signals from 2t1m probes and absolute pressure signals versus superficial gas velocity.....	87

Figure 4.1 Flowchart of peak detection and selection algorithm adopted for signal processing.	90
Figure 4.2 Theoretical charge and current signals received from collision probe when a single bubble passed by.....	94
Figure 4.3 Principle of 2t1m probe (F configuration) to determine bubble rise velocity and size.	96
Figure 4.4 (a) Raw data, (b) peak-detected data and (c) peak-selected data, generated from 2t2mb probe in two-dimensional bubbling fluidized bed of glass beads.	99
Figure 4.5 Effects of different parameters on number of selected bubbles from a 40 s period of time-series signals (70 bubbles in total) in bubble selection algorithm of signal processing for 2t2mb probe in two-dimensional fluidized bed.	101
Figure 4.6 Comparisons of charge density from 2t2mb probe and Faraday cup measurements at different U_g in freely bubbling two-dimensional fluidized bed: (a) Static bed height 0.30 m with probe 0.22 m above distributor; (b) Static bed height 0.50 m with probe 0.42 m above distributor.....	106
Figure 4.7 Comparisons of bubble rise velocity from 2t2mb probe and video measurements under different U_g in freely bubbling two-dimensional fluidized bed: (a) Static bed height 0.30 m with probe 0.22 m above distributor; (b) Static bed height 0.50 m with probe 0.42 m above distributor.....	107
Figure 4.8 Comparison of decoupled (a) charge densities; (b) bubble rise velocities from 2t2mb probe by different decoupling methods in two-dimensional bubbling bed of 500-600 μm GB.....	108
Figure 4.9 Comparison of decoupled (a) particle charge densities; (b) bubble rise velocities from 2t2mb probe by different decoupling methods in two-dimensional bubbling bed of 106-212 μm GB.....	109
Figure 4.10 Decoupled bubble size and bubble rise velocities from 2t1mfF probe by two tips peak-times method at different U_g in freely bubbling two-dimensional fluidized bed of 500-600 μm GB.....	111
Figure 4.11 Comparison of charge densities and bubble rise velocities from 2t1mfF probe by different decoupling methods with Faraday cup and video measurements at	

different U_g in freely bubbling two-dimensional fluidized bed of 500-600 μm GB.....	112
Figure 4.12 Decoupled bubble size and bubble rise velocity from 2t1mfF probe by two current peaks tips method at different U_g in freely bubbling two-dimensional fluidized bed of 710-850 μm PE.....	114
Figure 4.13 Comparison of charge densities and bubble rise velocities from 2t1mfF probe by different decoupling methods with Faraday cup and video measurements at different U_g in freely bubbling two-dimensional fluidized bed of 710-850 μm PE.	115
Figure 4.14 Comparison of charge densities and bubble rise velocities from 2t1m probes of different configurations by different decoupling methods, Faraday cup and video measurements in freely bubbling two-dimensional fluidized bed of 710-850 μm PE at $U_g - U_{mf} = 0.09 \text{ m/s}$	116
Figure 4.15 Comparison of decoupled charge densities from 2t2mb probe by different decoupling methods and Faraday cup in 0.10 m ID three-dimensional bubbling bed of 500-600 μm GB.	118
Figure 4.16 Comparison of decoupled (a) charge densities; (b) bubble rise velocities from 2t2mb probe by T2-Ni, T2-TiN and TT2 methods in 0.30 m ID three-dimensional bubbling bed of 420-590 μm GB.	119
Figure 4.17 Comparison of charge densities and bubble rise velocities from 2t1mfF probe by different decoupling methods with Faraday cup measurement at different U_g in 0.30 m ID three-dimensional fluidized bed of original PE-I particles.	120
Figure 4.18 Decoupled charge densities from 2t1mfF probe and Faraday cup at different U_g in 0.30 m ID three-dimensional fluidized bed of original PE-I particles (probe: insertion 0.75 m above distributor, static bed height=0.88 m).	122
Figure 4.19 Decoupled charge densities from 2t1mfF probes at different axial locations and U_g in 0.30 m ID three-dimensional fluidized bed of original PE-I particles (probe 1: $z_1=0.25 \text{ m}$, probe 2: $z_2=0.70 \text{ m}$ and probe 3: $z_3=1.00 \text{ m}$, static bed height=0.88 m)....	123
Figure 4.20 Comparison of average relative errors with results from direct measurements and probes in two-dimensional bubbling bed of 500-600 μm GB.	124

Figure 4.21 Comparison of relative frequency distributions of decoupled bubble rise velocities from 1t1m probes located at different heights in pressurized column of original PE-II particles ($U_g = U_{mf} + 0.10$, absolute pressure in freeboard: 276 kPa).	126
Figure 5.1 Effect of sampling frequency on estimated charge density from 2t1mfF probe by (a) two tips peak-times method and (b) one-tip time-difference method when $U_g - U_{mf}$ changed abruptly from 0.02 to 0.11 m/s.	132
Figure 5.2 Effect of sampling time interval on estimated charge density from 2t1mfF probe by: (a) two tips peak-times method; and (b) one-tip time-difference method when $U_g - U_{mf}$ abruptly changed from 0.02 to 0.11 m/s.....	133
Figure 5.3 Current signals from 2t1mfF probe in freely bubbling two-dimensional fluidized bed of 500-600 μm GB when $U_g - U_{mf}$ abruptly changed from 0.02 to 0.11 m/s. (Fluidizing gas air: $T=23\pm 2^\circ\text{C}$, $RH=2\pm 2\%$.)	134
Figure 5.4 Comparison of charge densities and bubble rise velocities from 2t1mfF probe by different decoupling methods with Faraday cup and video measurements in freely bubbling two-dimensional fluidized bed of 500-600 μm GB when $U_g - U_{mf}$ changed from 0.02 to 0.11 m/s. ($f_s = 200$ Hz, $t_s = 10$ min, Fluidizing gas air: $T=23\pm 2^\circ\text{C}$, $RH=2\pm 2\%$).....	134
Figure 5.5 Comparison of charge densities and bubble rise velocities from 2t2mb probe by different decoupling methods with Faraday cup and video measurements in freely bubbling two-dimensional fluidized bed of 500-600 μm GB when $U_g - U_{mf}$ abruptly changed from 0.01 to 0.07 m/s. ($f_s = 200$ Hz, $t_s = 10$ min, Fluidizing gas air: $T=23\pm 2^\circ\text{C}$, $RH=5\pm 2\%$)	135
Figure 5.6 Current signals from 2t1mfF probe in freely bubbling two-dimensional fluidized bed of 500-600 μm GB at $U_g - U_{mf}=0.05$ m/s after 0.1 wt% Larostat 519 was added. (Fluidizing gas air: $T=22\pm 1^\circ\text{C}$, $RH=2\pm 1\%$.).	137
Figure 5.7 Comparison of charge densities from 2t1mfF probe by different methods with Faraday cup, and decoupled bubble rise velocities in freely bubbling two-dimensional fluidized bed of 500-600 μm GB at $U_g - U_{mf}=0.05$ m/s after 0.1 wt% Larostat 519 was added. (Fluidizing gas air: $T=22\pm 1^\circ\text{C}$, $RH=2\pm 1\%$.).	138

Figure 5.8 Cumulative charge and current signals from 2t1mf Γ probe in freely bubbling two-dimensional fluidized bed of original PE-I particles when $U_g - U_{mf}$ changed abruptly from (a) 0.04 to 0.18 m/s; (b) 0.18 to 0.04 m/s. (Fluidizing gas air: $T=24\pm1^\circ\text{C}$, $\text{RH}=6\pm1\%$).....	139
Figure 5.9 Comparison of charge densities and bubble rise velocities from 2t1mf Γ probe with Faraday cup and video measurements in freely bubbling two-dimensional fluidized bed of original PE-I particles when $U_g - U_{mf}$ was increased abruptly from 0.04 to 0.18 m/s, then decreased abruptly from 0.18 to 0.04 m/s.....	140
Figure 5.10 Current signals from 2t1mf Γ probe in freely bubbling 0.30 m ID three-dimensional fluidized bed of original PE-I particles when $U_g - U_{mf}$ changed from (a) 0.04 to 0.19 m/s; (b) 0.19 to 0.04 m/s. (Fluidizing gas air: $T=40\pm5^\circ\text{C}$, $\text{RH}=15\pm4\%$).....	141
Figure 5.11 (a) Comparison of charge densities from 2t1mf Γ probe with Faraday cup measurement in freely bubbling 0.30 m ID three-dimensional fluidized bed with original PE-I particles when $U_g - U_{mf}$ was increased abruptly from 0.04 to 0.19 m/s, and then decreased abruptly from 0.19 to 0.04 m/s . (b) Corresponding derived bubble rise velocities.	141
Figure 5.12 Current signals from 2t1mr Γ probe in freely bubbling 0.30 m ID three-dimensional fluidized bed of original PE-I particles when $U_g - U_{mf}$ was changed from (a) 0.18 to 0.05 m/s; (b) 0.05 to 0.20 m/s. (Fluidizing gas air: $T=40\pm5^\circ\text{C}$, $\text{RH}=15\pm4\%$).....	142
Figure 5.13 (a) Comparison of charge densities from 2t1mr Γ probe with Faraday cup measurement in freely bubbling 0.30 m ID three-dimensional fluidized bed with original PE-I particles when $U_g - U_{mf}$ changed abruptly from 0.18 to 0.05 m/s, then from 0.05 to 0.20 m/s. (b) Corresponding derived bubble rise velocities.	143
Figure A.1 Photographs of 3D printed parts with metal tips and fabricated probes.....	162
Figure A.2 Photographs of ejector-funnel setup.	163
Figure A.3 Photographs of (a) motor-pulley and (b) vibration tray setups.	164
Figure A.4 Photographs of two-dimensional fluidization column (Its width is 0.307 m)....	165
Figure A.5 Photographs of 0.10 m ID and 0.30 m ID three-dimensional Plexiglas fluidization columns.....	166

Figure A.6 Photographs of 0.15 m ID pressurized three-dimensional stainless steel fluidization column.....	167
Figure B.1 XPS of Ni and TiN tips before and after experiments.....	174
Figure B.2 Schematic of setup for testing probe response time.	174
Figure B.3 Changes in mean currents, ratio and difference of mean currents from Ni and TiN of 2t2ma probe in 0.10 m ID freely bubbling fluidized bed when U_g changed continuously from 0.22 to 0.36 m/s. ($f_s = 100$ Hz, $t_s = 5$ min, Fluidizing gas air: $T=22\pm2^\circ\text{C}$, $\text{RH}=10\pm2\%$).....	176
Figure B.4 Experimental minimum fluidization velocity (U_{mf}) curve for original PE-I (100-1500 μm) in two-dimensional fluidization column.	179
Figure B.5 Experimental minimum fluidization velocity (U_{mf}) curve for sieved PE (710-850 μm) in two-dimensional fluidization column.	179
Figure B.6 Experimental minimum fluidization velocity (U_{mf}) curve for GB (106-212 μm) in two-dimensional fluidization column.	180
Figure B.7 Experimental minimum fluidization velocity (U_{mf}) curve for GB (500-600 μm) in two-dimensional fluidization column.	180
Figure B.8 Experimental minimum fluidization velocity (U_{mf}) curve for original PE-II (wide size distribution) in pressurized three-dimensional fluidization column. (absolute pressure in freeboard: 138 kPa)	181
Figure B.9 Experimental minimum fluidization velocity (U_{mf}) curve for original PE-II (wide size distribution) in pressurized three-dimensional fluidization column. (absolute pressure in freeboard: 276 kPa)	181
Figure B.10 Experimental minimum fluidization velocity (U_{mf}) curve for original PE-II (wide size distribution) in pressurized three-dimensional fluidization column. (absolute pressure in freeboard: 414 kPa)	182
Figure B.11 Particle size distribution of GB (500-600 μm).	183
Figure B.12 Particle size distribution of GB (106-212 μm).	183
Figure B.13 Particle size distribution of GB (420-590 μm).	184
Figure B.14 Particle size distribution of original PE-I (100-1500 μm).	184
Figure B.15 Particle size distribution of sieved PE (710-850 μm).	184

Figure B.16 Example of synchronized frame with 2t2mb probe signal from freely bubbling two-dimensional fluidized column at $U_g=0.39$ m/s.....	185
Figure B.17 Labview VI for simultaneous start of analog input and output.....	186
Figure B.18 Cumulative charge signals from 2t2mb probe in freely bubbling two-dimensional fluidized column with glass beads at different U_g (Static bed height: 0.30 m, probe: 0.22 m above distributor, Exps 1 and 5 correspond to Table B.6).	190
Figure B.19 Locations of 1t1m probes in pressurized three-dimensional fluidization column.	192
Figure B.20 Cumulative charge (a) and current (b) signals from 1t1m probes in pressurized three-dimensional column ($U_g=U_{mf}+0.1$ m/s, absolute pressure in freeboard region: 276 kPa, $f_s=25$ Hz, $t_s=600$ s).	194
Figure B.21 Mean current signals from 1t1m probes in pressurized three-dimensional column ($f_s=200$ and 300 Hz, $U_g=U_{mf}+0.1$ m/s).	194
Figure B.22 FFT power spectra of raw current signals and noise from 1t1m probe (probe B) in pressurized three-dimensional column for different operating conditions ($f_s=300$ Hz).	195
Figure B.23 FFT power spectra of raw signal, noise and denoised signals by different methods from 1t1m probe (Probe B) in pressurized three-dimensional column ($U_g=U_{mf}+0.1$ m/s, absolute pressure in freeboard: 276 kPa and $f_s=300$ Hz)....	196
Figure B.24 Synchronized pressure (a) and current signal (1t1m probe, Probe A) (b) of 5 s period for different sampling frequencies at $U_g=U_{mf}+0.1$ m/s and absolute freeboard pressure of 276 kPa.	197
Figure B.25 Pressure and current signals from different 1t1m probes for different sampling frequencies at $U_g=U_{mf}+0.1$ m/s and absolute freeboard pressure of 276 kPa....	198
Figure B.26 (a) Mean and (b) standard deviation of denoised current signals from different 1t1m probes and sampling frequencies at $U_g=U_{mf}+0.1$ m/s and absolute freeboard pressure of 276 kPa.....	200
Figure B.27 FFT spectra of bed pressure (ΔP) (left) and current (1t1m probe, Probe C) (right) signals under different operating conditions for sampling frequency of 200 Hz.	201

Figure C.1 Representation of specific charge distribution due to two additive components.	202
Figure C.2 Simulated induced charges and currents for different D_B (50, 80 and 100 mm) when $q_{m0} = -1 \mu\text{C/kg}$	204
Figure C.3 Simulated induced charges and currents with different q_{m0} (-1, -2 and $-5 \mu\text{C/kg}$) when $D_B = 100 \text{ mm}$	204
Figure C.4 Simulated transfer currents from Ni and TiN tips of 2t2m probe caused by bubble passing and decoupled charge density and average particle velocity	205
Figure C.5 Schematic of model improvement	210

List of Symbols and Abbreviations

a_i	fitted constant in Eq. (2.5), dimensionless
A	area of parallel plate, m^2
A_p	probe tip surface area, m^2
b_i	fitted constant in Eq. (2.5), $\text{C s}^2/\text{kg m}^2$
c_i	fitted constant in Eq. (2.5), C/kg
C	capacitance between contact bodies (probe and particles), F
C_{\min}	minimum charge, C
d_s	average particle diameter, m
D	electric flux density, C/m^2
D_B	bubble size/diameter, m
D_P	ball probe diameter, m
E	electric field due to movement of cloud of particles, V/m
f	particle collision frequency, s^{-1}
f_s	sampling frequency, s^{-1}
H	cross-correlation integration time period, s
I	total current, A
\bar{I}	average current, A
k_b	constant in Eq. (C.10), F^{-1}
k_c	constant in Eq. (C.6), F^{-1}
k_e	constant in Eq. (C.9), F^{-1}
k_r	constant in Eq. (C.15), F^{-1}
L	vertical distance between probe center and tip of bubble injector, m
m_p	mass of particles, kg
n	number of collisions, dimensionless
n_0	characteristic number of particle electrification, dimensionless
q	charge on particles, C
q_e	equilibrium charge, C
q_i	initial charge, C
q_m	charge density or specific charge on particles, C/kg
q_{m0}	initial charge density or specific charge, C/kg
q_∞	charge on particle after collision, C
Q	squared distance between two attractors in Eq. (1.1)

Q	estimator of Q in Eq. (1.1)
Q_s	surface charge density on particle, C/m^2
R	cross-correlation function of two time-series signals
R_B	radius of bubble, m
R_p	radius of probe, m
RH	relative humidity
S	estimator for the normalized squared distance between two attractors, defined in Eq. (1.1)
t	time, s
t_s	sampling time interval, s
T	temperature, $^{\circ}C$
U_B	average bubble rise velocity, m/s
U_g	superficial gas velocity, m/s
U_{mf}	minimum fluidization velocity, m/s
V	total potential difference, V
V_p	average particle velocity, m/s
V_{np}	normal component of average particle velocity, m/s
V_{tp}	tangential component of average particle velocity, m/s
V_b	non-contact potential difference caused by space charge effect, V
V_c	contact potential difference based on surface work functions, V
V_C	variance in Eq. (1.1)
V_e	non-contact potential difference caused by image effect, V
W_s	mass flow rate of particles striking probe surface, kg/s
z_0	critical gap between contact bodies, m

Subscripts

B	bubble
sd	standard deviation
tran	transfer
ind	induction
max	maximum
min	minimum

Greek letters

α_i	fitted parameter in Eq. (2.13), kg/m
β_i	fitted parameter in Eq. (2.13), C s ² /kg m ²
γ_i	fitted parameter in Eq. (2.13), C/kg
Δq	transferred charge at time interval Δt , C
Δq_0	impact charge at zero initial charge, C
Δt	time interval during contact, s
Δx	moving distance of particles during time interval Δt , m
Δz	distance between upper and lower tips, m
$\Delta \tau$	time difference between maximum and minimum peaks from one tip, s
$\Delta \tau_B$	time for single bubble to pass probe, s
ε	local voidage, dimensionless
ε_{mf}	voidage at minimum fluidization, dimensionless
θ	collision angle, degrees
θ'	collision angle where current starts to decrease with increasing angle, degrees
λ	maximum tolerable time difference between current peaks from two materials, s
Π	permittivity of medium, F/m
Π_o	permittivity of vacuum or air, 8.854×10^{-12} F/m
Π_r	relative permittivity or dielectric constant, i.e. Π/Π_o , dimensionless
ρ_p	particle density, kg/m ³
φ	coefficient defining threshold value used in peak detection, dimensionless
ϕ_p	effective work function of particles, eV
ϕ_m	work function of metal, eV
ϕ_{tip}	ratio of mass of particles striking probe to mass of dropped particles, dimensionless
δ	lower boundary of ratio of current peaks from two materials, dimensionless
ω	upper boundary of ratio of current peaks from two materials, dimensionless

Abbreviation

Al	aluminum
FC	Faraday cup
GB	glass beads
Larostat 519	one type of antistatic additives

Ni	nickel
PE	polyethylene particles
PVC	polyvinyl chloride
SD	standard deviation
SS	stainless steel
TiN	titanium nitride
T1	transfer-induction method
T2	time difference method
TT1	two transfer currents method
TT2	two current peaks method
2t2m	dual-tip (two-material) probe
2t2ma	dual-tip (two-material) probe (design a)
2t2mb	dual-tip (two-material) probe (design b)
2t1m	dual-tip (one-material) probe
2t1mfF	dual-tip (one-material) probe (flat tips, F configuration)
2t1mf Γ	dual-tip (one-material) probe (flat tips, Γ configuration)
2t1mfL	dual-tip (one-material) probe (flat tips, L configuration)
2t1mr Γ	dual-tip (one-material) probe (rod tips, Γ configuration)
2t1mfr Γ	dual-tip (one-material) probe (flat and rod tips, Γ configuration)
1t1m	one-tip (one-material) probe (conventional probe)

Acknowledgements

First and foremost, I would like to express my sincere gratitude to my supervisors, Prof. Xiaotao Bi and Prof. John Grace, for their excellent guidance and continuous support in all my research efforts. Thanks Dr. Bi for giving me the opportunity to be part of renowned Fluidization Research Group; and thanks Dr. Grace for enlarging my vision of science. I am very treasured and honored to have such successful role models in my life.

I would like to thank my research committee members, Prof. Jim Lim and Prof. Jane Z. Wang, for their valuable suggestions, support and care throughout my PhD project. They always provide coherent answers to my endless questions.

I would like to acknowledge NOVA Chemicals Corporation and NSERC for providing financial support to this research project. Many thanks to Dr. Bob Quaiattini and others from NOVA Chemicals for reviewing and approval my publications, as well as helpful discussions.

I am grateful to fellow professors, graduate students, visiting scholars in the group and Department of Chemical and Biological Engineering. Special thanks to Prof. James Feng for letting me use the high speed camera; Prof. Norman Epstein, Prof. Naoko Ellis, Prof. Lifeng Zhang, Prof. Cai Liang, Dr. Turki A. Al-Smari, Dr. Farzaneh Jalalinejad, Dr. Zhiwei Chen, Dr. Yulong Ding and Mr. Hafiz Rahman for their continuous help, useful discussion and encouragement during my studies. I would also like to thank the staff in workshop, store and administration of the department for their professional support.

I wish to appreciate Dr. Ted Knowlton and Dr. Reddy Karri from PSRI, Prof. Allisa Park from Columbia University and Prof. Poupak Mehrani from University of Ottawa, for their helpful discussions and advices.

Last but not least, I am sincerely grateful to my parents for their endless support and encouragement throughout my years of education.

Chapter 1 Introduction

1.1 Electrostatics in gas-solid fluidized beds

Fluidization occurs when solid particles are transformed into a fluid-like state by being suspended in a gas [1]. Gas-solid fluidized bed reactors have advantages of rapid solids mixing, temperature uniformity, excellent heat transfer properties, relatively low pressure drops, ability to continuously add/remove particles and capacity to add liquids. Therefore they have been widely used in numerous industrial applications such as drying, coating, combustion, gasification, metallurgical ore roasting, fluid catalytic cracking, and acrylonitrile and polyethylene production.

Electrostatic phenomena in particle handling related processes are complex and unpredictable [2]. They were first reported in 1950s. The electrostatic charges in gas-solid fluidized bed reactors and gas-solid transport lines result from a balance between charge generation and dissipation, and can significantly affect the operation. They may be generated by different contact terms: particle-particle, particle-gas, and particle-wall. Charges can cause the particles to adhere to the reactor wall, then fuse and melt together on the reactor wall to form “sheets”. Significant reactor wall sheeting in polyolefin reactors can cause plugging of the reactor product discharge system or loss of fluidization. These consequences typically require reactor shutdown to have the sheets removed, with significant negative economic impact each time both in lost production and in maintenance costs to clean the reactor. Thus there are significant economic incentives to prevent the formation of wall sheets [3]. Moreover, accumulation of electrostatic charges can cause hazardous electrical discharges, leading to sparks, fires or even explosions.

1.2 Problem definition

To avoid the adverse effects of electrostatics outlined above, effective measurement techniques are needed to monitor electrostatic charges in fluidized beds. Understanding the cause of sheeting with metallocene catalysts in fluidized bed polyethylene reactors has for

many years been hampered by the lack of suitable instrumentation. Most sheeting incidents with these catalysts have occurred with little or no advanced warning by previously used process instruments, including conventional static probes [4-8]. Moreover, the development of high-activity catalysts combined with advanced reaction technologies has created a growing need to monitor electrostatic behaviour. This requires the development of reliable and accurate measurement techniques which can provide transient local particle charge density, as well as charge density distribution across a spectrum of particle sizes [9].

There are many different types of measurement tools to measure electrostatic charges, but none of these is standardized. Collision-type electrostatic probes [10, 11] are most common in industry. However, it is difficult to interpret voltage or current signals acquired by these probes. The current or voltage signal received from a collision probe not only reflects the particle charge density in the bed, but it is also a function of local dynamic properties, such as bubble size and rise velocity. Thus, the current or voltage from a collision probe is also influenced by changes in local hydrodynamics. The commonly-used collision probe cannot differentiate signal changes caused by charge density changes from those due to hydrodynamic changes. Charge density and hydrodynamic information are both embedded in the time-varying charge signals measured by electrostatic probes in fluidized bed reactors. To determine the charge density using collision probes, it is essential to decouple hydrodynamic information from charge variations.

An ideal probe would decouple the hydrodynamics from the charge density. Until now, electrostatic charge signals registered by collision probes have been poorly understood. Proper interpretation of these signals could help to understand the relationship between electrostatic charge and the hydrodynamics of fluidized beds.

1.3 Thesis objectives

The intention of this thesis is to provide a reliable tool to monitor *in-situ* particle charge density levels in reactors to assist in the prevention of charge buildup in the reactor, associated wall sheeting and possible accidents. Also this tool could help to measure the

dynamic electrostatic charging properties of bulk powders, assisting in the development of particle coating, mixing and transportation, pharmaceutical powders, their delivery systems and other industrial powder handing processes [12-14].

The objective of this study is to develop a model-based signal analysis tool in conjunction with experimental confirmation for monitoring electrostatic charges and hydrodynamics behaviour in gas-solid fluidized beds. The central goal is to *in-situ* measure particle charge density levels and bubble properties inside fluidized beds by a novel electrostatic probe combined with suitable signal analysis methods. Other objectives include:

- To improve the interpretation and understanding of charge signals registered by electrostatic probes;
- To monitor the electrostatics and hydrodynamics changes in gas-solid fluidized bed;
- To examine the effects of particle properties and column scale on particle charging and signal analysis;
- To improve understanding of electrostatic charge buildup and dissipation processes in gas-solid fluidized beds.

1.4 Thesis outline

Chapter 1 introduces the background and objectives of this study, then reviews relevant literature on electrostatics and hydrodynamics in fluidized beds, electrostatic measurement techniques, particle charging models and electrostatic signal analysis in pneumatic transportation and the fluidized beds. Chapter 2 describes the design/fabrication and calibration of novel electrostatic probes. The results from measurements of fabricated probes in different fluidized beds are presented in Chapter 3. Chapter 4 focuses on proposing several signal analysis and decoupling methods and provides results from analyzing the probe signals. The ability of the probes for *in-situ* monitoring of charge and hydrodynamic changes in fluidized beds is reported in Chapter 5. Chapter 6 presents overall conclusions and recommendations for future work.

1.5 Interaction between electrostatics and hydrodynamics in gas-solid fluidized beds

Electrostatic charges have been found to influence fluidized bed hydrodynamics, including bubble size and shape, particle velocity and fines entrainment in different fluidization equipment [15-18]. In circulating fluidized beds, electrification of the particles has been found to affect gas and solid velocities. Modeling of a riser [19] revealed that an electrical field can force particles towards the outer wall, so that electrostatic charges can promote the well-known tendency for most particles to reside in an outer annular layer in the circulating fluidized bed risers. Electrical charges in the bed can affect bubble size, but contradictory results have been reported in the literature. Some have indicated an increase in bubble size [15], whereas others [16] reported a decrease in bubble size due to increasing bed charge. Some researchers tried to find the charge distribution around the bubbles in a two-dimensional fluidized bed by interpreting collision probe and induction probe signals [20-24]. Their results suggested that the charge density outside the bubble gradually decreases toward the bubble-dense phase interface, with a nearly zero charge density inside the bubble. Jalalinejad et al. [25] adapted the Computational Fluid Dynamics Two-Fluid-Model in MFIX (an open-source code originated by the U.S. Department of Energy) to investigate the effect of electrostatics on hydrodynamics. This model predicted that electrostatic charges can cause a single bubble to elongate and rise more quickly.

Changes of hydrodynamics in gas-solid fluidized beds could cause a change in electrostatics signals registered by probes because of the change in the size and rise velocity of bubbles, as well as contacts among particles, and between the particles and reactor wall. Effects of several factors (e.g. pressure, superficial gas velocity, bubble size, initial bed height and distributor) on bed electrification have been investigated [16, 26, 27]. To determine the charge density and the hydrodynamics using static probes, one needs to separate hydrodynamic information from charge signals.

1.6 Electrostatic charge measurement techniques

The fundamental electrical quantities of measurements are electrostatic charge, current (charge transfer rate), and voltage (electric potential difference). Electrical signal data are usually expressed as charge density (C/m^3 , C/kg) or current density (A/m^3 , A/kg) [28]. Charge density on particles resulting from different powder operations are summarized in Table 1.1. With few exceptions, polymeric powders are poor conductors (with a volume resistivity of $10^{8-16} \Omega m$). For industrial grade polymeric powders, the level of charge produced per unit mass of powder depends more on the amount of work done on the powder during handling/processing than on the chemical composition of the material [29]. Fluidization results in the highest charge density, likely because of the greater surface area over which charges can be generated.

Table 1.1 Charge density on particles by different powder operations [3, 29].

Operation	Charge density ($\mu C/kg$)
Sieving	$10^{-5} \sim 10^{-3}$
Pouring	$10^{-3} \sim 10^{-1}$
Scroll feed transfer	$10^{-2} \sim 1$
Grinding	$10^{-1} \sim 1$
Micronizing	$10^{-1} \sim 10^{-2}$
Pneumatic conveying	$1 \sim 10^2$
Fluidization	$10 \sim 10^2$

The polarity and charge density on each particle provide crucial information on the degree of particle charging and the magnitude of electrostatic forces acting on individual particles [9]. Various techniques have been used to measure particle charge density in gas-solid flow systems. There are two main techniques to measure the electrostatic charges— Faraday cup (direct method) and electrostatic probes (indirect method).

1.6.1 Faraday cup and particle trajectory tracking methods

A Faraday cup is a double-wall vessel of any suitable shape. The outer wall is grounded and forms an electrical screen preventing external charges from affecting the measurements. The

inner wall is connected to an electrometer which measures the charge by detecting the voltage built-up across a known capacitance, as shown in Figure 1.1. When a charged object enters the inner cup, an equal and opposite charge is induced on the wall of the inner cup. This charge is stored on the capacitor in the electrometer and measured [30].

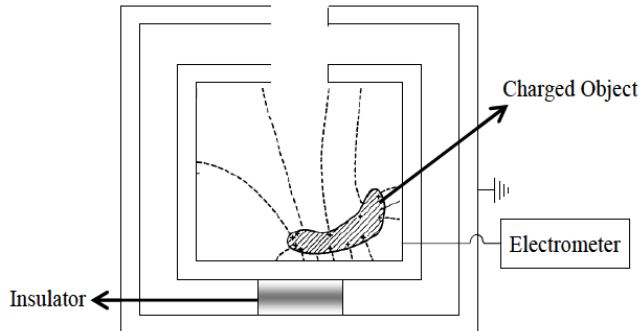


Figure 1.1 Schematic of a Faraday cup (adapted from Cross [30]).

Based on this principle, Mehrani et al. [31] developed a Faraday cup fluidization column with a copper column (diameter 0.1 m, height 2.1 m) inside a surrounding copper column (diameter 0.2 m, height 1.7 m) as the outer cup. The outer column was grounded to eliminate external electrical interference. The fluidization column was insulated from other parts of the inner and outer columns by Teflon cylinders and a Teflon distributor plate, and connected to an electrometer to measure the charges induced on the wall. Recently, an improvement was made so that bed material and fines can be discharged directly into two separate Faraday cups at the top and bottom of the bed, as shown in Figure 1.2 [32-34]. In this way, the average charge density in the bed and fines could be measured after each fluidization test. The Faraday cup measures the charge density of particles withdrawn (sampled) from the fluidized bed, so it is unable to reveal the local transient charge density distribution inside the bed. As an off-line measurement tool, it is unable to monitor industrial reactors *in-situ*. Moreover, charge generation or dissipation during particle sampling may affect the measurement accuracy. The Faraday cup is an open system susceptible to variations in environmental factors such as atmospheric air humidity, electromagnetic noise and sample discharging from the fluidized bed, and this renders it unreliable [14].

In particle trajectory tracking, single particles are ejected from the bed into a homogenous electric field by means of a local pneumatic impulse, as shown in Figure 1.3. Trajectories of ejected particles are captured by a camera, and particle charge densities are then determined by analyzing the trajectories of ejected particles subject to the electric and gravitational fields [35].

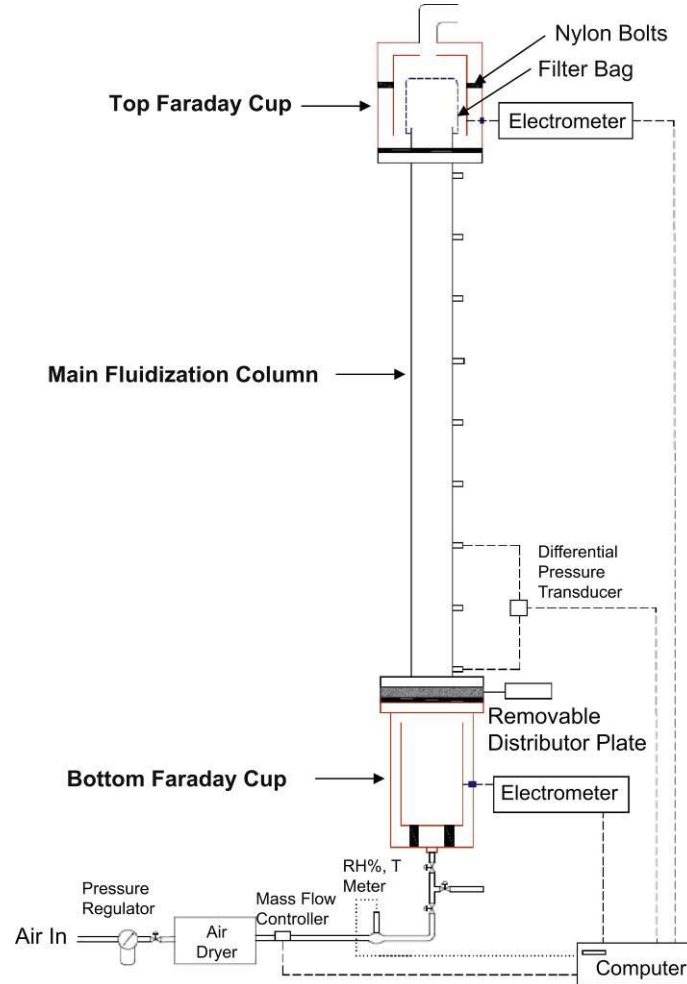


Figure 1.2 Faraday cup column with quick-opening distributor for measuring particle charging (adapted from Sowinski et al. [32]).

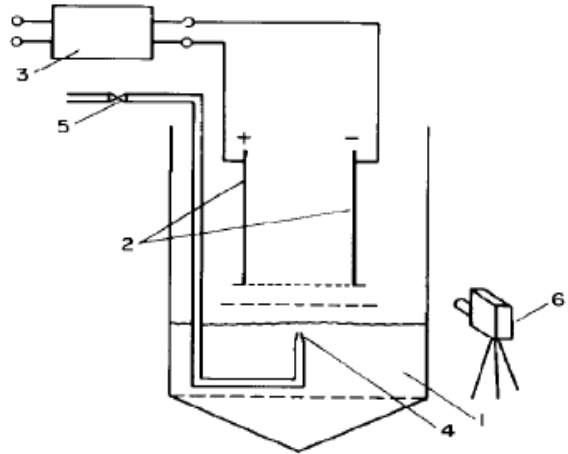


Figure 1.3 Experimental setup for particle trajectory tracking (1) fluidized bed (2) air-plate capacitor (3) high tension source (4) “pneumatic gun” (5) valves (6) motion-picture camera (adapted from Wolny [35]).

1.6.2 Probes

Electrostatic charge buildup inside fluidized beds has been measured by electrostatic probes of three major types: Capacitance Probes, Induction Probes and Collision Probes. Unlike the Faraday cup, which is a static measurement tool, electrostatic probes signals contain dynamic information on particle charging and hydrodynamics inside the bed.

1.6.2.1 Capacitance probes

Guardiola et al. [36, 37] used a capacitance probe to measure the degree of electrification in fluidized beds, as shown in Figure 1.4. In their technique, the probe and distributor were considered to be parallel metallic plates, while the bed acted as a dielectric medium. The probe-to-distributor voltage drop was measured. This method averages the charge over most of the bed cross-section.

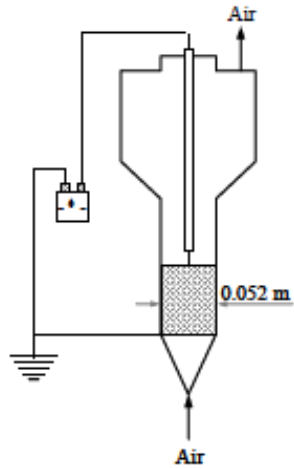
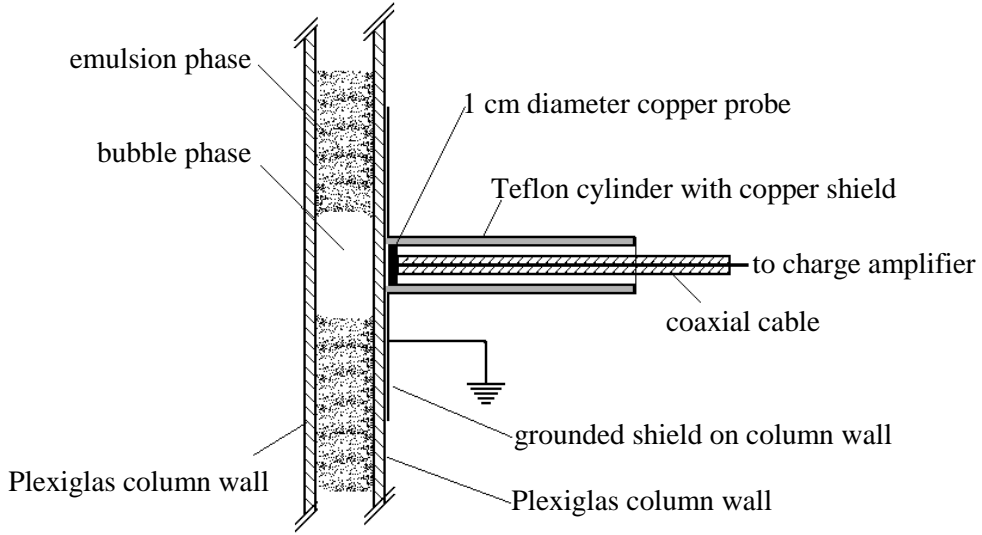


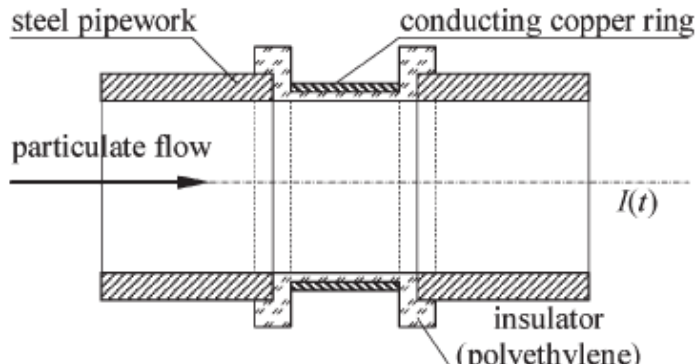
Figure 1.4 Capacitance probe (adapted from Guardiola et al. [36]).

1.6.2.2 Induction probes

The fundamental principle of an induction probe is that a real charge induces an image of itself on a conducting surface. There are two main types. One involves a ball or bar probe with a shielded head, as shown in Figure 1.5(a) [22]. Another, often used in pneumatic conveying systems, is a ring probe, as shown in Figure 1.5(b) [38]. These non-contacting probes have the advantage of not disturbing the flow since they are not directly exposed to the fluidized material. However, their disadvantage is that they are not directly exposed to the fluidized material. Particle-wall interactions, rather than particle-particle interactions, determine the output. Therefore induction probes are unsuitable for providing local information on non-homogeneous flow systems.



(a)



(b)

Figure 1.5 (a) Induction probe (adapted from Chen et al. [22]) and (b) Copper ring probe (adapted from Armour-Chelu et al. [38]).

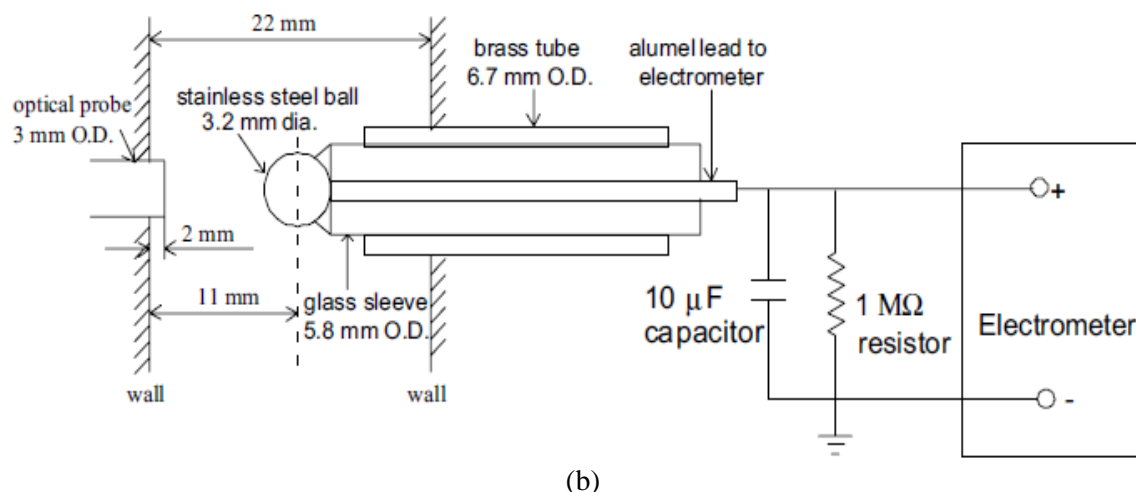
1.6.2.3 Collision probes

Collision probes are the most commonly used to measure electrostatics in the industry. A unit is shown in Figure 1.6(a). Made of highly conductive materials, they are often used to measure the charge or current induced and transferred to the probe tip by charged particles. Ciborowski and Włodarski [39] developed an electrode made of platinum wire (0.5 mm diameter), ending in a “smallish” (~5 mm diameter estimated based on a photograph) ball, tethered inside the fluidized bed by a silk thread and connected to an electrometer to measure

the electrical potential in a fluidization column of 0.06 m diameter and 0.555 m height. Fujino et al. [40] adopted a similar approach by inserting into the fluidized bed a spherical brass terminal of 6.0 mm diameter, tethered by a nylon thread and connected to an electrometer. A grounded brass distributor plate served as the reference electrode. Park et al. [41] and Chen et al. [11] mounted collision ball probes (as shown in Figure 1.6(b)) to measure charges induced and transferred by particles surrounding rising bubbles in a two-dimensional fluidized bed. Moughrabiah et al. [42, 43] and Wang et al. [44] installed collision probes at various heights along their columns to measure the charge distribution inside fluidized beds. The collision ball probes used by previous researchers and their features are compared and summarized in Table 1.2.



(a)



(b)

Figure 1.6 Schematics of (a) industrial and (b) laboratory collision probes (adapted from Park et al. [45] and Chen et al. [11]).

Table 1.2 Summary of collision probes previously used in fluidized beds.

Reference	Structure & materials		
	Layers (from outside to inside)	Connect to electrometer (electrode)	Probe tip
Ciborowski and Wlodarski [39]	N/A (Mounted with the help of silk thread)	Platinum wire	Platinum ball (0.5 mm D)
Fujino et al. [40]	N/A	Nylon thread	Brass ball (6 mm D)
Tardos and Pfeffer [10]	N/A	N/A	N/A
Park & Chen et al. [21, 41]	Brass tube (6.7 mm O.D.)→Glass sleeve (5.8 mm O.D.)	Alumel	Stainless steel ball (3.2 mm D)
Moughrabiah et al. [42]	Brass tube (12.7 mm O.D.)→Polyethylene tube (8.75 mm O.D.)→Ceramic tube (5.5 mm O.D.)→Teflon tube	Copper wire	Stainless steel ball (5.3 mm D)
Wang et al. [44]	Teflon sleeve (6.8 mm D)→Brass sleeve (5.2 mm)→Teflon sleeve (3.8 mm)	Brass	Copper bar (1 mm)

Table 1.3 lists the measurement techniques used to determine particle charge density in laboratory gas-solid fluidized beds. Collision probes have rarely been employed for this purpose because the current or voltage signals received from them not only reflect the particle charge density in the bed, but also local dynamic properties, such as bubble size and velocity.

Table 1.3 Summary of charge density measurement techniques used in gas-solid fluidized beds.

Researchers	Flow regime in the bed	Particles	Measurement technique	Signal and interpretation
Tardos and Pfeffer [10]	Bubbling	Porcelain	Faraday cup	$q_m=q/m_p$
Fasso et al. [46]	Bubbling	Glass beads	Faraday cup	$q_m=q/m_p$
Wolny and Opaliński [47]	Bubbling	Polystyrene	Faraday cup	$q_m=q/m_p$
Wolny and Kaźmierczak [35]	Bubbling	Polystyrene	Tracking particle trajectory	Single particle trajectory, numerical analysis of trajectory of charged particle in electrical and gravitational field
Napier [48]	Bubbling	Glass beads, sugar	Field meter	$q_m=q/m_p$
Jiang [49]	Fast Fluidization	FCC, Polyethylene	Faraday cup	$q_m=q/m_p$
Tucholski and Colver [50]	Fast Fluidization	Glass beads	Faraday cup	$q_m=q/m_p$
Mountain et al. [51]	Bubbling	Polymers	Faraday cup	$q_m=q/m_p$
Ali et al. [52]; Zhao et al. [53]	Bubbling	Polyamide	Faraday cup	$q_m=q/m_p$
Revel et al. [54]	Slugging	Polyethylene	Faraday cup	$q_m=q/m_p$
Murtomaa et al. [55]	Bubbling	Glass beads, lactose, cellulose	Faraday cup	$q_m=q/m_p$
Chen et al. [11]	Single bubbles	Glass beads	Collision Probe	Charge, fitting C_{min} to a charge induction model with known bubble size
Mehrani et al. [56]; Omar et al. [57]	Bubbling	Glass beads, Polyethylene	Faraday cup column	$q_m=q/m_p$
Chen et al. [23, 24]	Bubbling	Glass beads	Multi induction probes	Induced charge, signal reconstruction to obtain charge density around bubble
Sowinski et al. [33, 34]	Bubbling and slugging	Polyethylene	Faraday cup column	$q_m=q/m_p$

1.7 Particle charging models

Although the above measurement techniques provide information about electrostatics in fluidized beds, what these signals really mean is largely unknown. Several groups have attempted to develop models to link the charges on particles in pneumatic transport lines and gas-solid fluidized beds to signals registered by different types of probes.

1.7.1 Models for pneumatic transport

Dilute flow in pneumatic transport pipelines is relatively simple because it is a dilute phase flow, and the measured charge or current is mainly caused by collisions between the particles and the wall. Zhu and Soo [58] modified a previous ball probe theory to apply to a dense gas-solid suspension, to estimate the electric current passing through the ball probe due to collisions between the probe and particles in pneumatic transport lines by analogy between the mechanisms of electric charge transfer and heat transfer. Cole et al. [59] proposed that charge transfer depends on the total potential difference V , which is made up of three parts: V_c based on the surface work functions, V_e caused by the image effect and V_b caused by the space charge effect. Based on this, Matsusaka et al [60, 61] proposed a theory of wall charging in gas-solid pipe flow, in which the current flow to the pipe wall caused by collisions between particles and the outer wall depends on the mass flow rate and charge density. They also introduced a way to measure the mass flow rate and charge density of particles simultaneously by two short pipes made of different materials of substantially different work function.

1.7.2 Models for fluidized beds

The situation in the fluidized bed is more complex than in pneumatic transport pipelines. Park et al. [20] introduced a model to illustrate the linkage between signals from ball probes and specific charge density of bed particles. The total charge consists of two parts: induced charge and transferred charge. Charge induction occurs when a charged object repels electrons from, or attracts electrons to, the surface of a second object. This creates a charged region in the second object being charged. Charge transfer occurs to generate a contact

potential difference between contacting surfaces when different materials come into contact with each other. The model considered the situation where a single gas bubble surrounded by charged particles passed a probe. The charges on particles induce charges onto the probe, and charges on particles are also transferred to the probe due to collisions between the particles and probe. The model has some limitations: There is uncertainty in estimating the dielectric constant; frictional charging between the probe and particles is neglected; the charge density on the surface of the bubble is assumed to be uniform, but it is not uniform in practice; particles inside the bubble which affect the output when the probe is inside the bubble are neglected.

Chen et al. [21] modified this model by considering the charge distribution around the bubble and the background charge density, subject to charge build-up on particles remote from the bubble; they also allowed for the effect of bubble wakes and drift. The model predictions for bubbles passing the probe were in good agreement with experimental results.

1.8 Electrostatic signal analysis

Signals from fluidized beds such as absolute or differential pressure signals [62-66], voidage [67, 68], vibration [69] and acoustic signals [70-72], have been widely analyzed in the literature. Unlike those signals which are affected by only one physical factor, such as pressure signals, electrostatic signals contain both hydrodynamics and charge information. This section first reviews electrostatic signals from pneumatic conveying systems, followed by the analysis techniques for electrostatic signals from different fluidization systems in the literature.

1.8.1 Electrostatic signals from pneumatic transportation

In pneumatic conveying, charges are mainly generated by collisions between particles and pipe inner walls. Signals from two separate electrostatic rings are often cross-correlated to measure the solid flow rate, concentration and particle velocity [73-76]. Matsusaka et al. [77] analyzed the charge signals from a detection metal pipe. The signals varied over a wide range, from positive to negative, and contained two components, one induced by the

transport of a cloud of charged particles and the other transferred by repeated impacts of particles with the inner wall. The average velocity of the cloud flowing in the pipe can be obtained from the time interval between peak signals measured with a detection pipe. The Hilbert–Huang transform (HHT) or a neural network has been used to analyze electrostatic fluctuations detected by a ring-shape electrostatic sensor, revealing information on the gas-solid flow regime and hydrodynamics in pneumatic transport [78-81]. The HHT of the electrostatic fluctuation signal can show how the instantaneous frequencies and amplitudes of the electrostatic fluctuation vary with time, thus revealing its non-linear and non-stationary intrinsic nature. The energy distribution of intrinsic mode functions (IMFs) with different scales shifts from coarse scale (low frequency oscillations) to fine scale (high frequency oscillations) with increasing superficial gas velocity and decreasing particle concentration.

Zhang et al. [82] developed an integrated electrostatic and capacitance technique for measuring the volumetric concentration of coal and biomass, obtained from the outputs of electrostatic and capacitance sensors by a dual regression method in a three phase flow in a pneumatic conveying pipeline. Hussain et al. [83] developed a ring-shaped induction sensor for measuring charge and polarity of charged particles. Bunchattheeravate et al. [84] developed a method to predict particle charging in a straight pipe by a calibration equation and parameters. First, experiments on particle charging in a 1 m long pipe section were performed to obtain a model equation with two parameters related to the properties of the particle and pipe wall materials. Then, with equation and parameters, the particle charging in a straight pipe of any given length can be predicted. However the prediction of particle charging by this method has two limitations: first, particle charging must be via an impact charging mechanism; second, the particle, pipe wall materials and the operating conditions in the prediction must be the same as those in which the parameters and equation were determined.

Overall, the charge signals from the pneumatic conveying system have been given much attention, whereas there has been little analysis of the electrostatic signals from fluidization systems. Due to the complexity of flow in fluidized beds, it is difficult to interpret voltage or current signals measured by collision-type electrostatic probes inside fluidized beds.

1.8.2 Electrostatic signals from fluidized beds

This section reviews work on analysis of electrostatic signals by statistical, time-frequency, non-stationary analysis and signal reconstruction methods. Some studies have also shown that electrostatic signals can provide useful information on local fluidization characteristics [85], moisture content [86, 87], proportion of fines in the bed [88] and bed level [44].

1.8.2.1 Statistical analysis

Mean and standard deviation are the most commonly used characteristics for characterizing electrostatic levels in fluidized beds. In industrial applications, signals measured by electrostatic probe (see the example shown in Figure 1.7) are processed by means of averaging, with periods of averaging from 10 milliseconds to 10 hours. The signal may also be treated to provide a root mean square (RMS), a standard deviation of the signal, an absolute value of the signal, or an average absolute value of the signal [6, 8, 89].

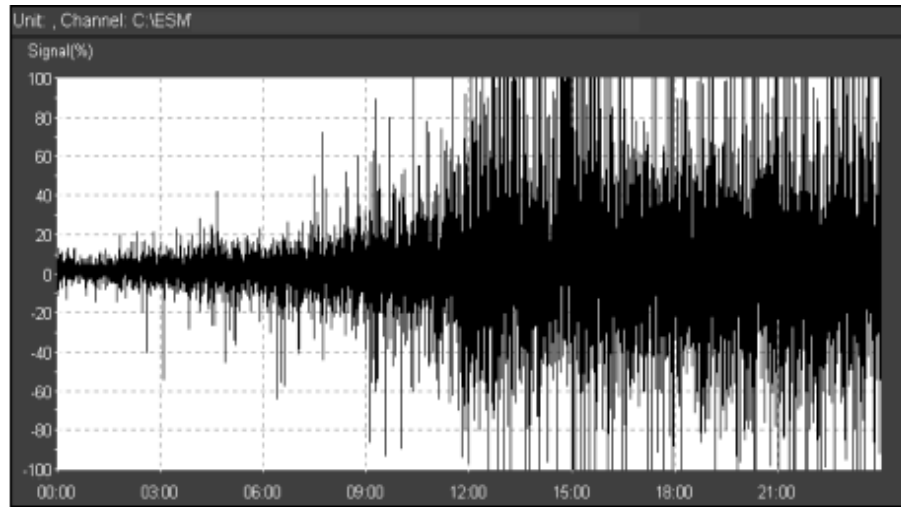


Figure 1.7 Sample real-time reactor electrostatic probe data (Marino [90]).

The simplest method analyzing electrostatic signals is to plot a sequence of data points of the measured signal. Boland et al. [91, 92] observed that the voltage signals from a shielded ball probe are similar in trend to pressure signals in the bed. The mean of current/charge generally represents the net transferred part, while the standard deviation of current/charge portrays the net induction part [93]. The experimental set-up of Liu et al. [94] consisted of a pressurized

gas-solid fluidized column and a charge measurement system. Seven collision probes were deployed at different radial and axial positions. Experiments were then carried out at different operating pressures and superficial gas velocities. The pressure drop across the bubbling bed was also measured. The charge behaviour of various probes was investigated by comparing the fluctuations and polarity of charge signals. The influence of superficial gas velocity on the charge signals was studied by comparing standard deviations of the pressure drop and cumulative charge signals. When the superficial gas velocity increased, the standard deviations of both pressure drop and cumulative charges increased, and the characteristic frequency of cumulative charges changed, consistent with the pressure drop signals.

Tiyapiboonchaiya et al. [27] investigated the average current measured by several copper strips in a three-dimensional Plexiglas column when fluidizing polypropylene particles. It was found that the average current reached a maximum value in the lower part of the bed and decreased with increasing height, because of more collisions among particles, between solids and walls, and greater friction between the solid and gas at a higher inlet gas velocity.

Park and Fan [45] studied electrostatic phenomena of high density polyethylene (HDPE) particles in a gas-liquid-solid fluidized bed, with liquid as the continuous phase. The results showed that the mean voltage measured by a commercial electrostatic probe did not change significantly with varying superficial gas velocity, whereas the standard deviation of the voltage output increased as the superficial gas velocity increased. As the superficial liquid velocity increased, the magnitude of both the mean and standard deviation of the voltage output increased.

Cheng et al. [95, 96] investigated electrostatic phenomena of sand particles in a combined triple-bed circulating fluidized bed, which was composed of a riser, a downer, a bubbling fluidized bed (BFB), a multi-tube solid distributor for the downer, a gas-solid separator and a gas-sealing bed, used to increase solids transfer from the BFB to the riser. The induced currents were measured by insulated copper rings outside the walls in the upper region of the riser, lower region of the downer and gas-sealing bed. With increasing superficial velocity in the gas-sealing bed, the average induced currents first increased and then approached a

constant, consistent with the variation of solid flux and average solids holdup. With increasing superficial gas velocity in the riser, the average induced current in the riser increased. On the other hand, the average induced current decreased in the downer with increasing downward superficial air velocity.

Bi et al. [93] asserted that the standard deviations of current signals from a collision ball probe reflect changes in local hydrodynamics, as well as in particle charge density. Normalized by average values, the dimensionless standard deviation could be a good indicator of local hydrodynamics.

Application of higher-order moments, such as skewness and kurtosis of electrostatic signals has not been reported in the literature.

1.8.2.2 Time-frequency analysis

Time-frequency analysis is typically carried out with the aid of the Fourier transform [64]. Yao et al. [16] plotted the power spectrum and power density distribution of signals from a collision ball probe and differential pressure fluctuations for passage of a single bubble. They observed a high degree of similarity between the two signals, confirming that the signals from the ball probe were influenced by the local hydrodynamics. Liu et al. [94] compared the power spectral distribution of charge signals and pressure drop across the bed. It was found that a probe 0.54 m above the distributor experienced a transition of characteristic frequency from 0 to \sim 1 Hz, similar to pressure drop fluctuations. The characteristic frequency of the charges from this probe varied in a manner consistent with that of the pressure drop when the superficial gas velocity changed. Cheng et al. [95] analyzed the power spectra of induced current, showing that some frequency peaks from the riser were almost independent of the superficial gas velocity, indicating that these peaks might be caused by electrostatics and/or noise in the signal and not affected by the flow structure. The dominant frequency in the downer was fixed at 0.017 Hz, which may be because of the low frequency variation of solids mass flux and solids holdup, as well as the co-current flow pattern in the downer.

1.8.2.3 Non-stationary analysis

Many systems are chaotic and time series signals can be analyzed in phase space, with the long-term evolution of the system forming a topological structure called an attractor [97]. The attractor of a system answers the question “where is the system if one waits long enough”; it is a fingerprint of the system, reflecting its hydrodynamic state [98]. Demirbas et al. [99] analyzed the charge signals from an induction probe in a 2D fluidized bed by standard deviation and attractor comparison methods. The standard deviation demonstrates the degree of local charge separation, represented by the difference between the minimum and maximum of the data points (as measured by an electrometer) at a specific location. The attractor comparison method is based on the idea that the state of a fluidized bed at a given time can be determined by projecting all variables governing the system in a multidimensional space. The attractor comparison method statistically compares the attractors re-constructed from time series (for a selected reference period and evaluation period) and calculates a value, the S-value, defined as:

$$S = \frac{\hat{Q}}{\sqrt{V_c(\hat{Q})}} \quad (1.1)$$

where \hat{Q} is the estimator of Q , Q is the squared distance between two attractors, and V_c is variance. For attractors generated by the same mechanism, S has an expectation of zero and a standard deviation of one. An S -value > 3 indicates with more than 95% confidence that two attractors were generated by different mechanisms [100]. The authors compared the S -values of pressure and charge fluctuations while varying the relative humidity and found that the S -values of pressure and charge fluctuations were insensitive to RH in the first 150 min, and began to differ after the RH level decreased to less than 27%. There is no report on characterizing electrostatic signals in terms of other non-linear characteristics such as K entropy, Lyapunov exponent and correlation dimension.

Yu et al. [101] analyzed electrostatic potential signals from fluidized beds by Hurst analysis of wavelet decomposed signals. The micro-scale signal had only one Hurst exponent < 0.5 , whereas the meso-scale signals had one Hurst exponent > 0.5 and another < 0.5 , and the macro-scale signals had only one Hurst exponent > 0.5 . These three scales are believed to

reflect the action of particles, bubbles and macroscopic dynamics. For bubbling fluidization, the energy percentage of the meso-scale component is the highest, confirming that the electrostatic signals mainly reflect the motion of bubbles. The energy percentages of the three scales were sensitive to transitions in flow patterns.

1.8.2.4 Signal reconstruction

Electrical capacitance tomography (ECT) imaging is based on reconstruction of permittivity distribution from the measured capacitance. Electrostatic tomography (EST) involves static charge imaging of charged particles [102, 103]. It has been found that strong electrostatics can affect the ECT and could result in failure of data acquisition [104]. Zhou et al. [105] proposed a dual-mode sensor technique which uses the permittivity distribution obtained from ECT to provide a priori knowledge for the inversion of EST.

In order to determine the charge distribution around a single rising bubble in a two-dimensional fluidized bed, Chen et al. [23] reconstructed the charge signals measured by four induction probes with the assumption that the bubble is symmetrical and charge around the bubble remains the same as it rises. The emulsion phase far from the bubble was found to be charged negatively, and charge density decreased toward the bubble-dense phase interface, nearly reaching zero inside the bubble.

Chen et al. [11] tried to deduce particle charge density from charge signals recorded by a ball probe during single bubble injection experiments. Bubble size was estimated from the injected bubble volume, and charge density was estimated by inserting bubble diameter into an equation which represents the induced charge received by the probe when the injected bubble passes.

These options, from statistical and time-frequency to non-stationary and signal reconstruction, again show that the signals are influenced by local hydrodynamics. The signals contain useful information on charge levels in fluidized beds coupled with hydrodynamics. However, these methods were not able to derive the particle charge density and hydrodynamic property from the cumulative charge signals. Statistical and time-

frequency analyses are simple, but they cannot decouple particle charge density from probe signals. Non-stationary analysis and signal reconstruction methods may need complicated signal processing procedures and additional instrumentation. Hence, new model-based signal analysis methods are needed to extract the particle charge density and bubble properties.

Chapter 2 Probes Design, Fabrication and Calibration

2.1 Introduction

An electrostatic probe with two tips/sensors is proposed to decouple particle charge density and hydrodynamics. Two dual-tip probes were designed and constructed: one uses signals from two detectors of different materials with significantly different work functions to extract the charge density on particles and the bubble rise velocity by solving two equations, one for each probe. The other consists of two vertically-aligned tips of the same material. In this case, bubble properties were first obtained by analyzing the signals, and then used in estimating the particle charge density.

2.2 Design and fabrication

2.2.1 Design

2.2.1.1 Dual-tip (two-material) probe

A dual-tip (two-material) probe was designed and fabricated for the measurement of charge densities in bubbling fluidized beds. Unlike the two short pipes proposed by Matsusaka et al. [60], which are not suitable for local and online measurements of charge density in fluidized beds, the probes which are often used in fluidized beds can supply local and real-time information.

A probe containing two materials of significantly different work functions was developed. Titanium nitride (TiN) and nickel (Ni) were selected as the probe materials for their large difference in work functions (TiN: 2.9 eV and Ni: 5.0-5.4 eV, respectively, as shown in Table 2.2), relatively high hardness, low cost and widespread availability.

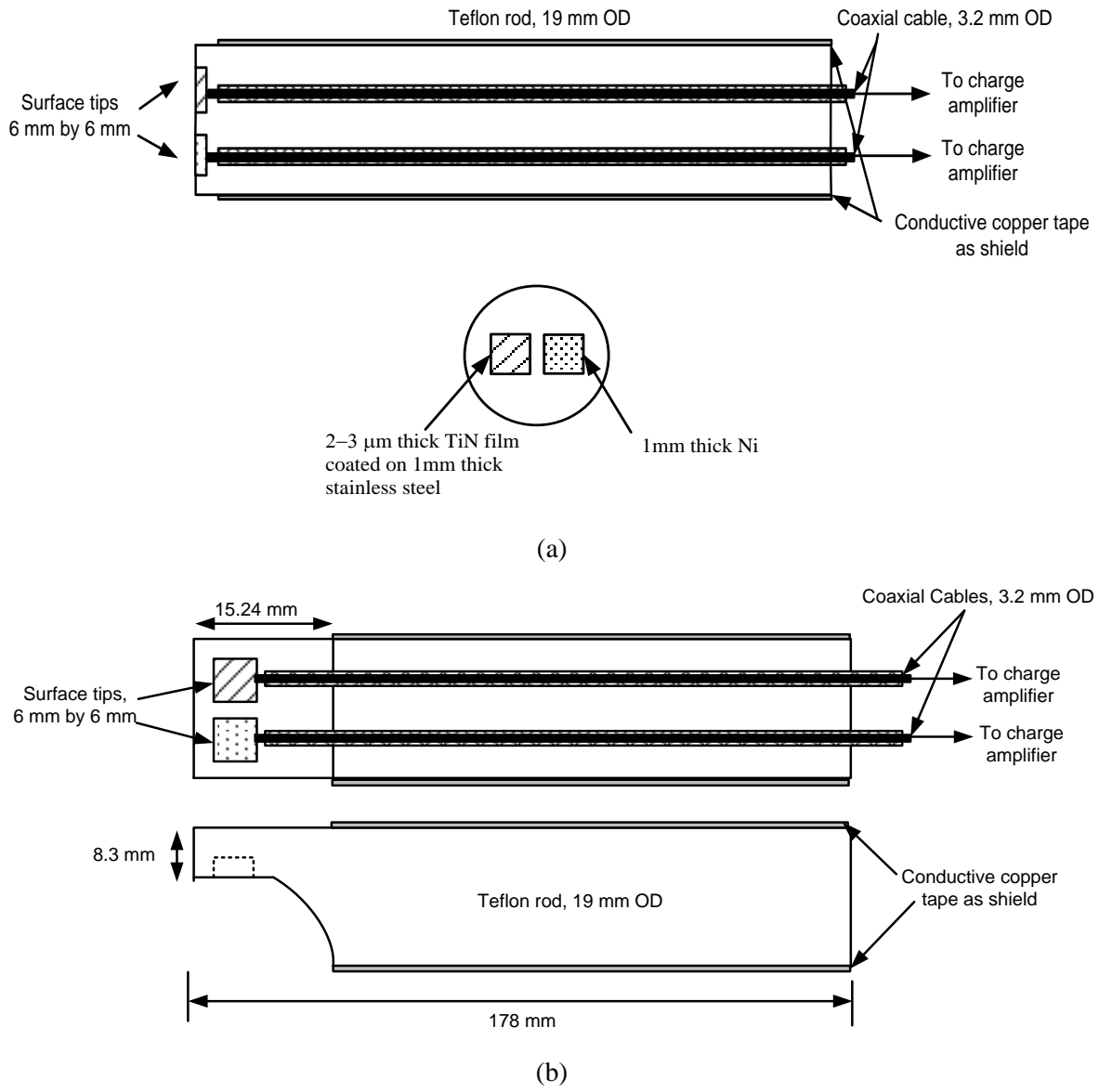


Figure 2.1 Schematic of dual-tip (two-material) probes: (a) design a; (b) design b.

Figure 2.1(a) illustrates one schematic design of the probe: In this case, the probe tip contains two metal pieces, each 6×6 mm in cross-section and 1 mm thick, attached to coaxial cables. If the probe tip size is too large, it may disturb local flow and be insensitive to the particle and bubble dynamics; if it is too small, the signals it registers from surrounding charged particles may be too weak compared to background noise. The probe tip size was selected based on initial tests which showed a reasonable response from the electrometer used in this study. A Teflon rod of 19 mm outer diameter prevented charge leakage and maintained a

high resistance to the ground. A copper tape was rounded outside the Teflon rod as electrical shield and grounded during measurements to reduce background electrical noise from the column walls.

Results presented below in Section 2.5.1.5 for tests when continuous streams of particles were directed onto the surface of the probes showed that the largest differences between currents transferred to/from the two probe materials occurred when the charged particles struck the probe at right angles. Therefore, a second probe was designed to allow charged particles to directly strike downward-facing metal tips, as shown in Figure 2.1(b).

2.2.1.2 Dual-tip (one-material) probe

Figure 2.2 shows a schematic of a dual-tip (one-material) probe with different configurations. Each tip is a square nickel piece (for consistence with the dual-tip (two-material) probe), 6×6 mm in cross-section and 1 mm thick, connected to a coaxial cable. The probes are suspended vertically in the bed to allow charged particles to directly strike their downward-facing metal surfaces. The probe was fabricated so that each tip can be retracted, with the results that the probe can be configured into a collision-collision probe with both tips protruding, “F” configuration, or a collision-induction probe, with only one tip exposed, “T” and “L” configurations. Also as shown in Figure 2.2, two types of probe tips were tested, one made of nickel, a 6×6 mm flat surface of thickness 1 mm; the other was made of stainless steel with a rod shape, 4 mm in diameter and 5 mm long.

This probe was designed with the two tips aligned one above the other; other possible configurations include side-by-side tips, one inner cylinder tip and the other outer annulus tip, and even probes with more than two tips. Those probes could be configured as collision probes or collision-induction probes. These probes can also be changed into induction-induction probes with both tips hidden. Because the calibration equation was obtained from a collision probe, the induction probe case was not tested in this work. Also the induction probe is unsuitable to provide local information on non-homogeneous flow systems (see Section 1.6.2.2).

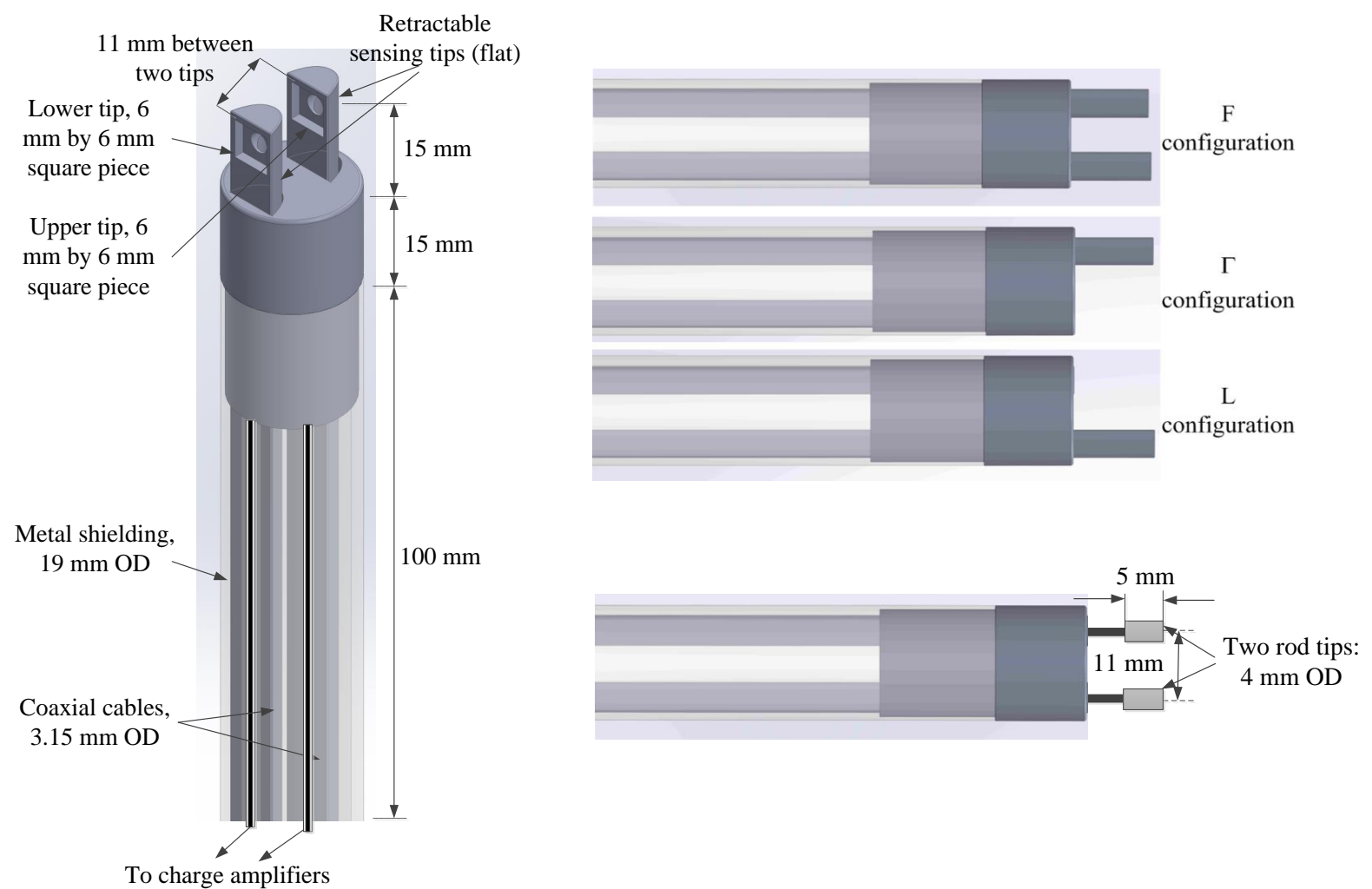


Figure 2.2 Schematic of dual-tip (one-material) probe with different configuration and tip shape: F configuration (two tips protruding); Γ configuration (upper tip protruding, lower tip retracted); L configuration (upper tip retracted, lower tip protruding); flat and rod shape tips.

The probes used in this work are summarized in Table 2.1.

Table 2.1 Summary of tested probes in this work.

Designation	Description	Diagram
2t2m	Dual-tip (two-material) probe	
	2t2ma (design a)	Figure 2.1(a)
	2t2mb (design b)	Figure 2.1(b)
2t1m	Dual-tip (one-material) probe	
	2t1mfF (flat tips, F configuration)	Figure 2.2
	2t1mf Γ (flat tips, Γ configuration)	Figure 2.2
	2t1mfL (flat tips, L configuration)	Figure 2.2
	2t1mr Γ (rod tips, Γ configuration)	Figure 2.2
	2t1mf Γ r (flat & rod tips, Γ configuration)	Figure 2.2
1t1m	One-tip (one-material) probe (conventional probe)	Similar to Figure 1.6(b)*

*See Moughrabiah et al. [42] for more precise diagram.

Both the 2t2m and 2t1m probes use two periods of signals provided by two sensing tips to decouple the signal. These two types of dual-tip probes are compared in Section 4.4.5.

2.2.2 Fabrication

The probes were fabricated by the following steps:

1. Probe head and tips were drawn in Solidworks® software and printed by a 3D printer (Objet30) using a proprietary material (VeroWhite). The printed parts were non-conductive and maintained high resistance to the ground, while a shield reduced background electrical noise from charges buildup on the column walls.
2. Metal sheets (25×25 mm in cross-section) were cut, filed into small pieces (6×6 mm in cross-section), and glued to coaxial wires by conductive epoxy. Inappropriate gluing may cause signal drift.
3. The coaxial wires were connected to Female BNC connectors by soldering.
4. The electrical insulation and performance of the probe were tested. The metal mesh of the two coaxial cables should not contact the tip. This prevents charge leakage and eliminates interference between the two current signals. In addition, the electrical wires should be as short as possible to minimize noise. Initial Tests showed that the charge measured by the probe with no contact with particles was close to the baseline (e.g. 0.001 V), two orders of magnitude less than when the probe was struck by charged particles (e.g. 0.1 V).

Resolving signal drift from a fabricated probe is illustrated by a case study in Appendix B.5.

Photographs of the fabricated probes appear in Appendix A.1.

2.3 Calibration of probes outside fluidized bed

The 2t2m probe is intended for use in a fluidized bed where complex two-phase flow, including bubbles and a dense phase are present. Thus the probe was tested and calibrated for both dilute phase and dense phase gas-solid flows in an ejector-funnel setup, which is able to generate charge densities on the particles with different magnitude and polarity. The probe was also tested by dropping charged particulate flows generated from a vertical tube and vibration tray setup, to make sure that there was a difference in the charge/current signals from the probe. The origin of such difference in the signals from the probe was also investigated in a motor-pulley setup, where the probe only experienced induced charge. Details are provided in the following paragraphs.

2.3.1 Ejector-funnel setup

A 2t2ma probe (see Table 2.1) was calibrated by using an ejector-funnel setup shown in Figure 2.3a and Appendix A.2. For dilute phase experiments, the Plexiglas funnel was removed. Glass beads were fed through a glass funnel and evenly dispersed into an ejector (RAV375H, AIR-VAC), then passed through a 90° elbow-type fitting and a straight vertical pipe. Four combinations of polyvinyl chloride (PVC, 25 mm long and 24 mm ID), stainless steel (SS, 22 mm long and 26 mm inner diameter) and aluminum (Al, 23 mm long and 25 mm inner diameter) were selected for the 90° elbow and pipe, as shown in Figure 2.3b. For dense phase experiments, the Plexiglas funnel collected the charged particles from the ejector, and then dropped them onto the probe surface.

In this case, glass beads belonging to Geldart Group B were used with a volume weighted mean diameter of 624 μm and size distribution of 360-830 μm , determined by a Malvern Mastersizer 2000. According to Cross [30], electron energies in an insulator are a function of

electron position in energy distribution, surface impurities and local atomic structure, as well as the chemical properties of the material. Therefore, the work function of an insulator must be determined experimentally. The work function, dielectric constant and resistivity of silicon dioxide (the major component of glass) and different types of glass are provided in Table 2.2. Before each test, the glass beads were washed with ethanol and water, then dried overnight to eliminate impurities and dust. All these tests were conducted at room temperature of 19~23°C; with environmental relative humidity of 27~52%.

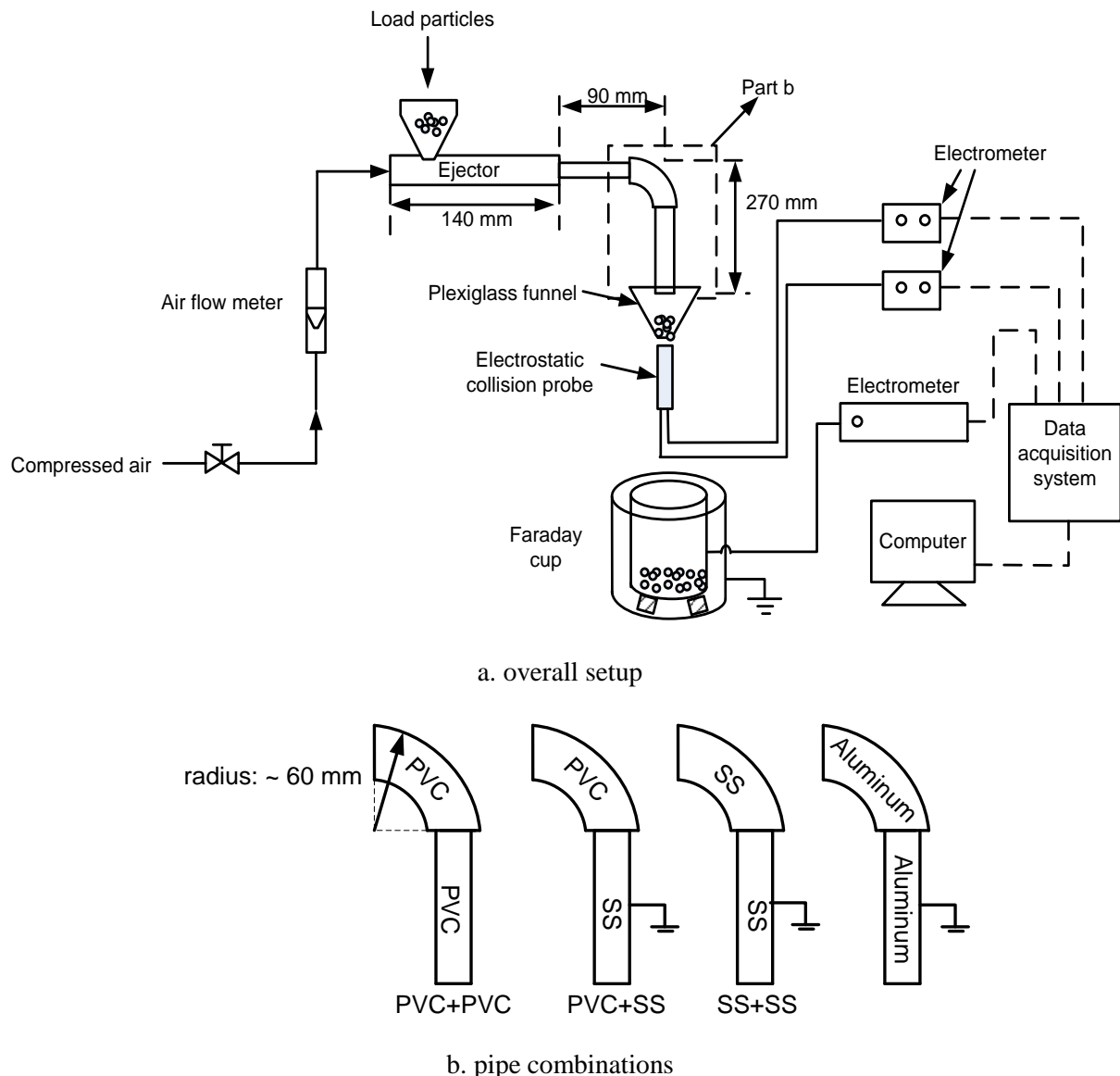


Figure 2.3 Schematic of experimental apparatus for ejector setup: (a) overall setup; (b) elbow and pipe combinations. (PVC: polyvinyl chloride; SS: stainless steel) (not to scale)

Table 2.2 Electrical properties and hardness of different materials used in the experiments [74, 106-115].

Materials	Glass	Titanium nitride (TiN)	Nickel (Ni)	Stainless steel (SS)	Polyvinyl chloride (PVC)	Aluminum (Al)
Property						
Work function, eV	silicon dioxide: 5.0	2.9	5.04-5.35 [107] 4.96-5.03 [108]	4.4	4.85 [109] 5.13 [110]	4.06~4.26 [107] 3.38~4.08[108]
Hardness, kg/mm ²	560	2300	1340	N/A	N/A	N/A
Dielectric constant	silicon dioxide: 3.78 iron-sealing glass: 8.41	N/A	N/A	N/A	3.2	N/A
Conductivity, S/m or Volume resistivity, Ω.cm	iron-sealing glass :1E ¹⁰ Ω.cm soda-borosilicate: 7E ⁷ Ω.cm silicon dioxide: >1E ¹⁹ Ω.cm	3~7E ⁷ S/m	1.43E ⁷ S/m [107] 6.9E ⁻⁶ Ω.cm [108]	1.45E ⁶ S/m [111] 90E ⁻⁶ Ω.cm [108]	1E ¹⁴ Ω.cm	3.5E ⁷ S/m [112] 2.62E ⁻⁶ Ω.cm [108]

2.3.1.1 Charge density

The total net charge, q (C), on particles after they pass through the ejector-funnel setup, was measured by an electrically insulated Faraday cup, connected to an electrometer (Keithley Model 6514). This Faraday cup was composed of an inner copper vessel of 150 mm inner diameter and an outer copper cup of 200 mm inner diameter, insulated from each other by Teflon blocks, with the outer cup grounded. The charge density, q_m (C/kg), of particles was obtained by dividing the net charge by the mass of particles collected by the Faraday cup,

$$q_m = \frac{q}{m_p} \quad (2.1)$$

2.3.1.2 Mass flow rate

The particle mass flow rates onto the probe tip surface were measured by a sampling probe, with dimensions identical to that of the probe, but without metal plates, so that particles enter the rectangular openings, are collected and then weighed. This allows ϕ_{tip} , the mass fraction of particles striking the probe, to be calculated as

$$\phi_{tip} = \frac{m_{p,collected}}{m_{p,dropped}} \quad (2.2)$$

2.3.1.3 Transferred current

The probe was placed 50 mm below the pipe orifice/Plexiglas funnel and aligned with the pipe/funnel. The charge signals from the two metal tips were amplified by two electrometers (Kistler model 5010B) and logged into a computer by a data acquisition card (PCIe-6321, National Instrument) and Labview software, with a sampling frequency of 100 Hz. For each run, the current transferred from particles to the probe was calculated by least-square linear fitting of the cumulative charge vs time curve, with the transferred current corresponding to the slope.

2.3.1.4 Particle velocity

Figure 2.4 shows the technique used to measure the average particle velocity (V_p) in dilute phase flow. A high-speed video camera (MS70K, Mega Speed), operating at 4000 frames per second, obtained images of particles striking the probe. The particle velocity was then calculated by dividing distances travelled by the time interval. Twenty particles were analyzed in each case. The particle velocity in dense phase flow was varied by changing the vertical distance between the funnel orifice and the probe surface, since the particle velocities decrease with decreasing acceleration distance [116]. The angle of collision (θ) (see Figure 2.4) was also varied.

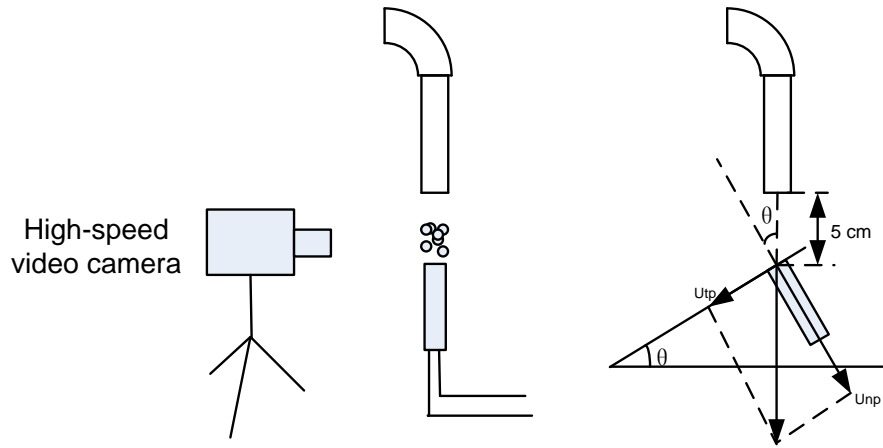


Figure 2.4 Schematic of technique for measuring average particle velocity at different angles of inclination of probe.

2.3.2 Motor-pulley setup

A motor-pulley system was built to check the induced charges on the 2t2m probe, as shown in Figure 2.5 and Appendix A.3. A DC compact gear motor (12 V, max 50 rpm) drives a plastic ball (0.38 m diameter) vertically at a constant velocity by rotating a pulley and a string. The ball can be moved upward or downward by changing the rotational direction of the motor. In each experiment, the plastic ball was charged negatively by rubbing with hair before being moved upward, then downward at 0.1 m/s. A 2t2mb probe (see Table 2.1) was placed at the middle of the total height in such a way that it would not hinder the ball's movement (no contact with the ball), with different positions as shown in Figure 2.5, to avoid differences in the relative horizontal positions of the probe and two tips. Because the ball is

much larger than the probe tip, induced charges received by the probe may be affected if the charged ball passes the probe asymmetrically. This can be verified by orienting the probe both upward and downward if there is any asymmetry.

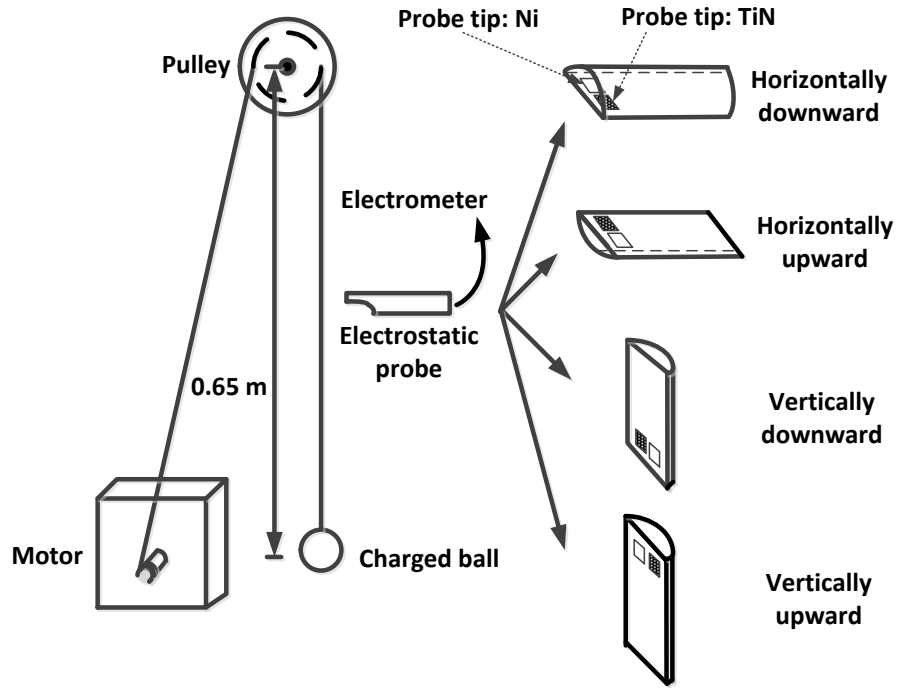


Figure 2.5 Experimental setup of motor-pulley system and different positions of 2t2mb probe tip (not to scale).

2.3.3 Vertical tube setup and vibration tray setup

Figure 2.6 shows a schematic of the vertical tube setup. Glass beads were loaded into a funnel with a flow control valve. Then a steady continuous flow of particles was allowed to drop through a vertical Plexiglas tube (0.05 m inner diameter) and collide with the probe. Particles gained charge through colliding with the tube inner surface. A 2t2ma probe (see Table 2.1) was used to measure the charges on the particles. The probe was placed at two locations in order to change the contact angle between the probe tip and the particulate flow: at the bottom of the tube with the probe tip surface facing upward and at the side of the tube with the probe tip surface vertical. The charge density on the particles was measured by a Faraday cup located at the bottom of the tube.

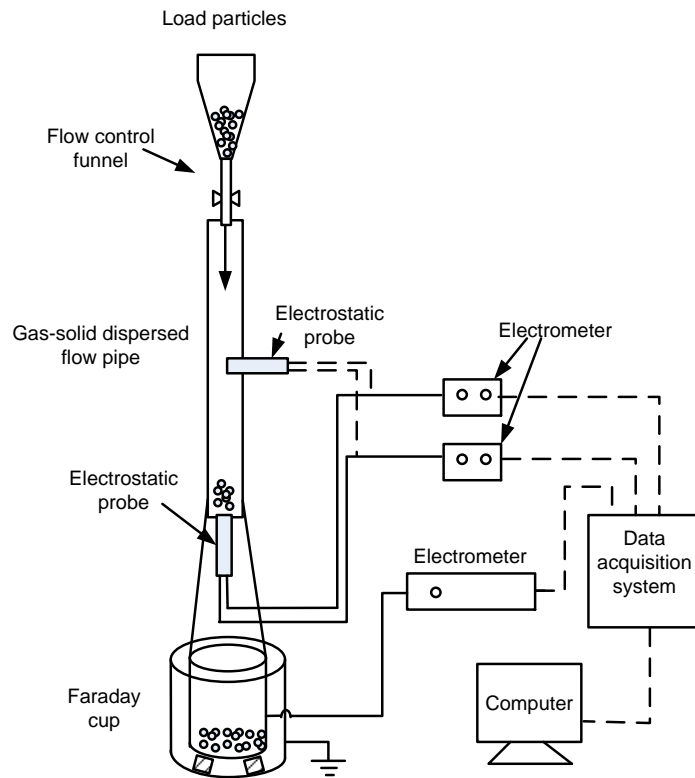


Figure 2.6 Schematic of experimental apparatus for vertical tube setup (not to scale).

Figure 2.7 shows a schematic of the vibration tray. Glass beads were continuously loaded onto a vibrated tray (ERIEZ 15A) and gain charges via contacts between the particles and metal tray. After the charged particles have collided with the probe, their charge densities were measured by the Faraday cup.

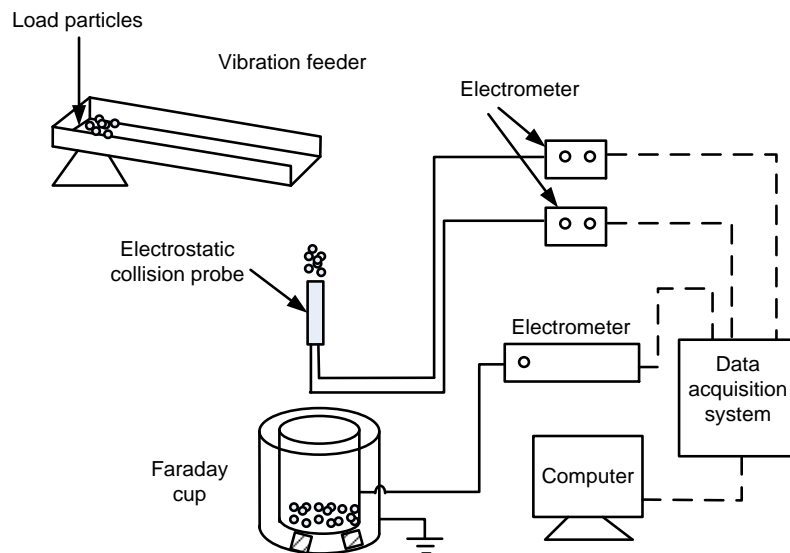


Figure 2.7 Schematic of experimental apparatus for vibration tray setup (not to scale).

2.4 Calibration of probes inside fluidized bed

Figure 2.8 shows a schematic of the two-dimensional Plexiglas fluidization column with inside dimensions 0.307 m wide, 22 mm thick and 1.24 m high (a picture is shown in Appendix A.4). The distributor contained seven evenly-spaced holes of 3 mm diameter. Three ports were installed on the back wall of the column to accommodate the electrostatic probe, in addition to a sampling port on the front wall and a bubble injection port. The sampling port (6.35 mm in diameter, inclined downward at 30° to the vertical) and the electrostatic probe were located on opposite faces of the column at the same height and horizontal position, in order to provide corresponding localized measurements.

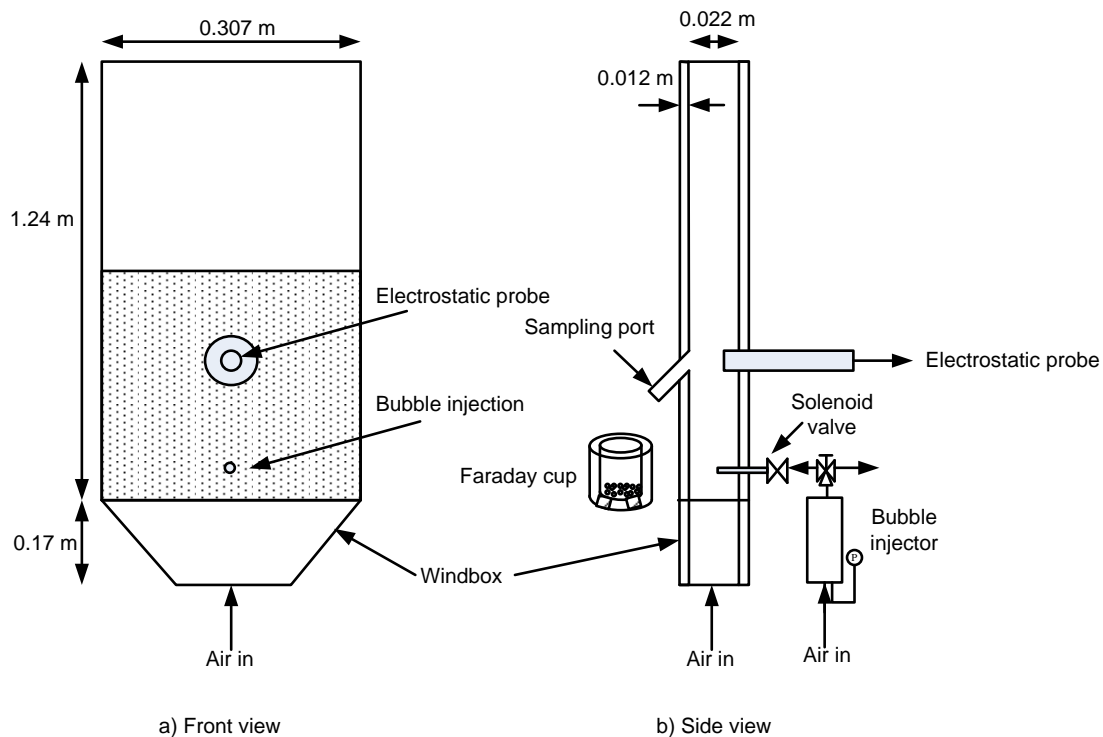


Figure 2.8 Schematic of two-dimensional column, bubble injection system and charge measurement system (not to scale).

Extra dry air was supplied to the bubble injector, where both compressed air and nitrogen, controlled by separate flow meters, were used as the fluidizing gas for the main column. The particles were glass beads, sieved to a size range of 500-600 μm , washed with water and ethanol, and dried in an oven overnight to eliminate possible impurities, dust and moisture. The bed was fluidized at different superficial gas velocities, with static bed heights of 0.30

and 0.50 m, and with the probe 0.22 and 0.42 m above the distributor, respectively. The average volumetric fraction of glass beads in the static bed was measured to be 0.63. All experiments were conducted at room temperature, 19~23°C. The relative humidity and temperature of both the gases and the environment were monitored by a humidity and temperature indicator (VAISALA HM141).

Charges on the particles inside the column were measured by both a Faraday cup (direct method) and a fabricated collision probe (indirect method). The Faraday cup results provided in-bed particle charge densities, which were used for probe calibration. Particles emerging from the sampling port passed through a sampling tube and dropped into the Faraday cup. The total lengths of the sampling port and the tube were designed to be as short as possible (~0.15 m). At the beginning of each sampling process, a plug at the end of the tube was removed and particles resting inside the sampling port and tube, as well as a small volume of bed particles, were first discharged and discarded until charge equilibrium was established in the sampling system. Particles from the bed were then continuously dropped into the Faraday cup, after which the plug was replaced to stop the sampling.

For bubble injection experiments, gas was injected via a solenoid valve into the column from a stainless steel cylinder of volume 1000 ml. The size of the injected bubbles was varied by adjusting the pressure in the cylinder and the opening time of the solenoid valve by means of a Labview program. A high-speed video camera (MS70K, Mega Speed), operating at 500 frames per second, recorded the bubble movement during single bubble injection and freely bubbling experiments. The electrostatic signal transmitted by the probe was synchronized with the frames recorded by the camera. Details of synchronization are illustrated in Appendix B.8. The probe was also sampled at 500 Hz in synchronization experiments. Based on the results in Sections B.10.1 and 5.3.1, for the dual-tip (two-material) and conventional probes, a sampling frequency of at least 100 Hz was required; and for the dual-tip (one-material) probe, a sampling frequency of 500 Hz was chosen. A sampling time of 5-10 min, which is higher than 2 minutes required for properly capturing the dynamic behaviour of the fluidized bed, was chosen for all the tested probes. Bubble rise velocities were determined from recorded video images using Image J software.

2.5 Results and discussion

2.5.1 Ejector-funnel setup

2.5.1.1 Electrostatic charging of particles in ejector-funnel setup

In the ejector-funnel setup, particles were charged by particle-particle and particle-wall collisions. The effects of gas velocity and pipe materials on the charge density of particles were examined.

2.5.1.2 Effect of pipe materials

Different elbow fittings and pipe materials (see Figure 2.3b) were utilized to change the charge density on the particles at the same mass flow rate or average particle velocity. Figure 2.9 shows that the particles gained positive charges when they interacted with PVC+PVC and PVC+SS pipes, and negative charges upon striking the SS+SS and Al+Al pipes. The polarity of charges on the particles depends on the work functions of the particles and contact materials. Of the four cases, PVC+PVC gave the highest positive cumulative charge on particles, while Al+Al provided the greatest negative cumulative charge. The 90° elbow pipe fitting mainly determined the final particle charge magnitude and polarity, because most charges were generated by collisions with the elbow. The cumulative charge curves in Figure 2.9 show an almost linear relationship between transferred charge and time, indicating uniform injection and flow of particles into the pipe.

In order to obtain reproducible results, all elbow fittings and pipes were grounded after each run, and the pipe was flushed with air to remove fine dust and dissipate charges on the pipe. For each run, the initial charges were maintained in the range of 0~2nC for the particles and < 1 nC for the pipe to minimize the possible influence of initial charges on the particles and the pipe wall. This approach was effective, as reflected by the almost constant slopes of the cumulative charge curves over the entire dropping periods of ~50 s in each case, as shown in Figure 2.9.

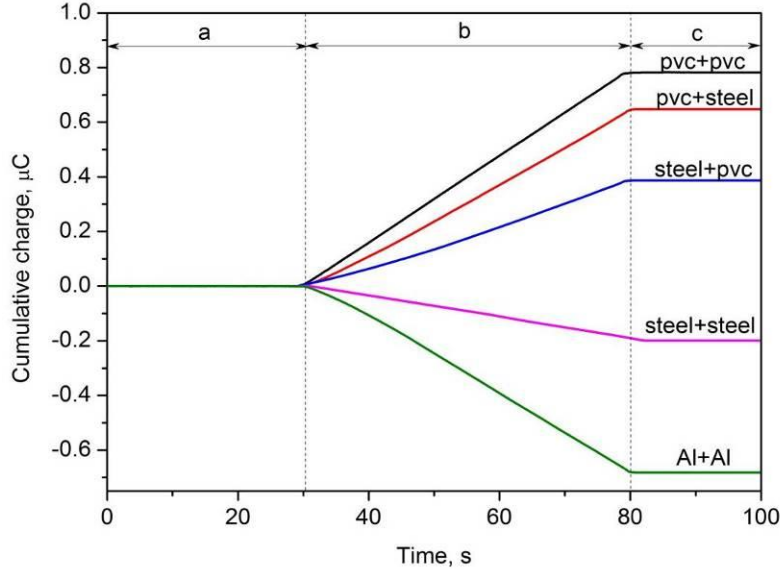


Figure 2.9 Charge carried by particles after passing through ejector setup shown in Figure 2.3b with different pipe materials; Average gas velocity =2.79 m/s (at outlet of vertical pipe with average pipe inner diameter is 25 mm).

2.5.1.3 Effect of gas velocity

Figure 2.10 shows that the cumulative charges increased with increasing gas velocity for the test with PVC+PVC. Similar trends were observed for PVC+SS, SS+SS and Al+Al pipe wall materials combinations. The abrupt change in slope for a gas velocity of 3.26 m/s was caused by an adjustment of the gas flow meter (increase in valve opening to required flow rate) in the middle of the test.

The above results indicate that the particle charge density could be altered by varying the gas velocity or by changing the pipe wall material. Watanabe et al. [117] developed an impact charging test rig for single particles acquiring charge during collision with a metal piece. The relationship between impact charge Δq and initial charge q_i was represented by a linear equation:

$$\Delta q = \Delta q_0 \left[1 - \frac{q_i}{q_e} \right] \quad (2.3)$$

where the characteristic charge Δq_0 is the transferred charge for particles with zero initial charge, and increases with increasing impact/collision velocity. The equilibrium charge q_e is

the charge needed to overcome the work function difference of two objects when there is no net charge transferred. It is independent of impact/collision velocity, but depends on the material properties. Our results are consistent with Eq.(2.3).

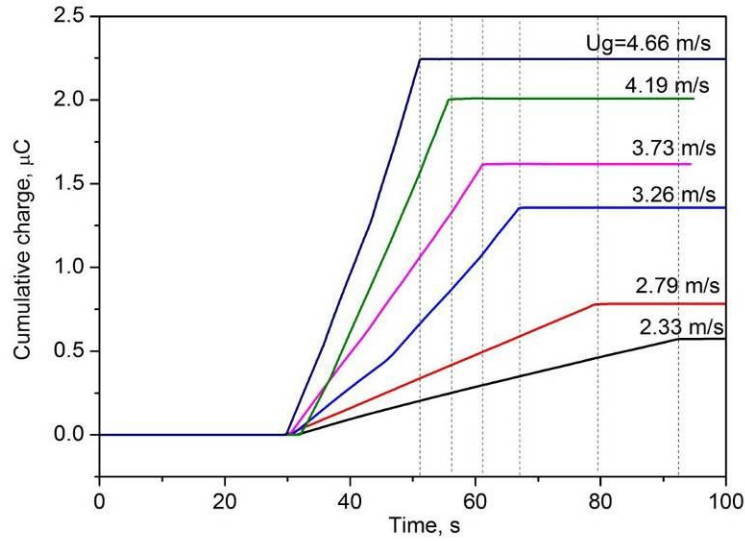


Figure 2.10 Charge carried by particles after passing through ejector setup with different gas velocities for PVC+PVC elbow and pipe combination (see Figure 2.3b).

2.5.1.4 Characteristics of particle charging with the probe

Figure 2.11 shows the charge density on particles in the dilute phase due to interactions with the four different pipe material combinations at different particle velocities, determined by the Faraday cup. Charge densities on the particles were reproducible in each case. Each reported value is the average of three measurements, with the error bars representing \pm one standard deviation from these values. As shown in Figure 2.10, the charge density typically increased with increasing gas velocity due to frictional charging. However, it did not change very much for SS+SS, compared with the other three wall material combinations. This discrepancy probably arose from differences in work functions and surface conditions (such as moisture content and roughness).

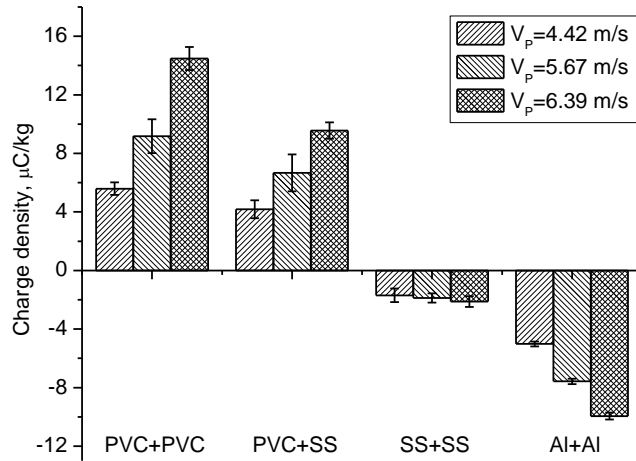


Figure 2.11 Measured charge densities on particles in dilute phase with different pipe materials and particle velocities.

The electrostatic charge signals measured by the probe are plotted in Figure 2.12, similar to the cumulative charge curve on particles measured by the Faraday cup. The charge, measured by the probe when charged particles contacted the probe surface, increased as particles continued to strike the probe surface over the dropping test period. The difference between the final and initial charges was the total charge transferred over the dropping test period, whereas the slope is a measure of the current transferred from the probe to the electrometer, regarded as the current transferred from the charged particles to the probe. Figure 2.12 shows that the transferred current varied with different charge densities on the particles. Similar results were found for other gas velocities. Figure 2.12 also shows that the transferred current measured by the Ni tip was larger than that measured by the TiN tip for the experimental conditions investigated. Eq. (2.3) predicts that the charge transferred during contact (Δq) depends not only on the equilibrium charge (q_e , which is related to the work function difference between particles and metal surface), but also on the initial charge on particles (q_i) and the characteristic charge (Δq_0 , which is related to particle contact velocity, effective contact area, surface condition and other material properties). The equilibrium charge transfer (q_e) is expected to be higher for the TiN tip than the Ni tip based on the work functions listed in Table 2.2 because the work function difference between TiN and glass is larger than that between Ni and glass, if one assumes that the work function of the glass beads used in the experiment is the same as that of pure SiO_2 . However, the magnitude of the

characteristic charge (Δq_0) is strongly influenced by the collision velocity between particles and the metal surface. As a result, the relative magnitude of transferred currents between the metal and the colliding particles for two different metals may vary (as shown in Figure 2.12) and even cross over when the particle velocity or flow rate changes [60].

The electric current generated from continuous collisions is given by

$$I_{tran} = -\frac{W_s}{m_p} \Delta q \quad (2.4)$$

This current is mainly transferred current, with the negative sign accounting for its direction.

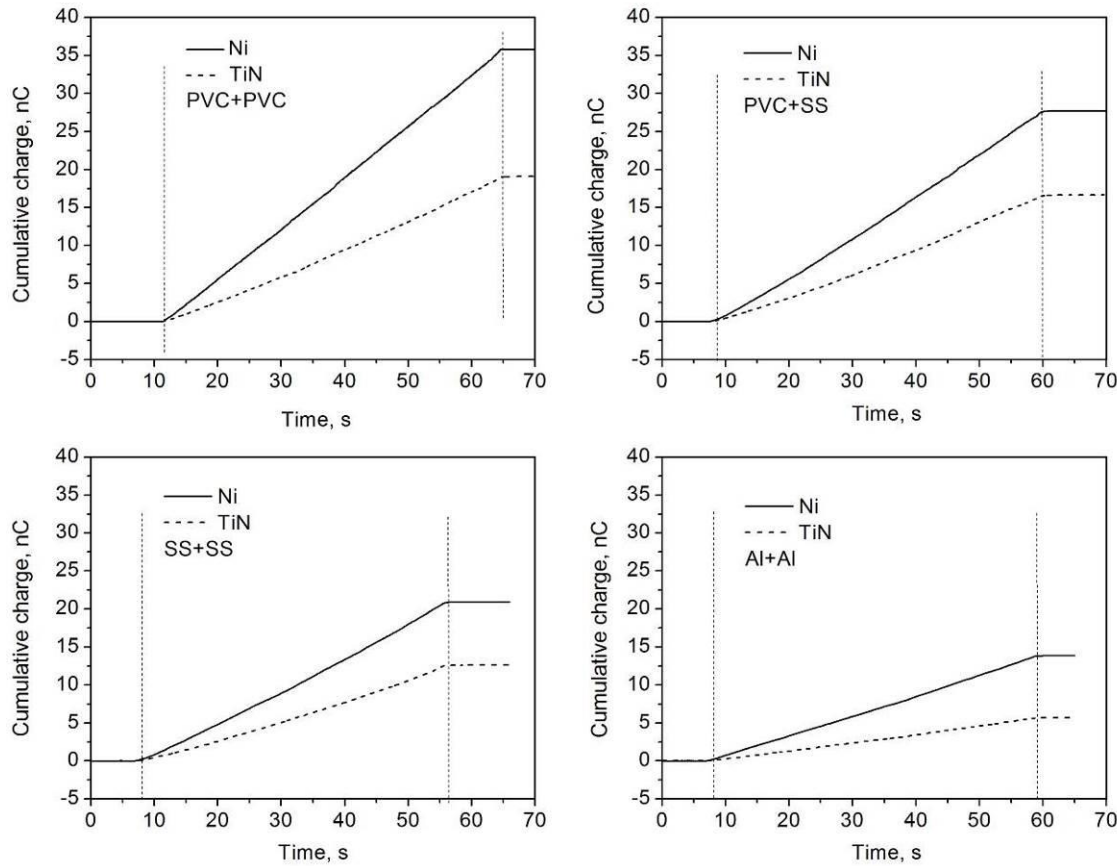


Figure 2.12 Typical cumulative charge signals measured by 2t2ma probe in dilute phase flow with different pipe materials; average particle velocity $V_p=4.42\text{m/s}$; collision angle $\theta=0$ degree.

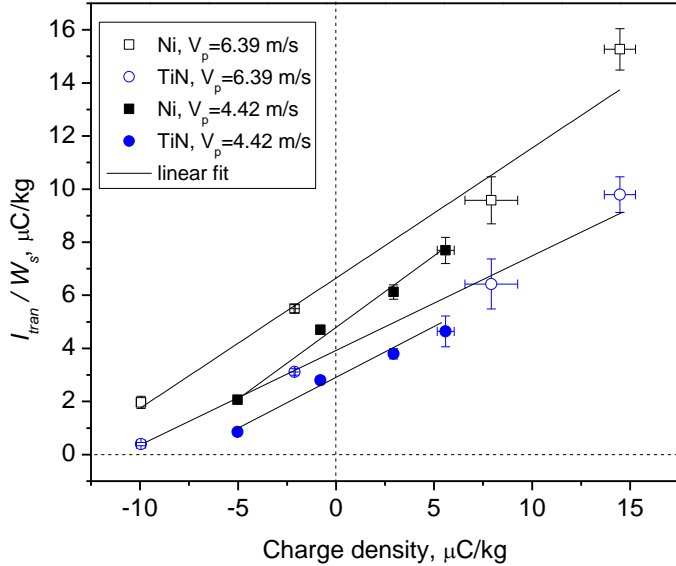


Figure 2.13 Characteristics of Ni and TiN tips at different particle velocities in dilute phase flow, collision angle $\theta=0$ degree; four pipe combinations as shown in Figure 2.14b.

Figure 2.13 plots the ratios of transferred current to mass flow rate at the probe tip against charge density for both probe tips. Error bars represent mean \pm one standard deviation of at least three repeated measurements. Linear relationships between I_{tran}/W_s and q_m for the two materials were obtained by least-squares fitting at a constant particle velocity. However, this linear equation varies with particle collision velocity: the higher the average particle velocity, the larger the current transferred to the probe. Therefore, the effect of particle velocity should be taken into consideration when correlating the transferred current, as in earlier correlations of John et al. [118] and Zhu and Soo [58]. The transferred current correlation proposed by Matsusaka et al. [60] does not include the particle velocity, whereas a similar equation developed by industrial vendors [90, 119] suggested a proportionality to the square of particle velocity. The following form of equation was able to correlate the transferred current from charged particles to probe tip with the particle charge density and collision velocity:

$$\frac{I_{\text{tran},i}}{W_s} = a_i q_m + b_i V_p^2 + c_i \quad (2.5)$$

Least-squares regression of all experimental data was conducted for the two materials exposed to dilute and dense phase flow, respectively. For dense phase flow ($0.87 \geq \varepsilon \geq 0.72$), fitting resulted in

$$a_i = 5.44, b_i = -1.32E^{-6}(C \cdot s^2 / kg \cdot m^2), c_i = -3.67E^{-7}(C / kg) \quad (Ni) \quad (2.6)$$

$$a_i = 2.99, b_i = -7.79E^{-7}(C \cdot s^2 / kg \cdot m^2), c_i = -6.13E^{-8}(C / kg) \quad (TiN) \quad (2.7)$$

For dilute phase flow ($\varepsilon > 0.99$),

$$a_i = 0.481, b_i = 8.84E^{-8}(C \cdot s^2 / kg \cdot m^2), c_i = 2.80E^{-6}(C / kg) \quad (Ni) \quad (2.8)$$

$$a_i = 0.346, b_i = 5.49E^{-8}(C \cdot s^2 / kg \cdot m^2), c_i = 1.53E^{-6}(C / kg) \quad (TiN) \quad (2.9)$$

Voidage within other range of values were not tested in this study. Obviously fitted constants a_i , b_i and c_i are related to the voidage, as shown in Eq. (C.28) of Appendix C.2, a_i are smaller as ε increases. b_i are more important for dense phase (Eqs. (2.6) and (2.7)) than dilute phase (Eqs. (2.8) and (2.9)). It is better that the probe could be calibrated in gas-solid flows with different voidage. The total net transferred charges include both triboelectrification and transfer of pre-charges. Therefore, the a_i , b_i and c_i constants are also functions of the properties of the probe materials and particles such as the dielectric constant of particles, work function difference between the probe tip material and the bed particles, probe tip size and particle size and shape (Eq. (C.28) in Appendix C.2). Changes in temperature and pressure are assumed not to significantly affect physical properties other than the work function of the probe tip and particles, which may also be affected by surface and environmental conditions. The experimental and calculated values from Eq. (2.5) with the above a , b and c values are compared in a parity plot in Figure 2.15. Coefficient of determination $R^2 = 0.98$ and 0.96 were found for Ni and TiN in the dilute phase flow, whereas R^2 was 0.94 and 0.95 for dense phase flow. Based on Eq. (2.5), the transferred current is a function of three variables: particle charge density (q_m), solid flow rate (W_s) and particle contact velocity (V_p). W_s is related to V_p by

$$W_s = \rho_p (1 - \varepsilon) V_p A_p \quad (2.10)$$

Since the transferred current is now a function of q_m and W_s , with the two current signals from the probe, the charge density in the fluidized bed can be estimated by solving Eqs. (2.5) and (2.10) together.

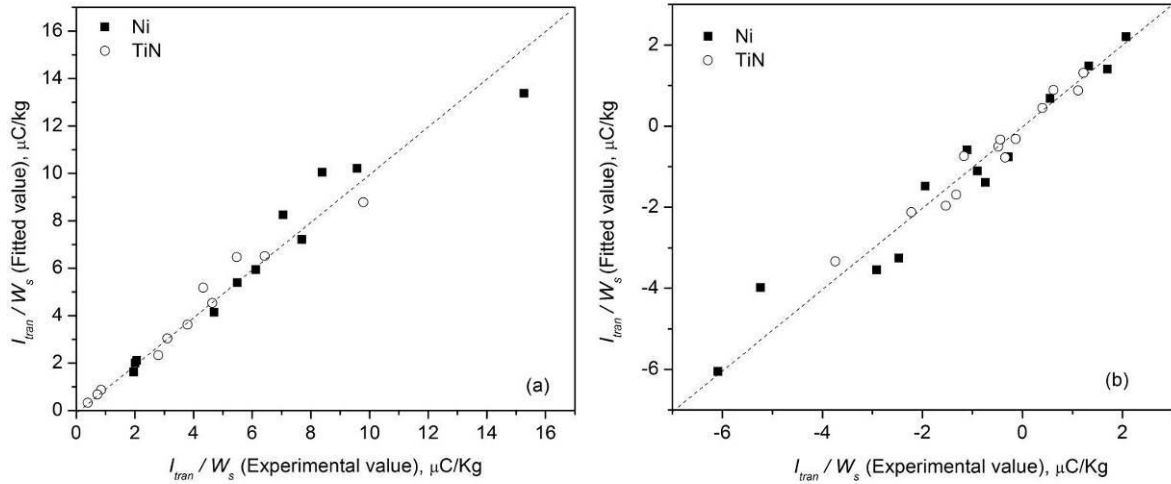


Figure 2.15 Comparison of fitted and experimental data for (a) dilute phase flow ($\varepsilon > 0.99$), and (b) dense phase flow ($0.87 \geq \varepsilon \geq 0.72$).

2.5.1.5 Effect of collision angle on current transfer from particles to probe

The effect of collision angle was investigated by inclining the probe surface to the solids flow, as shown in Figure 2.3b. Figure 2.16 shows the relationship between $-I_{tran}/W_s$ and collision angle θ for the two materials at different particle velocities in dilute phase for the Al+Al pipe material. Three runs were performed for each condition, with error bars again representing \pm one standard deviation from average values (three samples). For both materials, a higher normal component of collision velocity resulted in larger current transferred, consistent with the results in Section 2.5.1.3. $-I_{tran}/W_s$ for both materials first increased (from negative to positive), then decreased, as the collision angle increased from 0 to 90° , with a maximum at $\theta = 60^\circ$. Changing the collision angle alters the effective or projected contact area between the probe tip and charged particles. According to a rolling-slipping model [120], charged particles start to roll on the probe tip as they collide with the probe tip. For the contact angle smaller than a critical value, $\theta \leq \theta'$, increasing collision angle increases the effective contact area because of an increase in rotation of particles on the probe tip surface; for $\theta > \theta'$, the slipping (or sliding) effect increases gradually with angle, and the rolling speed of particles decreases, leading to a decrease in effective contact area. Figure 2.16 also shows that the polarity of the transferred current changes from positive to negative as the collision angle increases.

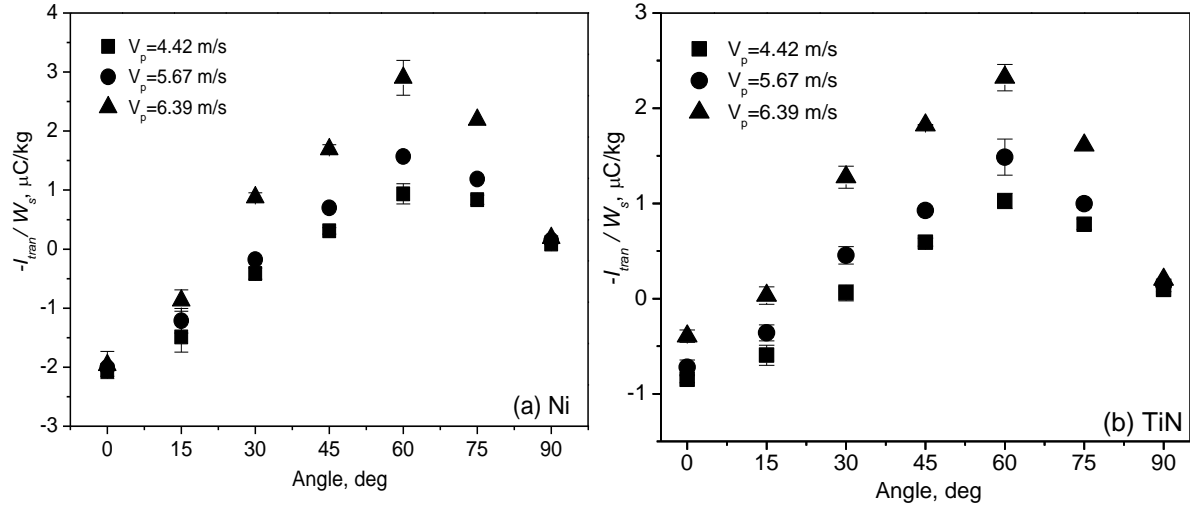


Figure 2.16 Relationship between $-I_{\text{tran}}/W_s$ and collision angle θ at different particle velocities for two tips in dilute phase flow: (a) Ni and (b) TiN.

Tanoue et al. [121] also found that the polarity of transferred current changes from positive to negative as impact angle increases when negatively charged glass beads continuously struck a rotating aluminum target for 10 min. They suggested that a contaminated layer of glass beads on the metal surface changed the effective contact area, leading to the polarity changes through a reversal of effective contact potential difference. John et al. [118] observed that total transferred charge is influenced by the polarity of charges on the particles when the charged aerosol particles collide with the metal surface. They explained this effect by assuming a p-n junction [122] at the particle-probe contact with both the probe surface and particles treated as semiconductor materials. For positive triboelectric charge, the particle surface material is p-type, and the probe surface material is n-type. When neutral particles contact the probe, electrons flow from the probe to the particles and positive charges are transferred from the particles to the probe until the contact potential is equilibrated. If the particles carry a negative charge, this produces a negative bias voltage across the junction, impeding charge transfer, and the effects are reversed.

In our case, the glass beads were pre-charged negatively by the ejector-funnel setup (Al+Al), and the triboelectric charge to be generated from particle-wall collision was expected to be positive based on Figures 2.11 and 2.12. The total net transferred charges include both triboelectrification and transfer of pre-charges. When the collision angle increased, the

normal component of particle velocity decreased, leading to less triboelectrification (positive charge decreases). At the same time, the increase of collision angle extended the contact time during which the more charges were transferred from charged particles by electrical conduction (negative charge increases). So the net transferred charge changed from positive to negative as the collision angle increased. The sign and magnitude of the measured total transferred current are determined by the combined effects of reduced triboelectrification from normal collision and increased transfer of charges from charged particles to the probe tips.

Figure 2.17 shows the difference between transferred currents for the two probe tip materials with changing collision angle θ at constant particle velocity. The maximum difference was found at $\theta=0^\circ$, and decreased with increasing collision angle. Increasing the collision angle changed both the effective contact area and the normal component of collision velocity. When the collision angle increased, the transfer of charges on particles increased due to the increased contact time. Since the surface conductivities of the two metal tips were very similar (see Table 2.2), the charges transferred from particles to the two materials were similar. Meanwhile, as the normal component of particle velocity decreased, the triboelectrification, which is a strong function of the work functions of the two contact materials, was reduced, leading to a gradual decrease in the difference of total transferred currents from particles to the two probe materials.

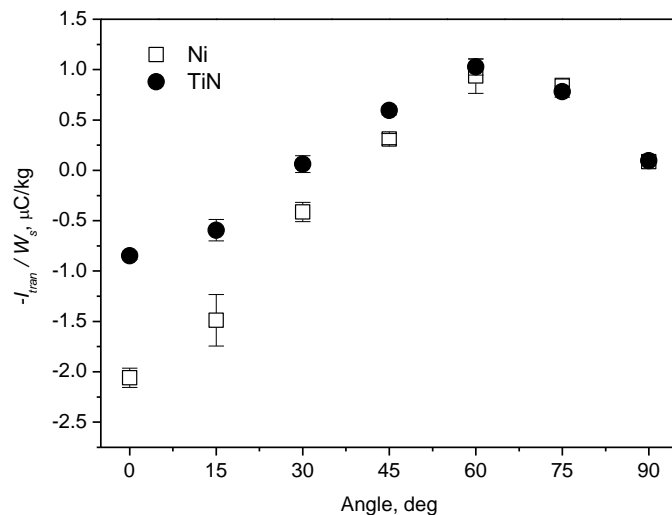


Figure 2.17 Relationship between $-I_{trans}/W_s$ and collision angle θ for two tips at $V_p=4.42$ m/s in dilute phase flow; pipe material combination: Al+Al.

2.5.2 Motor-pulley setup

To elucidate the difference in signals received by the two materials of the 2t2m probe when a charged object passes, a series of experiments was conducted in the motor-pulley setup and the two-dimensional fluidized bed to examine the performance of the two tips of different materials. In the motor-pulley calibration system, when the charged ball moved upward toward the probe, induced charges were detected by the probe, as shown in Figure 2.18. When the charged ball approached the probe, the induced charge measured by the probe negatively increased and reached a maximum magnitude; as the ball moved away from the probe, the magnitude of the induced charge decreased and almost returned to its original value. This was repeated four times, resulting in four peaks in the signal trace. The two probe tips of different materials showed almost the same minimum induced charges and signal traces.

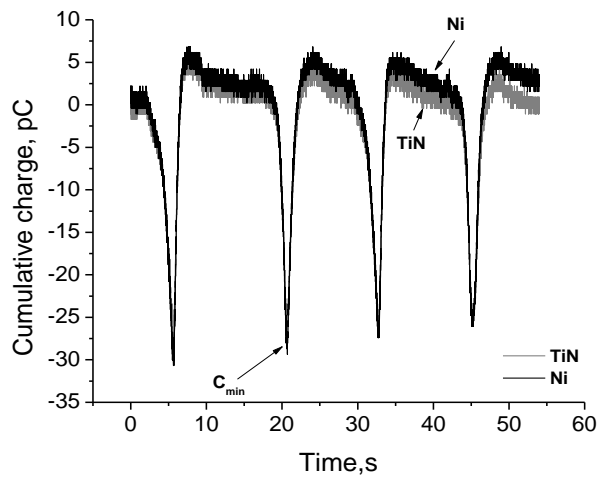


Figure 2.18 Cumulative charge signal measured by 2t2mb probe (facing vertically downward) when negatively charged ball passed by in motor-pulley setup.

To further check the difference in charge induction for the two materials, tests were carried out in the two-dimensional fluidized bed. To prevent direct contact with particles, the probe tip was covered by, in order of application, Teflon® PTFE tapes (for pipe thread and electrical insulation, respectively), tape and black electrical insulation tape. The particles were next fluidized at different superficial gas velocities to alter the charge levels on the particles. Figure 2.19 shows cumulative charge signals from the probe during single bubble

injection and free bubbling. Negligible differences are observed in the traces and amplitudes for signals from the two materials for these two cases. For single bubble injection, the charge signal first decreased due to the negatively charged bed particles which have a relatively higher charge density than was the case in Figure 2.24, and then showed a peak when the bubble passed. In free bubbling, the charge signals from the two tips did not show a substantial increase/decrease within 200 s, indicating that no significant transfer of charges was measured by the probe.

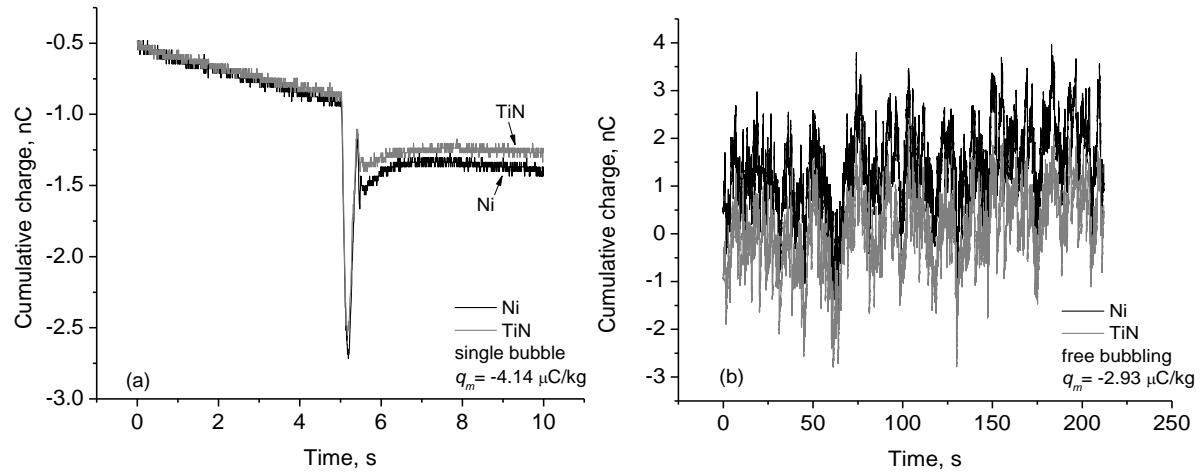


Figure 2.19 Cumulative charge signal measured by covered tips of 2t2mb probe in two-dimensional fluidized bed: (a) single bubble; (b) free bubbling, $U_g = 0.30$ m/s.

The difference between the two tips was quantified by the ratio of their minimum charges, i.e., $C_{\min, \text{TiN}} / C_{\min, \text{Ni}}$. Figure 2.20 (a) shows this ratio for the probe at different locations relative to the ball in the motor-pulley experiment. The ratio ranged from 0.89 to 1.12, with an average of 0.99. In Figure 2.20 (b), the ratio maintained an average value of 0.92 for various particle charge densities in the two-dimensional fluidized bed, confirming that the ratio of induced charges from the two materials varies very little with changing particle charge density.

From both the motor-pulley experiments and the fluidization experiments, we can conclude that the difference in charge/current signals for the two materials of the 2t2m probe arose mainly from charge transfer during particle-probe collisions. The small difference in induction charges may result from small differences in the probe tip sizes, as well as slight asymmetry of trajectory as charged objects passed the probe.

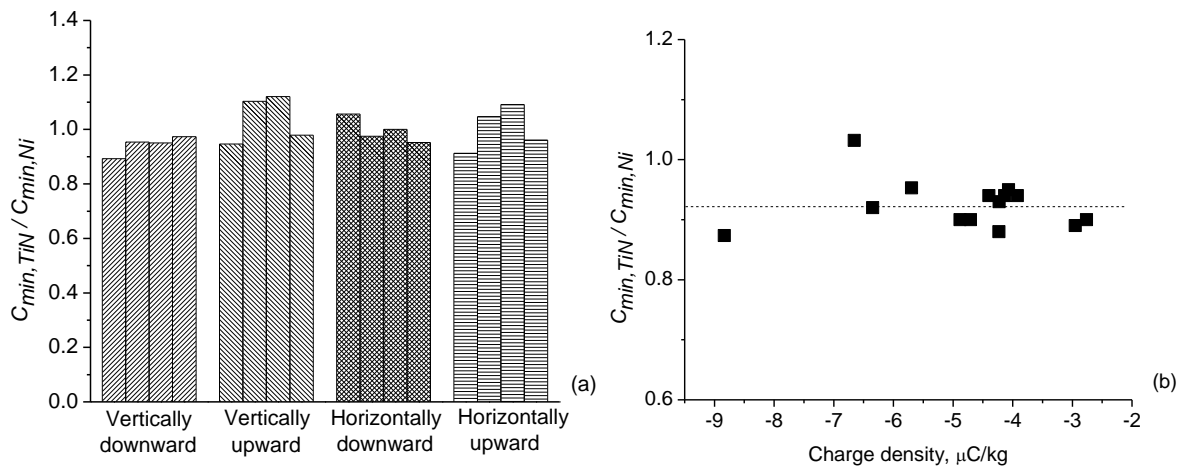


Figure 2.20 Ratio ($C_{min,TiN} / C_{min,Ni}$) from 2t2mb probe (see Table 2.1) (a) in motor-pulley setup; (b) in two-dimensional fluidized bed.

2.5.3 Vertical tube and vibration tray setups

Figure 2.21 shows cumulative charges from the 2t2ma probe (see Table 2.1) at two locations in the vertical tube setup.

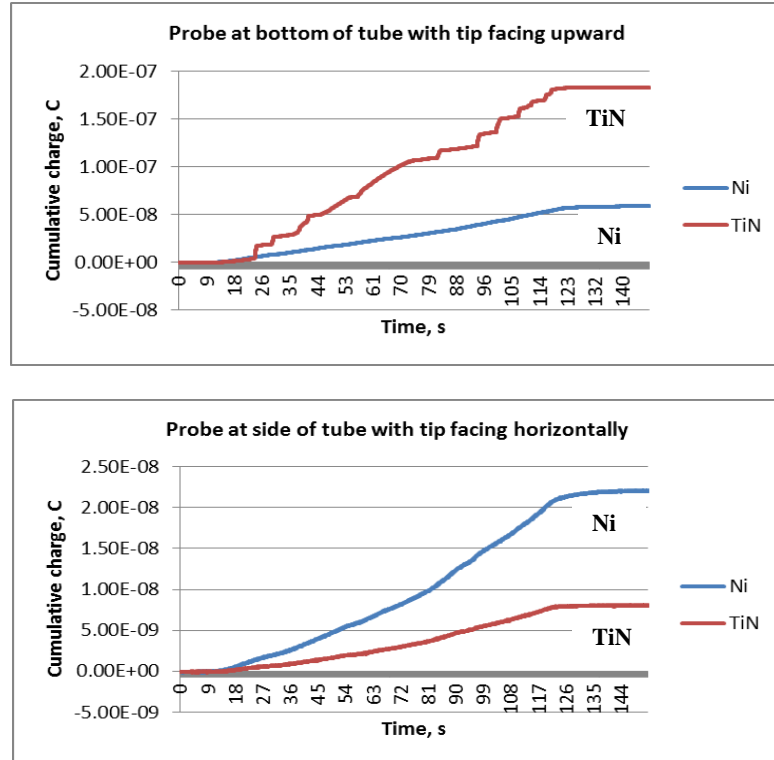


Figure 2.21 Cumulative charge signals from 2t2ma probe at different locations in vertical tube setup, shown in Figure 2.6.

For both locations, there were substantial differences between the signals from the two tips. The charge signals were higher in magnitude when the probe was located at the bottom of the tube, with its tip facing upward than when at the side with the tip oriented vertically. Also the relative magnitudes of signals from the two tips changed between these two cases, similar to the previous results in the ejector-funnel setup (Section 2.5.1). The probe was also rotated to change the relative positions of the two tips, in order to investigate whether differences could be caused by non-uniform particulate flow. Both cases showed that substantial differences existed between the signals from the two tips regardless of their relative positions.

The probe was also checked with one tip covered by Teflon tape and placed at the bottom of the tube. Charge signals from the probe with one tip covered appear in Figure 2.22. In both cases, the signals were compared between both tip uncovered and one tip covered. The slopes of signals from the covered tip decreased because of reduced charge transfer. Differences continued to exist in the signals from the two tips.

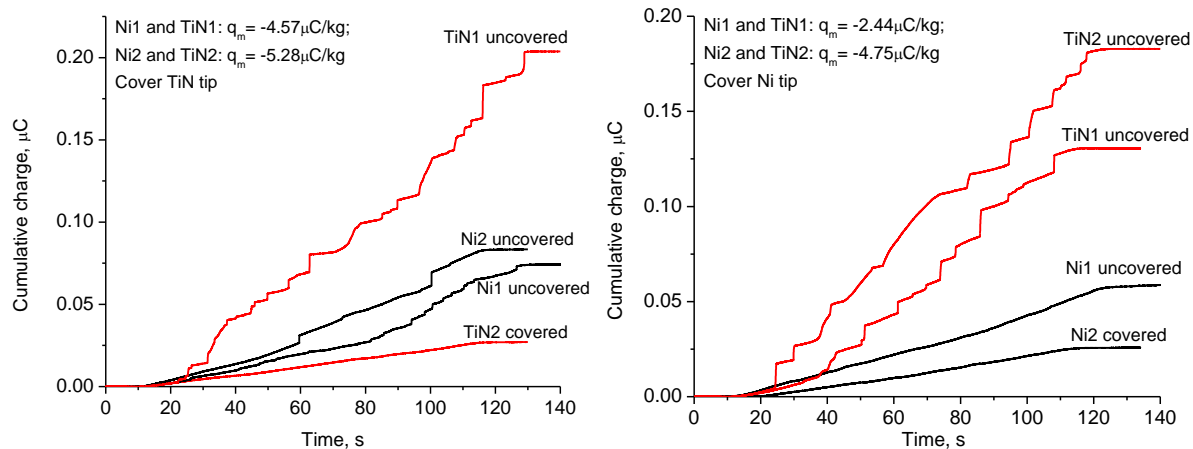


Figure 2.22 Comparison of cumulative charge signals from 2t2ma probe with both tips uncovered and one tip (Ni or TiN) covered in vertical tube setup (probe at bottom of tube with probe tip facing upward).

Cumulative charge signals from the probe in the vibration setup are plotted in Figure 2.23. When charged particles started to drop onto the probe surface, cumulative charges for both tips increased, reaching constant levels after dropping, with substantial differences between the two signals. The slopes of the charge signals versus time represent average currents transferred from the charged particles during the dropping. This confirms that there was a substantial difference between the signals from the two tips.

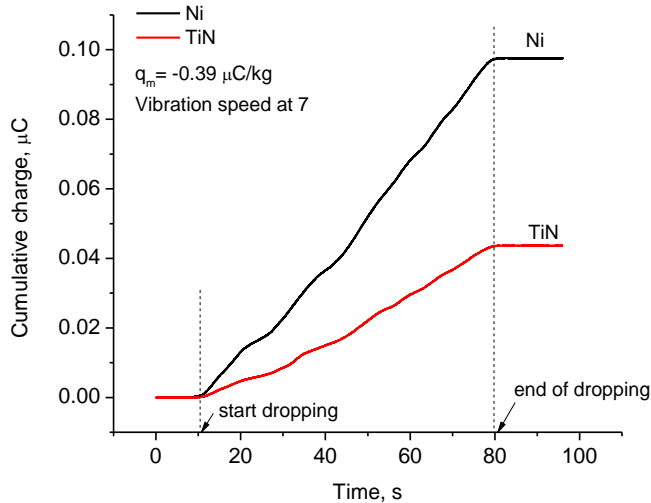


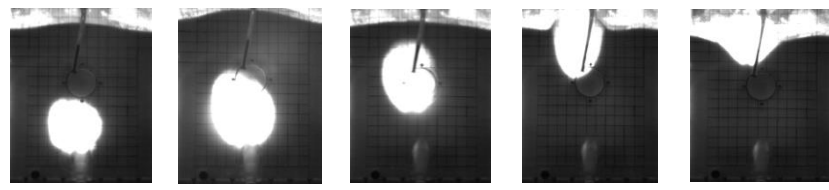
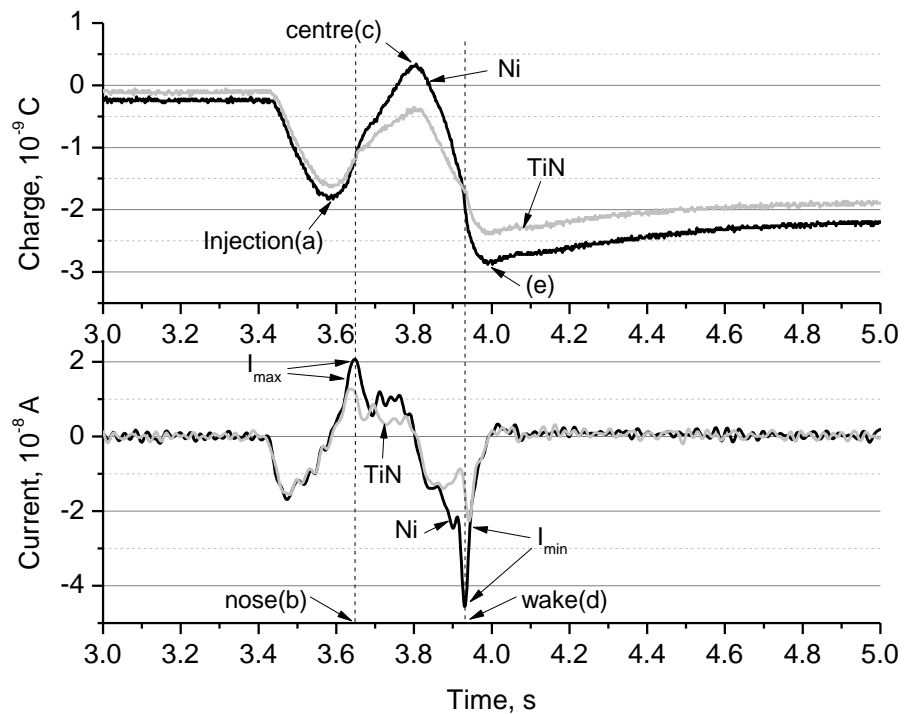
Figure 2.23 Cumulative charge signal from 2t2ma probe in vibration tray setup.

2.5.4 Two-dimensional fluidized bed

The 2t2m probe and 2t1m probe (see Table 2.1) were next deployed and calibrated in a thin “two-dimensional” fluidization column to assist with the interpretation and confirmation of results for single bubble injection experiments.

2.5.4.1 Single bubble injection experiments

Figure 2.24 shows typical charge and corresponding current signals measured by the 2t2mb probe (see Table 2.1) during single bubble injection with a background superficial gas velocity of U_{mf} . Gas was injected via a solenoid valve into the column from a stainless steel cylinder. The time-varying signal from the bubbling bed differs greatly from that determined previously for homogeneous continuous particle flow, which resulted in a nearly constant transfer current. In the fluidized bed, the current signal was strongly affected by local hydrodynamics, with fluctuations caused by passage of bubbles. Also the magnitude of particle charge density was much greater in the fluidized bed.



(a) 3.578 s (b) 3.648 s (c) 3.806 s (d) 3.930 s (e) 3.990 s

Figure 2.24 Charge (raw signal), current (derivative of charge) signal from 2t2mb probe and synchronized snapshots for single bubble injection in two-dimensional fluidized bed. (Back pressure for bubble injection: 345 kPa; solenoid valve opening time: 0.2 s; $\sim 2E-4$ m³ pressurized air injected; centre of probe location: 0.17 m above bubble injector; bubble injector: 0.04 m above distributor)

The two peak values of current signals, I_{\max} and I_{\min} , received by the electrostatic probe as each bubble passed, are directly related to the charge density of the particles surrounding the bubble, as well as to the bubble size, shape and rise velocity. Comparison of the synchronized video frames with current signals indicates that the first minimum corresponded to the moment of bubble injection, whereas the maximum peak, I_{\max} , was associated with the bubble nose reaching the probe, and the second minimum peak, I_{\min} , corresponded to the arrival of the bubble wake. I_{\min} arises from a combination of transferred

and induced currents, and is therefore a function of particle charge density and bubble properties. The difference in magnitudes of the minima corresponding to the two materials is due to different transferred currents. The charge density in the bed was changed by fluidizing particles at different U_g , then reducing U_g to U_{mf} and injecting a single bubble. Particle charge density was measured by discharging bed particles through the sampling port into the Faraday cup, with the results given in Table 2.3. It is seen that the magnitudes of I_{peak} (minimum peaks in this case because relative larger magnitude than maximum peaks) increased as the size of injected bubbles increased, while the particle charge density remained more or less constant, consistent with results reported previously [11, 41]. The magnitude of I_{peak} also increased as the particle charge density increased for a given bubble size.

Table 2.3 Directly measured charge density (q_m), bubble size (D_B) and rise velocity (U_B) and current peaks (I_{peak}) from single bubble injection experiments.

q_m (C/kg)	U_B (m/s)	D_B (m)	$I_{peak,Ni}$ (A)	$I_{peak,TiN}$ (A)
-8.02E-7	0.40	0.052	-1.29E-08	-1.21E-08
-8.70E-7	0.37	0.06	-1.76E-08	-1.44E-08
-1.04E-6	0.44	0.077	-2.06E-08	-1.76E-08
-9.00E-7	0.41	0.062	-2.27E-08	-1.61E-08
-9.66E-7	0.47	0.088	-2.80E-08	-2.45E-08
-1.77E-6	0.53	0.112	-3.43E-08	-2.94E-08
-1.55E-6	0.48	0.091	-3.60E-08	-3.09E-08
-7.74E-7	0.51	0.101	-3.61E-08	-3.11E-08
-1.05E-6	0.54	0.113	-3.77E-08	-2.95E-08
-1.68E-6	0.58	0.131	-4.42E-08	-3.29E-08
-1.05E-6	0.55	0.119	-4.89E-08	-4.09E-08
-2.14E-6	0.47	0.087	-5.96E-08	-2.95E-08

Figure 2.25 shows current signals measured by 2t1mfF probe (see Table 2.1) following single bubble injection into the bed of glass beads, with a background superficial gas velocity of U_{mf} . Comparison of the synchronized video frames with current signals from both tips shows an initial minimum of no interest corresponding to bubble injection, whereas the maximum peaks, $I_{max,2}$ from the lower tip and $I_{max,1}$ from the upper tip, are associated with the bubble nose reaching the probe, and the minimum peaks, $I_{min,2}$ and $I_{min,1}$, correspond to

arrivals of the bubble wake. The times corresponding to these peaks, $t_{\max,1}$ and $t_{\min,1}$ from the upper tip, $t_{\max,2}$ and $t_{\min,2}$ from the lower tip, were in order $t_{\max,2} < t_{\max,1} < t_{\min,2} < t_{\min,1}$, indicating that the injected bubble passed the two tips in succession.

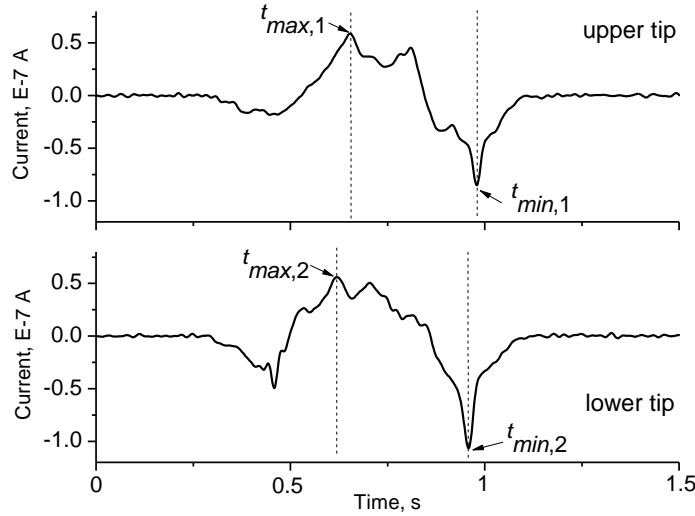
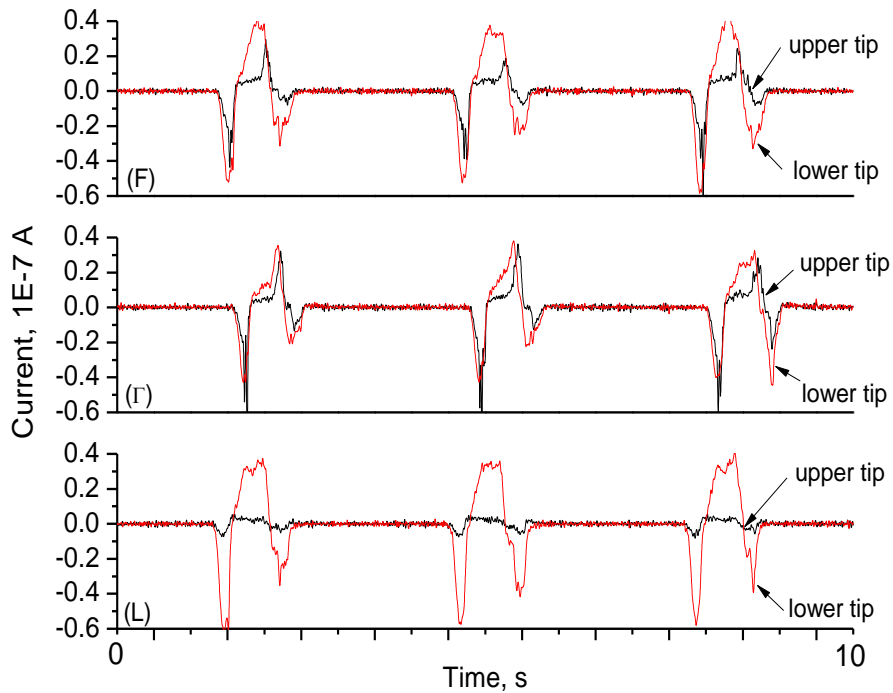


Figure 2.25 Current signals from 2t1mfF probe for single bubble injection in two-dimensional fluidized bed containing glass beads (Pressure in bubble injector: 345 kPa; solenoid valve opening time: 0.2 s; $\sim 2 \times 10^{-4} \text{ m}^3$ pressurized air injected; centre of probe port 0.17 m above bubble injection port; bubble injector: 0.04 m above distributor).

Current signals from the 2t1m probe with different configurations in multiple bubble injection experiments are shown in Figure 2.26. Clear time delays appeared between the peaks from both the F and Γ configurations, whereas the signal from the L configuration failed to show clear time delays between the peaks from the two tips. For F and Γ , one tip registers signals as a collision probe, while the other generates a reference signal caused only by induction. Comparison of the F and Γ signals shows that the peak amplitudes from the upper tip were larger for Γ , because of the lack of obstruction from the lower tip, while the amplitudes and shapes of peaks from the lower tip were similar for F and Γ . Comparison of the F and L signals reveals that the signals from the lower tip did not differ much, while the upper tip signal had much smaller peak amplitudes, and the shape of signals changed as well. This may be because of interference with the induced charge received by the upper tip (retracted) from the lower tip. The shape of current signals from each protruding tip was not affected by the presence of the other tip, and there was little change in peak amplitudes. The signals from the retracted tip were greatly affected by its position relative to the protruding tip.



(F: both tips protruding, Γ : only upper tip protruding, L: only lower tip protruding as shown in Figure 2.2.)

Figure 2.26 Current signals from 2t1m probe with different configurations for multiple bubble injections in two-dimensional fluidized bed containing glass beads (Pressure in bubble injector: 345 kPa; solenoid valve opening time: 0.2 s and closing time: 3 s; centre of probe port 0.17 m above bubble injection port; bubble injector: 0.04 m above distributor).

2.5.4.2 Freely bubbling experiments with synchronization

In the freely bubbling experiments, the electrostatic signals transmitted by the 2t2mb probe were synchronized with photographic frames recorded by the camera (see Section 2.4). The charge density was varied by changing the superficial gas velocity, and measured by releasing particles into the Faraday cup during freely bubbling. The charge density remained the same when the bed was continuously fluidized at constant U_g , but decreased when the superficial gas velocity was reduced to U_{mf} . Figure 2.27 shows the bed charge density measured from the sampling port by the Faraday cup after free bubbling when fluidizing with compressed air and with nitrogen. A higher charge density was generated with nitrogen as the fluidizing gas, presumably due to the lower humidity of the nitrogen. The charge density decreased for both cases after the fluidizing velocity was lowered to its minimum fluidization value. The charge density for using nitrogen showed a slight increase at 10 minutes, likely in error caused by the Faraday cup measurements, although it did not affect the overall

decreasing trend of charge density with time. When particles were fluidized, they acquired charges, mainly due to particle-particle and particle-wall collisions, whereas at minimum fluidization, collisions nearly disappeared and the charge generation rate decreased.

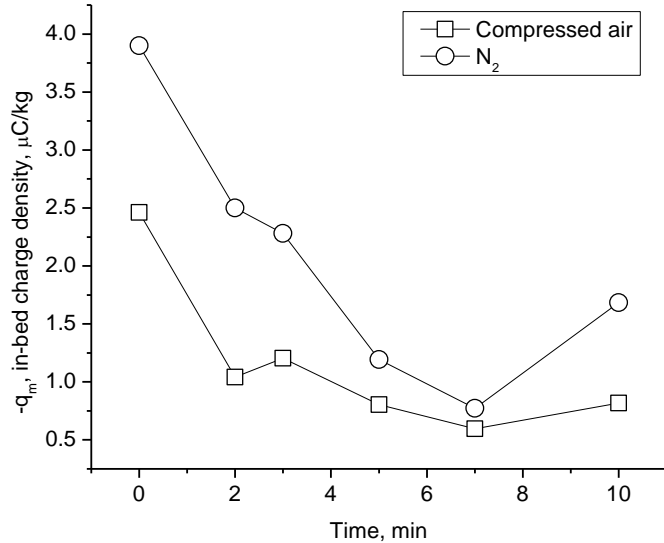


Figure 2.27 Charge density decay curve after cutting off gas flow following free-bubbling with compressed air (RH=10%) and nitrogen (RH=2%).

In these experiments, single bubbles passing the probe in vertical alignment were selected from recorded videos for analysis to obtain bubble rise velocity, and corresponding current peaks were selected from the synchronized 2t2mb probe signals. Results from freely bubbling experiments with synchronization appear in Table 2.4. The magnitudes of I_{peak} from both materials increased as the particle charge density increased, and a similar pattern was found when the bubble rise velocity increased. Comparison of Tables 2.3 and 2.4 reveals that particle charge densities were higher during freely bubbling than after single bubble injection, in agreement with results in Figure 2.27. The current peaks were also larger in free bubbling than for single bubble injection.

Table 2.4 Directly measured charge density (q_m), bubble rise velocity (U_B) and current peaks (I_{peak}) from freely bubbling experiments with synchronization (see Section 2.4).

$U_g - U_{mf}$ (m/s)	q_m (C/kg)	U_B (m/s)	$I_{peak,Ni}$ (A)	$I_{peak,TiN}$ (A)
0.12	-4.82E-6	1.05	-1.02E-6	-6.91E-7
0.12	-4.61E-6	1.05	-1.03E-6	-5.76E-7
0.12	-5.35E-6	0.91	-8.39E-7	-5.26E-7
0.12	-5.35E-6	1.11	-7.73E-7	-4.28E-7
0.12	-5.35E-6	0.91	-8.88E-7	-5.10E-7
0.09	-4.25E-6	0.77	-6.17E-7	-5.02E-7
0.09	-4.25E-6	0.77	-5.76E-7	-2.22E-7
0.09	-4.27E-6	0.91	-5.10E-7	-3.37E-7
0.09	-4.51E-6	0.91	-5.02E-7	-3.95E-7
0.09	-4.51E-6	0.71	-6.82E-7	-5.02E-7
0.06	-3.97E-6	0.67	-2.96E-7	-1.81E-7
0.06	-3.97E-6	0.80	-5.18E-7	-4.03E-7
0.06	-3.97E-6	0.67	-4.19E-7	-4.03E-7
0.06	-4.23E-6	0.77	-3.95E-7	-3.78E-7
0.06	-4.42E-6	0.83	-7.24E-7	-4.85E-7
0.06	-4.42E-6	0.83	-7.89E-7	-3.95E-7
0.02	-2.02E-6	0.59	-2.88E-7	-2.30E-7
0.02	-2.02E-6	0.59	-9.87E-8	-7.40E-8
0.02	-2.02E-6	0.56	-9.87E-8	-7.40E-8
0.02	-2.02E-6	0.40	-1.40E-7	-9.04E-8
0.02	-2.71E-6	0.63	-1.40E-7	-8.22E-8
0.02	-2.71E-6	0.43	-1.56E-7	-1.07E-7
0.02	-3.01E-6	0.53	-2.38E-7	-1.97E-7
0.02	-3.01E-6	0.50	-2.22E-7	-1.81E-7
0.02	-3.01E-6	0.43	-2.80E-7	-2.47E-7

2.5.4.3 Probe equations

The transferred current from charged particles to the probe tip in a particulate flow system can be related to charge density and particle velocity by Eq. (2.5) with a_i , b_i and c_i being fitted constants. The solid flow rate at the probe tip, W_s , can be expressed by Eq. (2.10). With

the particle velocity in the bubble nose and wake regions approximated by the bubble rise velocity and the voidage near the bubble by ε_{mf} , the voidage at minimum fluidization, Eq. (2.5) can be re-arranged into the following form which represents the transferred current received by the probe when the bubble nose/wake contacts the probe.

$$I_{tran,i} = \rho_p (1 - \varepsilon_{mf}) U_B A_p (a_i q_m + b_i U_B^2 + c_i) \quad (2.11)$$

Induced current equation was obtained from fitting the simulation results based on a simple charge induction model [21] (see Appendix C.1):

$$I_{ind,i} = -0.17 q_m U_B^{1.1} \quad (2.12)$$

The total current arises from a combination of transferred and induced currents. Based on Eqs. (2.11) and (2.12), an equation of the following form

$$I_{peak,i} = \alpha_i q_m U_B + \rho_p (1 - \varepsilon_{mf}) U_B A_p (\beta_i U_B^2 + \gamma_i) \quad (2.13)$$

is proposed to represent the current peaks from the two materials. Eq. (2.13) was fitted to measured data ($I_{peak,i}$, q_m and U_B) for bubbles passing the probe from both single bubble injection (Table 2.3) and freely bubbling experiments with synchronization (Table 2.4), with different particle charge densities (q_m) and bubble rise velocities (U_B). For the present case with $\rho_p = 2500 \text{ kg/m}^3$, $\varepsilon_{mf} = 0.37$ for the dense phase and $A_p = 3.6E-5 \text{ m}^2$ (cross-sectioned area of probe tip surface),

$$\alpha_1 = 0.21(\text{kg / m}), \beta_1 = 4.59E-7(\text{C} \cdot \text{s}^2 / \text{kg} \cdot \text{m}^2), \gamma_1 = 2.95E-6(\text{C / kg}) \quad (\text{Ni}) \quad (2.14)$$

$$\alpha_2 = 0.15(\text{kg / m}), \beta_2 = 2.90E-6(\text{C} \cdot \text{s}^2 / \text{kg} \cdot \text{m}^2), \gamma_2 = 1.21E-6(\text{C / kg}) \quad (\text{TiN}) \quad (2.15)$$

The experimental and calculated values from Eq. (2.13) with the above α , β and γ values are compared in a parity plot in Figure 2.28. Coefficients of determination were $R^2 = 0.90$ and 0.85 for Ni and TiN, respectively. Note that more experimental data could help in the fitting, thereby improving the accuracy of the measurements. The fitted constants are likely related to the properties of the probe materials and particles (see Section 2.5.1.4). $I_{peak,1}$ and $I_{peak,2}$ represent the current peaks from the two materials when the bubble nose/wake contacted the probe.

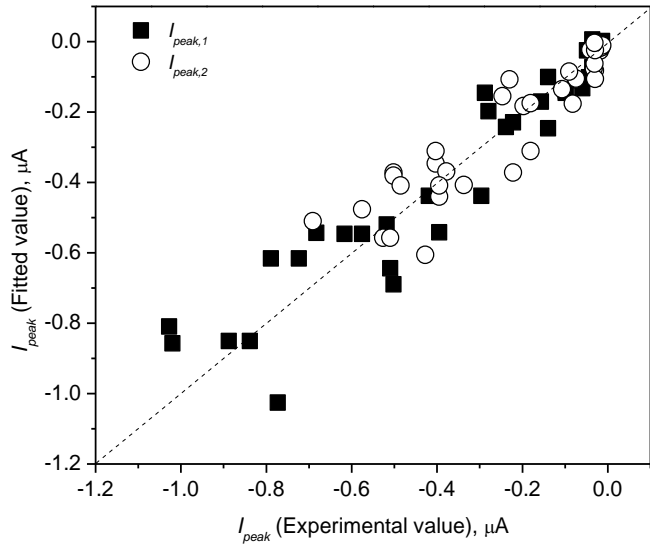


Figure 2.28 Comparison of empirical correlation (Eqs. (2.13-2.15)) and experimental data for two probe materials.

For the dual-tip (one-material) probe, assuming that the effect of probe dimension on the fitted values can be ignored, the same empirical correlation was used in analyzing signals from the probe with the same particles.

2.5.5 Probes calibrations with particles of different properties

2.5.5.1 Glass beads with a size range of 106-212 μm

Following a similar procedure as above, the 2t2mb probe (see Table 2.1) was calibrated with 106-212 μm GB. Single bubbles passing the probe in vertical alignment were selected from video recordings for analysis of bubble rise velocity, and corresponding current peaks were selected from the synchronized probe signals. Many data were discarded because of irregular bubble shapes or movement, such as coalescence, splitting or non-vertical passages. Maximum current peaks were picked from the signals at low U_g , while minimum peaks were selected from the signals at high U_g , because of the relative magnitudes at each U_g as shown in Figure 3.6. Parameters in Eq. (2.13) were fitted from measured I_{peak} , q_m and U_B data (see Table B.1 in Appendix B.1) from the synchronization experiments with $\rho_p = 2500 \text{ kg/m}^3$, $\varepsilon_{\text{mf}} = 0.37$ for the dense phase and $A_p = 3.6\text{E}-5 \text{ m}^2$ for the present case. Coefficient of determination $R^2 = 0.80$ and 0.79 were found for Ni and TiN in this case, respectively.

$$\alpha_1 = 0.23(\text{kg} / \text{m}), \beta_1 = 1.10E-6(\text{C} \cdot \text{s}^2 / \text{kg} \cdot \text{m}^2), \gamma_1 = 6.61E-6(\text{C} / \text{kg}) \quad (\text{Ni}) \quad (2.16)$$

$$\alpha_2 = 0.32(\text{kg} / \text{m}), \beta_2 = 5.05E-7(\text{C} \cdot \text{s}^2 / \text{kg} \cdot \text{m}^2), \gamma_2 = 1.04E-5(\text{C} / \text{kg}) \quad (\text{TiN}) \quad (2.17)$$

where α_i , β_i and γ_i are fitted constants in Eq. (2.13). Comparing parameters in Eqs. (2.14-15) and (2.16-17), most parameters became larger for small particles; and α_1 was larger than α_2 for large particles, but the opposite was found for small particles, consistent with Figures 3.6 and 3.7.

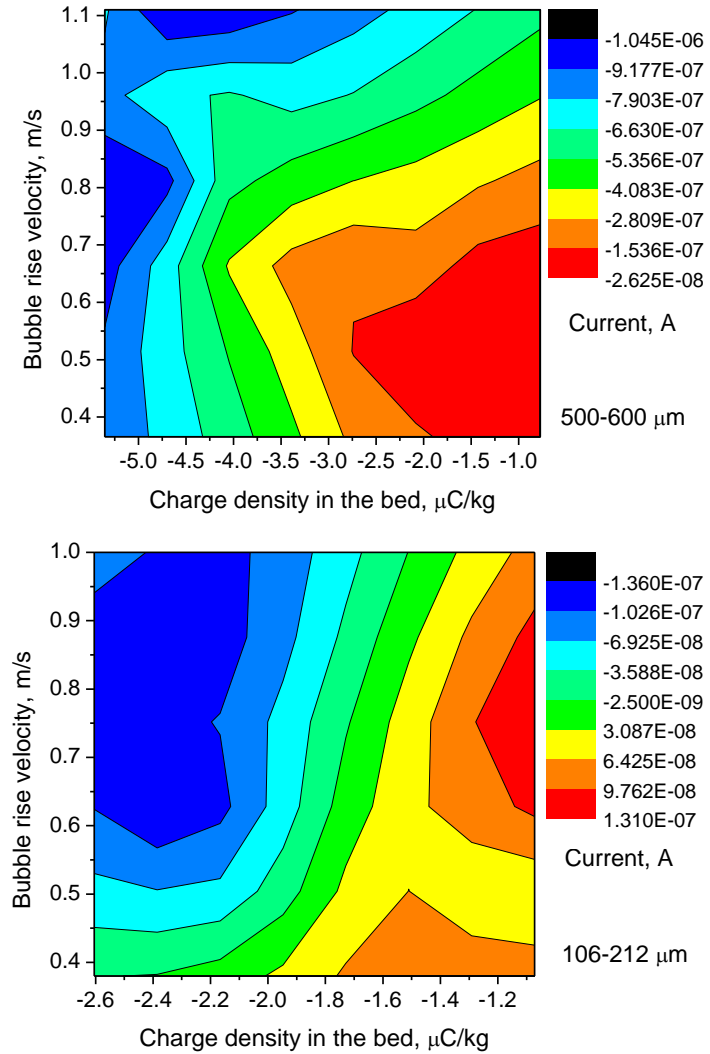


Figure 2.29 Contour plots of current peaks from Ni tip of 2t2mb probe as a function of bubble rise velocity and particle charge density from calibration experiments for 106-212 μm and 500-600 μm GB.

Figure 2.29 shows the relationships between measured data (I_{peak} , U_B and q_m) for glass beads with different mean size. For both cases, I_{peak} increased with increasing q_m when U_B was

constant. However, a different trend of U_B and I_{peak} relationship was found in the data from particles with different sizes. When q_m was constant, signal amplitudes from particles with larger mean size (500-600 μm) show a larger variation when increasing U_B than that from the particles with smaller mean size (106-212 μm). This suggests hydrodynamics have different effect on magnitudes of electrostatic signals for particles of different sizes.

2.5.5.2 Polyethylene (PE) particles with narrow and wide size ranges

Electrostatic charge generation is a well-known issue in polymerization reactors, leading to serious drawbacks, as discussed in Chapter 1. Polyethylene has particle properties which differ from those of glass beads in density, sphericity, roughness, dielectric constant etc. Due to these differences, the generation of electrostatic charge in fluidized bed may differ, resulting in different signals measured by electrostatic probes. Therefore, it is important to test the applicability of the proposed probes in fluidized beds of polyethylene particles.

Polyethylene resin powders used in this work were provided by NOVA Chemicals Corporation directly from their commercial fluidized bed reactors. Both original and sieved polyethylene particles were tested. The original ones had a relatively wide size range of 100-1500 μm , whereas the sieved ones had a relatively narrow size range of 710–850 μm . These size distributions were obtained by a Malvern Mastersizer 2000. (See Appendix B.7 for PSD graphs.) The minimum fluidization velocities were obtained from the intersection of two straight lines of pressure drop versus superficial gas velocities curves. (See Appendix B.6 for U_{mf} curves.)

Based on a similar procedure as above, calibration experiments with polyethylene particles of different size ranges were conducted with different particle charge density (q_m) and bubble rise velocity (U_B) in the freely bubbling bed. Current signals from the probe and differential pressure signals across the bed are compared in Figure 2.30. These indicate a similar bubble frequency of 1-2 Hz, again suggesting that the electrostatic signals and bed hydrodynamics are related.

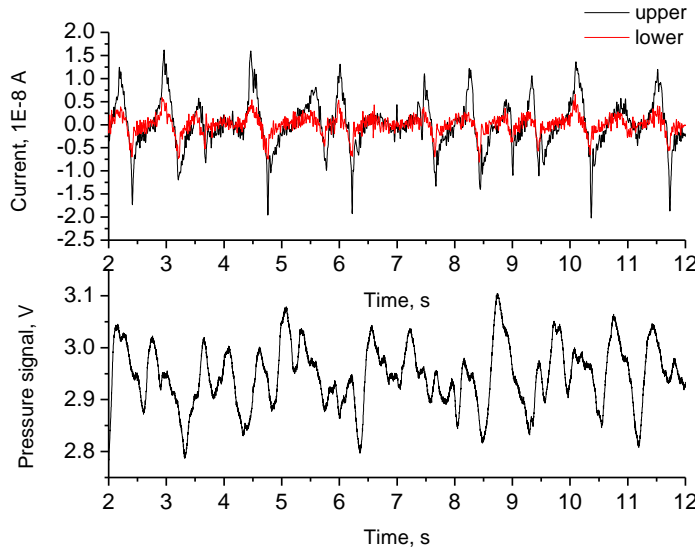


Figure 2.30 Synchronized 2t1mr Γ probe (inserted 0.42 m above the distributor) and differential pressure signals across the bed in two-dimensional fluidization column of 710-850 μm PE at $U_g = U_{mf} + 0.04$ m/s. (Fluidizing gas air: $T=23.2^\circ\text{C}$, RH=4.2 %)

2t1mf Γ and 2t1mr Γ probes (see Table 2.1) were tested. Eq. (2.13) was fitted to measured (I_{peak} , q_m and U_B) data (see Table B.2 in Appendix B.1) with $\rho_p=918 \text{ kg/m}^3$, $\epsilon_{mf}=0.55$ for the dense phase. Fitted constants are shown in Table 2.5, with R^2 larger than 0.80 for polyethylene particles and the probe tips material tested in this work. α_i , β_i and γ_i are fitted constants related to the properties of the probe materials and particles (see Section 2.5.1.4). The experimental and values obtained from Eq. (2.13) with the fitted α , β and γ values are compared in a parity plot in Figure 2.31. Similar to Figure 2.28, it is likely that more experimental data could improve the coefficient of determination and measurement accuracy. The properties of probe tip material, e.g. work function, electrical conductivity, tip size and shape, affect current signals and the calibration equation.

Table 2.5 Fitted parameters in Eq. (2.13) for different probe tips and particle size distributions of PE powders.

Case	α_i , kg/m	β_i , $\text{s}^2/\text{kg m}^2$	γ_i , C/kg	R^2	Particle size range of PE, μm	Tip shape	Tip size (cross- sectional area)	Tip material
(a)	2.74E-3	4.45E-8	2.64E-7	0.82	710-850	flat	3.6E-5 m^2	Nickel
(b)	6.06E-3	1.80E-7	2.18E-8	0.80	100-1500	flat	3.6E-5 m^2	Nickel
(c)	1.25E-2	2.49E-6	7.98E-7	0.89	710-850	rod	6.9E-5 m^2	Steel
(d)	2.16E-2	-1.27E-6	2.84E-6	0.85	100-1500	rod	6.9E-5 m^2	Steel

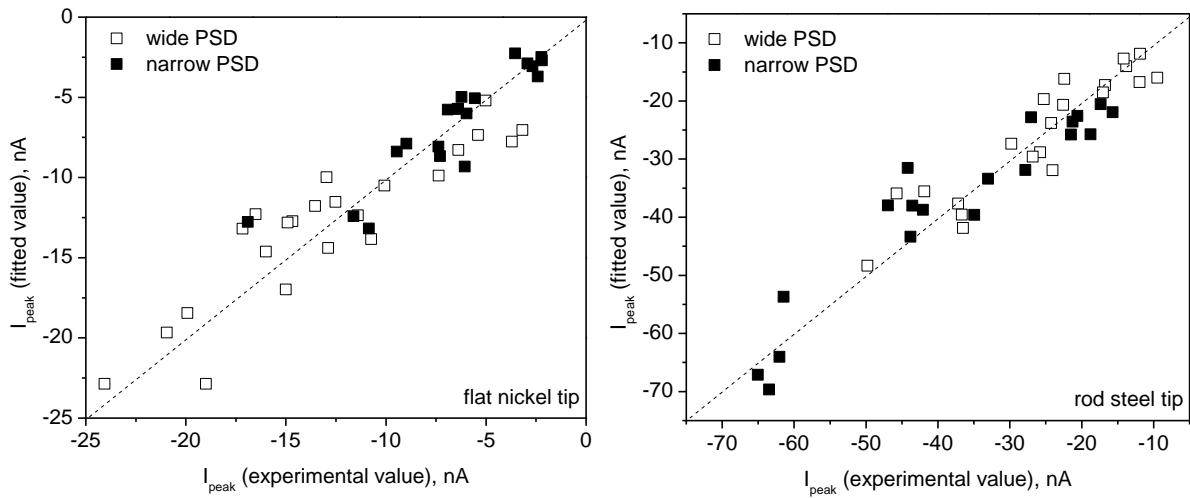


Figure 2.31 Comparison of fitted data (from Eq. (2.13)) and experimental data for different probe tips and particle size ranges of PE powders.

2.6 Summary

Two dual-tip probe designs were fabricated: a dual-tip (two-material) probe, consisting of side-by-side tips made of materials of significantly different work functions, and a dual-tip (one-material) probe, having two vertically aligned tips of the same material. With retractable tips, the dual-tip (one-material) probe can be configured into a collision-collision probe with both tips protruding (“F” configuration), or a collision-induction probe, with only one tip exposed (“T” and “L” configurations).

The dual-tip (two-material) probe was calibrated in an ejector-funnel experimental setup, with the charge density on the particles changed by varying the pipe material and gas velocities. Several major factors that affect the transferred charge were studied, including the charge density, solid flux, particle velocity and angle of impact. The results were fitted to a semi-empirical equation (Eq. (2.5)) to quantify the effects of these parameters on the transferred current received by the probe from charged particles. Two tips, made of two materials (Ni and TiN) whose work functions differ, show different transferred currents when struck by charged particles, with the difference depending on the particle charge density, impact/collision velocity and contact angle. The largest difference between transferred

currents from the two materials was obtained when the particles struck the probe surface at right angles.

Substantial differences were observed in charge and current signals from the tips made of the same two materials in both vertical tube and vibration tray setups, as well as in both single-bubble and freely bubbling experiments in the two-dimensional fluidized bed. From both motor-pulley experiments and fluidization experiments, the difference in charge/current signals for the two probe materials arose mainly from charge transfer. The probes were calibrated with glass beads and polyethylene particles of different sizes in both single bubble injection and freely bubbling modes in the two-dimensional fluidized bed. The electrostatic signal transmitted by the probe was synchronized with the frames recorded by the camera. Eq. (2.13) was fitted to measured data (I_{peak} , q_m and U_B) for bubbles passing the probe with different particle charge density (q_m) and bubble rise velocity (U_B) values. Several factors were found to affect the fitted parameters, in particular the dielectric constant of the particles, work function difference between the probe tip material and the bed particles, probe tip size and shape, and particle density and size distribution. For a dual-tip (one-material) probe, injected bubbles passed the two tips in succession and clear time delays appeared between the peaks from both the F and Γ configurations. The shapes of the current signals from each protruding tip were not significantly affected by the presence of the other tip, and there was little change in peak amplitudes. However, the signals from the retracted tip were greatly affected by its position relative to the protruding tip.

Chapter 3 Measurements in Gas-Solid Fluidized Beds

3.1 Introduction

In this Chapter, the probes developed in Chapter 2 are employed to measure electrostatic charges in a two-dimensional fluidization column and two three-dimensional columns of inner diameters of 0.10 m and 0.30 m, with glass beads and polyethylene particles with different size ranges as bed materials.

3.2 Experimental equipment and methods

3.2.1 Two-dimensional fluidization column

The two-dimensional fluidization column had an inside width of 0.307 m, a thickness of 22 mm and a height of 1.24 m, as shown in Figure 2.8. A sampling port and a probe port were located on opposite faces of the column at the same height (0.42 m above the distributor) and horizontal position (mid-point), in order to provide localized measurements. Particles from the sampling port were discharged into a Faraday cup to measure in-bed charge density directly. A high-speed video camera recorded bubble movement during experiments, with bubble rise velocities determined from the recorded video images. Details of the experimental facilities are provided in Section 2.4.

3.2.2 Three-dimensional fluidization column of ID 0.10 m

Figure 3.1 shows a schematic diagram of a 0.10 m ID three-dimensional fluidization column and charge measurement system. The cylindrical column was made of Plexiglas with an inner diameter of 0.10 m and a height of 1.0 m. A double perforated-plate distributor was installed at the bottom of the column, 0.17 m above the gas entrance. The top and bottom distributor plates both had 31 aligned orifices of diameters 2.0 mm (above) and 3.0 mm (below), with a fine metal screen ($\sim 38 \mu\text{m}$) between the two plates. Compressed air was introduced into the column, controlled by a panel-mount air flow meter. Electrostatic probes were inserted in two ways: either vertically from the top of the column into the dense phase

of the bed at the axis 0.11 m above the distributor, or horizontally from the side 0.10 m above the distributor. A sampling port (6.35 mm in diameter, inclined downward at 30° to the vertical) was installed on the column wall at the same height of the probe port in the dense phase region of the bed. Particles from the sampling port were discharged into a Faraday cup to measure the in-bed charge density directly. The static bed height was maintained at 0.20 m throughout the experiments. Details of the charge measurements can be found in Sections 2.3 and 2.4.

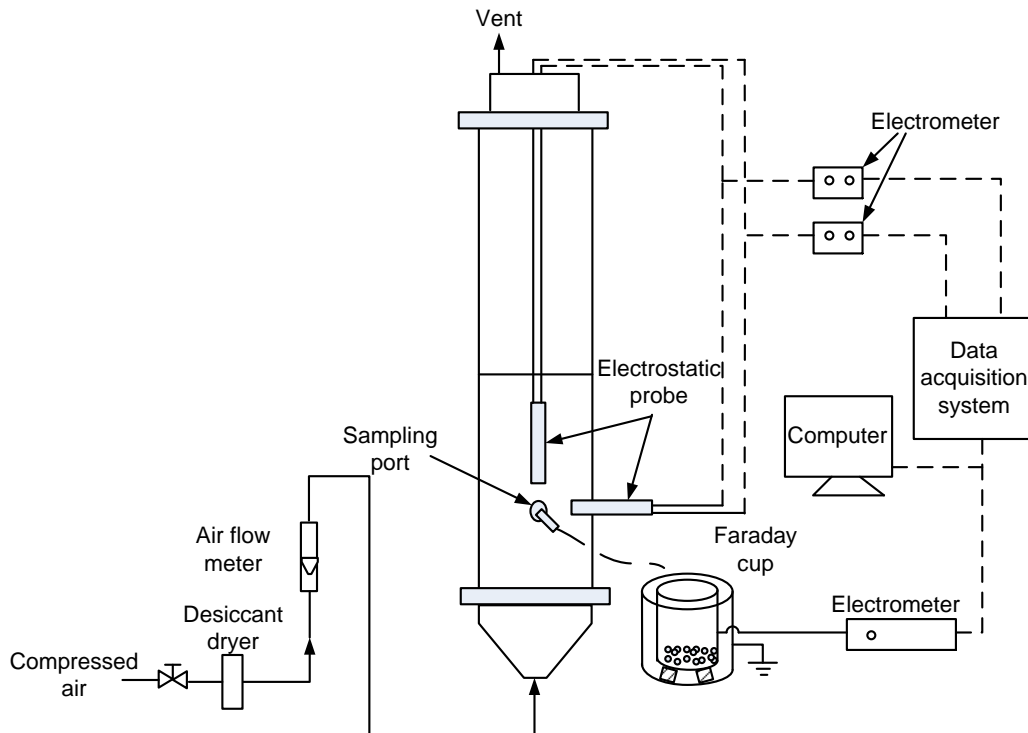


Figure 3.1 Schematic of 0.10 m ID three-dimensional column and charge measurement system (not to scale).

3.2.3 Three-dimensional fluidization column of ID 0.30 m

Free bubbling experiments were also performed in a three-dimensional fluidization column of inner diameter 0.30 m and height 4.5 m [67], as shown schematically in Figure 3.2 and Appendix A.5. A double perforated plate distributor containing top and the bottom plates, both having 98 holes, with diameters 5.6 mm and 64 mm, respectively, with a fine metal screen mesh ($\sim 38 \mu\text{m}$) sandwiched between the two plates to prevent particles from falling into the windbox. Fluidizing air was supplied by a blower with a maximum capacity of 425

Nm³/h at 69 kPa. The air flow rate was controlled by a by-pass line located close to the blower, and calculated from the pressure drop across an orifice plate. A sampling port (12.7 mm in diameter, inclined downward at 30° to vertical) was located 0.25 m above the distributor. Particles from the sampling port were discharged into a Faraday cup to measure in-bed charge densities directly.

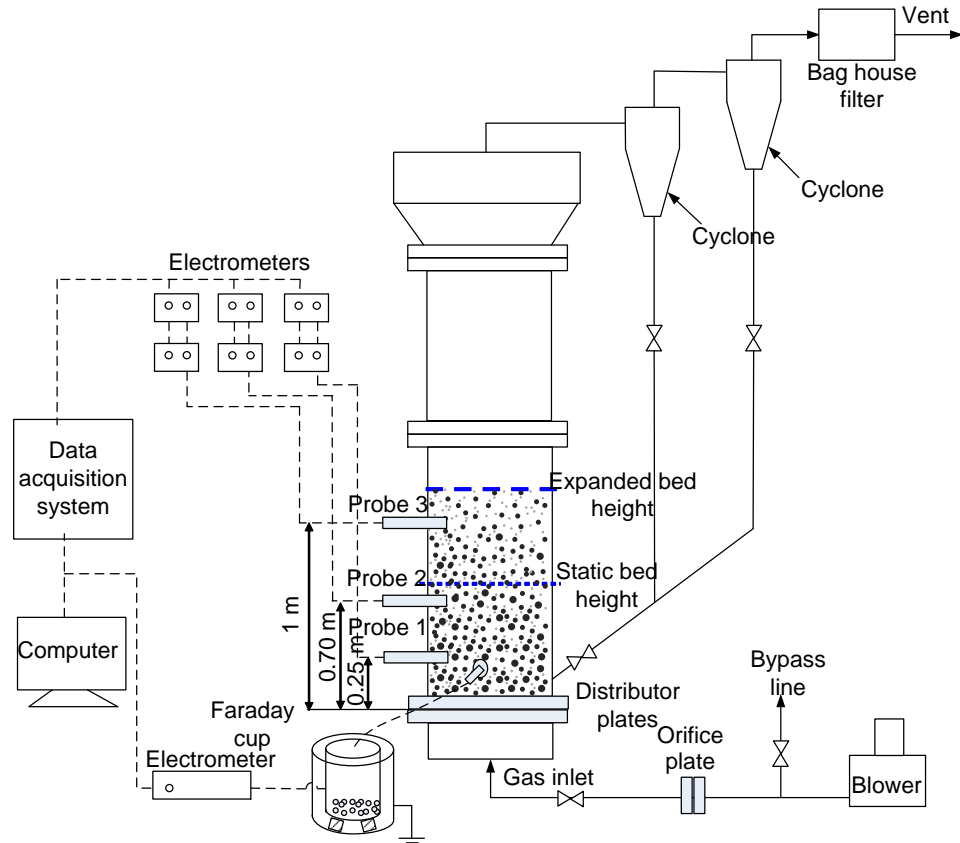


Figure 3.2 Schematic of 0.30 m ID three-dimensional column and charge measurement system (not to scale).

In some of the experiments, three 2t1m probes (see Table 2.1) were inserted at different heights along the axis of the column. Three probes were installed at the same time below the surface of the expanded bed. With increasing the superficial gas velocity, some fine particles were entrained from the top of the column and collected by two external cyclones. It was observed that the inside of the return leg was coated by polyethylene particles during the experiments, due to electrostatics.

Both relative humidity and temperature of the gases were monitored during all experiments at the exit of fluidization columns. Particles were washed with water and ethanol, and then dried overnight in an oven to eliminate dust and moisture. Both narrow and wide size ranges particles were tested. Each bed was fluidized at a certain superficial gas velocity for at least an hour (1.5 h for the 0.30 m ID column) to let the system reach steady state before measurements. All measurements were then performed three times at each superficial gas velocity. The order of the superficial gas velocities was chosen randomly. The probe signals were not synchronized with photographic images in these experiments.

3.3 Results and discussion

3.3.1 Results from two-dimensional fluidization column

The following experiments were conducted on different days from the synchronization experiments used for probe calibration. Therefore the data used to estimate q_m and U_B were not the same as those used to obtain the calibration equation.

3.3.1.1 Dual-tip (two-material) probe with 500-600 μm GB

A 2t2mb probe, as shown in Figure 2.1(b), was used. Figure 3.3 shows 5 s traces of charge signals and corresponding current signals from the probe for a superficial gas velocity of 0.50 m/s. The maximum and minimum peaks (I_{\max} and I_{\min}) were defined, for a series of bubbles rising and passing during freely bubbling. The variation in peak amplitudes is due to variations in bubble properties and trajectories in the freely bubbling flow regime. The magnitudes of peaks were normally larger for Ni than for TiN. This seems to be contradictory, given that the work function difference between TiN (2.9 eV) and glass beads (SiO_2 : 5.0 eV) is larger than that between Ni (5.0-5.4 eV) and glass beads (see Table 2.2). One might expect a higher work function difference between contacted objects to result in a larger transferred charge. However, the total transferred charge during contact depends not only on the work function between the particles and metal surface, but also on the initial charge on particles, contact velocity, effective contact area, surface conditions and other material properties [61, 118]. The total net transferred currents between the metal and the

colliding particles for two different metals may vary and even change direction when such factors as particle charge density, particle velocity or flow rate change [60]. Moreover, work functions of dielectric particles and metals can be significantly affected by surface and environmental conditions (e.g., roughness, geometry, contamination, oxide layer and surface chemistry) [84, 123]. Similar results were found in Sections 2.5.1.4 and 2.5.3.

By counting the number of peaks within a certain period of time, the void frequency could be estimated. For example, the estimated frequencies were ~ 1 Hz at $U_g=0.30$ m/s and $3\sim 4$ Hz at $U_g=0.50$ m/s. For all superficial gas velocities tested, there were measurable differences between the peak amplitudes for the Ni and TiN tips.

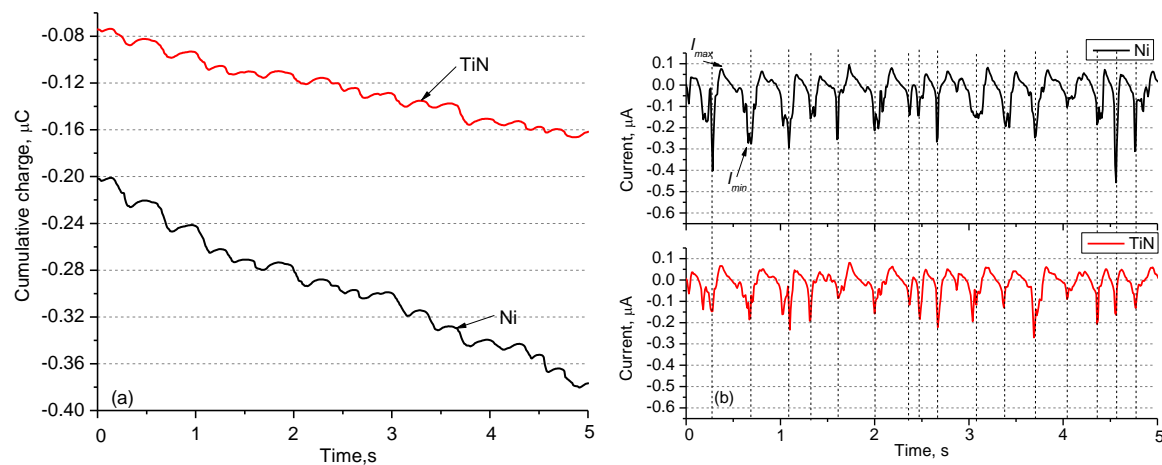


Figure 3.3 Cumulative charge (a) and current (b) signals from 2t2mb probe in freely bubbling two-dimensional fluidized bed of 500-600 μm GB with static bed height of 0.30 m at $U_g=0.50$ m/s over duration of 5 s. (Fluidizing gas air: $T= \sim 22^\circ\text{C}$, $\text{RH}= \sim 10\%$)

As noted above, as a bubble surrounded by charged particles passed the collision probe, two current peaks appeared with opposite signs, corresponding to the moments when the bubble nose and wake reached the probe. Both peaks involve summations of transferred and induced currents. The transferred currents are assumed to be the same when the bubble nose and wake contact the probe. The induced currents arise by charged particles passing the probe, but not necessarily contacting the probe tip. If, for example, a bubble with negatively charged particles passes the probe, a negative induced charge is registered by the conductive probe tip. After passage of the bubble, the induced charge returned to zero. A positive induced current was registered at the maximum peak, followed by a negative induced current of equal

magnitude at the minimum peak. Because of near front/back symmetry for rising bubbles, the magnitudes of the induced currents should be similar, as indicated by the simulation results in Appendix C.1. Therefore the average of the maximum and minimum peak values cancels out the induced charges, as demonstrated by a simple induction model:

$$I_{\max} = I_{tran} + I_{ind} \quad (3.1)$$

$$I_{\min} = I_{tran} - I_{ind} \quad (3.2)$$

$$\text{so that } I_{tran} = (I_{\max} + I_{\min})/2 \quad (3.3)$$

$$\text{and } I_{ind} = (I_{\max} - I_{\min})/2 \quad (3.4)$$

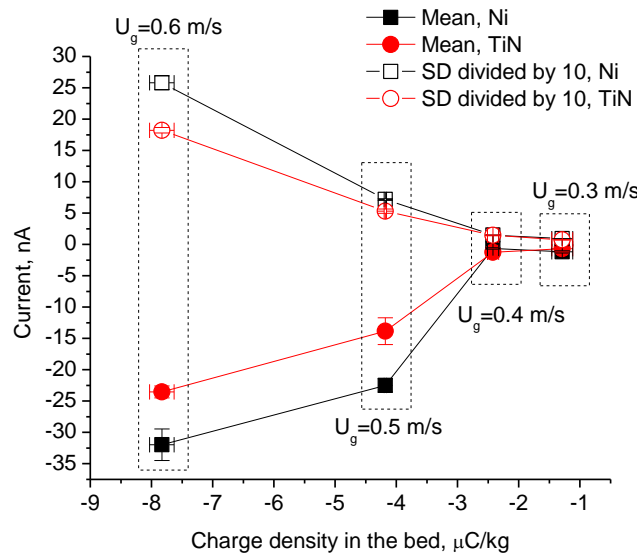


Figure 3.4 Mean and standard deviation of current as a function of superficial gas velocity and particle charge density in freely bubbling two-dimensional fluidized bed with a static bed height of 0.30 m.

The mean and standard deviation (SD) of current are plotted in Figure 3.4 as a function of charge density and superficial gas velocity. Both the mean and SD increased as the in-bed charge density and superficial gas velocity increased, with the difference between the two materials increasing in a similar manner. This again suggests that the charge/current signals measured by an electrostatic probe in a fluidized bed are affected by both particle charge density and bed hydrodynamics. The charge inside the fluidized bed is closely related to the charge density on the particles inside the bed, as well as to the bed hydrodynamics. Generally, the mean current represents the net transferred current [93]. Although single

bubble experiments showed that bubbles may split after contacting the probe, the average transferred current, \bar{I}_{tran} , and average induced current, \bar{I}_{ind} , could still be related via Eqs. (3.3-3.4) to the average of the maximum and minimum peaks heights, \bar{I}_{\max} and \bar{I}_{\min} .

Figure 3.5 compares $(\bar{I}_{\max} + \bar{I}_{\min})/2$ and $(\bar{I}_{\max} - \bar{I}_{\min})/2$ from the two materials. It shows larger difference in the former than the latter for the two materials, suggesting that the difference in current signals from the two materials mainly results from the transferred parts, whereas the induced currents from the two materials are likely to be the same; this is consistent with the results in Section 2.5.2. Comparing mean currents in Figure 3.4 and $(\bar{I}_{\max} + \bar{I}_{\min})/2$ values in Figure 3.5, the former is much smaller in magnitude than the latter, with the difference between the two materials (Ni and TiN) much larger in the latter case than in the former. The mean current is low because of the weak signals (magnitude close to zero) associated with the passage of the emulsion phase far from the bubble and possible electrical noise. Figure 3.5 also shows that the magnitude of transfer currents from both materials increased as the superficial gas velocity and charge density increased, with the difference between the two signals increasing in a similar manner. Peak values are therefore used in the signal analysis in Chapter 4.

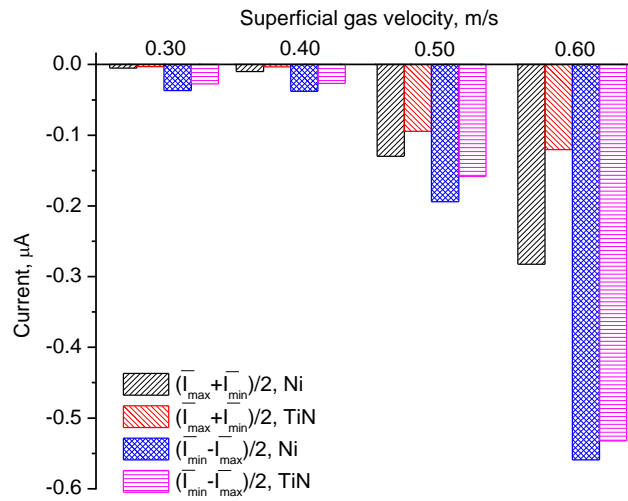


Figure 3.5 Comparison of $(\bar{I}_{\max} + \bar{I}_{\min})/2$ and $(\bar{I}_{\min} - \bar{I}_{\max})/2$ for both materials at different superficial gas velocities in two-dimensional fluidized bed with static bed height of 0.30 m.

3.3.1.2 Dual-tip (two-material) probe with 106-212 μm GB

Charge and current signals from the 2t2mb probe (see Table 2.1) with fluidizing 106-212 μm GB are illustrated in Figure 3.6.

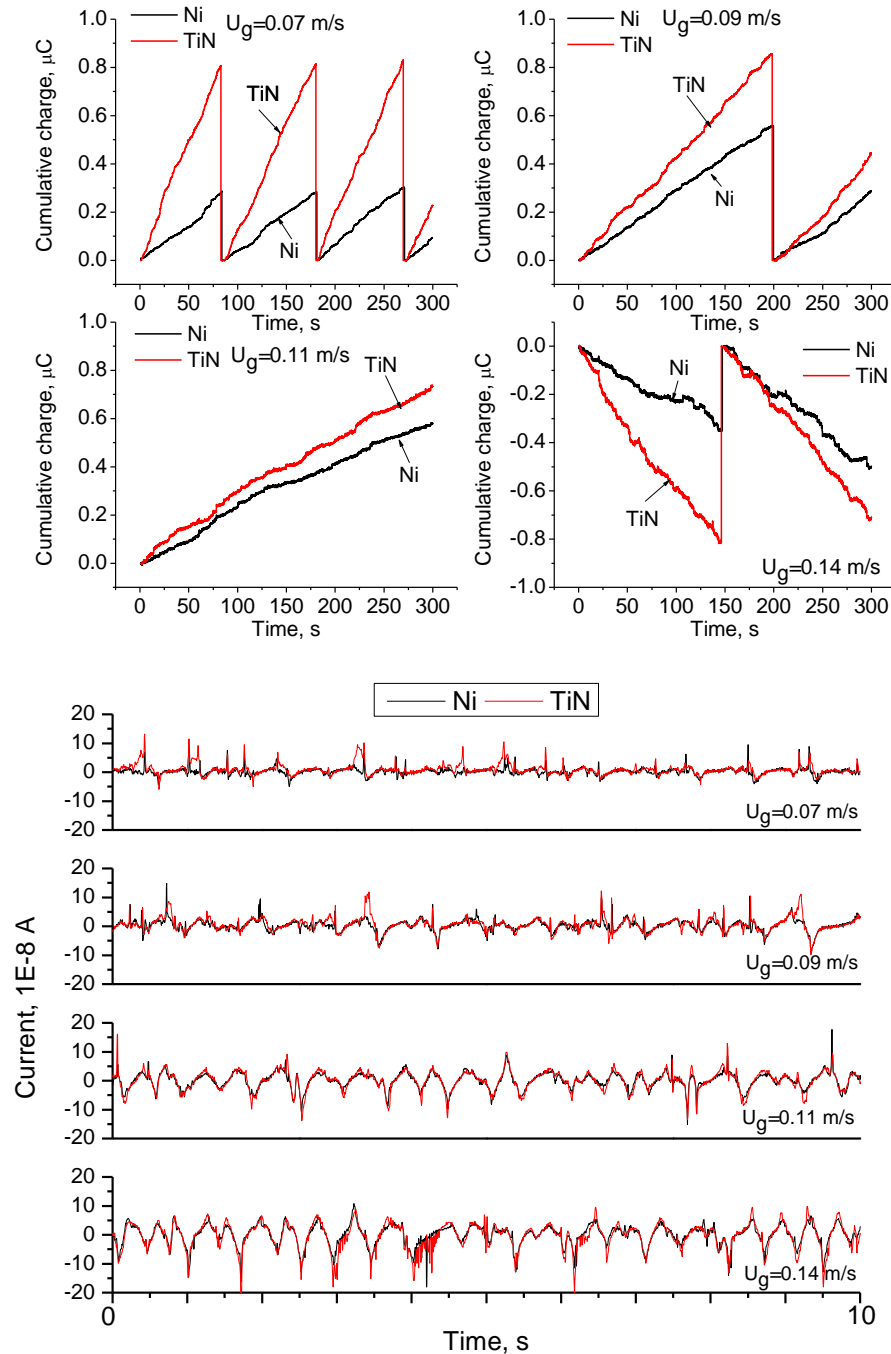


Figure 3.6 Cumulative charges and current signals from 2t2mb probe at different superficial gas velocity in two-dimensional freely bubbling bed of 106-212 μm GB. (Fluidizing gas air: $T = \sim 22^\circ\text{C}$, RH = $\sim 10\%$)

The charge signals from both tips first decreased, then increased with polarity changing from positive to negative, with increasing superficial gas velocity (U_g), indicating that the transferred current changed from positive to negative as U_g increased. The difference between the slopes of the charge signals from the two tips first decreased then increased with U_g increased. For 106-212 μm GB, in the current signals from the probe, positive peaks had higher amplitudes than negative peaks at $U_g=0.07 \text{ m/s}$, whereas the negative peaks were more dominant at $U_g=0.14 \text{ m/s}$. For 500-600 μm GB, the minimum peaks were always dominant for the tested range of U_g , and the charge signals were negative with the difference between the slopes of charge signals from the two tips increasing as U_g increased. Polarity change results were similar to those in Sections 2.5.1.5, 3.3.1.3 and as reported by others [2, 118, 121, 124, 125]. In this case, the polarity change may reflect the combined effect of tribocharging and transfer of charges from charged particles to the probe tips. The probe signal polarity is not necessarily the same as the polarity of the particles and the probe signal may not be used as an indication of the charge polarity on particles. It is necessary to extract the particle charge density from the probe signal. More results are shown in Appendix B.9.

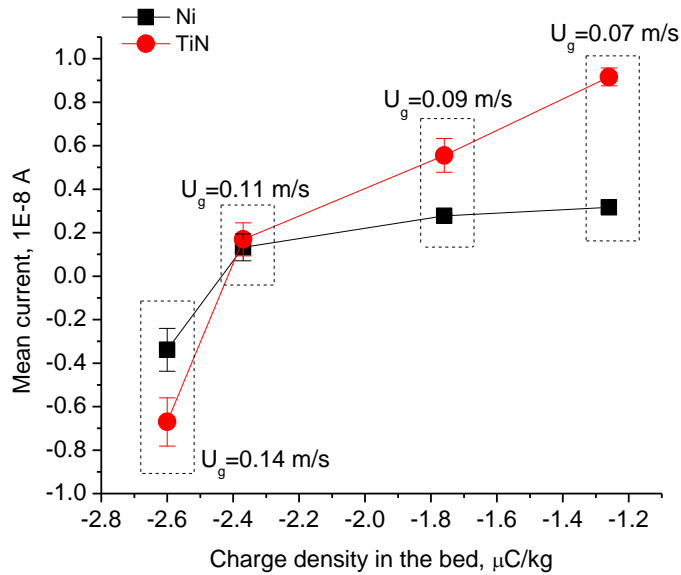


Figure 3.7 Mean currents as a function of superficial gas velocity and particle charge density for 106-212 μm GB.

The mean currents are plotted in Figure 3.7 as a function of charge density (q_m) and superficial gas velocity (U_g). The mean currents first decreased, then switched from positive to negative and increased in magnitude as U_g increased. The difference between the signals

from the two materials changed in a similar manner, consistent with the results in Figure 3.6. The relative magnitude of the net current transferred between the metal and contacting particles for the two metals may vary and even reverse with variation of such factors as particle properties, charge density, particle velocity and gas flow rate, as shown in previous results (see Sections 2.5.1.4, 2.5.3 and 3.3.1.1) and as reported by Matsusaka and Masuda [60].

3.3.1.3 Dual-tip (one-material) probe with 500-600 μm GB

2t1m probes, as shown in Table 2.1, were employed. The effect of superficial gas velocity on the 2t1mfF probe signals is shown in Figure 3.8. The slopes of cumulative charge signals increased for both tips, indicating increased charge transfer as U_g increased. The fluctuations from each tip also increased as U_g increased, because of the increase in bubble size and frequency. The fluctuations from the lower tip were larger than from the upper one, due to direct exposure to bubbles. The polarity of the cumulative charge signals from the lower tip changed as U_g varied, consistent with previous results and literatures. This may be because of the combined effect of triboelectrification and transfer of charges or contamination of the probe tip surfaces. The amplitudes of current signal peaks from both tips increased as U_g increased. The bubble frequency, found by counting peaks, also increased with increasing superficial gas velocity.

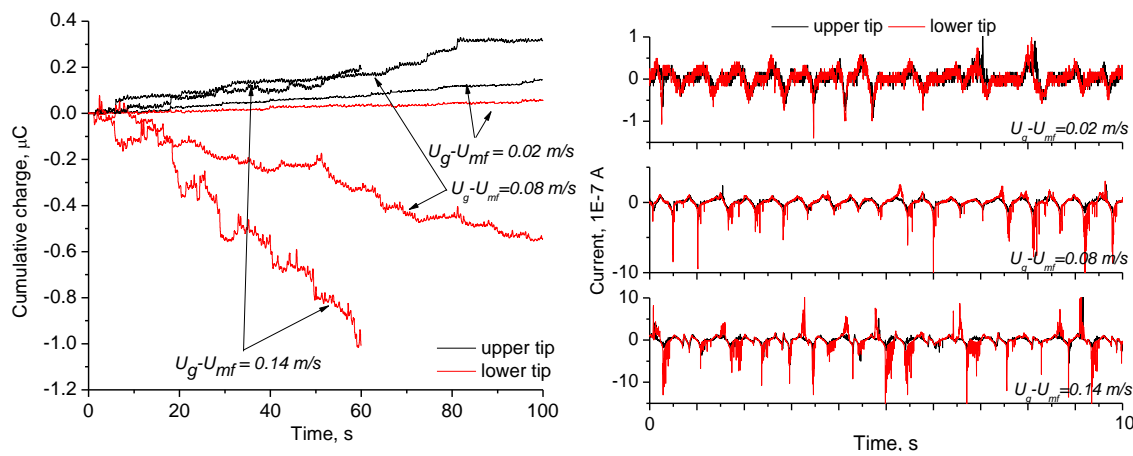
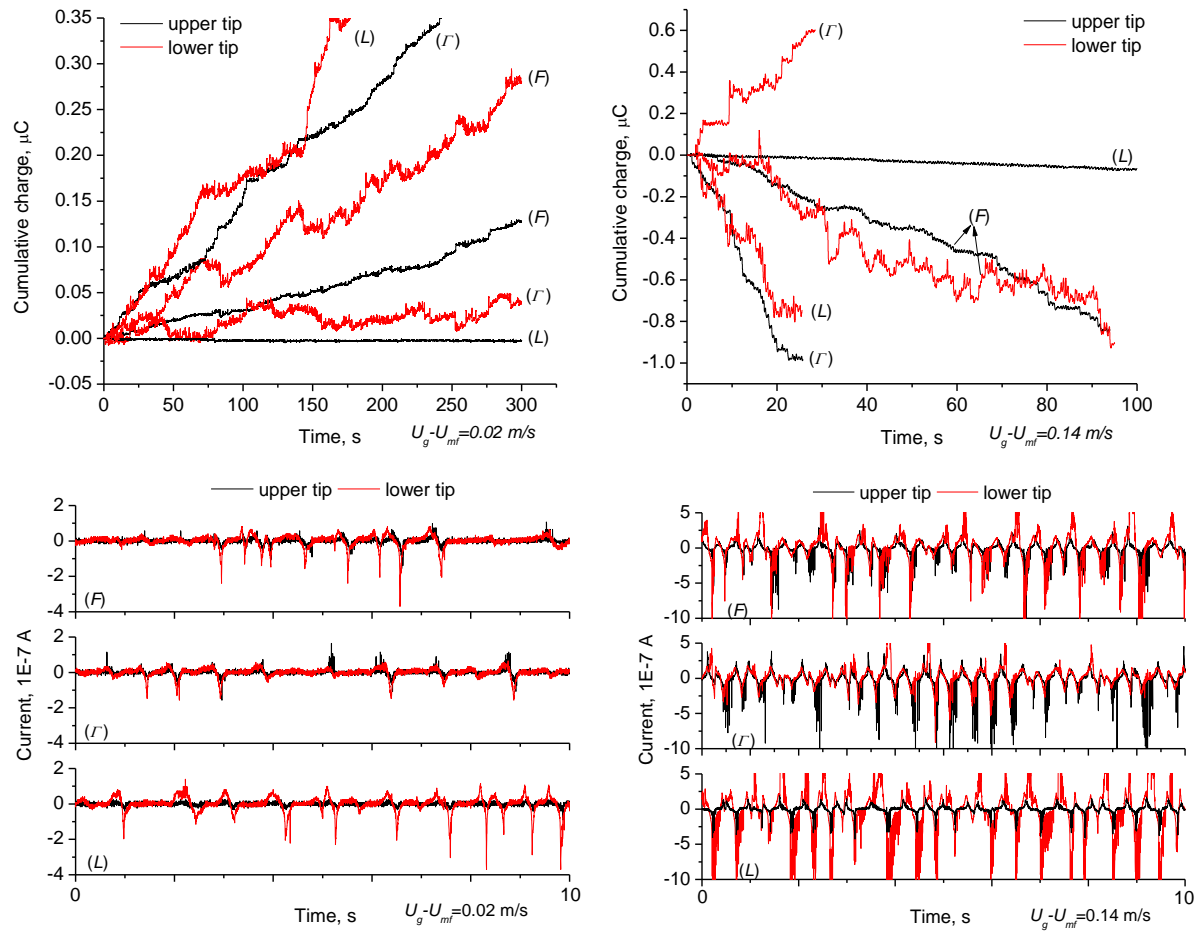


Figure 3.8 Cumulative charge and current signals from 2t1mfF probe in freely bubbling two-dimensional fluidized bed of 500-600 μm GB at different superficial gas velocities. (Fluidizing gas air: $T \sim 23^\circ\text{C}$, $\text{RH} \sim 3\%$)

The 2t1m probe with a different configuration (see Table 2.1) was also tested in the bed at different superficial gas velocities. The effects of different configurations on the cumulative charge and current signals from this probe are shown in Figure 3.9. Slopes of cumulative charge signals from the upper tip increased (positively at $U_g - U_{mf} = 0.02$ m/s and negatively at $U_g - U_{mf} = 0.14$ m/s) when the probe configuration changed in the order L, F, Γ . The current peak amplitudes increased as well. The slopes of cumulative charge signals and current peak amplitudes from the lower tip increased when the probe configuration changed in an order of Γ , F, L. At $U_g - U_{mf} = 0.14$ m/s, the cumulative charge signal from the lower tip increased positively, possibly due to the interference of charges on the column wall.



(F: both tips protruding, Γ : only upper tip protruding, L: only lower tip protruding as shown in Figure 2.2)

Figure 3.9 Cumulative charge and current signals from 2t1m probe with different configurations in freely bubbling two-dimensional fluidized bed of 500-600 μm GB at excess superficial gas velocities, $U_g - U_{mf} = 0.02$ and 0.14 m/s. (Fluidizing gas air: $T = \sim 23^\circ\text{C}$, $RH = \sim 3\%$)

3.3.1.4 Dual-tip (one-material) probe with 710-850 μm PE

Fouling/sheeting (0.20-0.25 m above static bed height) was observed on the column wall after fluidization. Since the relative magnitudes of signals from the two materials of the 2t2m probe may change for different operating conditions and particle properties, causing difficulty in signal processing (see Sections 2.5.1, 3.3.1 and 4.4.2.2), the 2t1m probe was employed for the polyethylene tests. Figure 3.10 shows cumulative charge and current signals from 2t1mfF probe in freely bubbling experiments at different superficial gas velocities. The slopes of cumulative charge signals, amplitudes of current peaks from both tips and bubble frequencies, all vs. time, increased as U_g increased. The cumulative charge signals from the lower tip showed little variation with changing superficial gas velocity, whereas in Figure 3.19 the slope of charge signals from the lower tip increased significantly as increasing U_g . This may because a possible thin layer of particles was coated on the lower tip surface at low U_g , but vanished by flushing effect as increasing U_g .

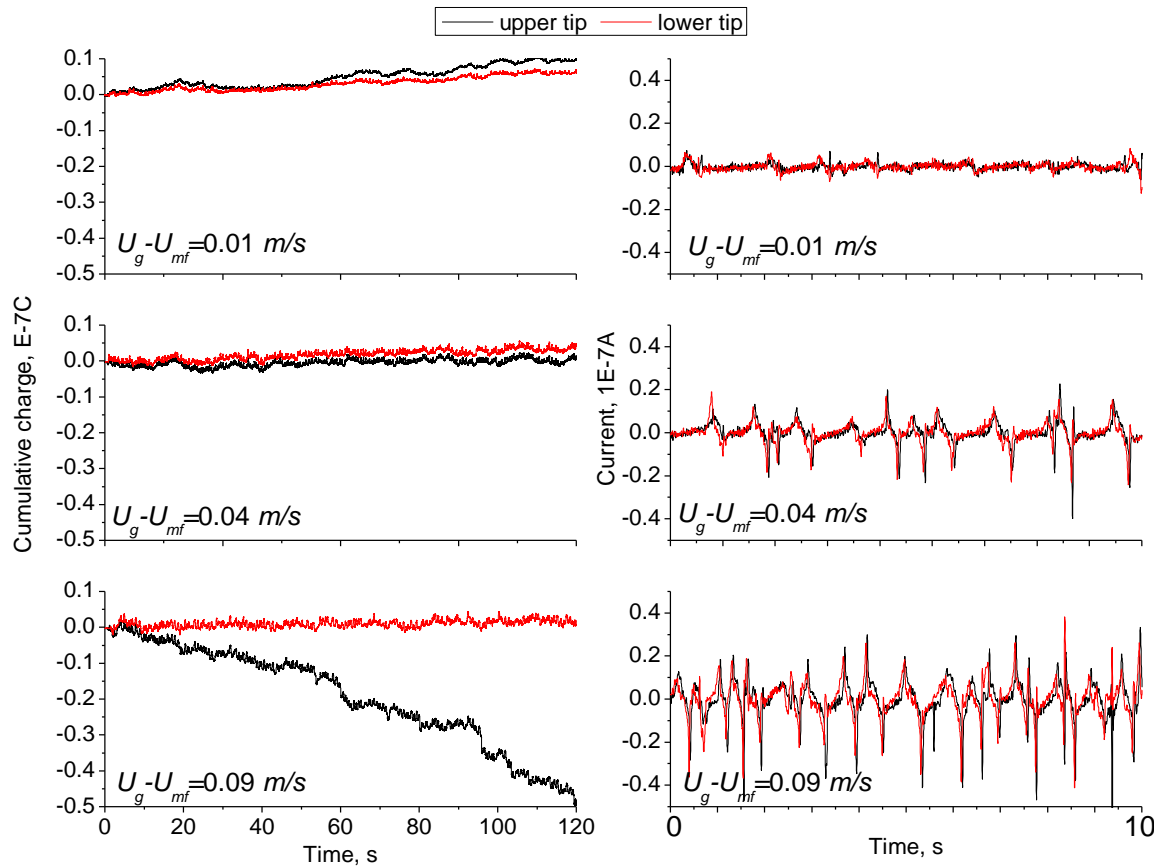


Figure 3.10 Cumulative charge and current signals from 2t1mfF probe in freely bubbling two-dimensional fluidized bed of 710-850 μm PE at different U_g . (Fluidizing gas air: $T \sim 23^\circ\text{C}$, $\text{RH} \sim 7\%$)

3.3.2 Results from three-dimensional fluidization column of ID 0.10 m

3.3.2.1 Effects of probe inserted distance and direction

Glass beads of size range of 500-600 μm were tested next. A 2t2ma probe (see Table 2.1) was inserted horizontally into the bed. The probe tip was moved from the centre to near the wall. Data were recorded 20 min after changing the probe position each time to achieve steady state. Typical cumulative charge signals from the probe are shown in Figure 3.11. The slopes of signals at the centre were larger than near the wall and the slope for TiN was larger than for Ni in both cases.

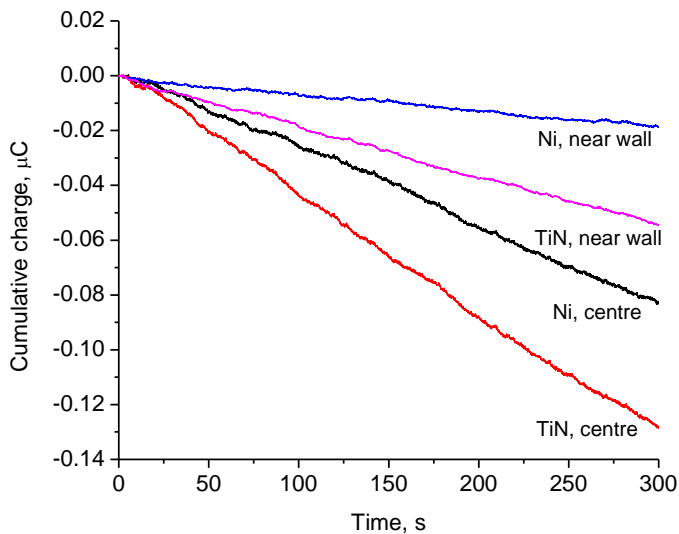


Figure 3.11 Cumulative charge signals from 2t2ma probe horizontally inserted to centre and near the wall in 0.10 m ID freely bubbling fluidized bed ($U_g=0.29 \text{ m/s}$). (Fluidizing gas air: $T= \sim 22^\circ\text{C}$, $\text{RH}= \sim 10 \%$)

Figure 3.12 shows that the magnitudes of the mean and SD of current for both materials decreased when the probe was moved from the centre of the column (probe insertion distance: 0.05 m) to near the wall (insertion distance: 0.005 m). When the probe was moved to the centre, the magnitude of both the mean and SD of currents for both materials increased. The results were repeatable. Due to the wall effect, hydrodynamics are weaker near the wall than in the centre of the column, resulting in lower frequency and intensity of particle-particle and particle-probe surface interactions. Differences existed in the mean and

SD of currents from the two materials, regardless of their relative positions. This difference was altered when the hydrodynamics and/or charge density inside the bed changed.

Cross-correlation and coherence function were also calculated to analyze current signals from the two materials. Results show that with almost no time delay between these two signals, the two signals corresponded well to each other at 0~10 Hz, but became unrelated at frequency > 50 Hz. The coherence function increased with increasing superficial gas velocity.

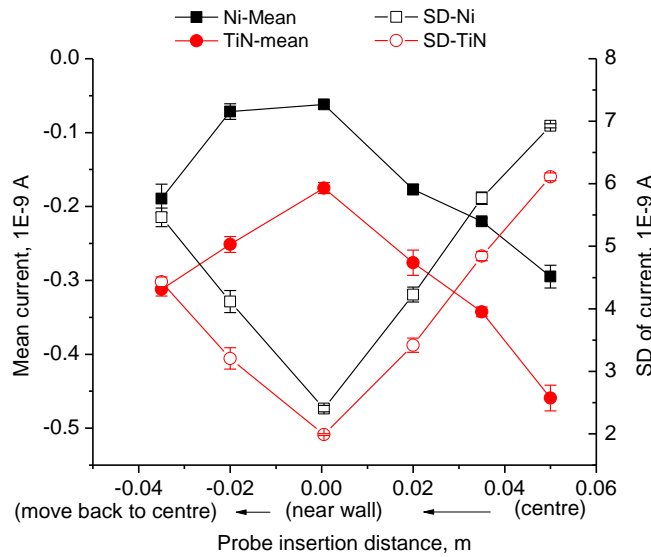


Figure 3.12 Mean and standard deviation of current signals from 2t2ma probe as a function of probe insertion distance.

Figure 3.13 shows the cumulative charges from the probe inserted at different angles into the column. The relative magnitude of transferred currents from the two materials differed in the two cases, indicating that the contact angle (probe insertion direction) between the particles and probe surface affects the magnitude of transferred current. Similar results are reported in Sections 2.5.1.4, 2.5.3, and 3.3.1. The slopes of the charges from the two materials and the difference between signals were larger when the probe was inserted vertically than that when it was inserted horizontally. The probe surface faced downward so that charged particles could directly strike the metal tips. The transferred current was larger from TiN than from Ni when the probe was inserted horizontally, consistent with Figure 3.11. Therefore, the probe was inserted vertically in the next of the experiments.

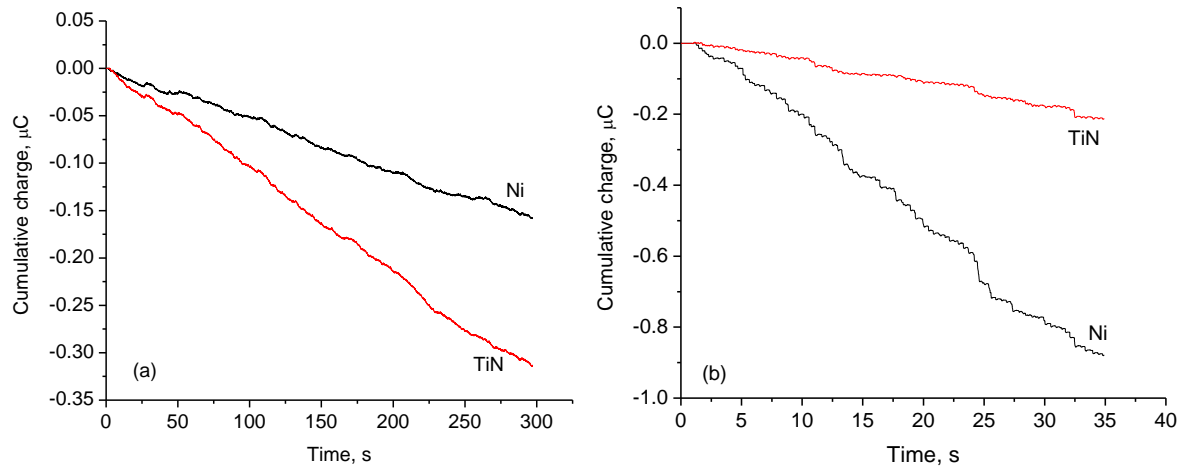


Figure 3.13 Comparison of cumulative charge signals from 2t2ma probe inserted: (a) horizontally and (b) vertically into 0.10 m ID freely bubbling fluidized bed ($U_g=0.33 \text{ m/s}$). (Fluidizing gas air: $T=22^\circ\text{C}$, RH= ~10 %)

3.3.2.2 Comparison of current signals

Figure 3.14 shows a typical time series of current signals measured by the 2t2ma probe (see Table 2.1) from a homogeneous particulate flow and a bubbling fluidized bed.

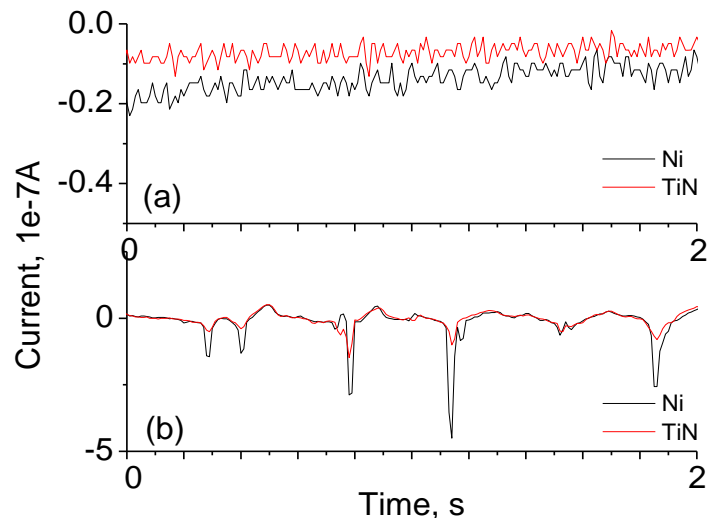


Figure 3.14 Typical current signals from: (a) homogeneous particulate flow with particles dropped from funnel; (b) 0.10 m ID freely bubbling fluidized bed.

In Figure 3.14(a), the particles were dropped continuously at a steady flow rate directly from a Plexiglas funnel, with an average particle velocity (V_p) of 0.86 m/s; the probe was placed 50 mm below the funnel exit and aligned with it, with the probe surfaces facing upward,

perpendicular to the particulate flow. The homogeneous continuous flow resulted in a constant transferred current, with small variations, and the current signal was smaller in magnitude than that in the fluidized bed because of a smaller charge density on the particles. In Figure 3.14(b), the particles were fluidized with a superficial gas velocity (U_g) of 0.36 m/s. The current signal was larger in magnitude in the bubbling fluidized bed than that in the homogenous dropping flow because of greater charges on the particles resulting from fluidization. The current signal was also strongly affected by local hydrodynamics, with fluctuations in the current signal caused by bubble movement.

Raw signals are presented at different superficial gas velocities (U_g) in Figure 3.15. Collisions of negatively charged particles with the probe resulted in a negative current. Because of the dimensions of the probe and the way the probe was inserted in the bed, the flat sensor pieces received little induced current, with most of the signals being contributed by the current transferred from collisions of charged particles. The peak amplitudes from both materials, as well as peak frequencies, increased with increasing U_g . The signals also showed a difference between the peak amplitudes from the two materials.

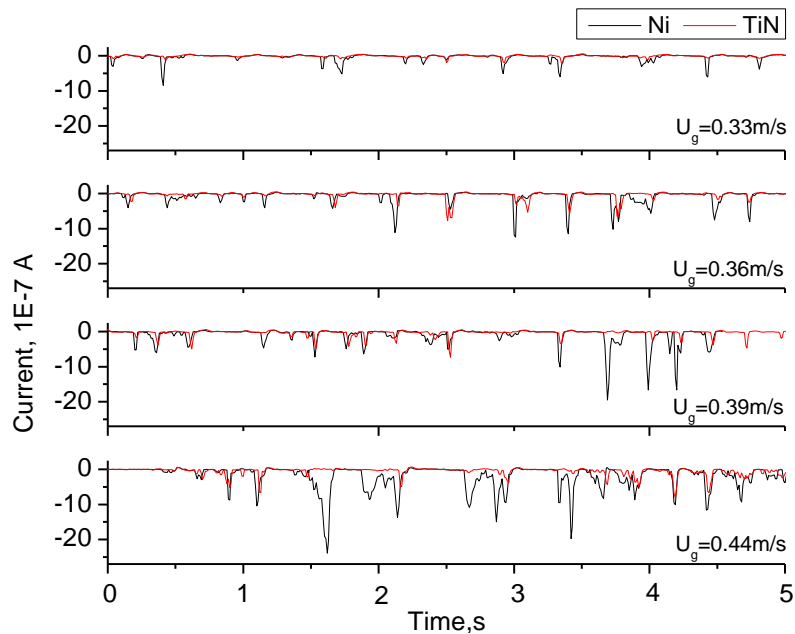


Figure 3.15 Current signals from 2t2ma probe inserted vertically into 0.10 m ID freely bubbling fluidized bed at different superficial gas velocities. (Fluidizing gas air: $T = \sim 22^\circ\text{C}$, $\text{RH} = \sim 10\%$)

3.3.2.3 Statistical and FFT analysis

Figure 3.16 shows the mean, standard deviation and normalized standard deviation of current signals from the probe in the freely bubbling fluidized bed. Both the mean and standard deviation of current signals increased as U_g increased, and the difference between the signals from the two materials also increased, consistent with the results in Figure 3.15. Also by measuring q_m from sampling particles out of the bed, it suggested that the mean currents from the two materials and the difference between these two currents increased as q_m increased. The difference between the two signals, which depends on the work function difference of the two probe-tip materials, varied as a result of changing the charge density and/or hydrodynamics. The work function difference is only expected to affect the transfer part, not the induction part, as indicated in Section 2.5.2. In this case, a 2t2ma probe was inserted vertically into the dense phase of the bed that the probe measured mainly charge transfer, so both mean and standard deviation of current signals from this novel probe include charge transfer information, and are influenced by the difference in material properties, as shown in Figure 3.16 (a) and (b). The normalized standard deviation cancels out the charge density and mainly reflects local hydrodynamics [93]. Figure 3.16(c) shows that the normalized standard deviations (standard deviation/mean) of the two materials increased as U_g increased.

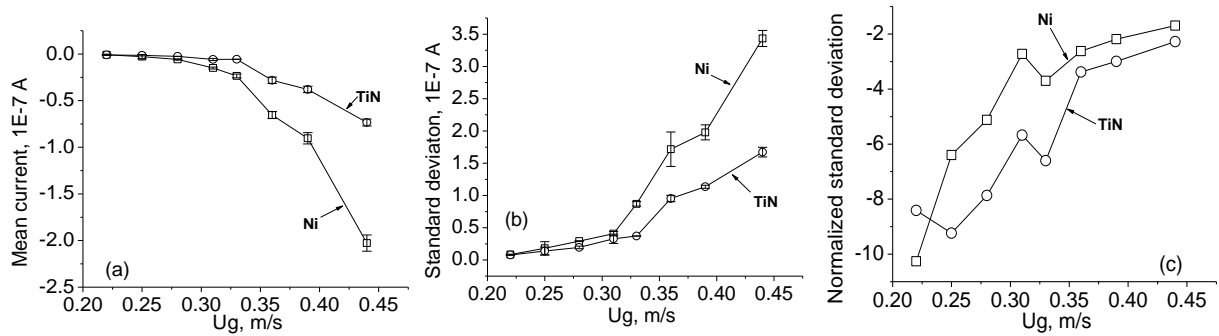


Figure 3.16 (a) Mean, (b) standard deviation and (c) normalized standard deviation of current signals from 2t2ma probe as function of superficial gas velocity in 0.10 m ID freely bubbling fluidized bed (probe inserted vertically). (Experiments for $U_g=0.22$, 0.25, 0.28 and 0.31 m/s were conducted on a different day as experiments for $U_g=0.33$, 0.36, 0.39 and 0.44 m/s)

Figure 3.17 shows the power spectrum of current signals, obtained from Fast Fourier Transformation (FFT) analysis. For both materials, the amplitude increased with increasing superficial gas velocity, confirming that current signals are closely related to hydrodynamics.

The amplitudes are always larger for Ni than for TiN, confirming that the difference in these two signals is significant. Both Ni and TiN show characteristic frequencies of 0~10 Hz at different gas velocities.

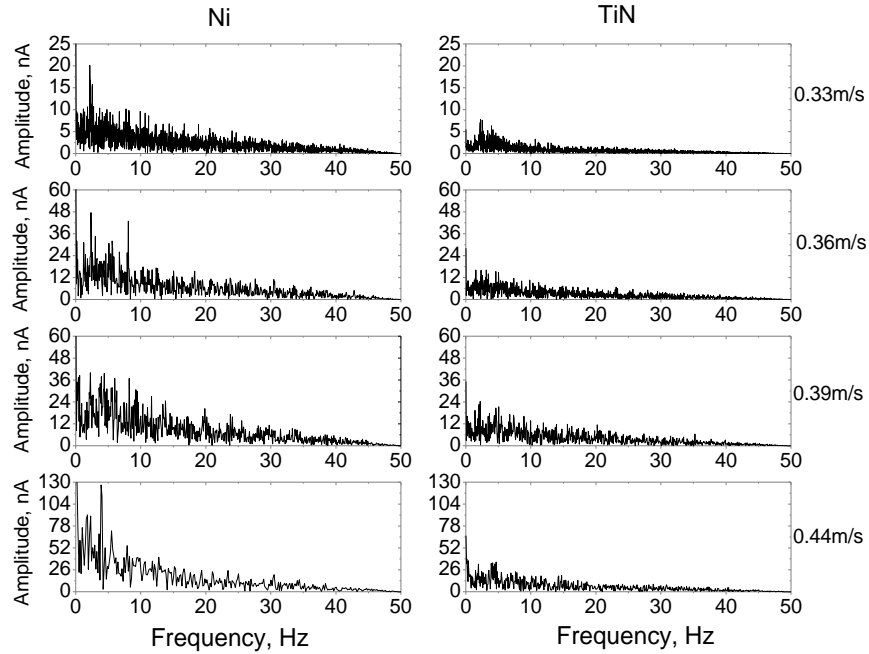


Figure 3.17 FFT of current signals from 2t2ma probe in 0.10 m ID freely bubbling fluidized bed at different superficial gas velocities.

3.3.3 Results from three-dimensional fluidization column of ID 0.30 m

3.3.3.1 Dual-tip (two-material) probe with 420-590 μm GB

Glass beads with a size range of 420-590 μm (Geldart group B, 30/40 mesh, Potters) were used in these experiments. A 2t2mb probe (see Table 2.1) was employed and inserted 0.25 m above the distributor to the centre to measure the charge inside the bed. The static bed height was 0.40 m. Figure 3.18 shows the current signals from the probe at different superficial gas velocities. The peak amplitudes and frequencies from both materials increased with increasing U_g . The peak amplitudes from the two materials also differed. Comparison of FFT probe signals with and without the air flow showed that the amplitude of noise was much smaller, so that the effect of noise could be ignored.

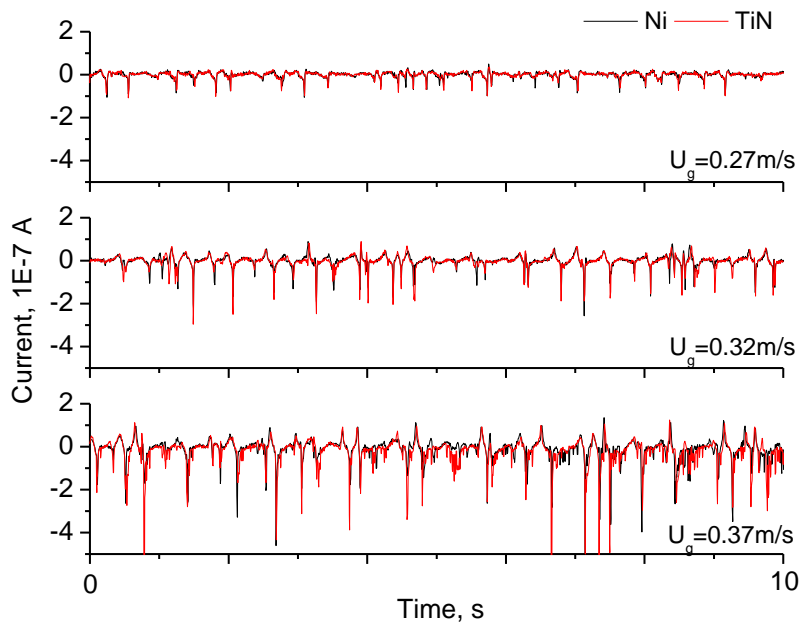


Figure 3.18 Current signal from 2t2mb probe in 0.30 m ID freely bubbling fluidized bed of 420-590 μm GB at different superficial gas velocities. (Fluidizing gas air: $T=40\pm 5^\circ\text{C}$, $\text{RH}=15\pm 4\%$)

3.3.3.2 Dual-tip (one-material) probe with original PE-I (100-1500 μm)

Since the relative magnitudes of signals from the two materials of the 2t2m probe may change for different operating conditions and particle properties (e.g. mean size and size distribution), causing difficulty in signal processing (see Sections 2.5.1, 3.3.1 and 4.4.2.2), the 2t2m probe may be unsuitable for particles of wide size distribution. 2t1m probes with different configurations and tip shapes (see Table 2.1) were next investigated with original polyethylene particles of relatively wide size distribution as the bed material. The static bed height was maintained at 0.40 m, with the probe inserted 0.25 m above the distributor to the axis to measure the charge inside the bed. Typical cumulative charge and current signals from probes at different U_g are shown in Figure 3.19. The slopes of cumulative charge signals vs time, amplitudes of current peaks from both tips and bubble frequencies all increased as U_g increased, consistent with our results from the two-dimensional fluidized bed (Section 3.3.1).

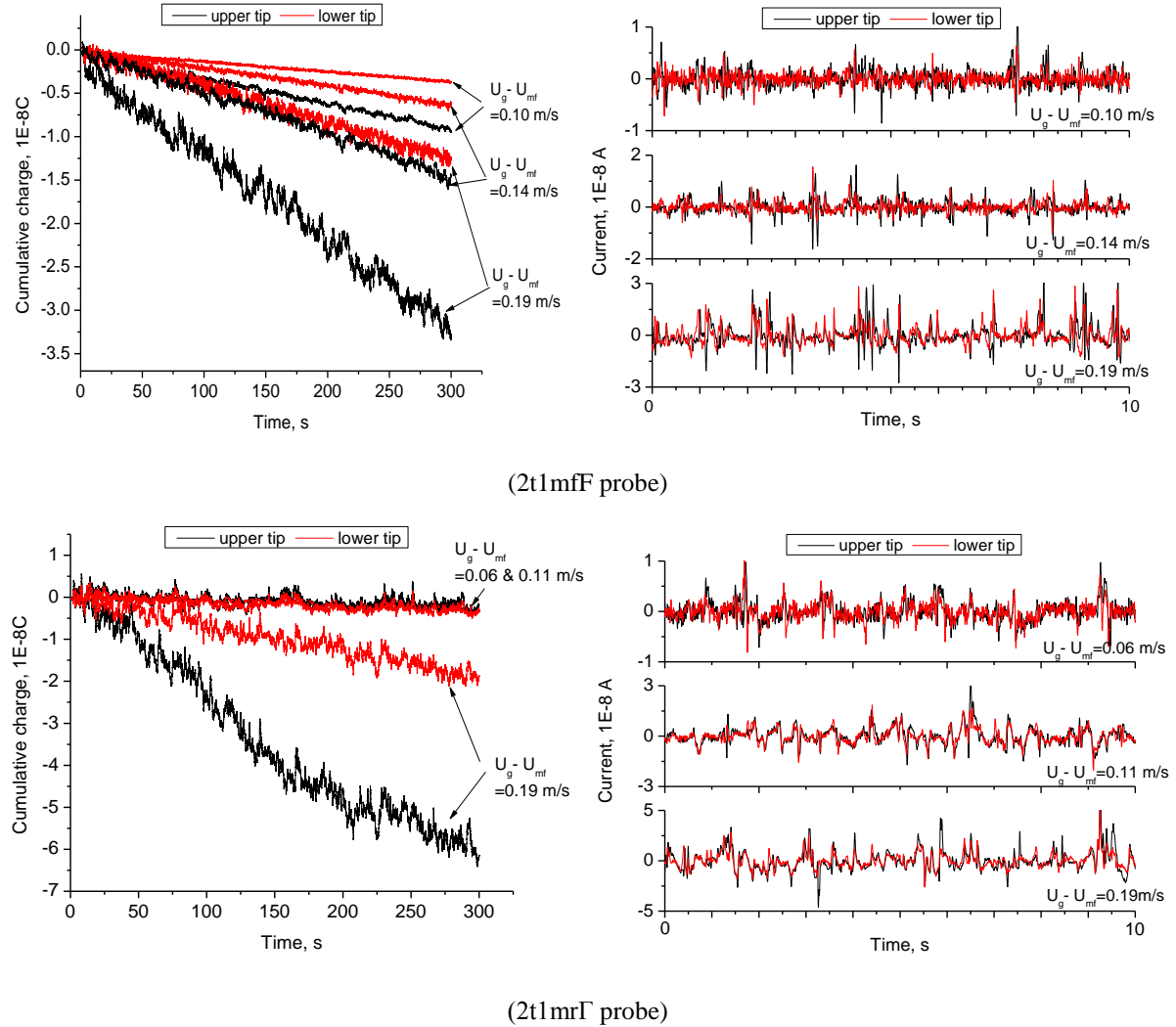


Figure 3.19 Cumulative charge and current signals from 2t1m probes at different U_g in freely bubbling 0.30 m ID three-dimensional fluidized bed of original PE-I particles. (Fluidizing gas air: $T=40\pm 5^\circ\text{C}$, RH=15±4 %)

It is of interest also to test multiple probes at different axial heights and higher superficial gas velocities, in the turbulent fluidization flow regime. The static bed height was maintained at 0.88 m. Figure 3.20 shows charge and current signals from a 2t1mr Γ probe (see Table 2.1, insertion 0.25 m above distributor) at different U_g . Slopes of charge signals from both upper tip (protruded) and lower tip (retracted), as well as the current peak frequency first increased then decreased as increasing U_g . Current peak amplitudes increased with increasing U_g . Note that the probe signal is related to charge density level and local hydrodynamics inside the bed. In the bubbling regime, where bubble coalescence was dominant, the bubble size and frequency increased with increasing U_g , so that more charge was generated by more and

stronger collisions between particles. Thus the slope of charge signal and the current peak amplitudes increased. In the turbulent fluidization flow regime, the charge induction decreased as large bubbles were replaced by small and transient voids, causing the slope of the charge signals to decrease. Because of decreased separation distance between leading-trailing voids and increased average distance between particles in the turbulent fluidization flow regime, current peak frequency and time gap between groups of peaks increased. The current peak amplitude, which is more related to the charge density and U_g , also increased.

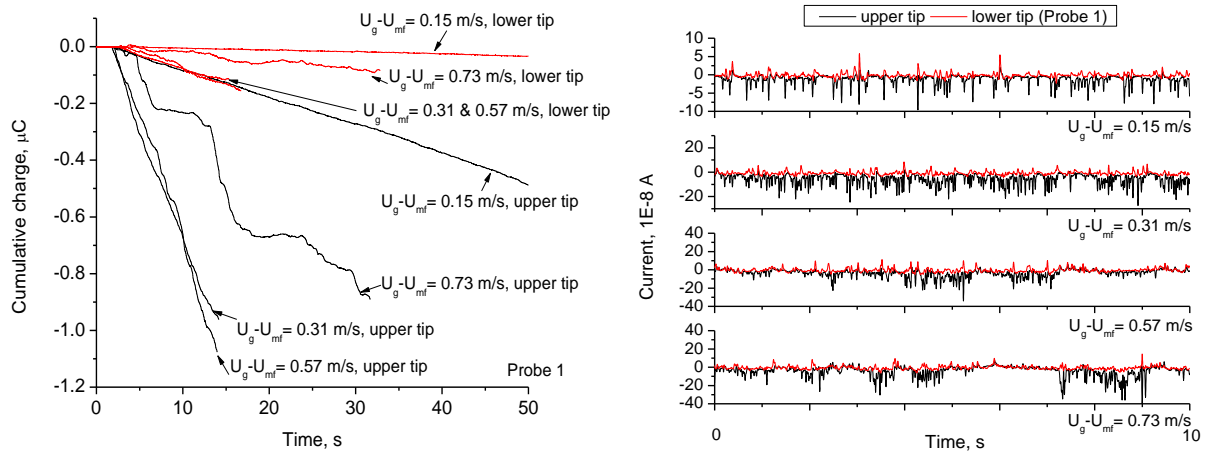


Figure 3.20 Cumulative charge and current signals from 2t1mfT probe (insertion 0.25 m above distributor) at different U_g in 0.30 m ID fluidized bed of original PE-I particles. (Fluidizing gas air: $T=40\pm 5^\circ\text{C}$, $\text{RH}=15\pm 4\%$)

Current signals from 2t1mfF probes at different height (Probe 1, 2, 3 as shown in Figure 3.2) are plotted in Figure 3.21. Current peak frequency decreased from Probes 1 to 3 as the bubbles coalesced and grew and the current peak frequency from Probe 1 was larger than that from Probes 2 and 3 because of more collisions near the distributor. Current peak amplitudes for Probes 1 and 3 were slightly larger than that from Probe 2, indicating there might be a small charge density distribution along the column height, although further validation is needed.

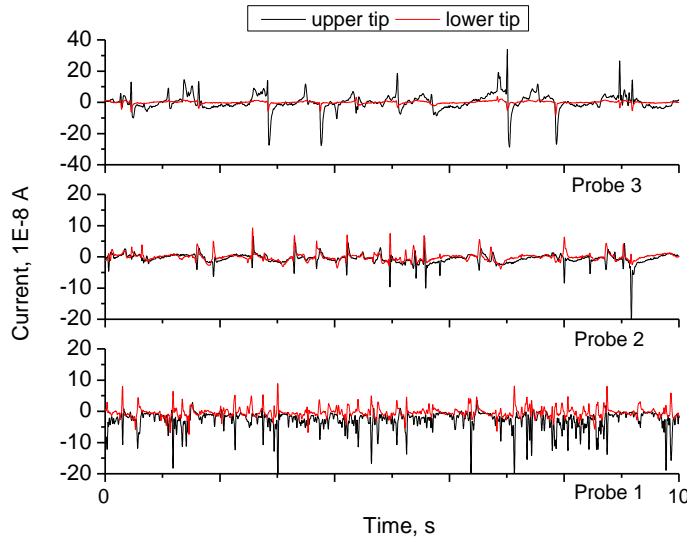


Figure 3.21 Current signals from 2t1mfF probes at different locations in 0.30 m ID fluidized bed of original PE. (probe 1: $z_1=0.25$ m, probe2: $z_2=0.70$ m and probe 3: $z_3=1.00$ m, $U_g-U_{mf}=0.24$ m/s) (Fluidizing gas air: $T=40\pm 5$ °C, RH=15±4 %)

Standard deviations (SD) of current signals from the upper tips of probes and absolute pressure signals at different U_g are shown in Figure 3.22. The transition velocity, U_c , determined from the maximum standard deviation of current signals, tended to decrease with increasing distance above the distributor. This transition velocity (~0.5-0.6 m/s) is different from the values determined from pressure fluctuations (~0.9 m/s) and from the correlation based on absolute pressure measurement (0.84 m/s) [126, 127]. Similar results were found for corresponding superficial velocity of maximum heat transfer coefficient and U_c from standard deviation of pressure fluctuations [128]. The electrostatic signals contain both charge and hydrodynamics information whereas the pressure signals only reflect hydrodynamics inside the bed. The SD from Probe 1 was larger than that from Probe 2, possibly due to the higher charge density near the distributor than the middle of the bed, similar to results in Figure 3.21. The standard deviation of electrostatic signals was related to charge induction caused by passing voids. In the bubbling regime, bubble coalescence was dominant so that charge induction increased as the bubble size increased; in the turbulent fluidization flow regime, charge induction decreased as large bubbles were replaced by small and transit voids.

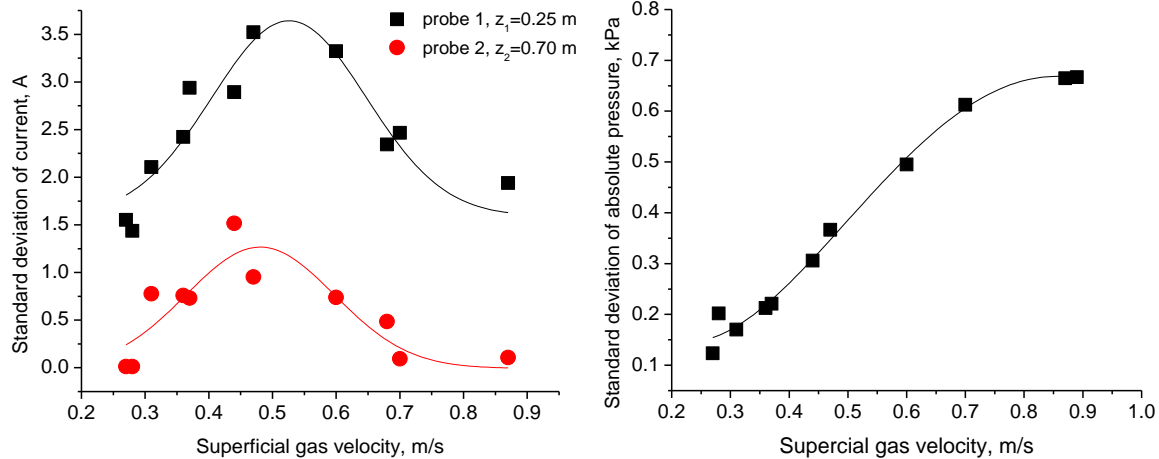


Figure 3.22 Standard deviations of current signals from 2t1m probes and absolute pressure signals versus superficial gas velocity.

3.4 Summary

The probes developed in Chapter 2 determined electrostatic charges on particles in fluidization columns of different shapes and scales: a two-dimensional column and two three-dimensional columns of inner diameters of 0.10 m and 0.30 m.

Based on experiments in these three columns, there were substantial differences between the signals (mean and standard deviation of currents and current peak amplitudes) for the Ni and TiN tips of dual-tip (two-material) probe at all superficial gas velocities tested. The differences were altered when the hydrodynamics and/or charge density inside the bed changed. These differences were independent of the relative position of the two materials. Current signals were strongly affected by local hydrodynamics in a bubbling fluidized bed. The sign of the cumulative charge signals does not necessarily represent the polarity of charge on the particles. The amplitudes of current signal peaks, as well as peak frequencies, increased with increasing the superficial gas velocity.

In the two-dimensional fluidization column, for a dual-tip (two-material) probe, both the mean and standard deviation increased as the in-bed charge density and superficial gas velocity increased, with the difference between the two materials increasing in a similar manner. The average transferred current, \bar{I}_{tran} , and average induced current, \bar{I}_{ind} , can be

related via Eqs. (3.3-3.4) to the average maximum and minimum peaks heights, \bar{I}_{\max} and \bar{I}_{\min} .

For a dual-tip (one-material) probe, the slopes of cumulative charge signals with time for both tips first increased then decreased as U_g increased. Fluctuations from the lower tip were larger than from the upper one, due to direct exposure to bubbles. For probes with different configurations, the slopes of cumulative charge signals and current peak amplitudes were greater for protruding tips than for retracted tips. Signals from the probes at different axial locations were different. A transition velocity determined from maximum standard deviation of the probe signals was different from the U_c obtained from pressure fluctuations and correlation.

Experiments in the 0.10 m ID column showed that the mean and SD of currents from two materials of the dual-tip (two-material) probe were larger at the centre than near the wall. Transferred currents from the two materials, as well as differences between them, were larger when the probe was inserted vertically rather than horizontally. Statistical analysis showed that the mean and standard deviations of current from both probe tips increased with increasing superficial gas velocity, suggesting that both transfer and induction charges increased. The normalized standard deviation (standard deviation/mean) of the two materials increased as superficial gas velocity increased, and the difference between them was nearly unchanged as the superficial gas velocity increased. From FFT analysis, both materials revealed increased amplitude with increasing superficial gas velocity, confirming that the current signals are strongly influenced by hydrodynamics and, at the same time, there are substantial differences between the two signals.

Chapter 4 Decoupling Electrostatic Signals from Gas-Solid Fluidized Beds

4.1 Introduction

Electrostatic signals registered by collision probes contain useful information, but are poorly understood. As reviewed in Chapter 1, several studies have analyzed the signals and found that electrostatics and hydrodynamics in fluidized beds are related. However, none of the earlier studies was able to decouple the signals to obtain charge density. The charge density carried on fluidized particles can assist on-line process monitoring and benefit understanding electrostatic phenomena. This chapter introduces signal selection criteria, processing procedures and decoupling methods for the probes tested in Chapters 2 and 3. Signals from these probes are analyzed, and the results from each method are compared with direct measurements in both two- and three-dimensional freely bubbling fluidized beds.

4.2 Signal analysis procedure

Charge/current signals measured by the custom-made probes were processed by first selecting appropriate peaks, followed by calculations using those peaks. Raw electrostatic signals contain noise picked up from the environment and exhibit baseline drift, usually due to weak conductive isolation of the probe. Therefore proper signal conditioning may be needed to pre-treat the signals. Two approaches are helpful to avoid or remove noise from signals: better grounding and shielding during signal acquisition, and filtering the recorded data [83].

4.2.1 Peak (bubble) detection

Electrostatic signals are related to bubble and particle movement inside fluidized beds. Selecting the appropriate peaks (bubbles) is important to eliminate irregular signals linked to bubble splitting, coalescence, rising obliquely or missing one of the two sensors. Bubble

movement is related to peaks in electrostatic signals. To select bubbles, a selection algorithm was developed in Matlab® as described in Figure 4.1. Codes are provided in Appendix C.3.

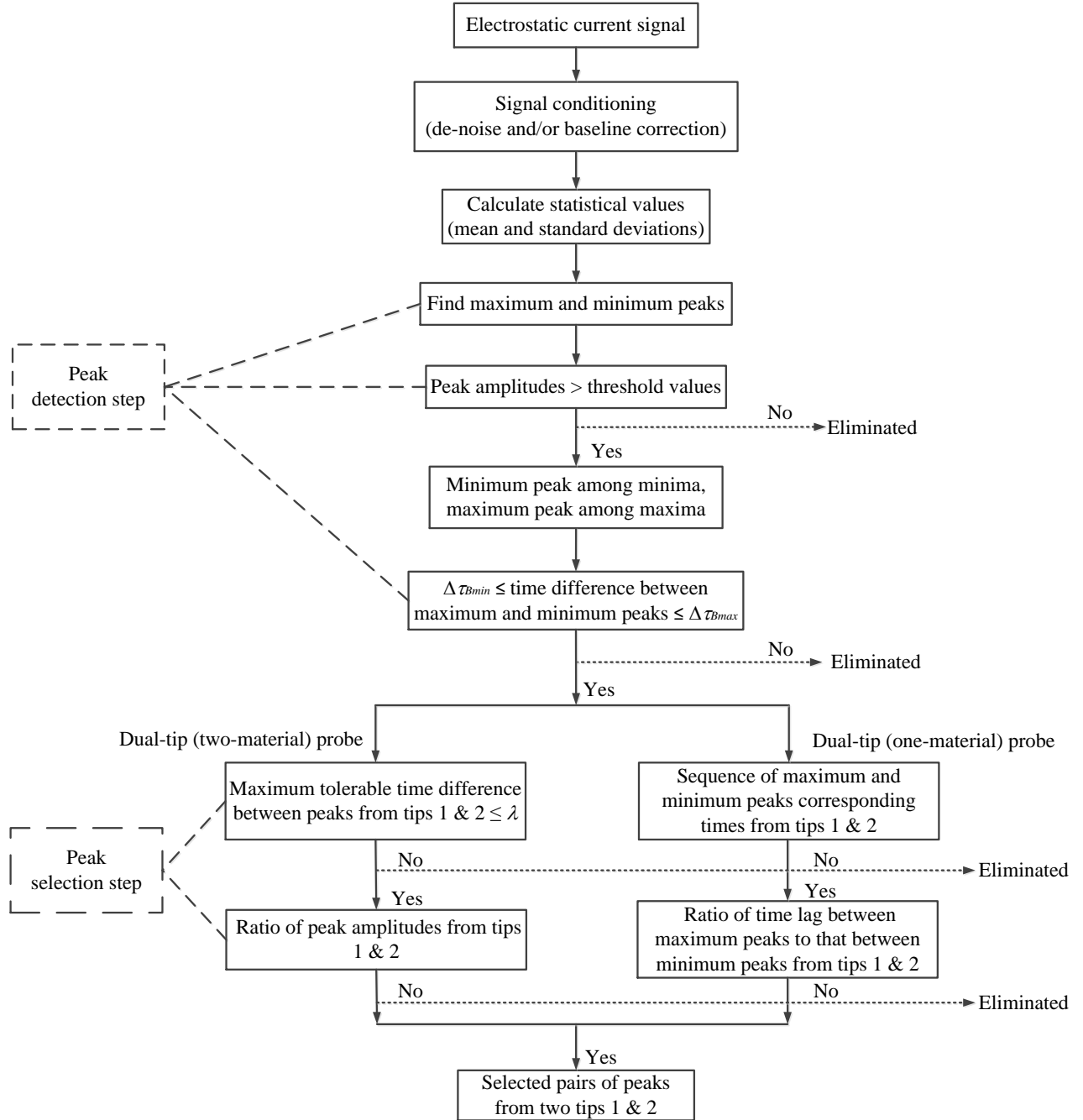


Figure 4.1 Flowchart of peak detection and selection algorithm adopted for signal processing.

After signal conditioning (de-noise and/or baseline correction), average current (\bar{I}) and standard deviation (I_{sd}) can be calculated from the raw signal from the probe. A sudden increase or decrease in the current signal indicates the passage of a bubble. Minimum and maximum peaks are identified wherever there is clear evidence of bubble passage, starting with a distinct peak from a bubble nose and completed by another from the wake. The magnitudes of the minimum and maximum peaks (I_{min} and I_{max}) from both tips are also compared with two threshold values, based on the average and standard deviation of the raw signals. Current signals which do not cross the threshold may be due to signal changes not directly linked to bubble passage, or to irregular bubbles reaching the probe. We impose the criteria:

$$I_{\max,1}(i) > \bar{I}_1 + \varphi I_{sd,1} \quad I_{\min,1}(i) < \bar{I}_1 - \varphi I_{sd,1} \quad (4.1)$$

$$I_{\max,2}(i) > \bar{I}_2 + \varphi I_{sd,2} \quad I_{\min,2}(i) < \bar{I}_2 - \varphi I_{sd,2} \quad (4.2)$$

where \bar{I} and I_{sd} are the mean and standard deviations of the raw signal, and subscripts 1 and 2 denote two tips.

Extremes among the minima and maxima are identified to ensure that only one minimum peak and one maximum peak exist within each signal segment, representing a single bubble. The time difference between adjacent maximum and minimum peaks from a tip represents the time for a bubble to pass the probe, and is thus related to bubble size. We require

$$\Delta\tau_{B\max} \geq |t_{\max,1}(j) - t_{\min,1}(j)| \geq \Delta\tau_{B\min} \quad (4.3)$$

$$\Delta\tau_{B\max} \geq |t_{\max,2}(j) - t_{\min,2}(j)| \geq \Delta\tau_{B\min} \quad (4.4)$$

where $\Delta\tau_{B\max}$ and $\Delta\tau_{B\min}$ represent the times for maximum and minimum allowable bubbles to pass the probe. These criteria (Eqs. (4.1-4)) define the peaks caused by passing bubbles.

4.2.2 Peak (bubble) selection

Signals from a second tip (electrode) of the probe were then used together with the first tip signals to select appropriate bubbles. The criteria depend on how the two tips are configured.

4.2.2.1 Dual-tip (two-material) probe

For a dual-tip (two-material) probe with two side by side tips, the current peaks, from the two different materials should appear at the same time to ensure that the bubble contacted the two tips simultaneously, so that:

$$|t_{peak,1}(j) - t_{peak,2}(j)| \leq \lambda \quad (4.5)$$

where λ is the maximum tolerable time difference between current peaks from the two materials, and subscripts 1 and 2 denote the two tips.

Also, the ratio of the current peaks from two tips is a function of the difference between the two materials. A smaller ratio means a larger difference between currents from two materials. The amplitude from TiN and Ni tips differs and needs to be tested for each case. For example, if the amplitudes of current peaks from TiN were smaller than that from Ni,

$$\delta \leq \frac{I_{peak,2}(j)}{I_{peak,1}(j)} \leq \omega \quad (4.6)$$

where δ and ω are the chosen lower and upper boundaries of the ratio.

4.2.2.2 Dual-tip (one-material) probe

For a dual-tip (one-material) probe with two tips vertically aligned, signals were selected if they satisfied the following criteria. The maximum and minimum peaks corresponding times ($t_{max,1}$, $t_{min,1}$, $t_{max,2}$, $t_{min,2}$) should follow the sequence $t_{max,2} < t_{max,1} < t_{min,2} < t_{min,1}$, where subscripts 1 and 2 denote the upper and lower tips, separated by a distance much smaller than the bubble size. A ratio of time lag between maximum peaks from the two tips to the time shift between minimum peaks from the two tips, is required to be within the interval of 0.8–1.2, allowing a reasonable range of deviations for bubbles passing the two tips vertically, based on criteria used in signal analysis of optical fiber probes [129]. Hence we require

$$\left. \begin{aligned} t_{max,2} < t_{max,1} < t_{min,2} < t_{min,1} \\ 0.8 < \frac{t_{max,1} - t_{max,2}}{t_{min,1} - t_{min,2}} < 1.2 \end{aligned} \right\} \quad (4.7)$$

All pairs of peaks that satisfied these criteria are selected and used for calculation.

4.3 Decoupling methods

Charge density, as well as bubble rise velocity, can be calculated by different decoupling methods using amplitudes and corresponding times of selected pairs of peaks.

4.3.1 Charge transfer and induction model

The charge transfer and induction model developed by Park et al. [20] and Chen et al. [21] simulated the transferred and induced charges received by a collision probe due to a single bubble passing in a fluidized bed. The following assumptions were made:

- a. The total charge/current received by the probe consists of two components: charge induction and charge transfer. For highly charged particles, charge separation is much smaller than charge transfer and is neglected.
- b. Each bubble is spherical, with its diameter remaining constant as the bubble rises at a constant velocity after injection.
- c. Only one bubble contacts the probe at a time.
- d. No particles are inside the bubble, and charges are negligible inside bubbles.
- e. The charge distribution is obtained by superposition of two simple components: a uniformly charged bed with specific charge q_m and a charged spherical ball with uniform charge density $-q_m$.
- f. The velocities of particles in the nose and wake regions are related to the bubble rise velocity.

As a bubble with surrounding charged particles passes a collision probe, an image charge is induced. For example, if a bubble surrounded by negatively charged particles passes the probe, a negative charge is registered by the conductive probe tip, as shown in Figure 4.2. The negative charge reaches a minimum (C_{\min}) when the probe is inside the bubble. As shown in Section 3.3.1, I_{tran} and I_{ind} , which represent the transferred and induced currents when the bubble nose/wake makes contact with the probe, can be derived from the maximum and minimum peaks via Eqs. (3.3) and (3.4). It is assumed that the charge density of particles surrounding bubbles is the same, regardless of the bubble size, shape and movement at a particular location inside the bed.

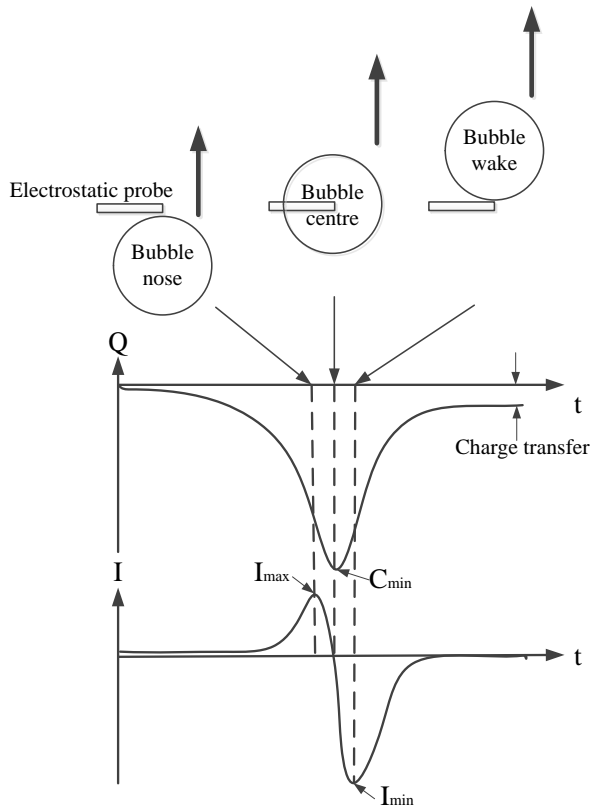


Figure 4.2 Theoretical charge and current signals received from collision probe when a single bubble passed by.

4.3.2 Dual-tip (two-material) probe

4.3.2.1 Transfer-induction method (Solving for U_B and q_m together)

The transfer and induction currents are both functions of particle charge density and hydrodynamic properties in the fluidized bed, such as bubble diameter and rise velocity. They can be decoupled by solving the simultaneous equations for the transfer and induction parts:

$$I_{tran} = f(q_m, U_B(D_B)); \quad I_{ind} = g(q_m, U_B(D_B)) \quad (4.8)$$

For 2t2m probe, the transfer current equation (Eq. (2.5)) for two materials can be obtained by calibrating the probe in a charged particulate flow system (Section 2.5.1). The solid flow rate (W_s) is related to average particle velocity (V_p) by Eq. (2.10) with the particle velocity in the bubble nose and wake regions approximated by the bubble rise velocity and the voidage near

the bubble by ε_{mf} , the voidage at minimum fluidization. The induced current could be related to charge density and bubble rise velocity by Eq. (2.12).

4.3.2.2 Two transfer currents/current peaks methods (Solving for U_B and q_m together)

Different signals, generated from the two tips, could be used as well if calibration equations for the two tips are known, so that q_m and U_B can be estimated by solving the two equations for the tips together. For a dual-tip (two-material) probe, the following two methods could be used based on the transfer and total current for the two materials.

- (a) Two transfer currents method: The two materials produce different transfer currents. Therefore, the signal can be decoupled by simultaneous solving two transfer equations.
- (b) Two current peaks method: The total currents from the two materials differ. The total current is a sum of the transfer and induction parts:

$$I_{total} = I_{tran} + I_{ind} = h(q_m, U_B(D_B)) \quad (4.9)$$

Application of Eq. (4.9) to each of the two materials allows the current signal to be decoupled. Equations of this form corresponding to the current peaks for two materials were obtained (Eq. (2.13)) by calibrating the probe with different particle charge density (q_m) and bubble rise velocity (U_B) for single bubble injection and free bubbling experiments (Section 2.5.4).

4.3.2.3 Time-difference method (Solving for U_B first, then q_m)

The time interval between adjacent maximum and minimum peaks in the current signal represents the time for a single bubble to pass the probe. Since the probe is much smaller than the bubble, the distance through which the bubble moves is related to the bubble diameter.

$$\Delta\tau = \frac{D_B}{U_B} \quad (4.10)$$

The bubble diameter is related to its rise velocity for isolated bubbles [130, 131] by

$$\left. \begin{aligned} U_B &= U_g - U_{mf} + 0.711\sqrt{gD_B} && \text{three-dimensional fluidized bed} \\ U_B &= U_g - U_{mf} + 0.597\sqrt{gD_B} && \text{two-dimensional fluidized bed} \end{aligned} \right\} \quad (4.11)$$

From Eqs. (4.10) and (4.11), the bubble rise velocity U_B and diameter D_B can be estimated first, after which q_m can be solved by inserting U_B into the transfer, induction or total current relationships, Eqs. (4.8) or (4.9).

4.3.3 Dual-tip (one-material) probe

Instead of using empirical correlation of Eq. (4.11), one could measure bubble rise velocity, then particle charge density could be estimated by inserting that rise velocity into Eq. (4.9).

Figure 4.3 shows the probe with two tips separated vertically by a known distance, Δz . When a bubble passes, each tip registers a current signal, with maximum and minimum peaks corresponding to arrival of the bubble nose and wake. The time lag between the peaks from the two tips, Δt , can be used to determine the bubble rise velocity, and the bubble size can be estimated from the time difference $\Delta\tau$ between the times corresponding to arrival of the bubble nose and wake from either tip, as shown in Eq. (4.10). Note that the measured bubble size is the pierced chord length of the bubble.

$$U_B = \frac{\Delta z}{\Delta t} \quad (4.12)$$

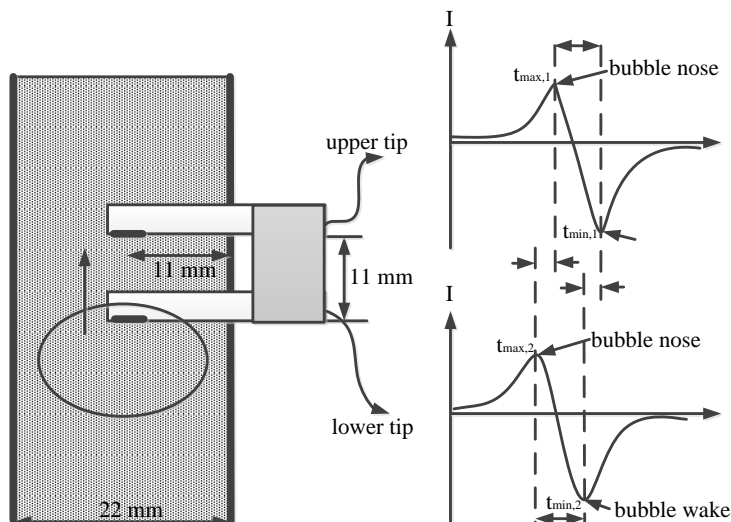


Figure 4.3 Principle of 2t1m probe (F configuration) to determine bubble rise velocity and size.

4.3.3.1 Two-tips cross-correlation (time-average) method

The time lag, Δt , can be obtained by cross-correlation or Eq. (4.13). The cross-correlation function of time-series signals from two tips is:

$$R_{I_1 I_2}(\Delta t) = \frac{1}{H} \lim_{T \rightarrow \infty} \int_0^H I_1(t) I_2(t + \Delta t) dt \quad (4.13)$$

where Δt is the time shift for the cross-correlation (coefficient) function to reach a maximum, indicating the time delay where two signals are best aligned, corresponding to the average time for bubble passage between the two tips. For a known Δt , U_B and q_m can then be obtained from Eqs. (4.12) and (4.9).

4.3.3.2 Two-tips peak-times (dynamic) method

The other way to obtain the time lag Δt is based on the time difference between peaks from the upper and lower tips. Selected pairs of peaks representing bubbles were used to calculate the time lag, Δt , and time difference, $\Delta\tau$, by

$$\Delta t = \frac{(t_{\max,1} - t_{\max,2}) + (t_{\min,1} - t_{\min,2})}{2} \quad (4.14)$$

$$\Delta\tau = \frac{(t_{\min,1} - t_{\max,1}) + (t_{\min,2} - t_{\max,2})}{2} \quad (4.15)$$

Then U_B and D_B were estimated by Eqs. (4.12) and (4.10), respectively. While q_m was calculated from Eq. (4.9) based on the current peaks from each tip.

4.3.3.3 One-tip time-difference (dynamic) method

Similar to the dual-tip (two-material) probe, signals from one tip could also be used to estimate bubble rise velocities and particle charge densities, as explained in Section 4.3.2.3.

The two tips cross-correlation method gives time-average from signals recorded over a period of time, while the two tips peak-times and one-tip time-difference methods provide dynamic values for specific times. For a probe with F configuration (both tips protruding), q_m from the lower tip is preferred because bubbles reaching the lower tip are affected less by the

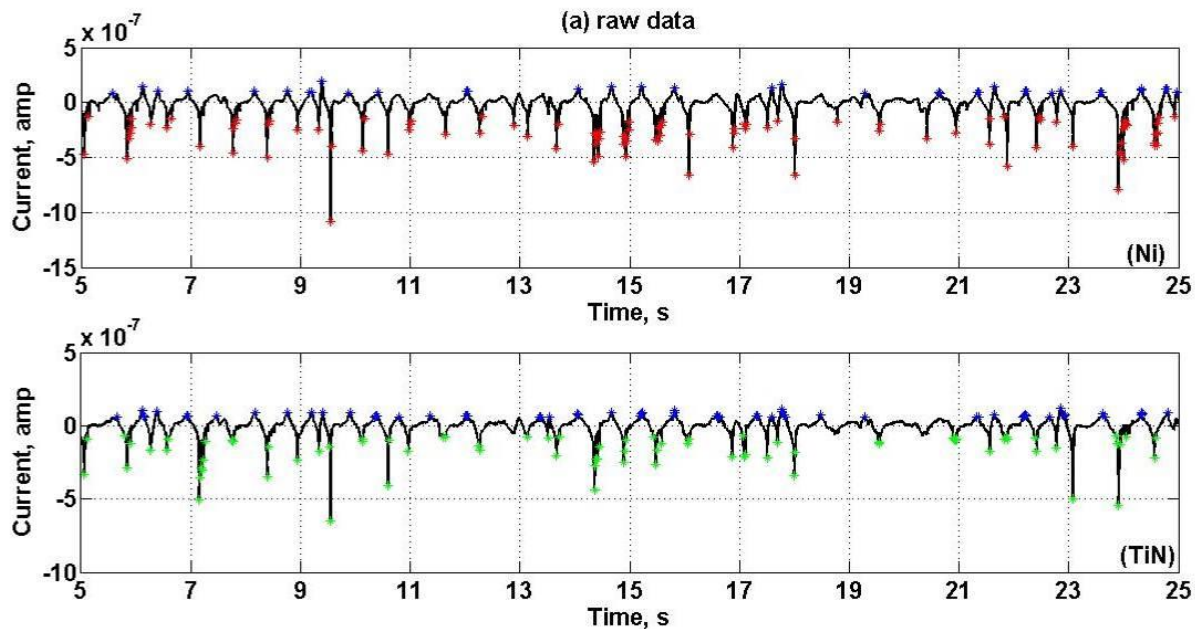
probe, whereas for only one tip protruding, results are applied from that tip. Error bars were generated by applying the Student t distribution to find 90% confidence intervals.

4.4 Results and discussion

4.4.1 Signal processing

4.4.1.1 Effects of bubble selection criteria

Figure 4.4 shows raw data, peak-detected data and peak-selected data from the 2t2mb probe (see Table 2.1) after applying the bubble selection criteria to a same 20 s period of time signals from the two-dimensional bubbling bed. The algorithm picks peaks (bubbles) based on the chosen criteria. The Peak-detected data show detected peaks after applying Eqs. (4.1-4) and the peak-selected data represent selected peaks after applying Eqs. (4.5) and (4.6).



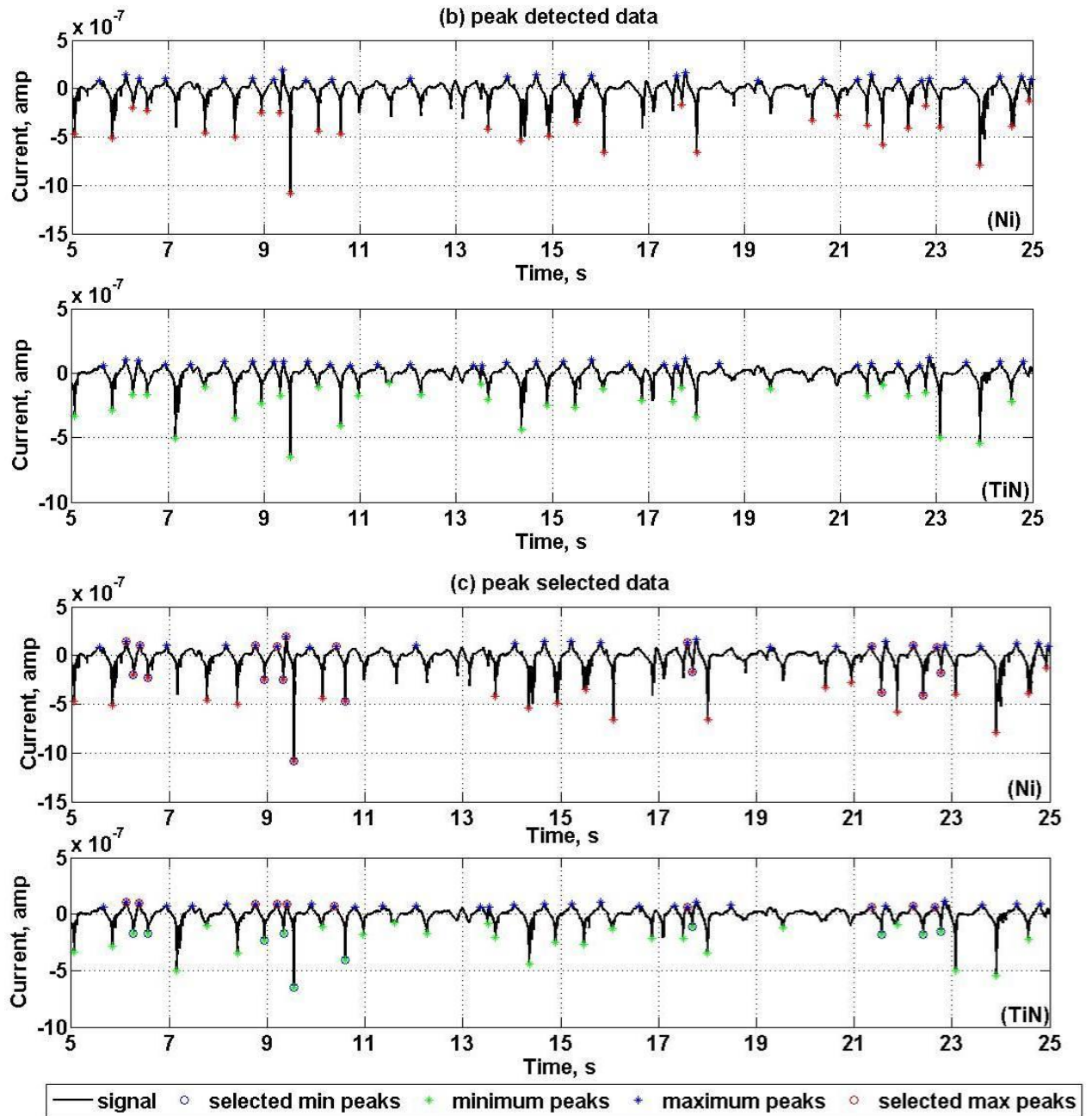


Figure 4.4 (a) Raw data, (b) peak-detected data and (c) peak-selected data, generated from 2t2mb probe in two-dimensional bubbling fluidized bed of glass beads.

To choose the proper criteria and improve the accuracy of the bubble selection algorithm, as well as calculation results, the effect of each parameter on selected bubble numbers was investigated while keeping other parameters constant, as shown in Figure 4.5. A 40 s period of time-series signal with a total of 70 bubbles from the probe was adopted for analysis.

The total current is the sum of the transfer and induction components; the mean current represents the net transferred current, and the standard deviation represents the net induction current. The φ coefficient (see Eqs. (4.1) and (4.2)) affects the threshold that defines the amplitude of a peak. The number of bubbles selected decreased with increasing φ , decreasing sharply beyond $\varphi = 1$. Thus, φ was chosen to be 1 for subsequent analyses. The maximum tolerable time difference between current peaks from the two materials (tips), λ (see Eq. (4.5)), levels off beyond 0.01 s. This seems to be a sensitive value for λ . Also λ was smaller than 0.01 based on comparison of the probe signal with synchronized video images. The upper and lower boundaries of ratio of current peaks from the two materials (tips), ω and δ (see Eq. (4.6)) are the most sensitive factors. The number of selected bubbles increases when the upper boundary ω is increased, and becomes stable beyond $\omega = 1$. On the other hand, the number of selected bubbles decreases when the lower boundary δ increases. A larger ratio of current peaks from the two materials (tips), means a larger difference between the signals from the two materials (tips), causing more bubbles to be selected. However, an extremely large or small ratio implies a non-vertical bubble trajectory, for example acceptance of bubbles moving in such a way that most particles only collide with one tip. Such cases were observed in the videos. Differences in current signals from the two tips mainly arose from the transfer components, so ω was chosen as 1 based on the average ratio of induction parts. δ was taken as 0.4 based on analyzing the signals from the fluidized bed and dropping tests of charged particles (Sections 2.5.4 and 2.5.1). Time for maximum and minimum allowable bubbles to pass the probe, $\Delta\tau_{B_{max}}$ and $\Delta\tau_{B_{min}}$, are related to minimum and maximum allowable bubble sizes ($D_{B_{min}}$ and $D_{B_{max}}$) by Eqs. (4.3) and (4.4). The number of selected bubbles slightly decreased with increasing $D_{B_{min}}$ and increased with increasing $D_{B_{max}}$ and became stable after $D_{B_{max}} = 0.2$ m. Too small a bubble size may cause probe signals too weak to be undetected, and the maximum bubble size needs to be smaller than the column width (0.3 m). Also from visual observations of recorded videos, 0.01 and 0.2 m were chosen as the $D_{B_{min}}$ and $D_{B_{max}}$ for current analysis.

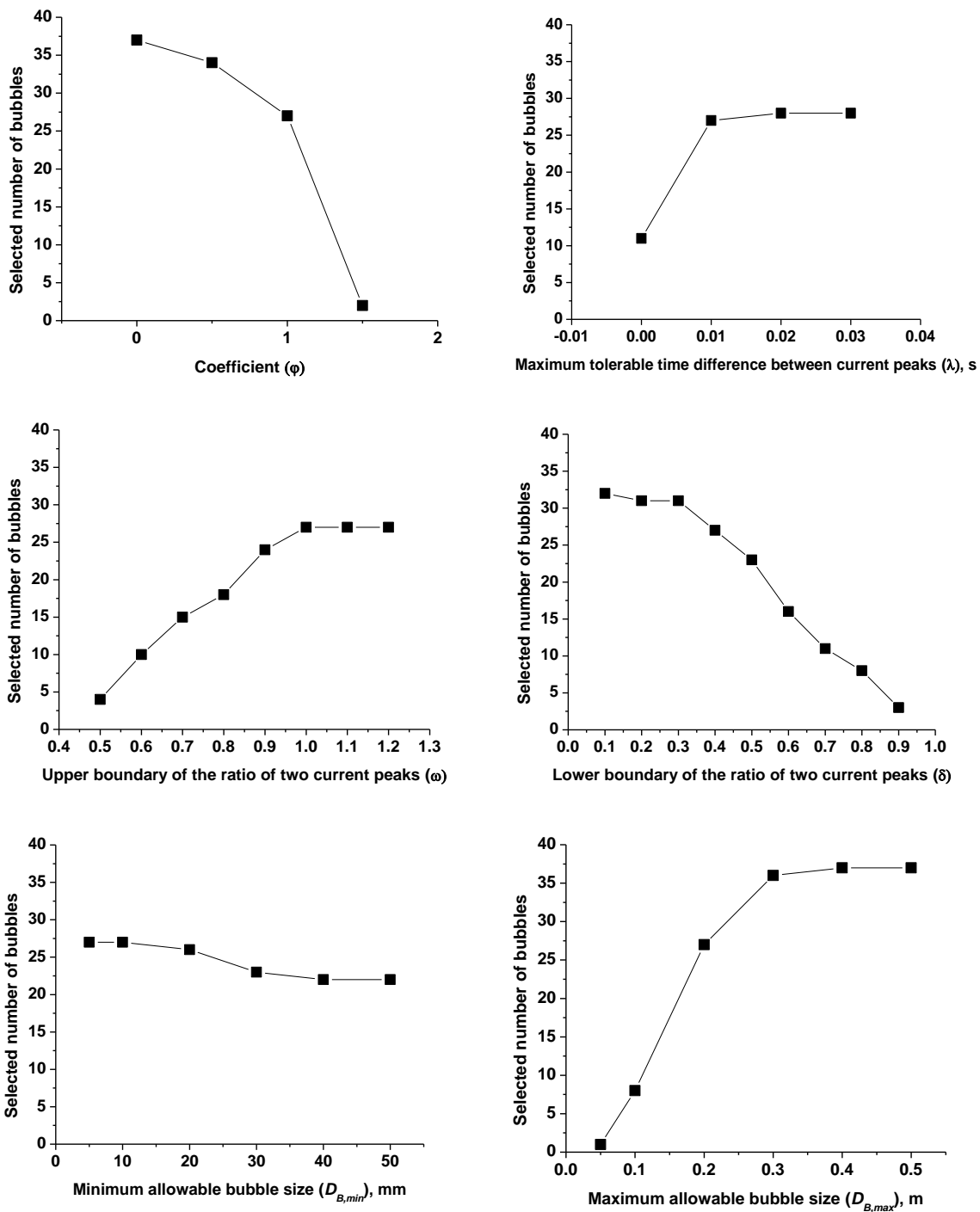


Figure 4.5 Effects of different parameters on number of selected bubbles from a 40 s period of time-series signals (70 bubbles in total) in bubble selection algorithm of signal processing for 2t2mb probe in two-dimensional fluidized bed.

4.4.1.2 Effect of decoupling methods

Different decoupling methods identified in Section 4.3.2 were applied to the current signal from 2t2mb probe (see Table 2.1) in the two-dimensional fluidized column. Each tip (Ni or TiN) of the probe can be regarded as a 1t1m probe. Table 4.1 provides decoupled q_m and U_B obtained by different methods for a signal segment of ~1 s duration (represents one bubble) from the probe in the bubbling two-dimensional bed with different superficial gas velocities. Results calculated by the transfer-induction method (T1) from each tip were represented as T1-Ni and T1-TiN, respectively. In the time-difference method (T2), U_B was first obtained from the time interval between adjacent peaks, and then inserted into calibration equations to calculate q_m . Three equations, representing induced, transfer and peak currents, were used to decouple the signal for each material. In total six q_m results were obtained based on six equations for the two materials (tips), referred to as T2-Ni-ind, T2-TiN-ind, T2-Ni-tran, T2-TiN-tran, T2-Ni-peak and T2-TiN-peak. For two tips, the two transfer currents method (TT1) and two current peaks method (TT2) were applied to decouple the signal.

The particle charge densities measured by the Faraday cup (FC) serve as a reference. q_m decoupled by the T2-Ni-ind, T2-TiN-ind, T2-Ni-peak, T2-TiN-peak and TT2 methods have the same order of magnitudes and similar trends as those measured by a Faraday cup. U_B decoupled by T2 and TT2 methods also have the same order of magnitudes and trends as the results from video analysis. U_B decoupled by method TT2 was larger than that decoupled by the T2 method, and a similar trend was found in bubble nose velocities ($U_{B,nose}$) and bubble wake velocities ($U_{B,wake}$) as velocities derived from video analysis.

The T2-Ni-peak, T2-TiN-peak and TT2 methods were selected for further evaluation because these methods do not require separation of transfer and induction components in the signals. The signals from the probes represent total charge or current. To separate these two components, one needs to identify each segment of signal caused by every bubble movement; however, peaks are often affected by bubble interaction and splitting [132]. The model assumes that bubbles have a constant velocity when contacting the probe; however videos show that the interaction between bubble and the probe may cause the wake to rise more quickly than the nose, leading to inaccurate results when seeking to separate the transfer and

induction parts of the signal. Hence, if one wants to separate the transfer and induction parts, a combined collision and induction probe may be a better option. The T2 method first estimates U_B when decoupling the signal, while the TT2 method uses additional information provided by the probe to deconvolute the signal. The decoupled results require accurate calibration equations and proper signal processing to eliminate unwanted bubbles. Two current peaks method (TT2) likely gave closer charge density results compared with those from Faraday cup measurement. Time-difference method (T2) showed less scatter results because of using bubble rise velocity correlation.

Table 4.1 Decoupled charge densities and bubble rise velocities based on different decoupling methods for one segment of signals (~1 s duration) for two-dimensional bubbling fluidized bed at different superficial gas velocities, U_g .

U_g , m/s	Decoupled charge densities, $-q_m$, $\mu\text{C/kg}$										
	T1-Ni	T1-TiN	T2-Ni-ind	T2-TiN-ind	T2-Ni-tran	T2-TiN-tran	T2-Ni-peak	T2-TiN-peak	TT1	TT2	FC
0.29	0.46	0.41	1.46	1.09	0.33	0.26	2.36	2.02	-0.13	1.82	2.02
0.33	0.77	0.82	2.06	1.31	0.85	0.93	3.41	2.93	0.26	2.62	3.97
0.36	1.12	1.23	2.69	1.88	1.13	1.30	4.30	4.11	0.39	3.88	4.27
0.39	1.86	8.29	4.58	3.09	2.51	3.19	7.24	7.00	0.65	6.43	4.82

U_g , m/s	Decoupled bubble rise velocities, U_B , m/s										
	T1-Ni	T1-TiN	T2-Ni-ind	T2-TiN-ind	T2-Ni-tran	T2-TiN-tran	T2-Ni-peak	T2-TiN-peak	TT1	TT2	Video
									$U_{B,nose}$	$U_{B,wake}$	
0.29	1.24	1.06	0.43	0.43	0.43	0.43	0.43	0.43	N/A*	0.70	0.40
0.33	1.34	0.84	0.55	0.55	0.55	0.55	0.55	0.55	1.81	0.81	0.63
0.36	1.56	1.04	0.71	0.71	0.71	0.71	0.71	0.71	2.22	0.81	0.63
0.39	1.73	0.31	0.76	0.76	0.76	0.76	0.76	0.76	3.32	0.88	0.59

*Complex number when solving equations.

T1: Transfer-induction method (Section 4.3.2.1)

TT1: Two transfer currents method (Section 4.3.2.2(a))

TT2: Two current peaks method (Section 4.3.2.2(b))

T2: Time-difference method (Section 4.3.2.3)

FC: Faraday cup

ind: Induction

tran: Transfer

4.4.2 Results from two-dimensional fluidization column

4.4.2.1 Dual-tip (two-material) probe with 500-600 μm GB

Gauss' law may be used to give an upper limit on the particle charge that can accumulate before ionization of the surrounding fluid occurs [3]. Charge accumulation on the surface of a dielectric particle is related to the electric field at the particle surface. For a spherical particle in a mono-ionized field, a saturation charge is reached due to a DC corona discharge when the attractive field due to the field distortion equals the repulsive field due to the charge on the particle. By equating the force due to the distorted field and the force of repulsion from the charged particle, the maximum surface charge density on the particle, Q_s (C/m^2), is given [11, 30, 133] by

$$Q_s = E \Pi_0 p \quad (4.16)$$

where $p = 3\Pi_r / (\Pi_r + 2)$, and Π_r is the relative permittivity of the particle. E is the electrical field around the particle. For an air breakdown potential of around 3000 kV/m and Π_0 , the permittivity of vacuum, of $8.85\text{E}-12 \text{ F}/\text{m}$, the maximum charge density in our experiments is estimated to be $1.9\text{--}2.3\text{E}-4 \text{ C}/\text{kg}$, with a relative permittivity of 3 [11], a particle density of $2500 \text{ kg}/\text{m}^3$ and a particle size range of 500-600 μm .

Initially, the two transfer current method (Section 4.3.2.2(a)) was applied with the calibration equations (Eqs. (2.5)-(2.7)) for transfer currents developed from gas-solid homogeneous flow. In addition, $(\bar{I}_{\min} + \bar{I}_{\max}) / 2$ from the two materials were assumed to correspond to transfer currents to estimate the charge density. However, the resulting values were an order of magnitude smaller than the charge densities measured by the Faraday cup. This suggests that the calibrations developed in homogeneous gas-solid flow cannot be applied directly to the freely bubbling fluidized bed because of the distributions of particle collision velocity and solid concentration associated with bubble movement.

As an alternative, the two current peaks method (Section 4.3.2.2(b)) was used to estimate the charge density and bubble rise velocity in freely bubbling beds with Eqs. (2.13)-(2.15), based on current peaks and measured charge density and bubble rise velocity for single bubbles.

The data used for calculation were from freely bubbling experiments without synchronization. Current peaks from the two materials were chosen from time-series data from the probe by applying the selection criteria and parameters described above ($\varphi=1$, $\lambda=0.01$ s, $D_{B\min}=10$ mm, $D_{B\max}=200$ mm, $\omega=1$ and $\delta=0.4$). For each pair of selected current peaks corresponding to passage of a suitable bubble, the charge density and bubble rise velocity were then estimated by solving Eq. (2.13) for the two materials simultaneously, with α_i , β_i and γ_i from Eqs. (2.14) and (2.15). At least 20 bubbles were selected for each superficial gas velocity and analyzed to obtain an average charge density and bubble rise velocity. Error bars were generated by applying the Student t distribution to find 95% confidence intervals. Bubbles are selected in a given size range, rising vertically aligned with the probe, and not involved in coalescence or splitting. Charge densities from the Faraday cup are averages of at least three determinations.

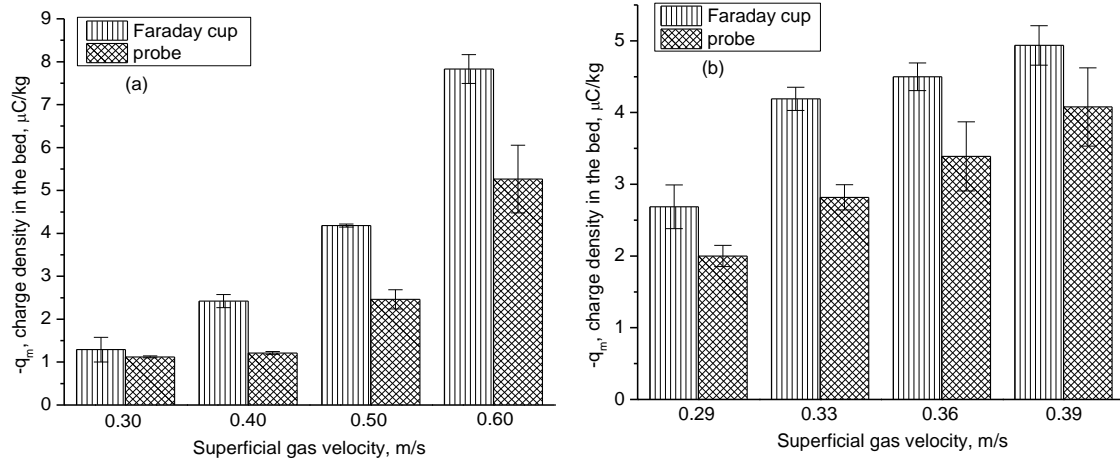


Figure 4.6 Comparisons of charge density from 2t2mb probe and Faraday cup measurements at different U_g in freely bubbling two-dimensional fluidized bed: (a) Static bed height 0.30 m with probe 0.22 m above distributor; (b) Static bed height 0.50 m with probe 0.42 m above distributor.

Figure 4.6 compares q_m derived from Eq. (2.13) with those measured by the Faraday cup based on particles withdrawn through the sampling port. q_m from both the Faraday cup and probe are of order $1\text{E}-6$ C/kg for two static bed heights, similar to values reported in the literature [40, 53] and much less than the maximum q_m estimated by Eq. (4.16). As expected, the magnitude of the charge density increases with increasing U_g for both direct and indirect measurements. Differences in charge densities from direct (Faraday cup) and indirect (probe)

measurements for $U_g = 0.6$ m/s are larger for case a (lower static bed height) than for case b. Note that the calibration equations were obtained in situations where bubbles were passing the probe one by one. However, in case a, with the probe closer to the distributor, videos showed that bubbles coalesced frequently in the lower section of the bed, likely making bubbles rise less vertically. The same factor led to a lower proportion of bubbles meeting all the discrimination criteria in case a than in case b.

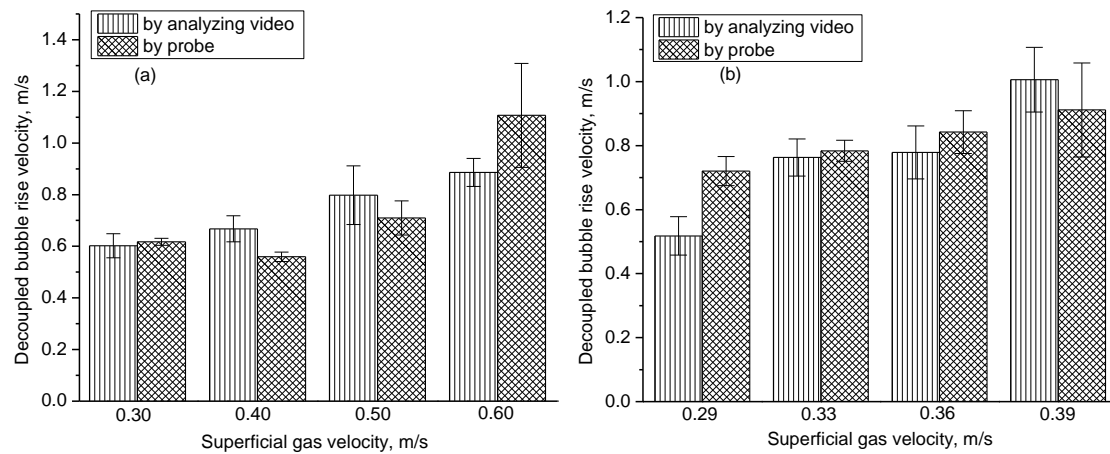


Figure 4.7 Comparisons of bubble rise velocity from 2t2mb probe and video measurements under different U_g in freely bubbling two-dimensional fluidized bed: (a) Static bed height 0.30 m with probe 0.22 m above distributor; (b) Static bed height 0.50 m with probe 0.42 m above distributor.

Figure 4.7 compares the estimated U_B from decoupling electrostatic charge signals with those obtained by analyzing videos of the two-dimensional bed at different U_g . The calculated U_B from the probe signals are similar in magnitude to those from the video images. Both methods indicate that, as expected, U_B increased with increasing U_g . The relative magnitudes of U_B obtained from the probe and video analysis are closer than the charge density results in Figure 4.6, with most error bars overlapping.

The charge density (q_m) and bubble rise velocity (U_B) were also estimated based the time-difference method (see Section 4.3.2.3). As shown in Figure 4.8, both calculated q_m and U_B varied in a consistent manner, with the same order of magnitude as those from direct measurements (Faraday cup for q_m and video analysis for U_B). In Figure 4.8(b), decoupled U_B from the time-difference method are closer to bubble nose velocity ($U_{B,nose}$) from video analysis and deviate less than those calculated by the two current peaks method which are

nearer to the ($U_{B,\text{wake}}$) bubble wake velocity, especially at higher superficial gas velocities. Note that Eqs. (2.14) and (2.15) were obtained based on $U_{B,\text{wake}}$ and the interaction of bubble and the probe may result in an unequal bubble rise velocities at the bubble nose and wake. Also it was found that U_B by the time-difference method were almost the same when derived from the Ni or the TiN tip at each superficial gas velocity.

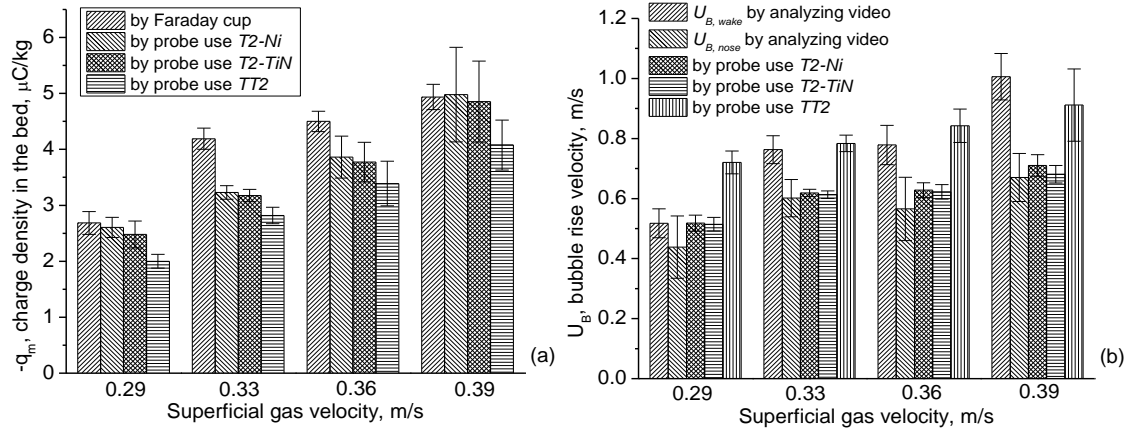


Figure 4.8 Comparison of decoupled (a) charge densities; (b) bubble rise velocities from 2t2mb probe by different decoupling methods in two-dimensional bubbling bed of 500-600 μm GB.

In general, the time-difference method could be used to analyze signals from the conventional collision probe of single electrode. A second electrode, however, is needed to select appropriate signals or bubbles before the decoupling method could be applied, based on the empirical relationship between the bubble rise velocity and bubble size. The two current peaks method is based on the difference between the signals from two tips of different materials.

4.4.2.2 Dual-tip (two-material) probe with 106-212 μm GB

The criteria with $\varphi=1$, $\lambda=0.01$ s, $\omega=2.5$ and $\delta=1$, $D_{B\min}=0.01$ m and $D_{B\max}=0.2$ m were next applied to data for this case. The upper and lower ratios of current peaks from the two materials were changed because of the variance in relative magnitudes of Ni and TiN tips for 106-212 μm GB. The charge density (q_m) and bubble rise velocity (U_B) are estimated by the previously developed decoupling methods (see Section 4.3.2).

Figure 4.9a compares the average charge densities from the probe with those measured by the Faraday cup, based on particles withdrawn through the sampling port. Comparison of Figures 4.8a and 4.9a indicated that the charge densities from the probe and Faraday cup are of the same order of magnitude and vary in a similar manner with changing U_g . In Figure 4.9b, U_B decoupled from the two current peaks method (TT2) for 106-212 μm GB failed to predict the trend of U_B with changing U_g , but the predicted U_B values from the time-difference method are closer to those obtained by video analysis. This figure also shows that U_B from the latter method are smaller than from the former, consistent with results in Figure 4.8b, because the bubble nose slowed down as the probe was approached, while the calibration equations for the two current peaks method were based on the wake velocity.

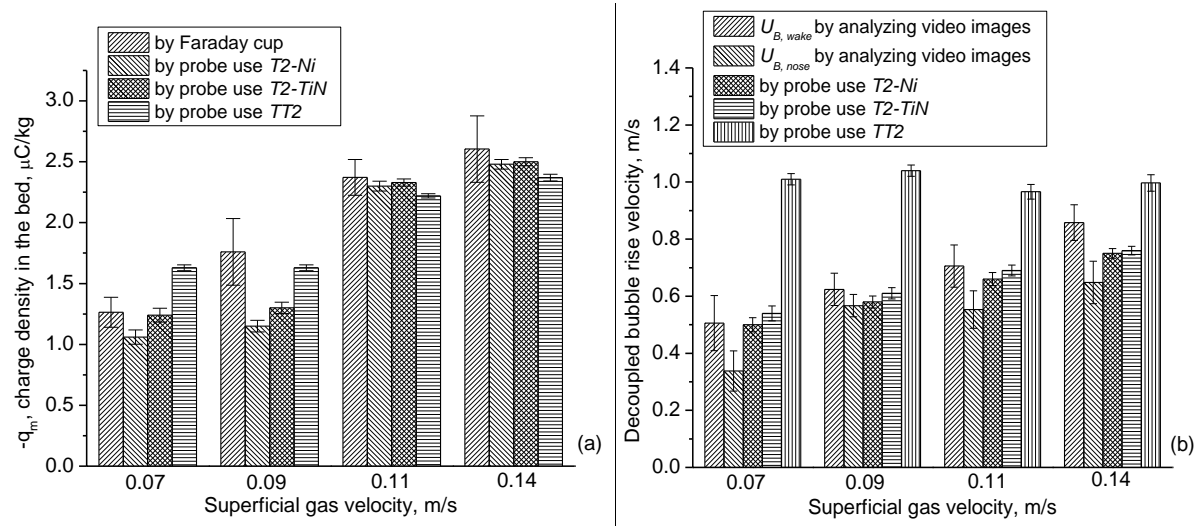


Figure 4.9 Comparison of decoupled (a) particle charge densities; (b) bubble rise velocities from 2t2mb probe by different decoupling methods in two-dimensional bubbling bed of 106-212 μm GB.

For particles with narrow size distribution but different mean size, probe signals and charge density results were compared. 500-600 μm GB generated more charge density than 106-212 μm GB (see Figures 4.8 and 4.9) and the charge signals and current peak amplitudes from the probe were larger for particles with larger mean size (see Figures 3.3 and 3.6). This is because the larger particle size generated larger momentum during particle-particle and particle-wall collisions [92].

For the 2t2m probe, the relative magnitude of signals from the two tips changes with operating conditions, e.g. particle velocity, flow rate and collision angle, as shown in Sections 2.5.1 and 2.5.3, and may also change with particle size from results presented in Section 3.3.1 and this section. Since the relative magnitudes of signals from the two materials are used to screen data in signal processing, particles of different properties (e.g. mean size and size distribution) may cause difficulty in signal processing. This suggests a 2t2m probe may be unsuitable for particles of a wide size distribution.

4.4.2.3 Dual-tip (one-material) probe with 500-600 μm GB

Probe signals were treated with criteria outlined in Section 4.2: coefficient φ was set to 0.5 for the maximum peaks and 1 for the minimum peaks, because of lower amplitudes of maximum peaks in signals from this work, minimum and maximum allowable bubble sizes ($D_{B\min}$ and $D_{B\max}$) were chosen as 0.01 m and 0.2 m, consistent with 2t2m probe. At each superficial gas velocity, about 4-15% pairs of peaks satisfied these criteria for glass beads and 5-22% for polyethylene particles. These pairs of peaks remained after applying the above criteria were then analyzed by applying the decoupling methods and probe calibration equation to extract charge density and bubble properties. In view of the random movement of bubbles in the fluidized bed, it is reasonable to see that only a small percentage of bubbles passed the local probe location vertically without splitting/coalescing.

Figure 4.10 shows the bubble rise velocity and diameter for bubbles analyzed by two tips peak-times. Although the bubble rise velocities and sizes covered broad ranges, the overall trend for individual bubbles followed Eq. (4.11), and the mean values were close to predictions from Eq. (4.11). As expected, both the mean bubble rise velocity and bubble size increased as U_g increased. The bubble pierced chord length changed during passing the probe because of obstruction by the tips. When ratios of time difference ($\Delta\tau$) for lower and upper tips were calculated for the selected bubbles at different U_g , the results were in the range of 0.88 to 1.2, with an average of 1.03 and a standard deviation of 0.07. This indicates that the bubble size (pierced chord length) was indeed influenced by the intrusive probe tips (F

configuration) and altered within a reasonable range when passing the two vertical tips based on the chosen criteria.

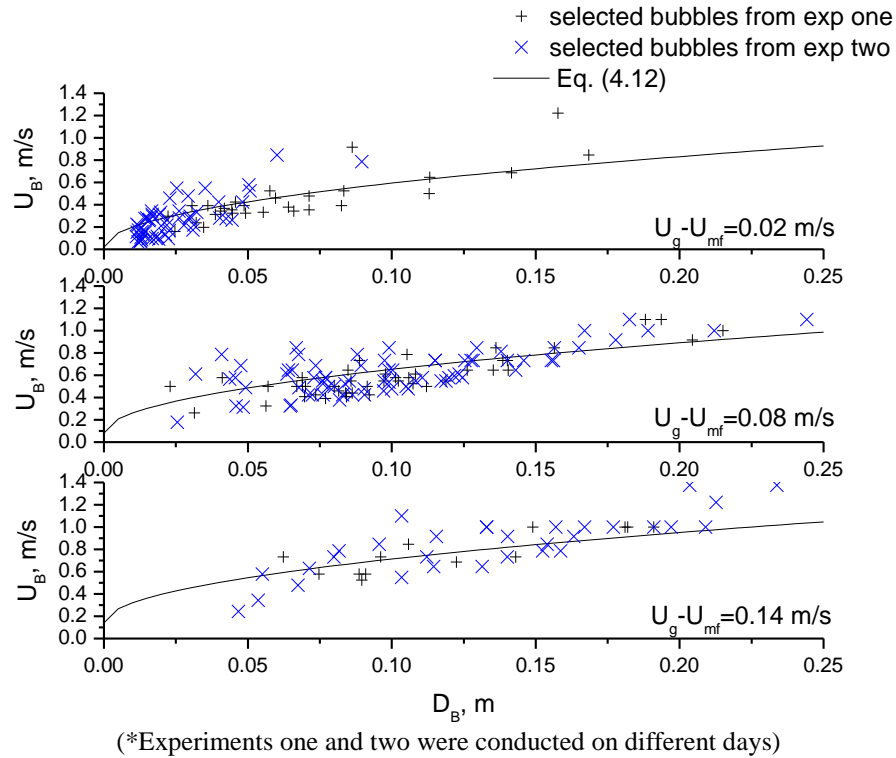


Figure 4.10 Decoupled bubble size and bubble rise velocities from 2t1mfF probe by two tips peak-times method at different U_g in freely bubbling two-dimensional fluidized bed of 500-600 μm GB.

Signal analysis results from the 2t1mfF probe (see Table 2.1) are shown in Figure 4.11, with U_B derived from all three methods compared with those derived from video images. U_B from the probe were similar in magnitude to those from the video images. All results indicate that U_B increased with increasing superficial gas velocity. The one-tip time-difference method showed less scatter because of the use of bubble rise velocity correlation (Eq. (4.11)). Also U_B by the one-tip time-difference method was similar when derived from either the upper or lower probe tip. Average relative absolute discrepancies between the results from the direct (video analysis) and indirect measurements were 13% for the two tips cross-correlation method, 12% for the two tips peak-times method and 18% for the one-tip time-difference method. The two tips cross-correlation and two tips peak-times methods likely resulted in smaller relative absolute discrepancies due to the use of directly measured U_B values.

Charge density, q_m , from the 2t1mfF probe and the Faraday cup for different U_g are compared in Figure 4.11. Results from all three methods are similar in magnitude and consistent with those measured by the Faraday cup. The average relative absolute discrepancies between the probe and Faraday cup measurement were 27% for the two tips cross-correlation method, 29% for the two tips peak-times method and 30% for the one-tip time-difference method.

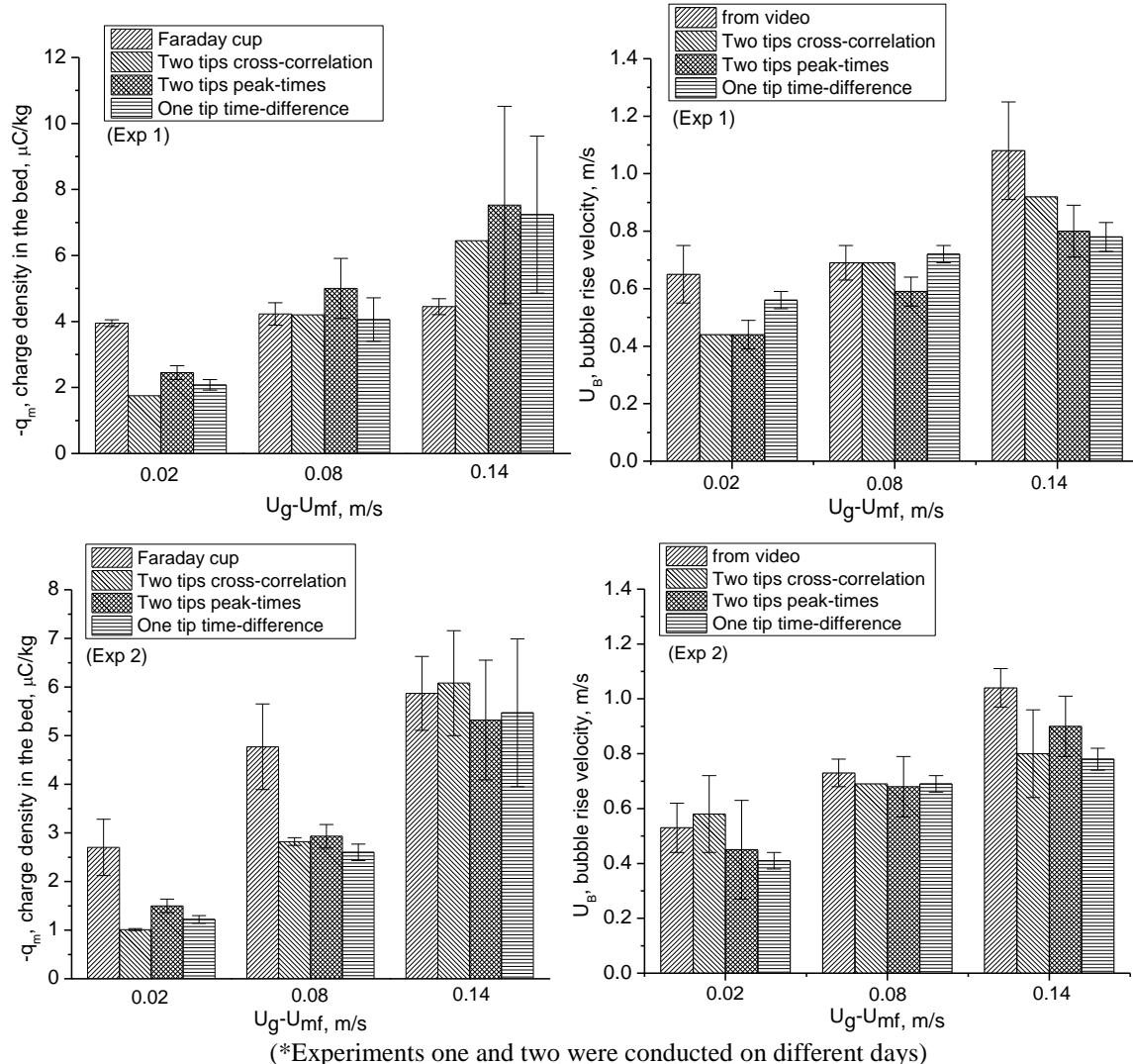


Figure 4.11 Comparison of charge densities and bubble rise velocities from 2t1mfF probe by different decoupling methods with Faraday cup and video measurements at different U_g in freely bubbling two-dimensional fluidized bed of 500-600 μm GB.

Results from the probe with different configurations (shown in Figure 2.2) are compared in Table 4.2. The Γ probe (only upper tip protruding) was intended to provide smaller errors

than the F probe (two tips protruding). Decoupled U_B from the F probe by the two tips peak-times method seems to be smaller than from the other two methods, possibly because the two tips were not well aligned. The one-tip time-difference methods produced U_B values closer to direct values from video recordings than the other two methods.

Table 4.2 Estimated charge densities and bubble rise velocities from 2t1m probe with different configurations by different decoupling methods at different U_g in freely bubbling two-dimensional fluidized bed of 500-600 μm GB.

Two tips cross-correlation method (Section 4.3.3.1)

		F: both tips protruding	Γ : only upper tip protruding
$U_g - U_{mf}$, m/s	Faraday cup	Charge densities, $-q_m$, $\mu\text{C}/\text{kg}$	
0.02	3.44 ± 0.18	1.66	1.03
0.08	4.76 ± 0.27	3.61	3.78
0.14	4.93 ± 0.74	6.36	6.79
$U_g - U_{mf}$, m/s	Video image	Bubble rise velocities, U_B , m/s	
0.02	0.55 ± 0.08	0.53	0.59
0.08	0.70 ± 0.07	0.70	0.62
0.14	1.06 ± 0.12	0.80	0.69

Two tips peak-times method (Section 4.3.3.2)

		F: both tips protruding	Γ : only upper tip protruding
$U_g - U_{mf}$, m/s	Faraday cup	Charge densities, $-q_m$, $\mu\text{C}/\text{kg}$	
0.02	3.44 ± 0.18	3.20 ± 0.63	2.40 ± 0.60
0.08	4.76 ± 0.27	6.27 ± 0.93	5.58 ± 1.08
0.14	4.93 ± 0.74	9.41 ± 2.10	6.07 ± 1.09
$U_g - U_{mf}$, m/s	Video image	Bubble rise velocities, U_B , m/s	
0.02	0.55 ± 0.08	0.45 ± 0.22	0.39 ± 0.22
0.08	0.70 ± 0.07	0.40 ± 0.08	0.25 ± 0.05
0.14	1.06 ± 0.12	0.48 ± 0.08	0.63 ± 0.09

One-tip time-difference method (Section 4.3.3.3)

		F: both tips protruding	Γ : only upper tip protruding
$U_g - U_{mf}$, m/s	Faraday cup	Charge densities, $-q_m$, $\mu\text{C}/\text{kg}$	
0.02	3.44 ± 0.18	1.85 ± 0.41	1.32 ± 0.13
0.08	4.76 ± 0.27	3.23 ± 0.38	2.24 ± 0.25
0.14	4.93 ± 0.74	5.59 ± 1.26	4.36 ± 0.48
$U_g - U_{mf}$, m/s	Video image	Bubble rise velocities, U_B , m/s	
0.02	0.55 ± 0.08	0.55 ± 0.10	0.52 ± 0.04
0.08	0.70 ± 0.07	0.72 ± 0.03	0.74 ± 0.04
0.14	1.06 ± 0.12	0.78 ± 0.03	0.75 ± 0.03

4.4.2.4 Dual-tip (one-material) probe with 710-850 μm PE

Bubble rise velocities and sizes derived from the two tips peak-times method are plotted in Figure 4.12. The overall trend of individual bubbles is consistent with Eq. (4.11), but the mean values are smaller than predicted by this equation. When ratios of the time difference ($\Delta\tau$) for the lower and upper tips were calculated for the selected bubbles at different U_g , the results were in the range of 0.85 to 1.2 with an average of 1.0 and a standard deviation of 0.07. Again the selected bubble pierced chord length varied within a reasonable range while passing the probe.

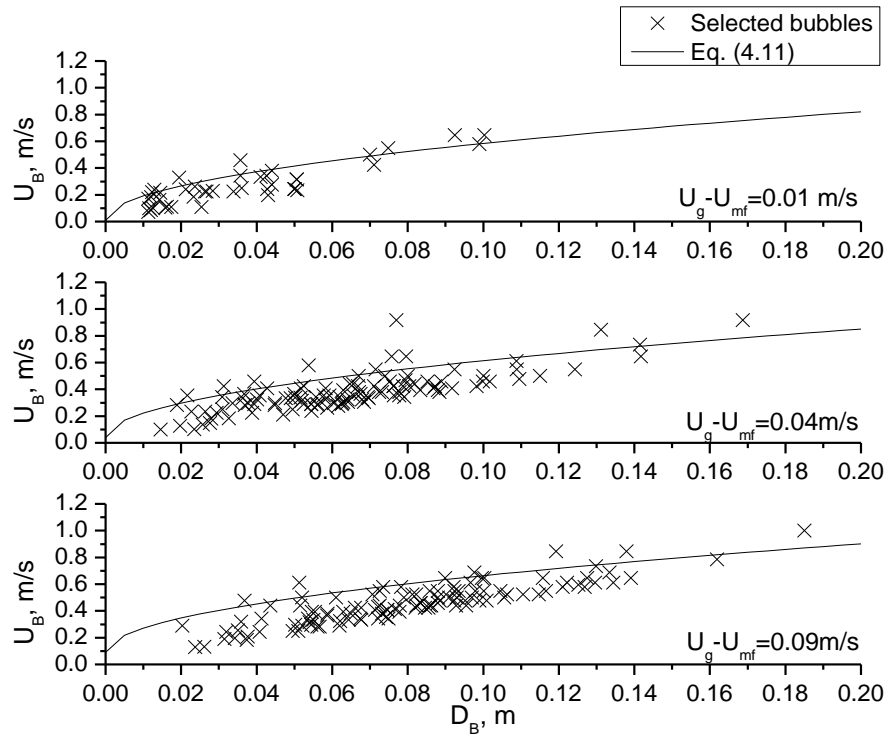


Figure 4.12 Decoupled bubble size and bubble rise velocity from 2t1mfF probe by two current peaks tips method at different U_g in freely bubbling two-dimensional fluidized bed of 710-850 μm PE.

From Figure 4.12, U_B estimated from the two tips peak-times and two tips cross-correlation methods were smaller than when derived from video recordings. U_B from the probe are similar in magnitude and changed in a consistent manner with those from the video analysis as U_g varied. The one-tip time-difference method agreed more closely with the video-measured U_B than the other two methods, with a relative absolute deviation of 15%. The relative differences between decoupled average U_B from the upper and lower tips were less

than 1.2% for different U_g , indicating that the decoupled U_B was similar when derived from either the upper or lower probe tip.

Based on Eq. (4.16), the maximum possible charge density in our experiments for polyethylene particles is expected to have been $3.3\text{--}3.9\text{E-}4 \text{ C/kg}$, for a particle relative permittivity of 2.3, particle density of 918 kg/m^3 and particle size range of $710\text{--}850 \mu\text{m}$ [11, 43]. As shown in Figure 4.13, q_m estimated from both methods was well below this maximum charge density and increased with increasing U_g , consistent with the Faraday cup data. Results from the one-tip time-difference method showed smaller error bars and were closer to the results from direct measurement, with a relative absolute error of 45%. This error was $\sim 15\%$ larger than the relative absolute error from the glass beads experiments, likely because of the empirical correlation used in calculating U_B , and error propagation when estimating q_m by Eq. (2.13).

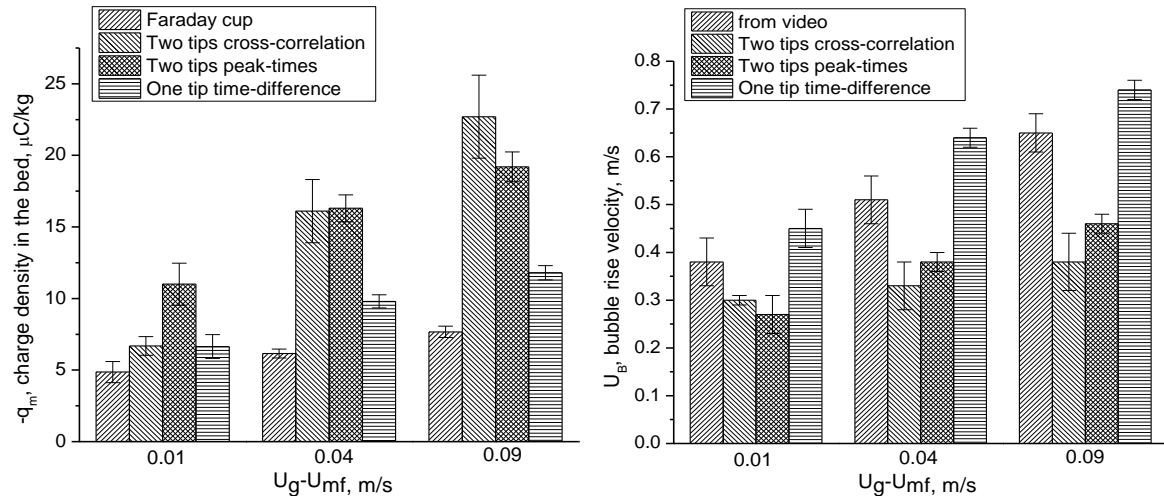


Figure 4.13 Comparison of charge densities and bubble rise velocities from 2t1mfF probe by different decoupling methods with Faraday cup and video measurements at different U_g in freely bubbling two-dimensional fluidized bed of $710\text{--}850 \mu\text{m}$ PE.

The probe with different configurations was also tested in the freely bubbling fluidized bed of polyethylene particles with the retractable tip protruding, and then retracted. Comparison of signals from cases F, Γ and L, revealed that cumulative charge signals from each tip decreased when it was retracted and was highest when it was the sole protruding tip (upper tip in Γ , lower tip in L), consistent with the glass bead results. Figure 4.14 shows decoupled

results from the probe with different configurations. At $U_g - U_{mf} = 0.09$ m/s, q_m and U_B estimated from the Γ probe have relative absolute discrepancies of 10% and 16%, respectively, which were closer to the direct measurements than for cases F and L. The one-tip time-difference method again resulted in smaller error bars than for the other two methods. The Γ probe tended to give the most accurate charge density results.

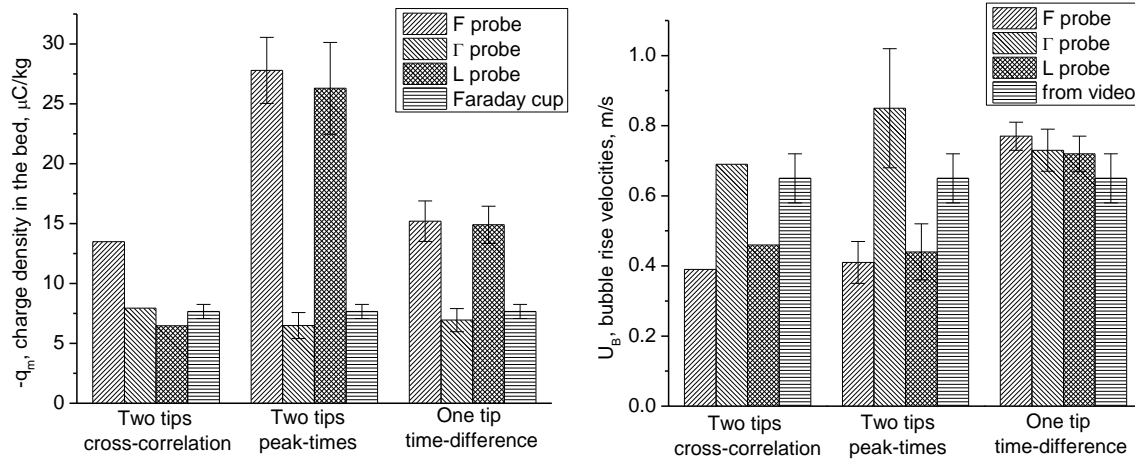


Figure 4.14 Comparison of charge densities and bubble rise velocities from 2t1m probes of different configurations by different decoupling methods, Faraday cup and video measurements in freely bubbling two-dimensional fluidized bed of 710-850 μm PE at $U_g - U_{mf} = 0.09$ m/s.

The discrepancies between results from the probes and direct measurements may arise from the calibration equation (with more experimental data needed to improve the coefficient of determination, R^2), signal processing criteria, and errors from direct measurements of q_m and U_B from the Faraday cup and video records. Most of the results have errors of 10-20% with a few falling between 20 and 30%. Considering the uncertainty and unpredictability of electrostatics, a maximum error of $\pm 30\%$ is regarded as acceptable. The Faraday cup is an open system susceptible to variations in environmental factors such as atmospheric air humidity, electromagnetic noise and additional charging/discharging during sample discharging from the fluidized bed, and this renders it an unreliable tool [14]. Although uncertainty and errors exist in Faraday cup measurement, it is the only available method to measure charge density on dielectric powders. Therefore, the results from the Faraday cup serve as a reference. The ability of the indirect collision probe signal decoupling method to estimate the particle charge density in fluidized beds is encouraging. The probe developed in

this study can thus serve as an online tool for monitoring changes in particle charge density, rather than providing accurate charge density values.

4.4.3 Results from three-dimensional fluidization column of ID 0.10 m

A 2t2ma probe (see Table 2.1) was inserted vertically from the top of the three-dimensional column. Time-series signals from the probe were examined to select pairs of minimum peaks from the two materials, corresponding to passage of vertically-traveling bubbles, for calculation purpose. The following criteria were applied for data screening ($\varphi=0.5$, $\lambda=0.03$ s, $\omega=1$ and $\delta=0.4$, see Section 4.2). Because the probe was vertically inserted in the bed and bubbles were greatly disturbed so that the criteria for bubble size ($D_{B\min}$ and $D_{B\max}$) in Eqs. (4.3) and (4.4) were not applied here. Coefficient φ (in Eqs. (4.1) and (4.2)) and maximum tolerable time difference λ (in Eq. (4.5)) were adjusted to have more than 20 data points selected at each velocity. The charge density (q_m) and bubble rise velocity (U_B) are estimated by solving Eq. (2.13) for the two materials simultaneously, using α_i , β_i and γ_i values from Eqs. (2.14) and (2.15).

Table 4.3 compares the charge densities (average values) from Eq. (2.13) with those measured by the Faraday cup, based on particles withdrawn through the sampling port. The charge densities from the Faraday cup and probe methods are of the same order of magnitude and vary in a similar manner with changing superficial gas velocity. The decoupled bubble rise velocities are within 0-1 m/s and increasing, as expected, with increasing superficial gas velocities.

Table 4.3 Average charge densities (q_m) measured by Faraday cup (FC) and decoupled from 2t2ma probe, and bubble rise velocities (U_B) decoupled from probe at different U_g in 0.10 m ID three-dimensional bubbling bed of 500-600 μm GB.

U_g , m/s	0.22	0.25	0.28	0.33	0.36	0.39	0.44
- q_m , FC	2.43	2.78	3.81	4.66	5.13	5.68	5.76
$\mu\text{C/kg}$ Probe	1.11	1.24	1.41	2.21	4.32	4.83	5.71
U_B , m/s	0.60	0.61	0.66	0.79	1.25	0.89	1.10

A 2t2mb probe (see Table 2.1) was inserted 0.10 m above the distributor in the centre of the bed. Current signals at different superficial gas velocities were treated with the same criteria for data screening ($\varphi=1$, $\lambda=0.01$ s, $D_{B\max}=0.2$ m and $D_{B\min}=0.01$ m, $\omega=1$ and $\delta=0.4$, see Section 4.2) as in Section 4.4.2. The particle charge densities (q_m) were estimated by the various analysis methods (see Section 4.3.2) and compared with those measured by Faraday cup in Figure 4.15. The charge densities from the probe are again of the same order of magnitude and vary in a consistent manner with those from the Faraday cup.

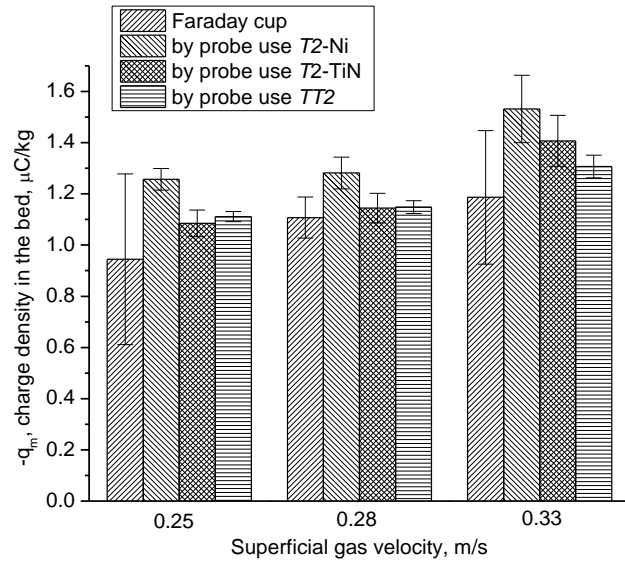


Figure 4.15 Comparison of decoupled charge densities from 2t2mb probe by different decoupling methods and Faraday cup in 0.10 m ID three-dimensional bubbling bed of 500-600 μm GB.

4.4.4 Results from three-dimensional fluidization column of ID 0.30 m

4.4.4.1 Dual-tip (two-material) probe with 420-590 μm GB

Comparison of the power spectra of raw and noise signals estimated from static (no air flow) experiments indicated that the effect of noise was negligible. Dynamic signals from the 2t2mb probe were screened using the same criteria parameters ($\varphi=1$, $\lambda=0.01$ s, $D_{B\min}=0.01$ mm, $D_{B\max}=0.2$ m, $\omega=1$ and $\delta=0.4$, see Section 4.2) as in Sections 4.4.2 and 4.4.3. Glass beads with a size range of 420-590 μm were used in these experiments.

Figure 4.16 compares q_m calculated from the probe by different methods with those measured by the Faraday cup based on particles withdrawn through the sampling port in the

three-dimensional column. These two sets of results follow a similar trend as the superficial gas velocity changes. Comparison of Figures 4.6a and 4.16a show that the charge densities in the three-dimensional column tended to be smaller than those from the two-dimensional column. This might be related to the higher moisture content and temperature of the air supplied to the three-dimensional column. The calculated U_B , as shown in Figure 4.16b, increased with increasing superficial gas velocity.

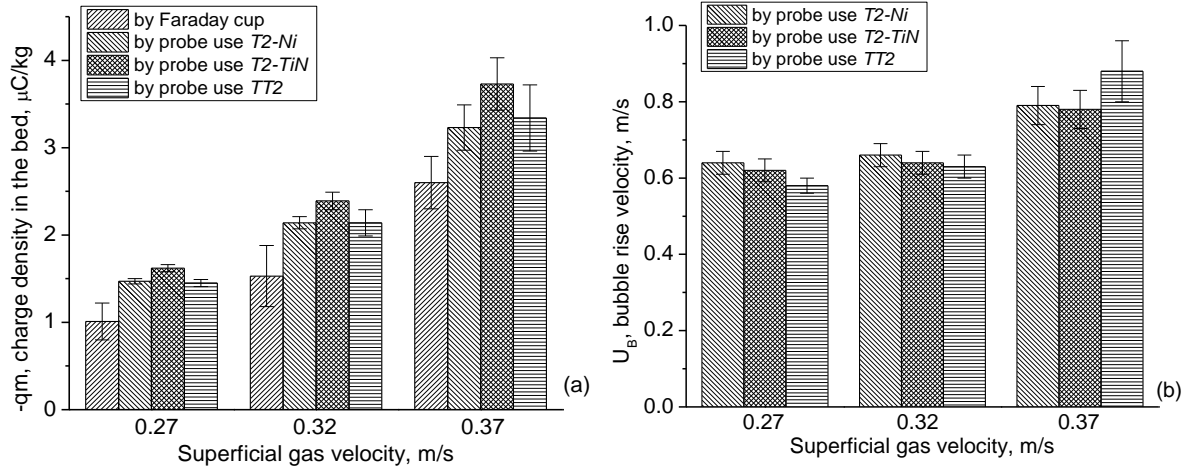


Figure 4.16 Comparison of decoupled (a) charge densities; (b) bubble rise velocities from 2t2mb probe by T2-Ni, T2-TiN and TT2 methods in 0.30 m ID three-dimensional bubbling bed of 420-590 μm GB.

4.4.4.2 Dual-tip (one-material) probe with original PE-I (100-1500 μm)

Dynamic signals from the 2t1m probes were screened using the same criteria parameters as in Section 4.4.2. Figure 4.17 compares q_m calculated from the probe by different methods (see Section 4.3.3) with those measured by the Faraday cup based on particles withdrawn through the sampling port (located 0.25 m above the distributor) in the three-dimensional column. Results from these two methods followed a similar trend as the superficial gas velocity changed. The calculated U_B , shown in Figure 4.17, increased with increasing superficial gas velocity. The effect of intrusive probe tips on the derived bubble size was also studied. Ratios of time differences ($\Delta\tau$) for the lower and upper tips calculated for the selected bubbles at different U_g fell into the range of 0.86 to 1.2, with an average of 1.0 and a standard deviation of 0.06. Again this indicates that the pierced chord lengths of selected bubbles varied within a limited range while passing the probe. The relative differences

between the decoupled average U_B from the upper and lower tips were less than 1.3% for different U_g , indicating that the decoupled U_B values were similar whenever derived from the upper or the lower probe tip.

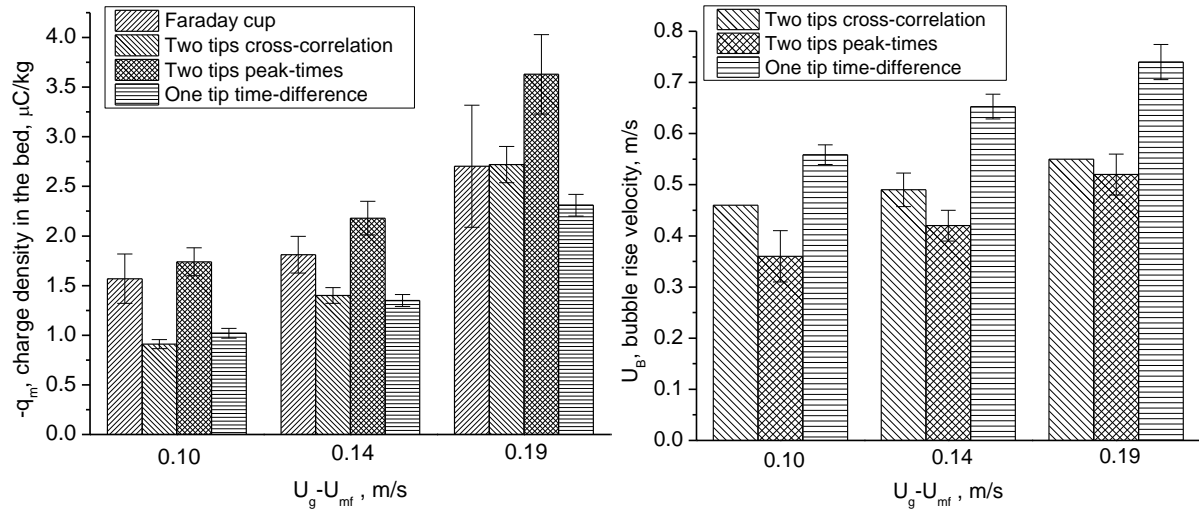


Figure 4.17 Comparison of charge densities and bubble rise velocities from 2t1mfF probe by different decoupling methods with Faraday cup measurement at different U_g in 0.30 m ID three-dimensional fluidized bed of original PE-I particles.

Several 2t1m probes with different configuration and tips (see Table 2.1) were also tested. Signals from these probes were analyzed by the one-tip time-difference method. As shown in Table 4.4, calculated U_B increased as U_g increased. q_m values were calculated by inserting U_B into different calibration equations. Charge densities from the probes and Faraday cup followed a similar trend as the superficial gas velocity changed. For the Γ probe, the horizontal distance between the protruding and retracted tips is important. If this distance is too large, signals from two tips may not be well correlated.

Table 4.4 and Figures 4.13a and 4.17a show that the charge densities in the three-dimensional column tended to be smaller than those from the two-dimensional column when fluidizing PE with wide and narrow size distributions in these two columns. Also the variations of charge density at different U_g in the three-dimensional column were smaller than that in the two-dimensional column. There are two possible reasons, one is the higher moisture content and temperature of the air supplied to the three-dimensional column and the greater wall contact area in the two-dimensional column. The other reason may be the effect of particle size distribution. Particles with a wider size distribution generated a smaller

charge density because of the possible bi-polar charging created by small and large particles [56, 134-136]. Most commonly, smaller particles tend to be charged negatively and larger particles positively [53, 137, 138], but opposite results have also been reported [43, 56]. Mono-size particles result in the same polarity of charge on particles because of less charge generation due to particle-particle contacts relative to particle-wall contacts. So that the average charge density was larger for particles with a narrow size distribution.

Table 4.4 Decoupled q_m and U_B from 2t1m probes with different configurations and tips and Faraday cup (FC) at different U_g in freely bubbling 0.30 m ID three-dimensional fluidized bed of original PE-I particles.

U_g - U_{mf} , m/s	q_m by probe, $\mu\text{C/kg}$	q_m by FC, $\mu\text{C/kg}$	U_B by probe, m/s
(a) 2t1mfF probe (see Table 2.1)			
0.10	1.02±0.05	1.57±0.25	0.56±0.02
0.14	1.35±0.06	1.81±0.19	0.65±0.02
0.19	2.31±0.11	2.70±0.61	0.74±0.03
(b) 2t1mfT probe (see Table 2.1)			
0.09	1.18±0.09	1.35±0.21	0.54±0.02
0.13	1.22±0.15	1.61±0.32	0.64±0.03
0.19	3.40±0.37	2.02±0.42	0.83±0.04
(c) 2t1mrΓ probe (see Table 2.1)			
0.06	3.67±0.08	1.24±0.24	0.49±0.03
0.11	3.68±0.13	1.55±0.17	0.65±0.03
0.19	3.70±0.22	2.07±0.38	0.83±0.05
(d) 2t1mfrΓ probe (see Table 2.1)			
0.04	1.56±0.15	1.30±0.52	0.51±0.03
0.11	2.02±0.18	1.55±0.31	0.69±0.05
0.19	3.69±0.54	1.94±0.60	0.80±0.05

Signal from the 2t1mfF probe (insertion 0.75 m above distributor, static bed height=0.88 m) was analyzed by the one-tip time-difference method (see Section 4.3.3.3). Figure 4.18 shows results from both the probe and Faraday cup as U_g increased up to 0.9 m/s. A similar trend was observed for the two measurements, with the charge density increasing with increasing U_g , then becoming more or less stable with increasing U_g . Beyond $U_g=0.6$ m/s, signal analysis could not pick up proper peaks caused by passing bubbles, because of complex flow in the turbulent fluidization flow regime in which it is hard to identify single passing bubbles: bubble coalescence is replaced by splitting and strong interaction between leading-trailing

voids. Average void velocity could still be obtained by using cross-correlation function of the signals from the lower and upper tips. However the calibration equation was obtained under the two-phase flow condition where probe signals corresponded to single bubbles passing aligned with the probes. So the calibration equation could not be applied. It is suggested that the probe should be calibrated under similar conditions as the actual operation.

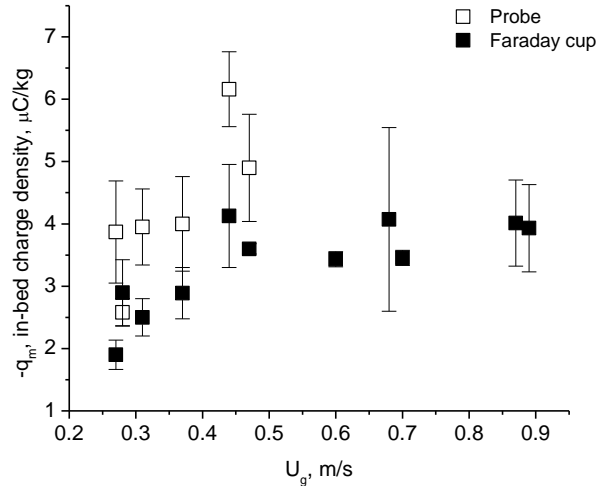


Figure 4.18 Decoupled charge densities from 2t1mfF probe and Faraday cup at different U_g in 0.30 m ID three-dimensional fluidized bed of original PE-I particles (probe: insertion 0.75 m above distributor, static bed height=0.88 m).

Current signals from 2t1mfF probes at different axial heights were analyzed and decoupled charge densities are shown in Figure 4.19. q_m near the distributor (Probe 1) and bed surface (Probe 3) are larger than that in the middle of the bed (Probe 2), possibly due to more collisions between particle-particle and particle-probe tip surface near the distributor, as well as highly charged fine particles near the bed surface during fluidization. The q_m near the distributor and in the middle of the bed increased as increasing U_g , while q_m near the top surface showed large variation, maybe due to unstable phenomena near the bed surface. Further validation of charge density distribution inside the bed by Faraday cup measurement is needed.

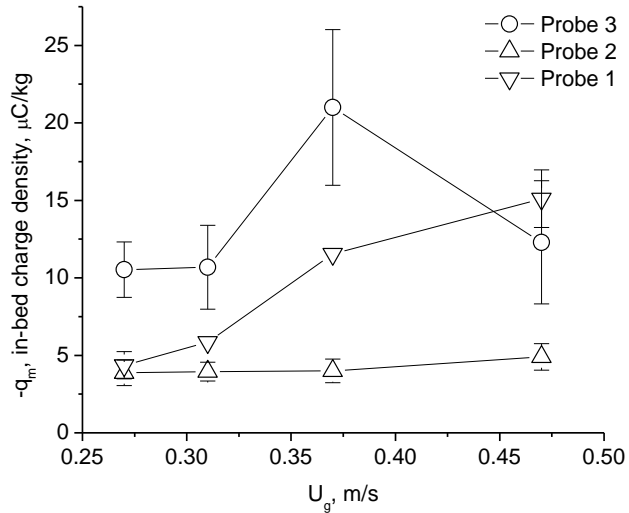


Figure 4.19 Decoupled charge densities from 2t1mfF probes at different axial locations and U_g in 0.30 m ID three-dimensional fluidized bed of original PE-I particles (probe 1: $z_1=0.25$ m, probe 2: $z_2=0.70$ m and probe 3: $z_3=1.00$ m, static bed height=0.88 m).

4.4.5 Comparison of two types of dual-tip probes

The dual-tip (two-material) probe (2t2m) and dual-tip (one-material) probe (2t1m) were compared based on probe tip, signal analysis and decoupled results. Both probes have two tips (electrodes). The dissimilarity is that the 2t2m probe tips are made of two different materials, placed side by side, whereas the 2t1m probe tips are made of the same material, with one tip above the other. Nickel and Titanium nitride were selected as probe tip materials in both cases. The Ni and TiN tips before and after experiments were characterized by X-ray Photoelectron Spectrometers (XPS) with results shown in Appendix B.2. XPS spectra for both tips before and after experiments were similar with metallic nickel and TiN identified in both cases, and that oxidation of both tips occurred within 8 nm of the surface (measurement depth of XPS), a very thin layer compared to the total thickness of 1 mm.

Both probes are able to estimate U_B and q_m aided by signal analysis and decoupling methods. The signal processing criteria are different, as well as the decoupling methods. For 2t2m probe, signal analysis is based on two equations, representing current peak values from the two different materials and depends on the properties of the tip materials and particles. From Sections 2.5.1, 3.3.1 and 4.4.2.2, the relative magnitudes of signals from these two tips may change for different operating conditions and particle properties, causing difficulty in

calibrating the probe and decoupling the signals when particle properties, e.g. mean size and size distribution, change with time. The advantage of the 2t1m probe is that they can determine U_B directly from the cross-correlation/time lag between electrostatic signals from the two probe tips.

Discrepancies between direct measurements (Faraday cup and video analysis) and two types of probes existed for the two-dimensional bubbling bed containing GB with a size range of 500-600 μm . For each type of probe, the average values from each decoupling method are compared. As shown in Figure 4.20, the average relative error of q_m from the 2t2m probe is lower than for the 2t1m probe, and the relative error of U_B from the former is larger than from the latter. For the 2t1m probe, U_B is measured directly from signals; for the 2t2m probe, on the other hand, U_B is calculated based on a calibration equation. A measurement error of the order of $\pm 30\%$ should be expected when using these probes. This suggests that the probe may be unable to provide highly-accurate values, but is able to provide trends and monitor changes with time for different operating conditions.

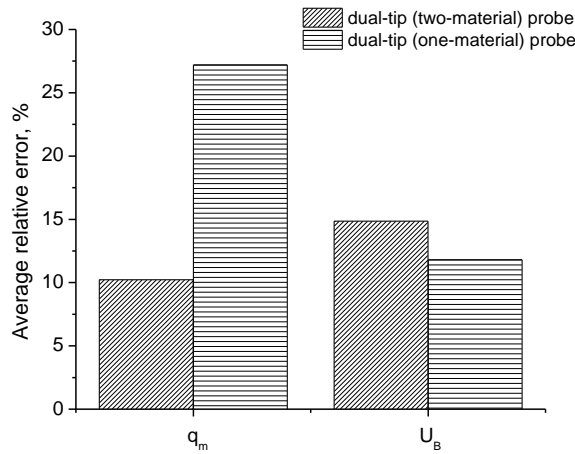


Figure 4.20 Comparison of average relative errors with results from direct measurements and probes in two-dimensional bubbling bed of 500-600 μm GB.

4.4.6 Signals from conventional single-tip probes in pressurised column with original PE-II

Experiments were also conducted in a pressurized gas-solid fluidization column of inner diameter 0.15 m and height of its straight section 2.0 m (as shown in Appendix A.6). The

column and charge measurement system were described by Moughrabiah et al. [42] and Liu et al. [94]. Several conventional single-tip electrostatic (1t1m) probes made by Moughrabiah et al. [42] were inserted at different positions in the pressurized stainless steel three-dimensional column to evaluate electrostatic charging behaviour of polyethylene particles. The major difference of this probe to our other probes is the number of tips, with the 1t1m probe having only a single tip.

The current signals from the 1t1m probe were analyzed by the time-difference method (Section 4.3). Although these signals were only screened by applying peak detection criteria (Eqs. (4.1-4.4)), the decoupled results could still be used to evaluate trends. The effects of superficial gas velocity and pressure are shown in Table 4.5. When the bed pressure was maintained constant, the mean U_B decoupled from the probe (probe B, located in the dense phase, as shown in Figure B.19) was within 0-1 m/s and increased as expected with increasing U_g . For constant U_g , the mean U_B decoupled from the probe first increased then decreased as the absolute pressure increased. The initial increase in U_B maybe because bubble flow is increasingly concentrated toward the centre of the column than at atmospheric pressure [139]. The subsequent decrease in U_B may be due to smaller bubbles leading to smoother fluidization [140].

Table 4.5 Mean bubble rise velocity (U_B) decoupled from the 1t1m probe in pressurized stainless steel three-dimensional column with original PE-II particles at different operating conditions.

	absolute pressure in freeboard, 138 kPa (Constant)		
superficial gas velocity (U_g), m/s	$U_{mf}+0.05$	$U_{mf}+0.10$	$U_{mf}+0.15$
mean U_B , m/s	0.406	0.486	0.608
$U_g=U_{mf}+0.10$ (Constant)			
absolute pressure in freeboard, kPa	138	276	414
mean U_B , m/s	0.486	0.527	0.504

The current signals from probes located at different heights were also analyzed by the time-difference method. As shown in Figure B.19, probe A was located in the lower part of the bed near the distributor, probe B in the middle part of the bed dense phase and probe C in the upper part of the bed. All three probes were inserted radially to just reach the axis of the column. As shown in Figure 4.21, the mean U_B decoupled from each probe increased slightly

with height, indicating increasing U_B along the column as the bubbles coalesced and grew. The one electrode probe could be used to calculate q_m and U_B , but the results were widely spread. More results on the effects of sampling parameters and signal conditioning, as well as statistical and time-frequency analysis of electrostatic signals from the conventional single-tip probes in the pressurized column can be found in Appendix B.10.

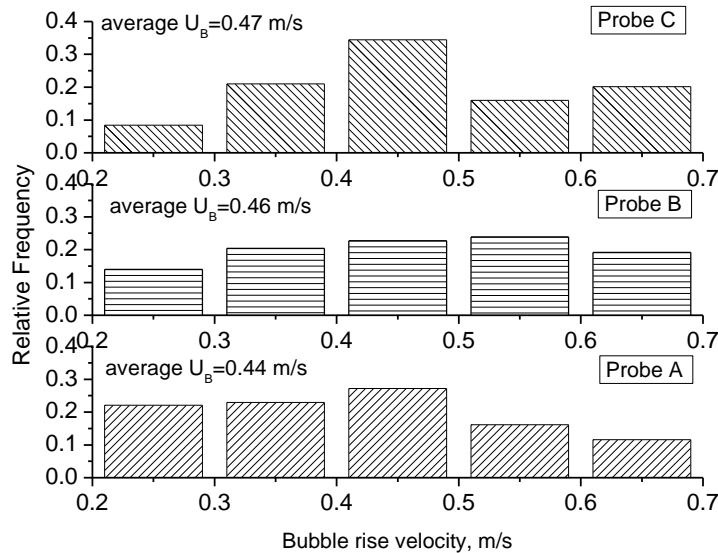


Figure 4.21 Comparison of relative frequency distributions of decoupled bubble rise velocities from 1t1m probes located at different heights in pressurized column of original PE-II particles ($U_g = U_{mf} + 0.10$, absolute pressure in freeboard: 276 kPa).

4.4.7 Differences between polyethylene and glass beads

Although generation of electrostatic charges depends on several factors, such as relative humidity and temperature of the fluidizing gas, results from the glass beads (GB) and polyethylene particles (PE) can be compared when obtained under similar operating conditions of excess superficial gas velocity, temperature and relative humidity. Based on Figures 3.8 and 3.10, current peak amplitudes registered by the probe were larger for the glass beads than for the polyethylene particles. This may be caused by the difference in particle density (GB 2500 kg/m³ vs. PE 918 kg/m³) and electrical conductivity. Glass beads, which are denser and thus have a higher momentum at the same particle velocity, as well as having a higher electrical conductivity, tend to transfer more charges when they collide with

the probe. The current signals for PE particles also show many sub-peaks around the major ones, as shown in Figure 3.10 and previous experimental results [43].

On the other hand, based on Faraday cup measurements, q_m for PE was higher than for GB at the same excess gas velocity, $U_g - U_{mf} = 0.09$ m/s (see Figure 4.11 and 4.13). This indicates that higher charge density was generated on the PE particles than on the GB in the fluidized bed. This is also supported by the strong electrostatic effects observed in gas-phase polymerization reactors. The higher charge density on PE particles is related to the difference in dielectric constant and hydrophobicity of the two types of particles. PE has a lower dielectric constant (2.3 F/m) [141] than GB (5-10 F/m) [142]. The PE used in this work is regarded as hydrophobic [143, 144], and hence not as susceptible to formation of a water film on the particle surface as hydrophilic materials, such as GB [145]. So charge dissipation from the PE particles was less than from the GB, affecting the net accumulation of charges. The results also indicate that the relative amplitudes of current or cumulative charge signals received from electrostatic probes are not always consistent with the relative amplitude of particle charge density for different particles or for operation at different conditions. Therefore, it is imperative to extract particle charge densities from signals received by electrostatic probes via the signal decoupling methods developed and demonstrated in this study.

4.5 Summary

Local particle charge density and bubble behaviour were estimated by collision probes of dual-tips based on the dynamic charge/current signals and calibrated equations. A signal processing procedure combined with a bubble selection algorithm is used to pre-treat raw signals from proposed probes. Decoupling based on a charge transfer and induction model extracted bubble properties and particle charge densities. Signals from the probes were processed from both two- and three-dimensional freely bubbling fluidization columns of different scale containing glass beads and polyethylene particles. Steady state experiments showed that both particle charge density and bubble rise velocity obtained from the probes were of the same order of magnitude and followed a similar trend with those directly

measured from Faraday cup and video images, respectively, as the superficial gas velocity changed.

For dual-tip (two-material) probe, time-difference method and two current peaks method were selected because of promising results in extracting q_m , compared with values directly measured by a Faraday cup. Decoupled U_B by time-difference method were closer to bubble nose velocity from video analysis and deviated less than ones calculated by a two current peaks method, which were closer to bubble wake velocity. Relative magnitudes of signals from the two materials may change for different operating conditions and particle properties, causing difficulty in calibrating the probe and in decoupling the signals. As a result, the 2t2m probe may be unsuitable for different particles, e.g. those of wide size distribution.

For dual-tip (one-material) probes, bubble rise velocity and bubble size for bubbles analyzed by two tips peak-times followed Eq. (4.11). Both the mean bubble rise velocity and bubble size increased as U_g increased. Results from one-tip time-difference method showed less scatter because of the use of bubble rise velocity correlation (Eq. (4.11)) and were closer to the results from direct measurement. Based on results from both two- and three-dimensional fluidized beds, the Γ probe with only the upper tip protruding and the F probe with two tips protruding provided closer agreement with the charge density results from Faraday cup measurements. The intrusiveness of the probe tips (F configuration) was investigated, and results show that bubble size varied within a reasonable range when passing the two vertical tips.

Differences in the signals and charge densities from glass beads and polyethylene particles are due to differences in particle properties such as density, dielectric constant, sphericity, roughness and hydrophobicity. Particles with the narrow size distribution and larger mean size generated a higher charge density. Charge signals and current peak amplitudes from the probe were larger for particles with a larger mean size. Analyzing signals from conventional single-tip probes showed widely scattered results.

Chapter 5 In-situ Monitoring in Gas-Solid Fluidized Beds

5.1 Introduction

Electrostatic charge generation from particle-particle and particle-wall contacts in gas-solid fluidized beds is virtually inevitable for most systems. Charged particles are known to cause problems including particle agglomeration and reactor wall fouling. Several methods have been reported for mitigating bed electrification and reactor fouling, such as: humidification, antistatic agents, or increasing the superficial gas velocity to clean the distributor plate [6, 8, 146, 147]. However, a reliable charge measurement tool capable of monitoring the charges is still missing. Commonly-used electrostatic probes cannot detect changes of in-bed particle charge density because cumulative charge signals from probes are affected by changes in both electrostatics and hydrodynamics. Also there are currently no techniques to measure charging of bulk powders and no standardized methods to measure electrostatics of pharmaceutical powders [14].

A suitable charge density measurement tool could identify potential risks earlier and prevent hazards due to electrostatic discharges. It could also monitor the effectiveness of different strategies intended to reduce the charge density to provide safer operation for handling dielectric powders. Ideally signal analysis should be neither time-consuming nor complicated, while being suitable for on-line analysis of large units.

In previous chapters, the novel probes investigated gave reasonable results in steady state experiments in response to charge density and hydrodynamics changes. However, it is necessary to test the probes' responses to continuous changes in the bed for the purpose of online monitoring.

In this chapter, the charge density level and hydrodynamics inside a two-dimensional fluidized column and a 0.30 m ID three-dimensional fluidization column were modified by abruptly changing the superficial gas velocity and by adding an antistatic agent while the

probes continuously monitored electrostatic charges. Signals from the probes are analyzed, and results are compared with those from a Faraday cup and video image analysis.

5.2 Experimental equipment and methods

As shown in Figure 2.8, the two-dimensional fluidization column has an inside width of 0.307 m, a thickness of 22 mm and a height of 1.24 m. The Plexiglas three-dimensional fluidization column is shown in Figure 3.2, with an inner diameter of 0.30 m and a height of 4.5 m. Details of the experimental facilities are provided in Sections 2.4 and 3.2. Glass beads with a narrow size range of 500–600 μm and polyethylene particles with a wide size range (100–1500 μm) were used as the bed materials. Because the 2t2m probe may be unsuitable for particles of wide size distribution (see Sections 2.5.1, 3.3.1 and 4.4.2.2), 2t1m probes with different configurations (see Table 2.1) were used in the tests covered in this chapter.

The static bed height was maintained at 0.50 m and the probe was located 0.42 m above the distributor in the two-dimensional fluidization column. In the three-dimensional column, the static bed height was maintained at 0.40 m and the probe was 0.25 m above the distributor. Both beds were operated in the free bubbling mode at a constant superficial gas velocity for at least an hour to reach steady state. Then measurements were started to continuously monitor the charge density and hydrodynamics for about an hour. Then superficial gas velocity was abruptly changed or antistatic agent was quickly added into the bed, with monitoring continuing for a further hour.

Time-series signals from the probes were analyzed by the procedure illustrated in Section 4.2. After selecting appropriate pairs of peaks, different methods (explained in Section 4.3) were applied to decouple the signals. For the 2t1m probe configured with two tips protruding (F configuration), current peaks from the lower tip were used to calculate q_m because of less interference than the upper tip. The results presented in this chapter are time-averaged values, with error bars corresponding to 90% confidence intervals.

5.3 Results and discussion

5.3.1 Effect of sampling parameters

For monitoring purpose, the probe response time needs to be faster than the time over which major changes occur in hydrodynamics and charge density. Simple tests, as described in Appendix B.3, suggested that the probe response time was of order 1 millisecond or less. In data processing of online monitoring, appropriate choices of the sampling time interval and measurement frequency are important. High sampling frequency (f_s) and long time interval (t_s) increase data volume, whereas low sampling frequency or short duration causes loss of information. Therefore, the effects of sampling parameters on decoupling results were first investigated. Raw signals from the 2t1mfF probe with a sampling frequency, f_s of 1000 Hz were first de-sampled into 500 Hz, 200 Hz and 100 Hz, for the same duration of 10 min, and then processed and analyzed by the criteria and methods outlined in Sections 4.2 and 4.3.

As shown in Figure 5.1, as f_s increased, the decoupled particle charge densities (q_m) from the probe by both two tips peak-times and one-tip time-difference methods increased and were closer to the Faraday cup results. However, the q_m results when $f_s=1000$ Hz were not stable and did not show as clear a change when U_g-U_{mf} changed abruptly from 0.02 to 0.11 m/s. Probe signals show that peak amplitude and corresponding time vary with sampling frequency, so that selected pairs of peaks were different, leading to different decoupled results at different sampling frequencies. Sampling at higher frequencies can pick up higher frequency signals of little or no interest which may cause unstable and inaccurate results. On the other hand, if f_s is too low, the probe cannot detect bubble rise velocity (U_B) within certain a distance interval. A sampling frequency of 200-500 Hz is recommended for the 2t1m probe.

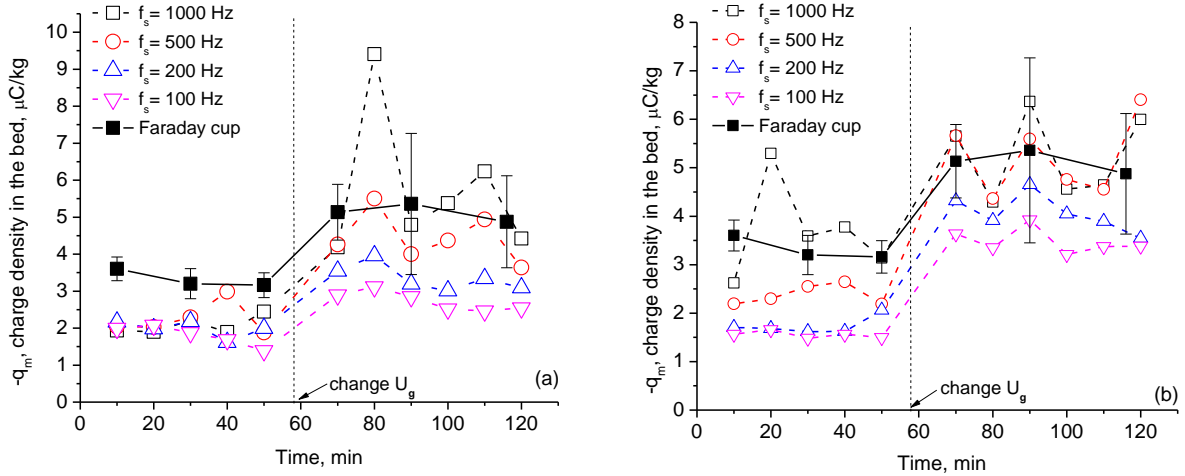


Figure 5.1 Effect of sampling frequency on estimated charge density from 2t1mfF probe by (a) two tips peak-times method and (b) one-tip time-difference method when $U_g - U_{mf}$ changed abruptly from 0.02 to 0.11 m/s.

The influence of sampling time interval for monitoring the electrostatics response of the fluidized bed subject to a stepwise change is shown in Figure 5.2. Continuous time-series signals from the probe with a constant sampling frequency of 200 Hz were divided into reduced periods with different time intervals (20, 10, 5 and 2.5 min). As t_s , the sampling time interval, decreased from 20 min to 2.5 min, q_m from the probe decoupled by different methods responded more quickly to changes in U_g . However, the error from each method also increased as the number of selected peaks decreased. The sampling time for steady state (characteristic time of the system) has been investigated in Section B.10.1 and results showed that a sampling interval at least 2 min was required. In this case, for a purpose of monitoring the change in charge density inside the bed subject to a stepwise change in U_g , a shorter sampling time interval will be preferred to capture the dynamic change. However, considering increased errors associated with decreased sampling time interval, a sampling interval of 5-10 min was chosen for the monitoring purpose in this case study.

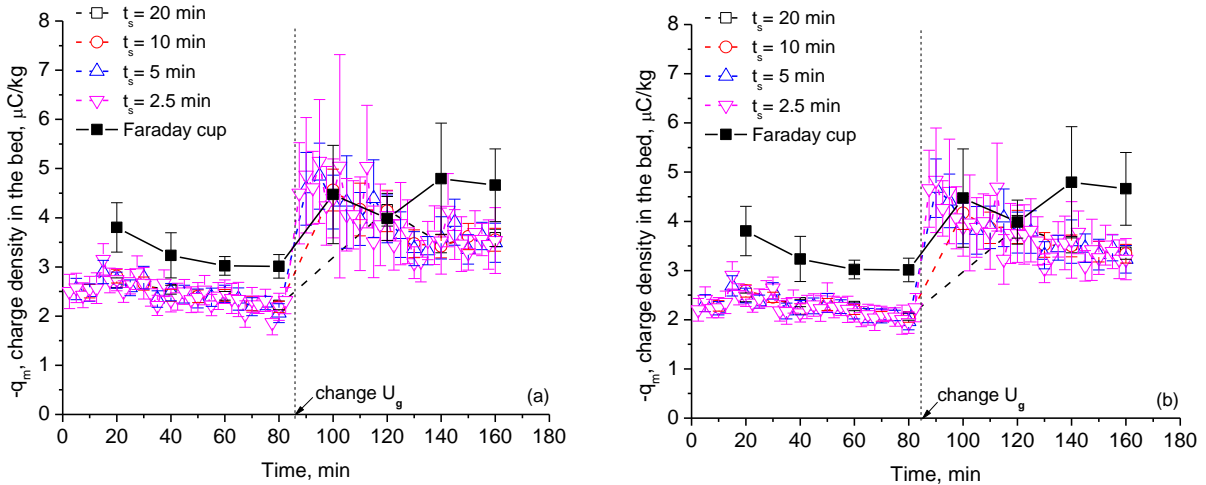


Figure 5.2 Effect of sampling time interval on estimated charge density from 2t1mfF probe by: (a) two tips peak-times method; and (b) one-tip time-difference method when U_g-U_{mf} abruptly changed from 0.02 to 0.11 m/s.

5.3.2 Changing U_g in two-dimensional bed of 500-600 μm GB

Dual-tip (one-material) probe

Electrostatic charges inside the bed have been found to be affected by fluidized bed hydrodynamics because of changes in bubble behaviour and contacts among particles and between particle and the reactor wall. Effects of changing several factors (e.g. pressure, superficial gas velocity, bubble size, initial bed height and distributor) on bed electrification have been investigated in previous work [16, 26, 27, 41, 42, 94]. However, continuous changes of particle charge density and hydrodynamics have not been properly monitored and evaluated.

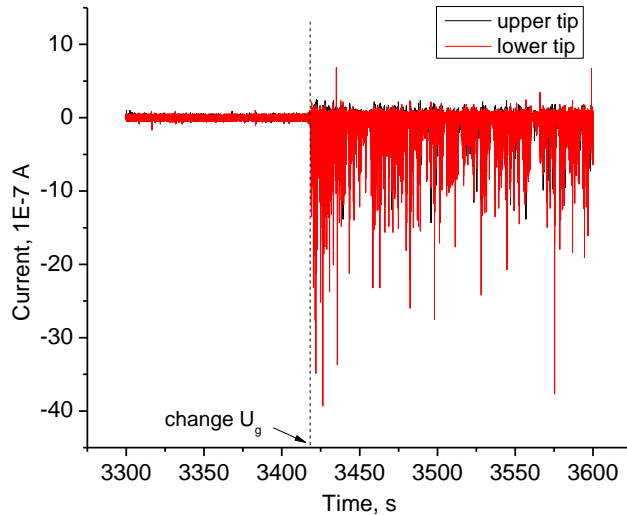


Figure 5.3 Current signals from 2t1mfF probe in freely bubbling two-dimensional fluidized bed of 500-600 μm GB when $U_g - U_{\text{mf}}$ abruptly changed from 0.02 to 0.11 m/s. (Fluidizing gas air: $T=23\pm2^\circ\text{C}$, $\text{RH}=2\pm2\%$.)

The current signals are plotted versus time in Figure 5.3. The current signals responded quickly and substantially to the change of U_g . Current signals from both tips increased in magnitude when U_g changed, with peak amplitudes from the lower tip again larger than from the upper tip. As shown in Figure 5.4, the predicted charge density and bubble rise velocity from the probe were of similar orders of magnitude with those obtained from Faraday cup measurement and analysis of video frames, respectively, and able to respond appropriately when the superficial gas velocity changed.

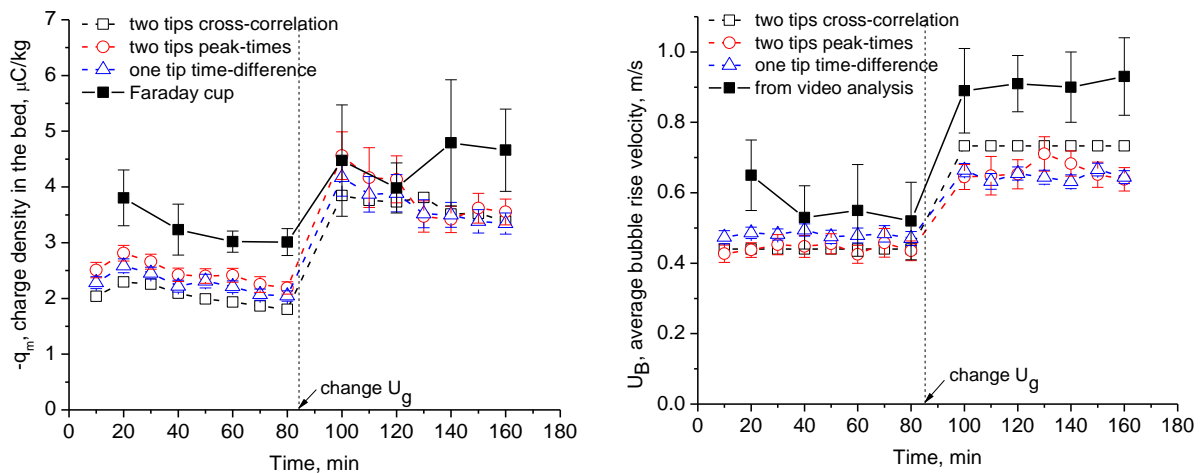


Figure 5.4 Comparison of charge densities and bubble rise velocities from 2t1mfF probe by different decoupling methods with Faraday cup and video measurements in freely bubbling two-dimensional fluidized bed of 500-600 μm GB when $U_g - U_{\text{mf}}$ changed from 0.02 to 0.11 m/s. ($f_s = 200$ Hz, $t_s = 10$ min, Fluidizing gas air: $T=23\pm2^\circ\text{C}$, $\text{RH}=2\pm2\%$)

Dual-tip (two-material) probe

A 2t2mb probe (see Table 2.1) was used to monitor the changes when the superficial gas velocity was raised abruptly from $U_g - U_{mf} = 0.01$ to 0.07 m/s. Results are shown in Figure 5.5. The resulting decoupled q_m and U_B changed consistently with results from direct measurements as U_g changed. q_m from two current peaks method (Section 4.3.2.2) were closer to the Faraday cup measurement results after U_g was abruptly changed. Also q_m data from Faraday cup measurements were smaller in magnitudes and varied less after abruptly increasing U_g , compared to Figure 5.4. This may be due to higher relative humidity and less of a step change in $U_g - U_{mf}$ (0.06 m/s rather than 0.09 m/s) in Figure 5.5 than in Figure 5.4, and the charge density level inside the bed may be unstable because of not enough fluidization time (U_g was changed just at 60 min, and might need a longer time).

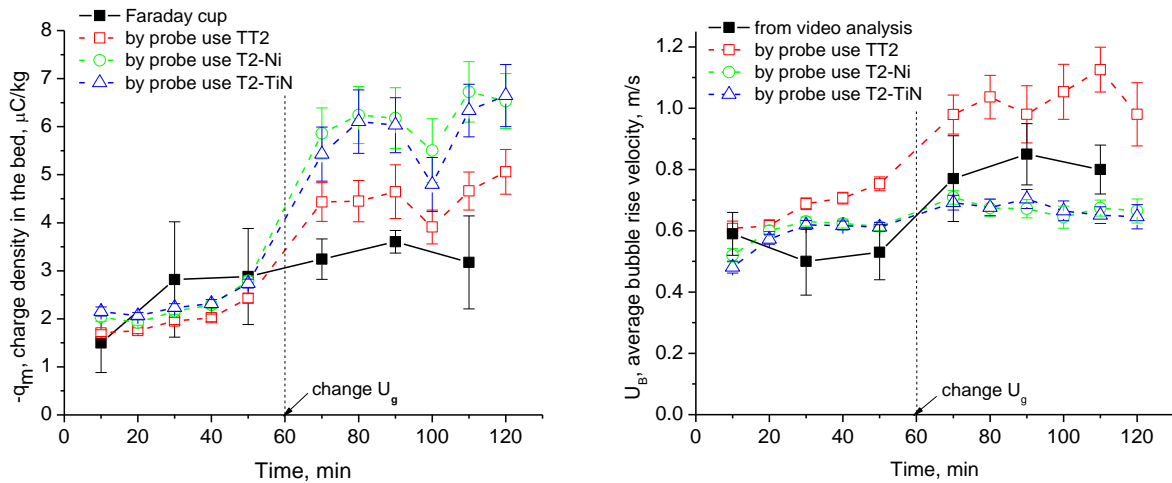


Figure 5.5 Comparison of charge densities and bubble rise velocities from 2t2mb probe by different decoupling methods with Faraday cup and video measurements in freely bubbling two-dimensional fluidized bed of $500\text{-}600\text{ }\mu\text{m}$ GB when $U_g - U_{mf}$ abruptly changed from 0.01 to 0.07 m/s. ($f_s = 200$ Hz, $t_s = 10$ min, Fluidizing gas air: $T=23\pm 2^\circ\text{C}$, $\text{RH}=5\pm 2\%$)

More experiments were conducted by using a 2t2ma probe in the 0.10 m ID three-dimensional fluidization column (see Figure 3.1) with glass beads. Two sets of experiments were conducted. In the first experiment, the bed was operated at different U_g for extended time intervals (1 h, 3 min or 20-30 s). Then U_g was abruptly changed with probe measurements taken over certain sampling intervals (3 min or 20-30 s). The results indicated

that the probe has a short response time (~ 1 ms) and is sensitive to changes in both hydrodynamics and charge density in the bed. In the second experiment, U_g was changed stepwise to several different values with about one hour between each shift. Results suggested that after changing U_g abruptly each time, mean currents from both Ni and TiN tips and in-bed charge density first increased, and then became stable as time increased. Both the mean currents and absolute difference between the mean currents from the two tips increased with increasing U_g . Details are shown in Appendix B.4.

5.3.3 Adding antistatic agent to two-dimensional bed of 500-600 μm GB

Since changing U_g changes both the charge density and hydrodynamics inside the bed, it is necessary to test the probe's ability to respond to charge density change alone. Wolny and Opalinski [47] concluded that the addition of fines neutralizes electric charges in the bed, independent of the electrical properties of the fines. The fines were said to change the contact conditions and transfer charges between particles in the bed, resulting in neutralization of the whole bed. Yao et al. [16] found that both the mean and standard deviation of mean current signals from a ball probe fell to insignificant levels after adding 0.1 wt% Larostat 519 powder to a freely bubbling bed of polyethylene resin particles. Larostat 519 (provided by BASF Chemical Company) is an antistatic agent which reduces static charge build-up during particle handling and processing. Its major component is quaternary ammonium salts, a non-polymeric cationic compound which is considered to be a hydrophilic additive [148]. It has a density of 520 kg/m^3 and a size range of $6\text{-}20 \mu\text{m}$. The Larostat particles are non-spherical, with uneven surfaces. Previous work [16, 41] has focused on examining the effect of fines addition on recorded current and charge buildup in the bed, but it is also necessary to quantify the time-variation of particle charge density and hydrodynamics following sudden addition of fines to the bed.

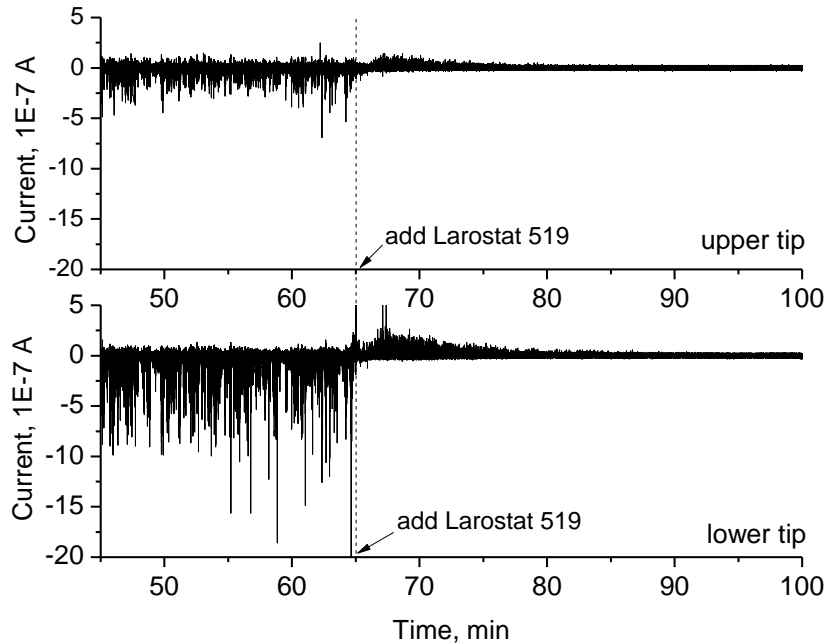


Figure 5.6 Current signals from 2t1mfF probe in freely bubbling two-dimensional fluidized bed of 500-600 μm GB at $U_g-U_{mf}=0.05$ m/s after 0.1 wt% Larostat 519 was added. (Fluidizing gas air: $T=22\pm1^\circ\text{C}$, RH=2±1%).

The bed was operated in the bubbling flow regime at $U_g-U_{mf}=0.05$ m/s overnight to reach steady state. Then 0.1 wt% Larostat 519 was added by pouring quickly from the top of the column. Figure 5.6 shows the current signals from the probe before and after adding the antistatic agent. Signals from both probe tips decreased by one order of magnitude as a result of adding the anti-static fines. Signals from after the adding were close to the baseline, reaching the minimum limit which the electrometer could measure. The current signal significantly decreased with polarity changed from negative to positive. From visual observation, wall fouling was significantly reduced and disappeared within a minute of adding the antistatic agent. As shown in Figure 5.7, q_m from the Faraday cup showed a significant drop when Larostat 519 was added. The addition of the antistatic agent increases the surface conductivity by increasing the water adsorption at low relative humidity. Probe signals before 70 min showed detectable amplitudes and therefore were chosen to analyze. Before the adding, decoupled charge densities were in same order of magnitude and close to Faraday cup results; after the adding, charge density predicted by the probe decreased consistently with Faraday cup measurement. Decoupled bubble rise velocities from the probe

were more or less the same (~ 0.6 m/s) before and after the addition over the limited period of time analysed.

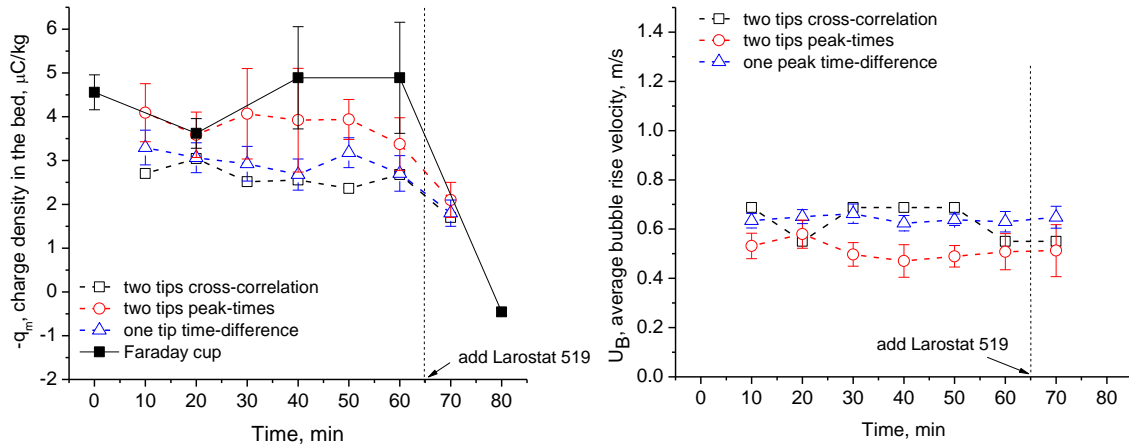


Figure 5.7 Comparison of charge densities from 2t1mfF probe by different methods with Faraday cup, and decoupled bubble rise velocities in freely bubbling two-dimensional fluidized bed of 500-600 μm GB at $U_g-U_{mf}=0.05$ m/s after 0.1 wt% Larostat 519 was added. (Fluidizing gas air: $T=22\pm 1^\circ\text{C}$, RH=2±1%).

5.3.4 Changing U_g in two-dimensional bed of 100-1500 μm PE

The ability of the probes to provide *in-situ* monitoring of charge density and hydrodynamics changes in the two-dimensional bed of original polyethylene particles was also tested. A sampling frequency of 500 Hz and sampling time interval of 10 min were selected for monitoring of the 2t1m probe (based on results in Section 5.3.1). The bed was first fluidized at $U_g-U_{mf}=0.04$ m/s for more than one hour to reach steady state before impulsively increasing to $U_g-U_{mf}=0.18$ m/s. The bed was then maintained at $U_g-U_{mf}=0.18$ m/s for one hour, before suddenly reduced to $U_g-U_{mf}=0.04$ m/s and fluidized for a further hour. Cumulative charge and current signals when U_g was changed are plotted versus time in Figure 5.8. Both the charge and current signals responded quickly and substantially to each step change in U_g . The cumulative charge signals from both probe tips became more negative at higher U_g . The slope from the upper tip (protruding) was larger than from the lower (retracted) tip because of greater transferred charge from direct contact with negatively charged particles. Correspondingly, the amplitudes of the current signals from both tips increased when U_g was increased and decreased when U_g decreased. Peak amplitudes from the upper tip were larger than from the lower tip, consistent with the charge signals.

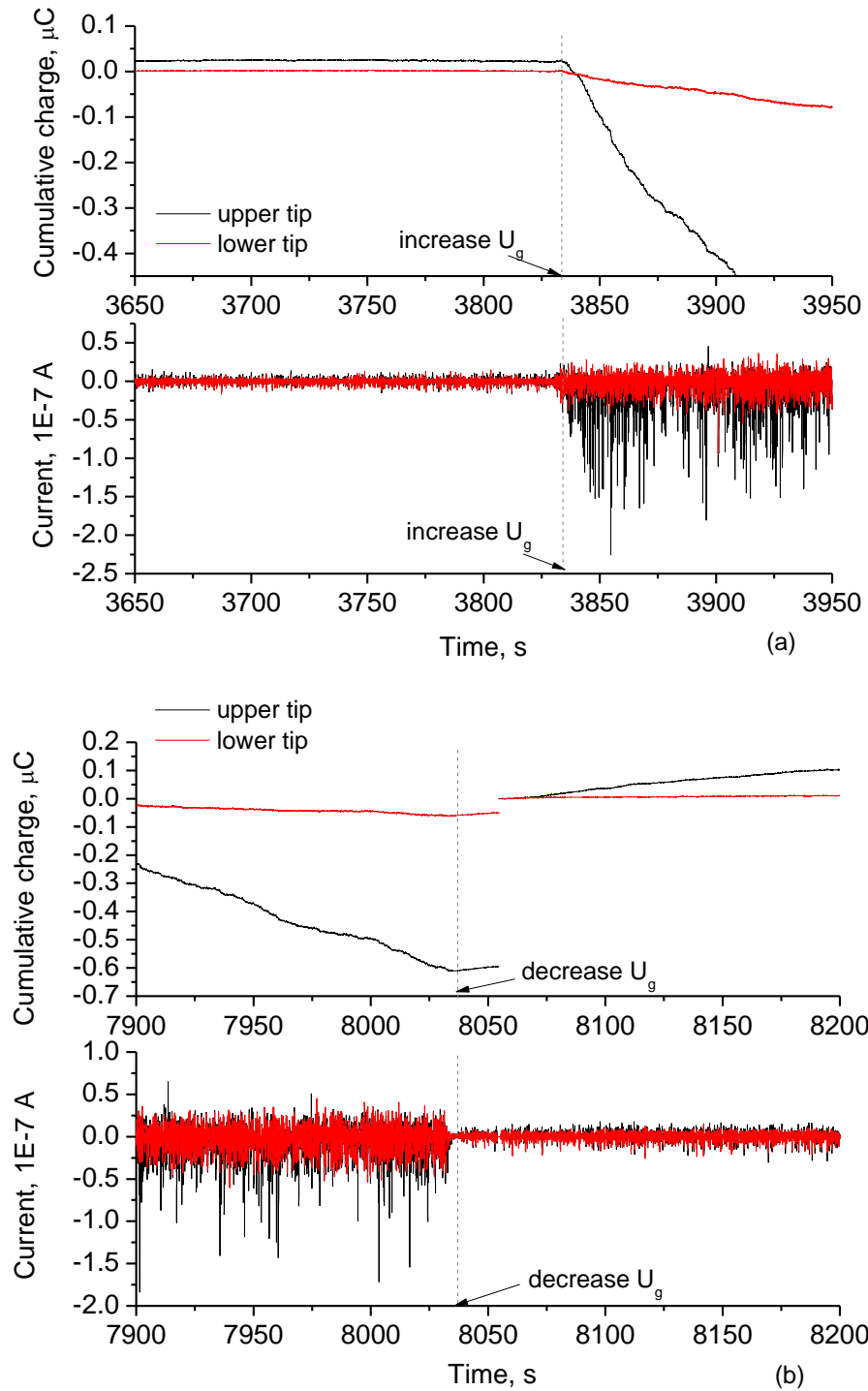


Figure 5.8 Cumulative charge and current signals from 2t1mfT probe in freely bubbling two-dimensional fluidized bed of original PE-I particles when $U_g - U_{mf}$ changed abruptly from (a) 0.04 to 0.18 m/s; (b) 0.18 to 0.04 m/s. (Fluidizing gas air: $T=24\pm1^\circ\text{C}$, $\text{RH}=6\pm1\%$)

The signals from the probe were treated according to the proposed selection criteria and decoupled by the one-tip time-difference method. As shown in Figure 5.9, the predicted

charge density and bubble rise velocity from the probe were of similar order of magnitude with those obtained from Faraday cup measurement and analysis of video frames, respectively. The probe was also able to capture the trends in particle charge density and bubble rise velocity when U_g was abruptly changed. At $U_g - U_{mf} = 0.18$ m/s, the errors from the probe results were larger than for $U_g - U_{mf} = 0.04$ m/s because of a smaller number of selected peaks. At higher U_g , the bubble flow was more vigorous, with more coalescence and splitting. As a result, fewer bubbles passed the probe vertically without splitting or coalescing.

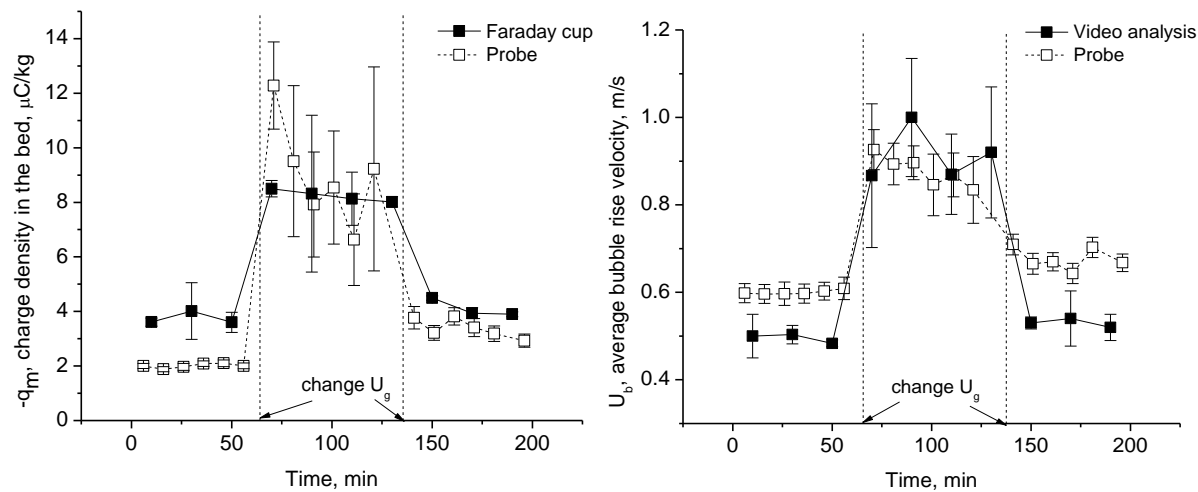


Figure 5.9 Comparison of charge densities and bubble rise velocities from $2t1mf\Gamma$ probe with Faraday cup and video measurements in freely bubbling two-dimensional fluidized bed of original PE-I particles when $U_g - U_{mf}$ was increased abruptly from 0.04 to 0.18 m/s, then decreased abruptly from 0.18 to 0.04 m/s.

5.3.5 Changing U_g in three-dimensional bed of 100-1500 μm PE

A $2t1mf\Gamma$ probe (see Table 2.1) monitored the charge density and bubble rise velocity in the three-dimensional fluidized bed of original polyethylene particles as the superficial gas velocity changed. Current signals from the probe versus time when U_g changed are compared in Figure 5.10. The amplitudes of current signals from both tips increased as U_g increased and decreased as U_g decreased, consistent with the results from the two-dimensional bed, plotted in Figure 5.8.

As shown in Figure 5.11, the estimated charge density from the probe was of similar order of magnitude and changed in a consistent manner with values obtained from Faraday cup

measurement. The bubble rise velocity from the probe followed a similar trend when U_g was changed.

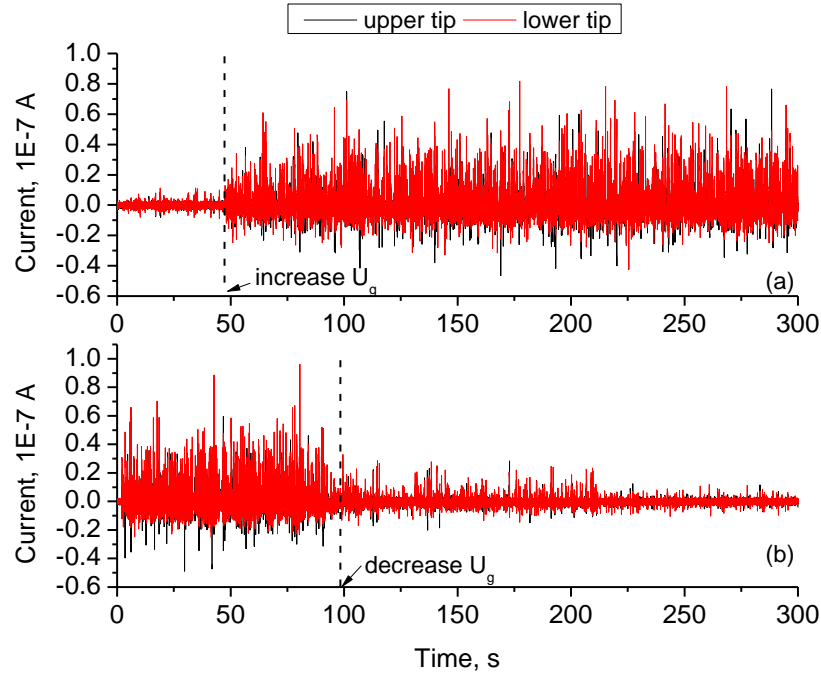


Figure 5.10 Current signals from 2t1mf Γ probe in freely bubbling 0.30 m ID three-dimensional fluidized bed of original PE-I particles when U_g - U_{mf} changed from (a) 0.04 to 0.19 m/s; (b) 0.19 to 0.04 m/s. (Fluidizing gas air: $T=40\pm 5$ °C, RH=15±4 %)

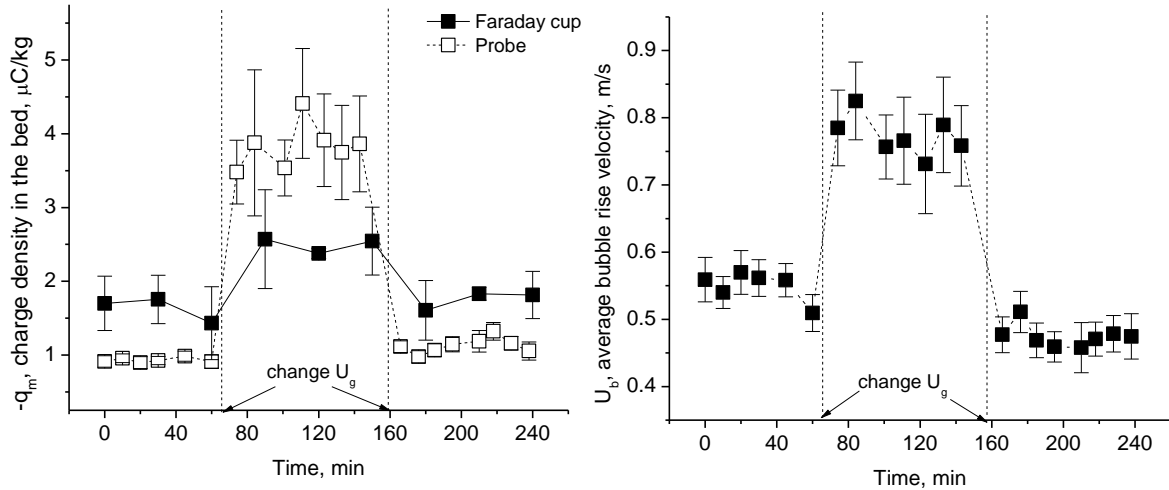


Figure 5.11 (a) Comparison of charge densities from 2t1mf Γ probe with Faraday cup measurement in freely bubbling 0.30 m ID three-dimensional fluidized bed with original PE-I particles when U_g - U_{mf} was increased abruptly from 0.04 to 0.19 m/s, and then decreased abruptly from 0.19 to 0.04 m/s. (b) Corresponding derived bubble rise velocities.

A 2t1mr Γ probe (see Table 2.1) was also tested. U_g was first increased then decreased. Current signals from the probe are shown in Figure 5.12, with derived charge density and bubble rise velocity in Figure 5.13. Similar to the results from the probe with a flat tip, charge density derived from the probe was of similar order of magnitude and changed in a manner consistent with those from Faraday cup measurement. However, larger quantitative difference existed between the probe results and the Faraday cup measurement, indicating that this kind of probe was less sensitive to charge density variation, similar to the results summarized in Table 4.4. This may be related to different probe tip shapes: a flat tip contacts with charged particles from one direction that signals are less affected by surrounding charged particles than a rod tip.

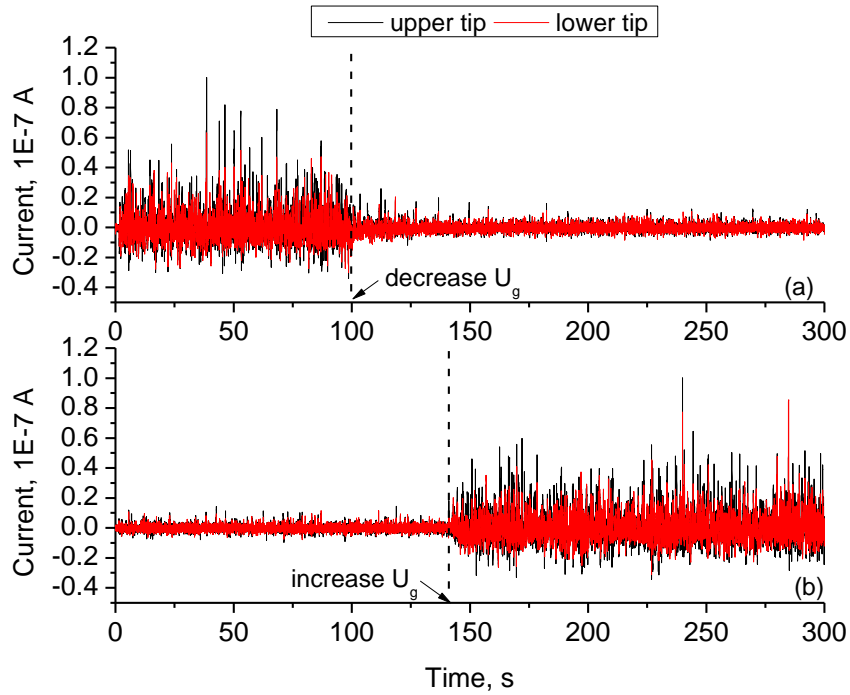


Figure 5.12 Current signals from 2t1mr Γ probe in freely bubbling 0.30 m ID three-dimensional fluidized bed of original PE-I particles when $U_g - U_{mf}$ was changed from (a) 0.18 to 0.05 m/s; (b) 0.05 to 0.20 m/s. (Fluidizing gas air: $T=40\pm 5$ °C, RH=15±4 %)

In-situ monitoring experiments in both the two-dimensional and three-dimensional columns showed that with the aid of proposed signal analysis method, the probe is able to capture changes in charge density and bubble behaviour as the operating conditions of the bed are modified.

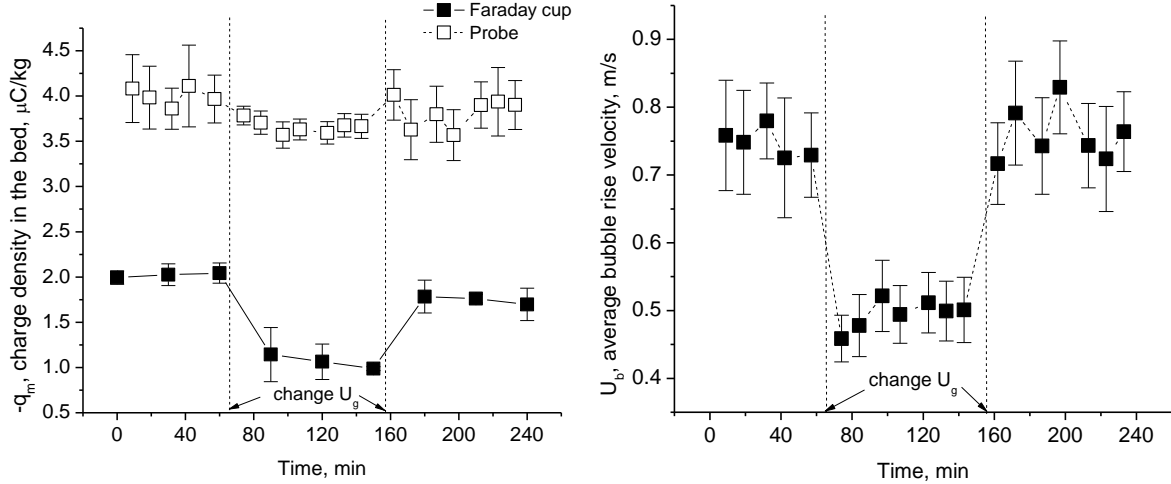


Figure 5.13 (a) Comparison of charge densities from 2t1mr Γ probe with Faraday cup measurement in freely bubbling 0.30 m ID three-dimensional fluidized bed with original PE-I particles when U_g - U_{mf} changed abruptly from 0.18 to 0.05 m/s, then from 0.05 to 0.20 m/s. (b) Corresponding derived bubble rise velocities.

5.4 Summary

The ability of currently developed probes for *in-situ* monitoring of charge density and hydrodynamics in freely bubbling beds has been demonstrated. Particle charge density and bubble properties in the bed were altered by abruptly changing superficial gas velocity or by impulsively adding antistatic agent to the bed. The probes were then utilized to quantitatively monitor the particle charge density and bubble rise velocity. A sampling frequency of 200-500 Hz and a sampling time interval of 5-10 min are recommended for our dual-tip (one-material) probe.

The current signals from the probes responded quickly and substantially to abrupt changes in U_g . In-bed charge density level changed over time after changing U_g and became stable after a certain period of time (about 1 h). By analyzing time-series signals from the probe, results from the probe were of similar order of magnitudes and changed consistently with those obtained from Faraday cup and video measurements when the superficial gas velocity (U_g) was changed. Charge densities from the Faraday cup decreased when Larostat 519 was added. The probe was able to capture the trends in particle charge density and bubble rise velocity when U_g changed.

Chapter 6 Overall Conclusions and Recommendations for Future Work

6.1 Conclusions

Several novel electrostatic probes combined with suitable signal analysis methods have been developed for *in-situ* measurement and monitoring of particle charge density levels and bubble properties inside fluidized beds.

6.1.1 Probes fabrication and calibration

Two dual-tip probe designs were fabricated: a dual-tip (two-material) probe, consisting of side-by-side tips made of materials of significantly different work functions, and a dual-tip (one-material) probe, having two vertically aligned tips of the same material. The two-material (Ni and TiN) probe was calibrated in an ejector-funnel experimental setup, with the charge density on the particles changed by varying the gas velocity and the material of construction of the exit pipe. The results were fitted to a semi-empirical equation (Eq. (2.5)) to quantify the effects of charge density, solid flux, particle velocity and angle of impact on current transferred to the probe from charged particles. The two tips showed different transferred currents when struck by charged particles, with the difference depending on particle charge density, impact velocity and contact angle. The difference between transferred currents from the two materials reached a maximum when particles struck the probe surface at right angles. Substantial differences were observed in charge signals from the two materials in both vertical tube and vibration tray setups, as well as in the current peaks from the two materials (Ni and TiN) in both single-bubble and freely bubbling experiments in a two-dimensional fluidized bed. Both motor-pulley experiments and fluidization experiments showed that the difference in charge/current signals for the two probe materials arose mainly from charge transfer.

The probes were calibrated with both single bubble injection and freely bubbling experiments in which the probe signals were synchronized with video images. For a dual-tip (one-material)

probe, bubble injection experiments showed that when an injected bubble passed the two tips in succession, clear time delays appeared between the peaks from both F and Γ probe geometries. The shapes of the current signals from each protruding tip were unaffected by the presence of the other tip, and there was little change in peak amplitude. However, signals from a retracted tip were greatly affected by its position relative to a protruding tip. Eq. (2.13) was fitted to measured data for bubbles passing the probe with different particle charge density (q_m) and bubble rise velocity (U_B). Probes were calibrated with glass beads and polyethylene particles with different size and size distribution in a two-dimensional fluidized bed, leading to calibration equations for calculating charge density. Several factors were found to affect the fitted parameters: dielectric constant of particles, work function difference between the probe tip material and bed particles, probe tip size and shape, and particle size distribution.

6.1.2 Measurements in gas-solid fluidized beds of glass beads and polyethylene

The novel probes were tested to measure electrostatic charges on particles in a two-dimensional fluidization column and cylindrical columns of inner diameter 0.10 m and 0.30 m. Glass beads and polyethylene particles of different mean size and size distributions were used. There were substantial differences between the signals (mean and standard deviation of currents and current peak amplitudes) for the side-by-side Ni and TiN tips of dual-tip (two-material) probe at all superficial gas velocities tested. These differences depended on the hydrodynamics and charge density inside the bed. Current signals were strongly affected by local hydrodynamics in a bubbling fluidized bed. The polarity and relative magnitude of current signals from the two tips made of different materials could have changed, and might even have reversed, for particles of different sizes when the superficial gas velocity and particle charge density changed. The sign of the cumulative charge signals does not necessarily represent the polarity of the charge on the particles. The amplitudes of current signal peaks, as well as peak frequencies, increased with increasing superficial gas velocity.

In the two-dimensional fluidization column, for a dual-tip (two-material) probe, both the mean and standard deviation of recorded current signals increased as the charge density and

superficial gas velocity increased. The average transferred current, \bar{I}_{tran} , and average induced current, \bar{I}_{ind} , were related via Eqs. (3.3) and (3.4) to the average maximum and minimum peaks heights, \bar{I}_{\max} and \bar{I}_{\min} .

For a dual-tip (one-material) probe, the slopes of cumulative charge signals with time increased for both tips, indicating increased charge transfer as the superficial gas velocity increased. The fluctuations from each tip also increased as U_g increased, because of the increase in bubble size and frequency. Fluctuations from the lower tip were larger than from the upper one, due to direct exposure to bubbles. For probes with different configurations, the slopes of cumulative charge signals and current peak amplitudes were greater for protruding tips than for retracted tips.

Experiments in the 0.10 m ID column showed that the mean and standard deviation of currents from the two materials of the dual-tip (two-material) probe were larger near the centre of the column than near the wall. Transferred currents from the two probe materials, as well as differences between them, were larger when the probe was inserted vertically rather than horizontally. The mean and standard deviations of currents from both probe tips increased with increasing superficial gas velocity, suggesting that both transfer and induction charges increased. The normalized standard deviation (standard deviation/mean) of the two materials increased as the superficial gas velocity increased, whereas the difference between them was nearly unchanged as the superficial gas velocity increased. FFT analysis confirmed that current signals are strongly influenced by bed hydrodynamics.

6.1.3 Signal analysis and decoupling

Local particle charge density and bubble behaviour were estimated by single collision probes of dual-tips based on the dynamic charge/current signals and calibration equations. A signal-processing procedure combined with a bubble selection algorithm was used to pre-treat signals. Several decoupling methods based on a charge transfer and induction model were examined. Signals from the probes were continuously processed by applying the signal processing procedures in both two- and three-dimensional freely bubbling fluidization beds.

Results indicated that both particle charge density and bubble rise velocity obtained from the probes were of the same order of magnitude and followed similar trends as those directly measured from Faraday cup and video images, respectively.

For a dual-tip (two-material) probe, a time-difference method and a two-current-peaks method were selected because of promising results in extracted particle charge density, compared with values directly measured by a Faraday cup. Decoupled U_B values from the time-difference method were closer to the bubble nose velocity ($U_{B,nose}$) from video analysis and deviated less than values calculated by two-current-peaks method. Relative magnitudes of signals from the two materials may change for different operating conditions and particle properties, causing difficulty in calibrating the probe and decoupling the signals. As a result, this probe may be unsuitable for particles of wide size distribution.

For the dual-tip (one-material) probe, rise velocity and size of bubbles analyzed by two tips peak-times method followed Eq. (4.11), and mean values were close to predictions from Eq. (4.11). Both the mean bubble rise velocity and the size increased as U_g increased. Results from one-tip time-difference method were more reproducible and closer to those from direct measurements. The Γ probe with only the upper tip protruding and the F probe with two tips protruding are in particular recommended for future applications because they provide closer agreement with charge density results from Faraday cup measurements. These probes are intrusive, but bubble size was not greatly affected when passing the two vertical tips.

Differences in the signals and charge densities for the glass beads and polyethylene particles investigated in this project reflect differences in particle properties such as density, dielectric constant, sphericity, roughness and hydrophobicity.

6.1.4 In-situ monitoring in gas-solid fluidized beds

The ability of the novel probes for *in-situ* monitoring of changes in charge density and hydrodynamics in freely bubbling beds was demonstrated. Particle charge density and bubble properties were altered by abruptly changing the superficial gas velocity or by adding

antistatic agent. The probes responded well to these changes. Charge densities decreased when the antistatic Larostat 519 powder was added.

Conventional electrostatic probe used in industry cannot decouple the hydrodynamics from particle charge density. The dual-tip (one-material) probe with F (two tips protruding) and Γ (lower tip retracted and upper tip protruding) configurations developed in this work could *in-situ* measure and monitor particle charge density levels. The hardware (probe) and software (data logging system and signal analysis) package has the potential to be installed and/or replace existing conventional static probe system in industrial powder handing processes (e.g. fluidization processes, mixing, coating and transportation).

6.2 Recommendations for future work

Further research on the following aspects would be needed to apply the dual-tip probes developed in this study as online measurement and monitoring tools for commercial reactors.

- Link decoupled information from the probes to wall sheeting/agglomeration data, for example in polyethylene reactors. Use the probe information to investigate charge generation and dissipation inside the bed.
- Due to difference in conditions of this study and industry, further test and calibrate probes in large-scale three-dimensional fluidized beds under different operating conditions close to those of industrial reactors.
- Investigate other probe designs, e.g. multifunctional (pressure + electrostatic) probes, where the bubble properties could be obtained from differential pressure measurements, then used to determine charge density.
- Test probe response to impulsive changes in relative humidity of the fluidizing gas.
- Compare probe hydrodynamics results with those from other measurement techniques (e.g. optical fiber probe) in the same setup (e.g. a travelling fluidized bed).

References

- [1] D. Kunii, O. Levenspiel, *Fluidization Engineering*, Butterworth-Heinemann 1991.
- [2] D.J. Lacks, The unpredictability of electrostatic charging, *Angewandte Chemie International Edition*, 51 (2012) 6822-6823.
- [3] G. Hendrickson, Electrostatics and gas phase fluidized bed polymerization reactor wall sheeting, *Chemical Engineering Science*, 61 (2006) 1041-1064.
- [4] Muhle M. E., Hagerty R. O., Szul J. F., Goode M. G., Britton L. G., Static measurement and detection in a gas phase polyethylene reactor, 2004.
- [5] R.O. Hagerty, M.E. Muhle, A.K. Agapiou, C. Kuo, M.G. Goode, F.D. Hussein, R.B. Pannell, J.F. Szul, Method for controlling sheeting in gas phase reactors, 2005.
- [6] E.J. Markel, R.O. Hagerty, F.D. Hussein, M.E. Muhle, Method and apparatus for controlling static charge in polyolefin reactors, 2010.
- [7] M.E. Muhle, R.O. Hagerty, Method for operating a gas-phase reactor at or near maximum production rates while controlling polymer stickiness, 2011.
- [8] E.J. Markel, R.O. Hagerty, R.W. Impelman, R.B. Pannell, C.F. Saladino, Methods for cleaning the distributor plate in a fluidized bed reactor system, 2013.
- [9] X.T. Bi, Electrostatic phenomena in fluidization systems: current status of understanding and future research needs, in: T. Knowlton (Ed.) 10th Circulating Fluidized Bed and Fluidization Technology, Engineering Conference International, Oregon, USA, 2011, pp. 41-57.
- [10] G. Tardos, R. Pfeffer, A method to measure electrostatic charge on a granule in a fluidized bed, *Chemical Engineering Communications*, 4 (1980) 665-671.
- [11] A.H. Chen, H.T. Bi, J.R. Grace, Measurement of particle charge-to-mass ratios in a gas-solids fluidized bed by a collision probe, *Powder Technology*, 135–136 (2003) 181-191.
- [12] N. Ellis, C.U. Yurteri, J. Ruud van Ommen, Continuous process to deposit nanoparticles onto microparticles, *Chemical Engineering Journal*, 181–182 (2012) 798-805.
- [13] K.S. Choi, M. Omar, X. Bi, J.R. Grace, Experimental study on electrostatic charging of polymer powders in mixing processes, *Journal of Loss Prevention in the Process Industries*, 23 (2010) 594-600.

- [14] J. Wong, P.C.L. Kwok, H.-K. Chan, Electrostatics in pharmaceutical solids, *Chemical Engineering Science*.
- [15] A. Wolny, W. Kaźmierczak, The influence of static electrification on dynamics and rheology of fluidized bed, *Chemical Engineering Science*, 48 (1993) 3529-3534.
- [16] L. Yao, H.T. Bi, A.-H. Park, Characterization of electrostatic charges in freely bubbling fluidized beds with dielectric particles, *Journal of Electrostatics*, 56 (2002) 183-197.
- [17] T.A. Alsmari, J.R. Grace, X.T. Bi, Effects of superficial gas velocity and temperature on entrainment and electrostatics in gas-solid fluidized beds, *Chemical Engineering Science*.
- [18] C.L. Briens, M.A. Bergougnou, I.I. Inculet, T. Baron, J.D. Hazlett, Size distribution of particles entrained from fluidized beds: Electrostatic effects, *Powder Technology*, 70 (1992) 57-62.
- [19] M.F. Al-Adel, D.A. Saville, S. Sundaresan, The Effect of Static Electrification on Gas–Solid Flows in Vertical Risers, *Industrial & Engineering Chemistry Research*, 41 (2002) 6224-6234.
- [20] A.-H.A. Park, H.T. Bi, J.R. Grace, A. Chen, Modeling charge transfer and induction in gas–solid fluidized beds, *Journal of Electrostatics*, 55 (2002) 135-158.
- [21] A. Chen, H. Bi, J.R. Grace, Effects of charge distribution around bubbles on charge induction and transfer to a ball probe in gas-solid fluidized beds, *Journal of Electrostatics*, 58 (2003) 91-115.
- [22] A. Chen, H.T. Bi, J.R. Grace, F.K. Van Willigen, J.R. Van Ommen, Measurement of charge distribution around a rising bubble in a 2-D fluidized bed, *AICHE Journal*, 52 (2006) 174-184.
- [23] A. Chen, H. Bi, J.R. Grace, Effects of probe numbers and arrangement on the measurement of charge distributions around a rising bubble in a two-dimensional fluidized bed, *Chemical Engineering Science*, 61 (2006) 6499-6510.
- [24] A. Chen, H.T. Bi, J.R. Grace, Charge distribution around a rising bubble in a two-dimensional fluidized bed by signal reconstruction, *Powder Technology*, 177 (2007) 113-124.
- [25] F. Jalalinejad, X.T. Bi, J.R. Grace, Effect of electrostatic charges on single bubble in gas–solid fluidized beds, *International Journal of Multiphase Flow*, 44 (2012) 15-28.

- [26] Y. Zhou, C. Ren, J. Wang, Y. Yang, K. Dong, Effect of hydrodynamic behavior on electrostatic potential distribution in gas–solid fluidized bed, *Powder Technology*, 235 (2013) 9-17.
- [27] P. Tiyapiboonchaiya, D. Gidaspow, S. Damronglerd, Hydrodynamics of Electrostatic Charge in Polypropylene Fluidized Beds, *Industrial & Engineering Chemistry Research*, 51 (2012) 8661-8668.
- [28] G.M. Colver, Instrumentation for Fluid Particle Flow, Chapter 3: Electrostatic Measurements, Noyes Publications, 1999.
- [29] N. Gibson, Static electricity — an industrial hazard under control?, *Journal of Electrostatics*, 40–41 (1997) 21-30.
- [30] J. Cross, *Electrostatics: Principles, Problems and Applications*, Adam Hilger 1987.
- [31] P. Mehrani, H.T. Bi, J.R. Grace, Electrostatic charge generation in gas-solid fluidized beds, *Journal of Electrostatics*, 63 (2005) 165-173.
- [32] A. Sowinski, F. Salama, P. Mehrani, New technique for electrostatic charge measurement in gas-solid fluidized beds, *Journal of Electrostatics*, 67 (2009) 568-573.
- [33] A. Sowinski, L. Miller, P. Mehrani, Investigation of electrostatic charge distribution in gas-solid fluidized beds, *Chemical Engineering Science*, 65 (2010) 2771-2781.
- [34] A. Sowinski, A. Mayne, P. Mehrani, Effect of fluidizing particle size on electrostatic charge generation and reactor wall fouling in gas–solid fluidized beds, *Chemical Engineering Science*, 71 (2012) 552-563.
- [35] A. Wolny, W. Kaźmierczak, Triboelectrification in fluidized bed of polystyrene, *Chemical Engineering Science*, 44 (1989) 2607-2610.
- [36] J. Guardiola, G. Ramos, A. Romero, Electrostatic behaviour in binary dielectric/conductor fluidized beds, *Powder Technology*, 73 (1992) 11-19.
- [37] J. Guardiola, V. Rojo, G. Ramos, Influence of particle size, fluidization velocity and relative humidity on fluidized bed electrostatics, *Journal of Electrostatics*, 37 (1996) 1-20.
- [38] D.I. Armour-Chelu, S.R. Woodhead, R.N. Barnes, The electrostatic charging trends and signal frequency analysis of a particulate material during pneumatic conveying, *Powder Technology*, 96 (1998) 181-189.

- [39] J. Ciborowski, A. Włodarski, On electrostatic effects in fluidized beds, *Chemical Engineering Science*, 17 (1962) 23-32.
- [40] M. Fujino, S. Ogata, H. Shinohara, The electric potential distribution profile in a naturally charged fluidized bed and its effects, *Int. Chem. Eng.*, 25 (1985) 149-159.
- [41] A.-H. Park, H. Bi, J.R. Grace, Reduction of electrostatic charges in gas-solid fluidized beds, *Chemical Engineering Science*, 57 (2002) 153-162.
- [42] W.O. Moughrabiah, J.R. Grace, X.T. Bi, Effects of pressure, temperature, and gas velocity on electrostatics in gas-solid fluidized beds, *Industrial and Engineering Chemistry Research*, 48 (2009) 320-325.
- [43] W.O. Moughrabiah, J.R. Grace, X.T. Bi, Electrostatics in gas-solid fluidized beds for different particle properties, *Chemical Engineering Science*, 75 (2012) 198-208.
- [44] F. Wang, J. Wang, Y. Yang, Distribution of electrostatic potential in a gas-solid fluidized bed and measurement of bed level, *Industrial and Engineering Chemistry Research*, 47 (2008) 9517-9526.
- [45] A.-H. Alissa Park, L.-S. Fan, Electrostatic charging phenomenon in gas–liquid–solid flow systems, *Fluidized Bed Applications*, 62 (2007) 371-386.
- [46] L. Fasso, B.T. Chao, S.L. Soo, Measurement of electrostatic charges and concentration of particles in the freeboard of a fluidized bed, *Powder Technology*, 33 (1982) 211-221.
- [47] A. Wolny, I. Opaliński, Electric charge neutralization by addition of fines to a fluidized bed composed of coarse dielectric particles, *Journal of Electrostatics*, 14 (1983) 279-289.
- [48] D. Napier, Generation of static electricity in a fluidized bed and in powder conveying, *Proceedings of 2nd World Congress on Particle Technology*, 1994.
- [49] P.J. Jiang, Zhang, J. P. and Fan, L. S., Electrostatic charge effects on the local solids distribution in the upper dilute region of circulating fluidized beds, in: H.a.L. Kwauk, J. (Ed.) *Circulating Fluidized Bed Technology V*, Science Press, Beijing, 1997.
- [50] D. Tucholski, G.M. Colver, Charging of glass powder in a circulating fluidized bed, *Industry Applications Conference, Thirty-Third IAS Annual Meeting. The 1998 IEEE*, 1998, pp. 1906-1912 vol.1903.

- [51] J.R. Mountain, M.K. Mazumder, R.A. Sims, D.L. Wankum, T. Chasser, P.H. Pettit, Jr., Triboelectric charging of polymer powders in fluidization and transport processes, Industry Applications, IEEE Transactions on, 37 (2001) 778-784.
- [52] F. Sharmene Ali, I.I. Inculet, A. Tedoldi, Charging of polymer powder inside a metallic fluidized bed, Journal of Electrostatics, 45 (1999) 199-211.
- [53] H. Zhao, G.S.P. Castle, I.I. Inculet, A.G. Bailey, Bipolar charging of poly-disperse polymer powders in fluidized beds, Industry Applications, IEEE Transactions on, 39 (2003) 612-618.
- [54] J. Revel, C. Gatamel, J.A. Dodds, J. Taillet, Generation of static electricity during fluidisation of polyethylene and its elimination by air ionisation, Electrostatic Phenomena in Particulate Processes, 135–136 (2003) 192-200.
- [55] M. Murtomaa, E. Räätänen, J. Rantanen, A. Bailey, E. Laine, J.-P. Mannermaa, J. Yliruusi, Electrostatic measurements on a miniaturized fluidized bed, Journal of Electrostatics, 57 (2003) 91-106.
- [56] P. Mehrani, H.T. Bi, J.R. Grace, Electrostatic behavior of different fines added to a Faraday cup fluidized bed, Journal of Electrostatics, 65 (2007) 1-10.
- [57] M. Omar, Choi K. C., Bi, X. T. and Grace, J. R., Effect of particle size and residence time on charging behavior of fine polymer powders in fluidized beds, in: Y.k. S. D. Kim, J. K. Lee, and Y. C. Seo, (Ed.) Fluidization XIIIKorea, 2010, pp. 233-240.
- [58] C. Zhu, S.L. Soo, A Modified Theory for Electrostatic-Probe Measurements of Particle Mass Flows in Dense Gas-Solid Suspensions, J Appl Phys, 72 (1992) 2060-2062.
- [59] B.N. Cole, M.R. Baum, F.R. Mobbs, An Investigation of Electrostatic Charging Effects in High-Speed Gas-Solids Pipe Flows, Proceedings of the Institution of Mechanical Engineers, Conference Proceedings, 184 (1969) 77-83.
- [60] S. Matsusaka, H. Masuda, Simultaneous measurement of mass flow rate and charge-to-mass ratio of particles in gas–solids pipe flow, Chemical Engineering Science, 61 (2006) 2254-2261.
- [61] S. Matsusaka, H. Maruyama, T. Matsuyama, M. Ghadiri, Triboelectric charging of powders: A review, Chemical Engineering Science, 65 (2010) 5781-5807.

- [62] R. Roy, J.F. Davidson, Similarity between gas-fluidized beds at elevated temperature and pressure, in: J.R. Grace, Shemilt, L.W., Bergougnou, M.A. (Ed.) *Fluidization VI*. Engineering Foundation, New York, 1989, pp. 293-300.
- [63] J. van der Schaaf, J.C. Schouten, F. Johnsson, C.M. van den Bleek, Non-intrusive determination of bubble and slug length scales in fluidized beds by decomposition of the power spectral density of pressure time series, *International Journal of Multiphase Flow*, 28 (2002) 865-880.
- [64] J.R. van Ommen, S. Sasic, J. van der Schaaf, S. Gheorghiu, F. Johnsson, M.-O. Coppens, Time-series analysis of pressure fluctuations in gas–solid fluidized beds – A review, *International Journal of Multiphase Flow*, 37 (2011) 403-428.
- [65] X. Bi, Flow regime transitions in gas–solids fluidization and transport, University of British Columbia, Vancouver, 1994.
- [66] H.T. Bi, A critical review of the complex pressure fluctuation phenomenon in gas–solids fluidized beds, *Chemical Engineering Science*, 62 (2007) 3473-3493.
- [67] N. Ellis, Hydrodynamics of gas-solid turbulent fluidized beds, University of British Columbia, 2003.
- [68] N. Ellis, H.T. Bi, C.J. Lim, J.R. Grace, Influence of probe scale and analysis method on measured hydrodynamic properties of gas-fluidized beds, *Chemical Engineering Science*, 59 (2004) 1841-1851.
- [69] M. Abbasi, R. Sotudeh-Gharebagh, N. Mostoufi, R. Zarghami, M.J. Mahjoob, Nonintrusive characterization of fluidized bed hydrodynamics using vibration signature analysis, *AICHE Journal*, 56 (2010) 597-603.
- [70] N. Salehi-Nik, R. Sotudeh-Gharebagh, N. Mostoufi, R. Zarghami, M.J. Mahjoob, Determination of hydrodynamic behavior of gas–solid fluidized beds using statistical analysis of acoustic emissions, *International Journal of Multiphase Flow*, 35 (2009) 1011-1016.
- [71] J. Wang, Y. Cao, X. Jiang, Y. Yang, Agglomeration Detection by Acoustic Emission (AE) Sensors in Fluidized Beds, *Industrial & Engineering Chemistry Research*, 48 (2009) 3466-3473.

- [72] Y.-q. Li, J.R. Grace, R.B. Gopaluni, H. Bi, C.J. Lim, N. Ellis, Characterization of gas-solid fluidization: A comparative study of acoustic and pressure signals, *Powder Technology*, 214 (2011) 200-210.
- [73] Y. Zheng, Q. Liu, Review of techniques for the mass flow rate measurement of pneumatically conveyed solids, *Measurement*, 44 (2011) 589-604.
- [74] H. Masuda, S. Matsusaka, H. Shimomura, Measurement of mass flow rate of polymer powder based on static electrification of particles, *Advanced Powder Technology*, 9 (1998) 169-179.
- [75] Y. Yan, B. Byrne, S. Woodhead, J. Coulthard, Velocity measurement of pneumatically conveyed solids using electrodynamic sensors, *Measurement Science and Technology*, 6 (1995) 515.
- [76] J.B. Gajewski, Electrostatic Nonintrusive Method for Measuring the Electric Charge, Mass Flow Rate, and Velocity of Particulates in the Two-Phase Gas-Solid Pipe Flows- Its Only or as Many as 50 Years of Historical Evolution, *Industry Applications, IEEE Transactions on*, 44 (2008) 1418-1430.
- [77] S. Matsusaka, H. Fukuda, Y. Sakura, H. Masuda, M. Ghadiri, Analysis of pulsating electric signals generated in gas-solids pipe flow, *Chemical Engineering Science (Control of Particulate Processes)*, 63 (2008) 1353-1360.
- [78] C. Xu, C. Liang, B. Zhou, S. Wang, HHT analysis of electrostatic fluctuation signals in dense-phase pneumatic conveying of pulverized coal at high pressure, *Chemical Engineering Science*, 65 (2010) 1334-1344.
- [79] L. Rongjun, Z. Bin, G. Wei, Signal analysis of electrostatic gas-solid two-phase flow probe with Hilbert-Huang transform, *Electronic Measurement & Instruments*, 2009. ICEMI '09. 9th International Conference on, 2009, pp. 2-486-482-490.
- [80] H.L. Hu, J. Dong, J. Zhang, Y.J. Cheng, T.M. Xu, Identification of gas/solid two-phase flow regimes using electrostatic sensors and neural-network techniques, *Flow Measurement and Instrumentation*, 22 (2011) 482-487.
- [81] Z. Wenbiao, W. Chao, W. Huaxiang, Hilbert-Huang transform based electrostatic signal analysis for characterization of dilute gas-solid two-phase flow, *Instrumentation and Measurement Technology Conference (I2MTC), 2011 IEEE*, 2011, pp. 1-6.

- [82] J. Zhang, H. Hu, J. Dong, Y. Yan, Concentration measurement of biomass/coal/air three-phase flow by integrating electrostatic and capacitive sensors, *Flow Measurement and Instrumentation*, 24 (2012) 43-49.
- [83] T. Hussain, W. Kaialy, T. Deng, M.S.A. Bradley, A. Nokhodchi, D. Armour-Chelu, A novel sensing technique for measurement of magnitude and polarity of electrostatic charge distribution across individual particles, *International Journal of Pharmaceutics*, 441 (2013) 781-789.
- [84] P. Bunchattheeravate, J. Curtis, Y. Fujii, S. Matsusaka, Prediction of particle charging in a dilute pneumatic conveying system, *AICHE Journal*, 59 (2013) 2308-2316.
- [85] C.L. Briens, L.A. Briens, E. Barthel, J.M. Le Blévec, A. Tedoldi, A. Margaritis, Detection of local fluidization characteristics using the V statistic, *Powder Technology*, 102 (1999) 95-103.
- [86] F. Portoghesi, F. Berruti, C. Briens, Use of triboelectric probes for on-line monitoring of liquid concentration in wet gas-solid fluidized beds, *Chemical Engineering Science*, 60 (2005) 6043-6048.
- [87] F. Portoghesi, F. Berruti, C. Briens, Continuous on-line measurement of solid moisture content during fluidized bed drying using triboelectric probes, *Powder Technology*, 181 (2008) 169-177.
- [88] J. McMillan, M. Dawe, C. Briens, F. Berruti, Measurement technique for the on-line detection of fines in a fluidized bed, *Measurement*, 44 (2011) 1436-1440.
- [89] E.J. Markel, R.L. Timothy, Method and apparatus for monitoring electrical properties of polymerization reactor wall film, 2013.
- [90] S.A. Marino, Polyethylene Reaction Analyses: Before, During and After, 2004.
- [91] D. Boland, Q.A.W. Al-Salim, D. Geldart, Static electrification in fluidised beds, *Chemical Engineering Science*, 24 (1969) 1389-1390.
- [92] D. Boland, D. Geldart, Electrostatic charging in gas fluidised beds, *Powder Technology*, 5 (1972) 289-297.
- [93] H.T. Bi, Chen, A.H., Grace, J.R., Monitoring electrostatic charges in fluidized beds, in: B.F. Bi X., and Pugsley T., (Ed.) Fluidization 12th, Engineering Conference International, 2007, pp. 1001-1008.

- [94] Z. Liu, X.T. Bi, J.R. Grace, Electrostatic charging behaviour of dielectric particles in a pressurized gas-solid fluidized bed, *Journal of Electrostatics*, 68 (2010) 321-327.
- [95] Y. Cheng, E.W.C. Lim, C.-H. Wang, G. Guan, C. Fushimi, M. Ishizuka, A. Tsutsumi, Electrostatic characteristics in a large-scale triple-bed circulating fluidized bed system for coal gasification, *Chemical Engineering Science*, 75 (2012) 435-444.
- [96] Y. Cheng, D.Y.J. Lau, G. Guan, C. Fushimi, A. Tsutsumi, C.-H. Wang, Experimental and numerical investigations on the electrostatics generation and transport in the downer reactor of a triple-bed combined circulating fluidized bed, *Industrial & Engineering Chemistry Research*, 51 (2012) 14258-14267.
- [97] N. Ellis, L.A. Briens, J.R. Grace, H.T. Bi, C.J. Lim, Characterization of dynamic behaviour in gas-solid turbulent fluidized bed using chaos and wavelet analyses, *Chemical Engineering Journal*, 96 (2003) 105-116.
- [98] C. M. van den Bleek, M.-O. Coppens, J. C. Schouten, Application of chaos analysis to multiphase reactors, *Chemical Engineering Science*, 57 (2002) 4763-4778.
- [99] B. Demirbas, J. Nijenhuis, C.U. Yurteri, J.R.v. Ommen, Towards monitoring electrostatics in gas-solid fluidized beds, *Canadian Journal of Chemical Engineering*, 86 (2008) 493-505.
- [100] J.R. van Ommen, M.-O. Coppens, C.M. van den Bleek, J.C. Schouten, Early warning of agglomeration in fluidized beds by attractor comparison, *AICHE Journal*, 46 (2000) 2183-2197.
- [101] X.-B. Yu, K. Jiang, Y. Xu, F. Wang, J.-D. Wang, Y.-R. Yang, Multi-scale and multi-fractal analysis of electrostatic potential signal in a gas-solid fluidized bed and recognition of fluidization pattern, *Beijing Ligong Daxue Xuebao/Transaction of Beijing Institute of Technology*, 30 (2010) 1235-1239.
- [102] W. Warsito, L.S. Fan, ECT imaging of three-phase fluidized bed based on three-phase capacitance model, *Chemical Engineering Science*, 58 (2003) 823-832.
- [103] B. Du, Marashdeh, Q., Warsito, W., Park, A.-H. A., and Fan, L.-S., developement of electrical capacitance volume tomography (ECVT) and electrostatic tomography (EST) for 3D density imaging of fluidized bed system, in: X.T.B. Berruti (Ed.) *The 12th International Conference on Fluidization - New Horizons in Fluidization Engineering*, 2007.

- [104] C.-H.W. Yongpan Cheng, Influence of electrostatics on instrumentation in fluidized bed measurements, The 7th International Symposium on Measurement techniques for Multiphase Flows, AIP Conf. Proc. , Tianjin, China 2011, pp. 335-341.
- [105] B. Zhou, J. Zhang, C. Xu, S. Wang, Image reconstruction in electrostatic tomography using a priori knowledge from ECT, Nuclear Engineering and Design, 241 (2011) 1952-1958.
- [106] V.S. Samsonov, Fomenko, G. V., Handbook of Thermionic Properties: Electronic work functions and richardson constants of elements and compounds, Plenum press data division, New York, 1966.
- [107] D.R. Lide, Handbook of Chemistry and Physics, 89th ed., CRC Press Inc,2008.
- [108] E.C. Jordan, Reference data for engineers: Radio, Electronics, Computers and Communications, 7th ed., Howard W. Sams & Company,1985.
- [109] D.K. Davies, Charge generation on dielectric surfaces, Journal of Physics D: Applied Physics, 2 (1969) 1533.
- [110] D.A. Seanor, Polymer Science, 2 (1972).
- [111] E. Glenn, "Resistivity of steel", The Physics Factbook, 2011.
- [112] R.A. Serway, Principles of Physics, 2nd ed., Saunders College Pub,1998.
- [113] K.C. Ludema, Friction, wear, lubrication: a textbook in tribology, CRC Press Inc,1996.
- [114] S.F. Krar, Gill,A. R., Exploring advanced manufacturing technologies, Industrial Press Inc,2003.
- [115] H. Masuda, S. Matsusaka, S. Nagatani, Measurements of powder flow rate in gas-solids pipe flow based on the static electrification of particles, Advanced Powder Technology, 5 (1994) 241-254.
- [116] R. Clift, J.R. Grace, M.E. Weber, Bubbles, Drops, And Particles, Dover Publications,2005.
- [117] H. Watanabe, A. Samimi, Y.L. Ding, M. Ghadiri, T. Matsuyama, K.G. Pitt, Measurement of Charge Transfer due to Single Particle Impact, Particle & Particle Systems Characterization, 23 (2006) 133-137.
- [118] W. John, G. Reischl, W. Devor, Charge transfer to metal surfaces from bouncing aerosol particles, Journal of Aerosol Science, 11 (1980) 115-138.
- [119] R. Dechene, Triboelectric vs. Electrostatic Induction Bag-Leak Detection, 2002.

- [120] A. Ema, D. Yasuda, K.-i. Tanoue, H. Masuda, Tribo-charge and rebound characteristics of particles impact on inclined or rotating metal target, *Powder Technology*, 135–136 (2003) 2-13.
- [121] K.-I. Tanoue, D. Yasuda, A. Ema, H. Masuda, Polarity change in the tribo-charge of particles with and without an initial charge, *Advanced Powder Technology*, 16 (2005) 569-584.
- [122] H.V. Malmstadt, C.G. Enke, S.R. Crouch, *Electronic measurements for scientists*, W. A. Benjamin, 1974.
- [123] S. Trigwell, M.K. Mazumder, R. Pellissier, Tribocharging in electrostatic beneficiation of coal: Effects of surface composition on work function as measured by x-ray photoelectron spectroscopy and ultraviolet photoelectron spectroscopy in air, *Journal of Vacuum Science & Technology A*, 19 (2001) 1454-1459.
- [124] H.T. Baytekin, A.Z. Patashinski, M. Branicki, B. Baytekin, S. Soh, B.A. Grzybowski, The mosaic of surface charge in contact electrification, *Science*, 333 (2011) 308-312.
- [125] H.T. Baytekin, B. Baytekin, J.T. Incorvati, B.A. Grzybowski, Material transfer and polarity reversal in contact charging, *Angewandte Chemie International Edition*, 51 (2012) 4843-4847.
- [126] H.T. Bi, N. Ellis, I.A. Abba, J.R. Grace, A state-of-the-art review of gas–solid turbulent fluidization, *Chemical Engineering Science*, 55 (2000) 4789-4825.
- [127] G. Sun, J.R. Grace, The effect of particle size distribution on the performance of a catalytic fluidized bed reactor, *Chemical Engineering Science*, 45 (1990) 2187-2194.
- [128] A. Stefanova, H.T. Bi, C.J. Lim, J.R. Grace, Heat transfer from immersed vertical tube in a fluidized bed of group A particles near the transition to the turbulent fluidization flow regime, *International Journal of Heat and Mass Transfer*, 51 (2008) 2020-2028.
- [129] M. Liu, Y. Zhang, H. Bi, J.R. Grace, Y. Zhu, Non-intrusive determination of bubble size in a gas–solid fluidized bed: An evaluation, *Chemical Engineering Science*, 65 (2010) 3485-3493.
- [130] J.F. Davidson, D. Harrison, *Fluidised Particles*, Cambridge University Press, Cambridge, 1963.
- [131] J.R. Grace, D. Harrison, The influence of bubble shape on the rising velocities of large bubbles, *Chemical Engineering Science*, 22 (1967) 1337-1347.

- [132] M. Rüdisüli, T.J. Schildhauer, S.M.A. Biollaz, A. Wokaun, J. Ruud van Ommen, Comparison of bubble growth obtained from pressure fluctuation measurements to optical probing and literature correlations, *Chemical Engineering Science*, 74 (2012) 266-275.
- [133] P. Jiang, H. Bi, S.-C. Liang, L.-S. Fan, Hydrodynamic behavior of circulating fluidized bed with polymeric particles, *AICHE Journal*, 40 (1994) 193-206.
- [134] D.J. Lacks, R.M. Sankaran, Contact electrification of insulating materials, *Journal of Physics D: Applied Physics*, 44 (2011) 453001.
- [135] L. Zhang, J. Hou, X.T. Bi, J.R. Grace, T. Janke, C. Arato, Electrostatic beneficiation of fly ash in a free-falling system, *Particuology*, 10 (2012) 154-160.
- [136] M. Jedrusik, A. Swierczok, R. Teisseyre, Experimental study of fly ash precipitation in a model electrostatic precipitator with discharge electrodes of different design, *Powder Technology*, 135–136 (2003) 295-301.
- [137] D.J. Lacks, A. Levandovsky, Effect of particle size distribution on the polarity of triboelectric charging in granular insulator systems, *Journal of Electrostatics*, 65 (2007) 107-112.
- [138] K.M. Forward, D.J. Lacks, R.M. Sankaran, Charge segregation depends on particle size in triboelectrically charged granular materials, *Physical Review Letters*, 102 (2009) 028001.
- [139] A.C. Hoffmann, J.G. Yates, Experimental observations of fluidized beds at elevated pressures, *Chemical Engineering Communications*, 41 (1986) 133-149.
- [140] P.A. Olwson, A.E. Almstedt, Influence of pressure and fluidization velocity on the bubble behaviour and gas flow distribution in a fluidized bed, *Chemical Engineering Science*, 45 (1990) 1733-1741.
- [141] M.A. Laughton, D.F. Warne, G.R. Jones, *Electrical Engineer's Reference Book*, Newnes2003.
- [142] J.R. Reitz, F.J. Milford, R.W. Christy, *Foundations of Electromagnetic Theory*, Pearson/Addison-Wesley2008.
- [143] W.R. Harper, *Contact and Frictional Electrification*, Clarendon Press1967.

- [144] D.W. van Krevelen, K.t. Nijenhuis, Properties of Polymers: Their Correlation with Chemical Structure; Their Numerical Estimation and Prediction from Additive Group Contributions, Elsevier Science, Amsterdam, 2009.
- [145] J.S. Forrest, Methods of increasing the electrical conductivity of surfaces, British Journal of Applied Physics, 4 (1953) S37.
- [146] M.G. Goode, D.M. Hasenberg, T.J. McNeil, T.E. Spriggs, Method for reducing sheeting during polymerization of alpha-olefins, 1989.
- [147] Song G. H., Rhee A. S., Lowder G. R., Method for reducing sheeting and static charges during polymerization of ethylene polymers, 1995.
- [148] W.C. Yang, Handbook of Fluidization and Fluid-Particle Systems, Taylor & Francis2003.
- [149] S.L Soo, Particulate and Continuum: Multiphase Fluid Dynamics, Hemisphere, New York, 1989.
- [150] T. Itakura, H. Masuda, C. Ohtsuka, S. Matsusaka, The contact potential difference of powder and the tribo-charge, Journal of Electrostatics, 38 (1996) 213-226.

Appendix A Photographs of experimental components

A.1 Fabricated probes

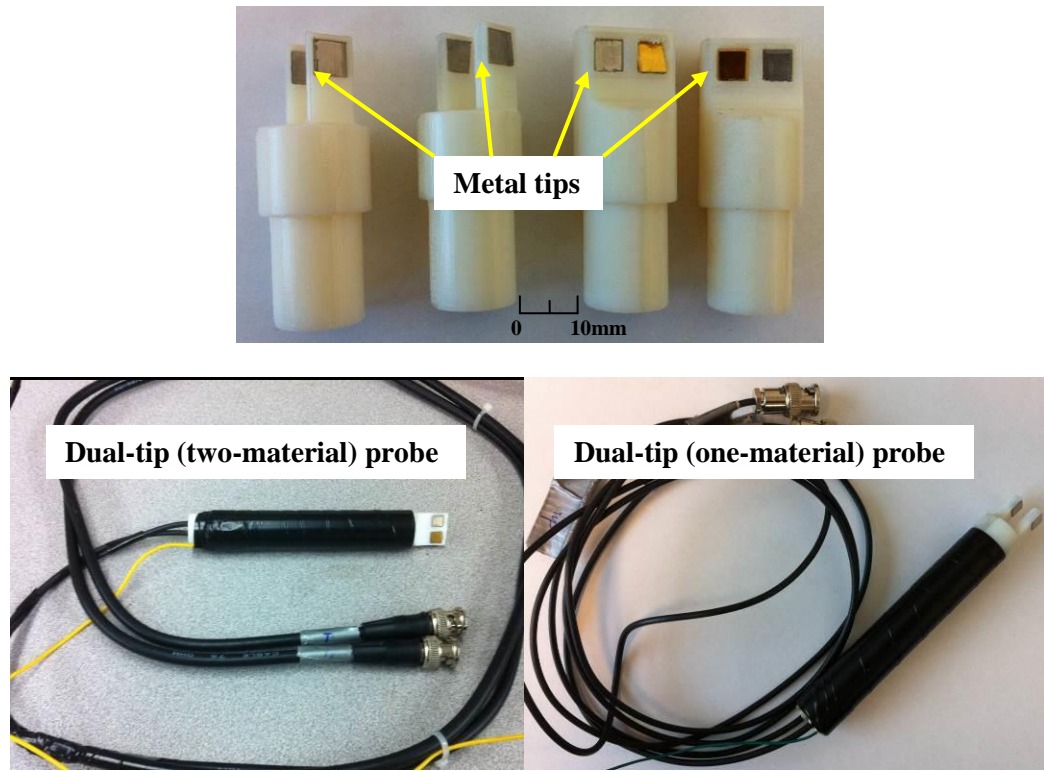


Figure A.1 Photographs of 3D printed parts with metal tips and fabricated probes.

A.2 Ejector-funnel setup

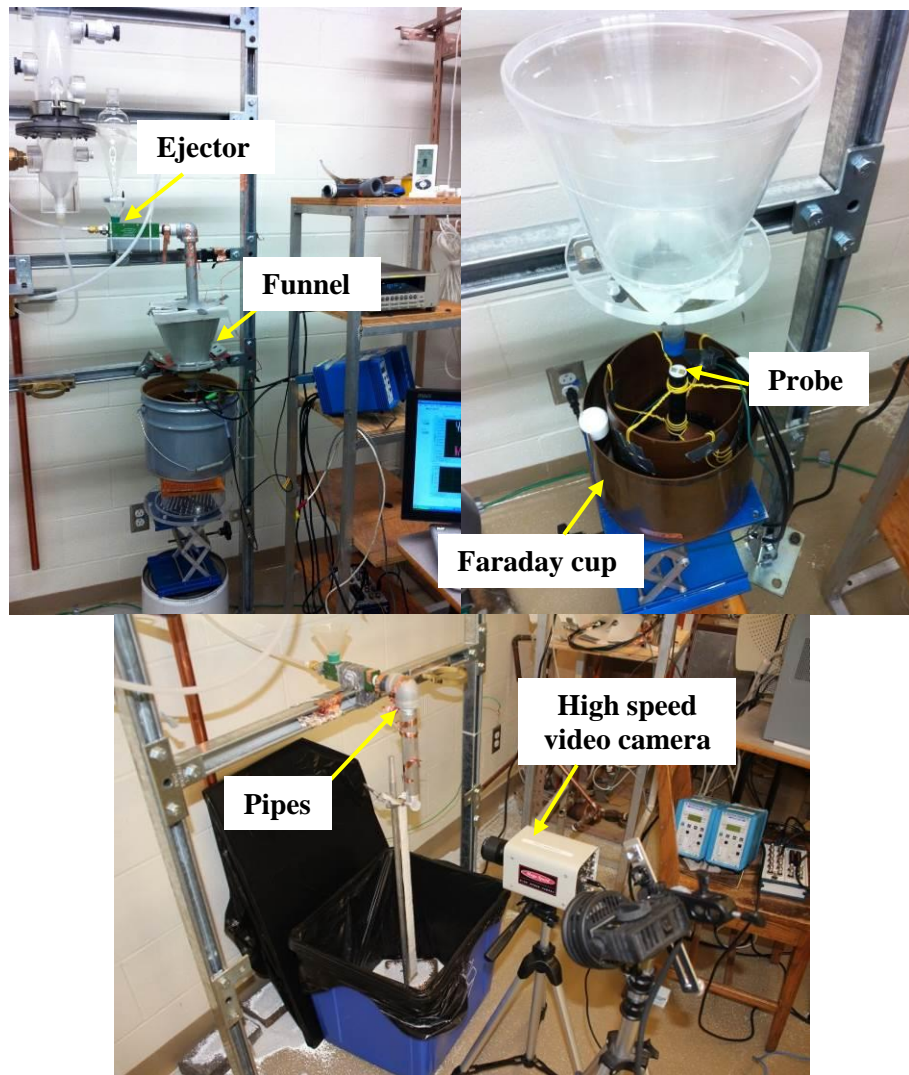


Figure A.2 Photographs of ejector-funnel setup.

A.3 Motor-pulley and vibration tray setups

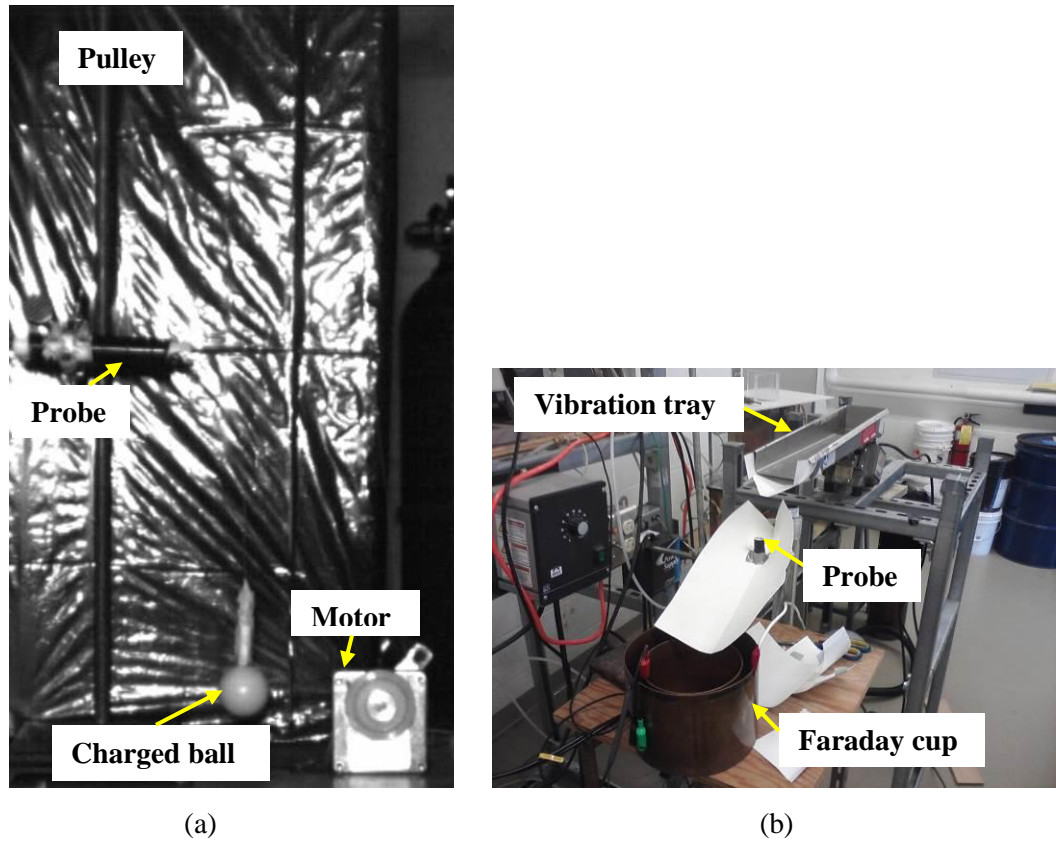


Figure A.3 Photographs of (a) motor-pulley and (b) vibration tray setups.

A.4 Two-dimensional fluidization column

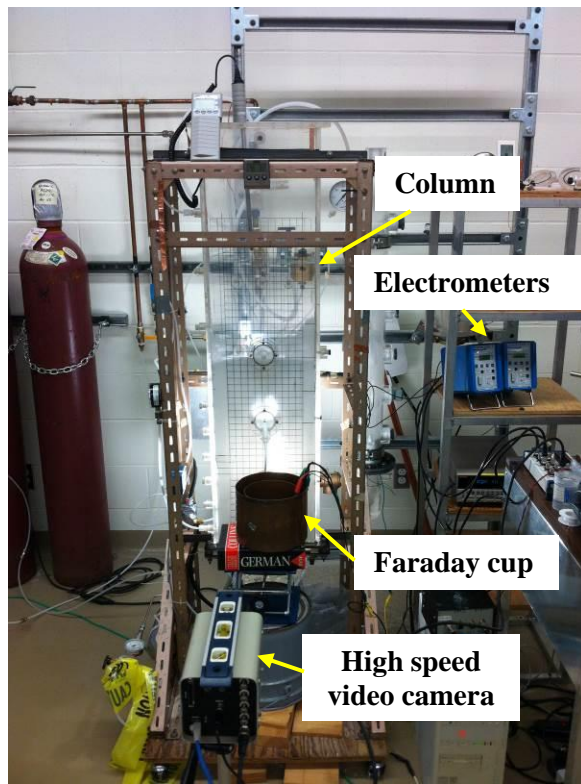


Figure A.4 Photographs of two-dimensional fluidization column (Its width is 0.307 m).

A.5 Three-dimensional Plexiglas fluidizizaton columns

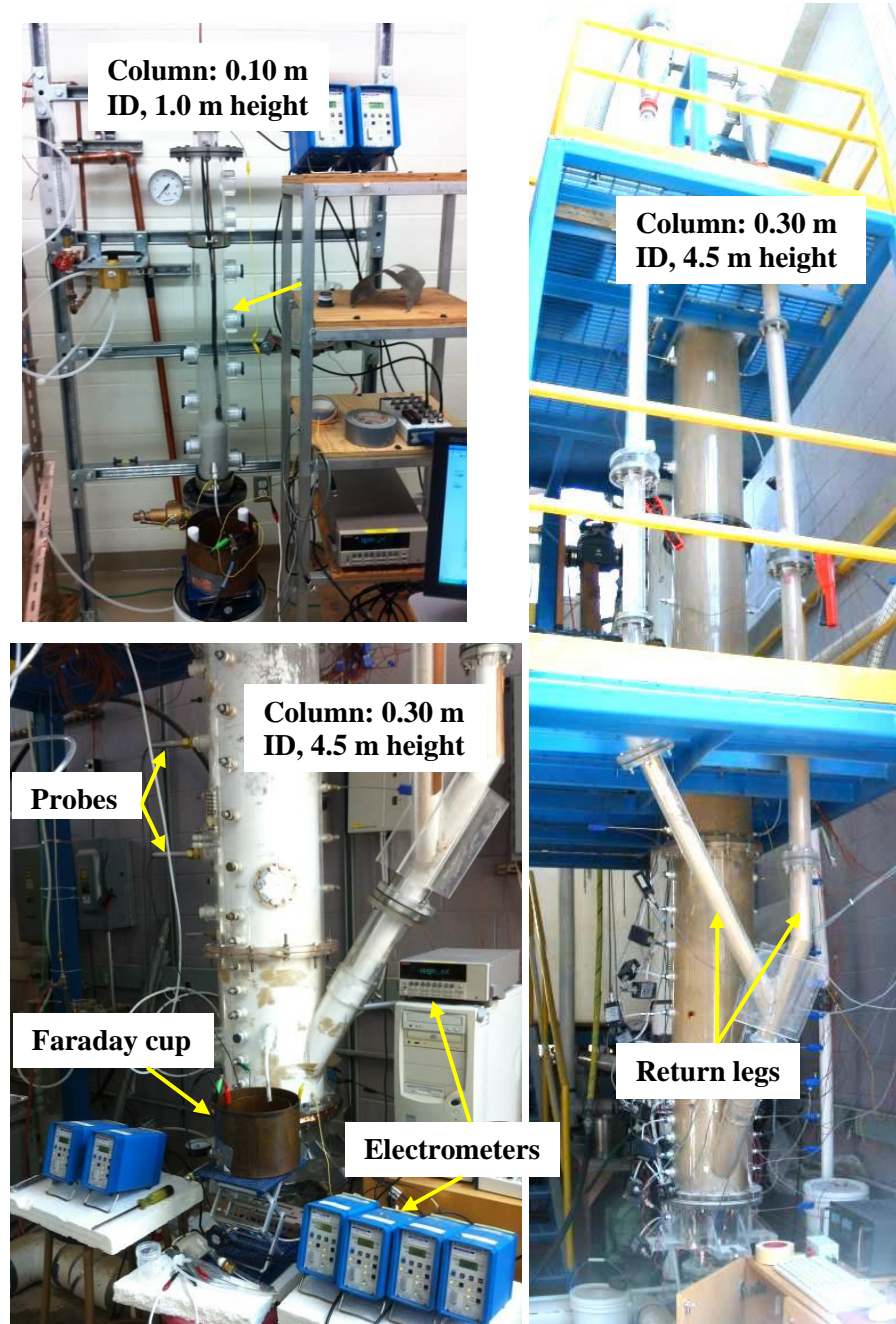


Figure A.5 Photographs of 0.10 m ID and 0.30 m ID three-dimensional Plexiglas fluidization columns.

A.6 Pressurized three-dimensional stainless steel fluidization column

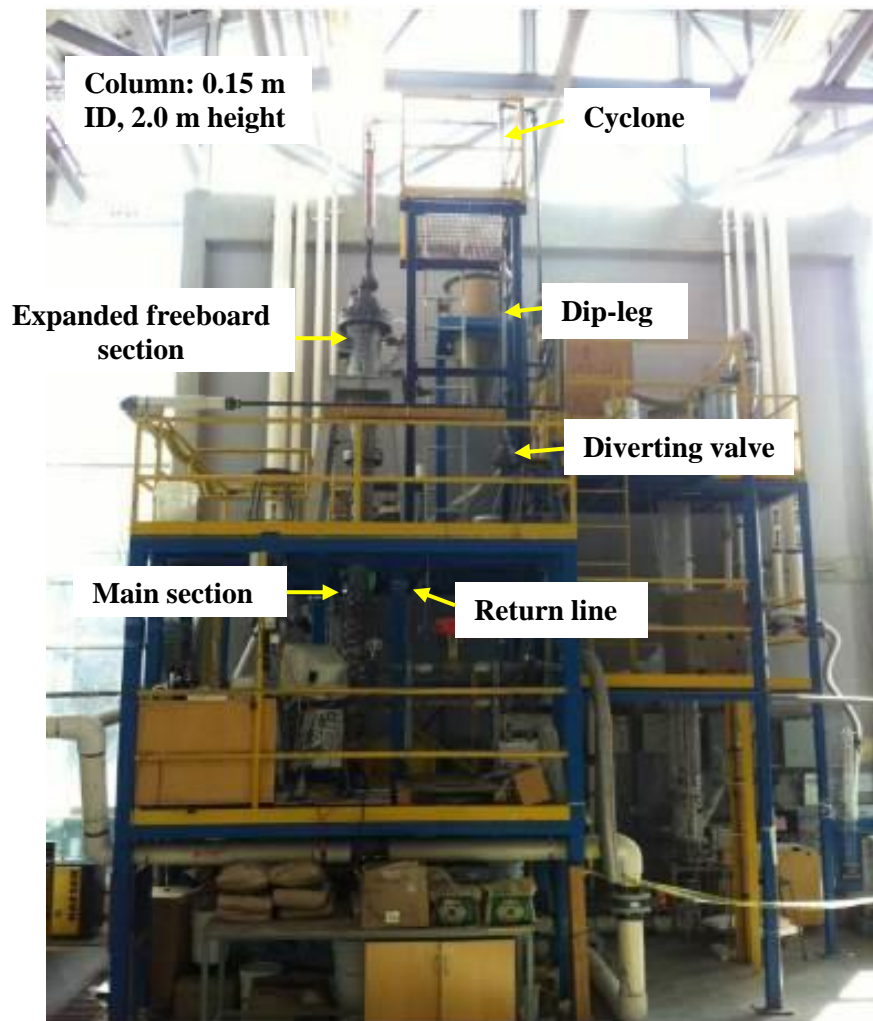


Figure A.6 Photographs of 0.15 m ID pressurized three-dimensional stainless steel fluidization column.

Appendix B Experimental details

B.1 Experimental data from calibration in two-dimensional fluidization column

Table B.1 Directly measured charge density (q_m), bubble rise velocity (U_B) and current peaks (I_{peak}) from synchronization experiments (see Section 2.4) with 2t2mb probe and 106-212 μm GB.

$U_g - U_{mf}$ (m/s)	q_m (C/kg)	U_B (m/s)	$I_{peak,Ni}$ (A)	$I_{peak,TiN}$ (A)
0.04	-1.11E-06	0.38	8.22E-08	1.40E-07
0.04	-1.10E-06	0.67	1.23E-07	1.56E-07
0.04	-1.42E-06	0.53	4.93E-08	1.97E-07
0.04	-1.51E-06	0.53	6.58E-08	9.87E-08
0.04	-1.07E-06	0.42	4.11E-08	9.04E-08
0.06	-1.37E-06	0.71	8.22E-08	9.87E-08
0.08	-2.09E-06	0.61	-9.87E-08	-1.07E-07
0.08	-2.09E-06	0.67	-8.22E-08	-1.07E-07
0.08	-2.43E-06	0.63	-1.23E-07	-9.87E-08
0.08	-2.43E-06	0.74	-9.87E-08	-1.32E-07
0.08	-2.54E-06	0.8	-1.48E-07	-1.97E-07
0.08	-2.58E-06	0.74	-1.23E-07	-1.40E-07
0.08	-2.37E-06	0.5	-6.58E-08	-9.04E-08
0.08	-2.37E-06	0.71	-7.40E-08	-6.58E-08
0.08	-2.37E-06	0.95	-1.07E-07	-9.87E-08
0.11	-2.37E-06	0.65	-1.40E-07	-2.20E-07
0.11	-2.37E-06	0.87	-1.32E-07	-1.89E-07
0.11	-2.60E-06	0.83	-1.15E-07	-1.40E-07
0.11	-2.60E-06	0.77	-7.40E-08	-1.23E-07
0.11	-2.60E-06	1	-7.40E-08	-1.23E-07
0.11	-2.55E-06	0.8	-1.07E-07	-1.40E-07
0.11	-2.55E-06	0.83	-1.64E-07	-2.06E-07
0.11	-2.30E-06	1	-9.87E-08	-1.64E-07
0.11	-2.30E-06	1	-1.40E-07	-1.56E-07
0.11	-2.30E-06	0.83	-1.73E-07	-2.30E-07

Table B.2 Directly measured charge density (q_m), bubble rise velocity (U_B) and current peaks (I_{peak}) from synchronization experiments (see Section 2.4) for different cases corresponding to Table 2.5. (Fluidizing gas air: $T=22\pm2^\circ\text{C}$, $\text{RH}=6\pm2\%$)

Case (a): 2t1mf Γ Probe and 710-850 μm PE			
U_g - U_{mf} (m/s)	q_m (C/kg)	U_B (m/s)	I_{peak} (A)
0.01	-3.98E-6	0.55	-2.42E-9
0.01	-3.98E-6	0.33	-3.55E-9
0.01	-3.98E-6	0.45	-2.68E-9
0.01	-4.42E-6	0.36	-2.92E-9
0.01	-4.42E-6	0.33	-2.20E-9
0.01	-4.01E-6	0.36	-2.23E-9
0.04	-5.87E-6	0.48	-6.39E-9
0.04	-6.63E-6	0.91	-1.16E-8
0.04	-6.53E-6	0.59	-7.38E-9
0.04	-6.53E-6	0.42	-6.91E-9
0.04	-6.53E-6	0.44	-5.97E-9
0.04	-5.38E-6	0.48	-5.56E-9
0.04	-5.48E-6	0.46	-6.23E-9
0.04	-5.48E-6	0.53	-6.42E-9
0.09	-6.27E-6	0.67	-7.30E-9
0.09	-6.77E-6	0.91	-1.69E-8
0.09	-6.98E-6	0.90	-1.09E-8
0.09	-6.98E-6	0.63	-6.06E-9
0.09	-6.98E-6	0.53	-8.98E-9
0.09	-6.98E-6	0.56	-9.46E-9

Case (b): 2t1mf Γ Probe and 100-1500 μm PE

$U_g - U_{mf}$ (m/s)	q_m (C/kg)	U_B (m/s)	I_{peak} (A)
0.06	-2.63E-06	0.34	-5.02E-09
0.06	-3.26E-06	0.37	-3.18E-09
0.06	-3.02E-06	0.42	-5.40E-09
0.06	-3.26E-06	0.53	-7.36E-09
0.06	-3.18E-06	0.42	-3.71E-09
0.06	-3.18E-06	0.45	-6.38E-09
0.09	-3.59E-06	0.48	-1.30E-08
0.09	-3.59E-06	0.56	-1.25E-08
0.09	-3.66E-06	0.56	-1.35E-08
0.09	-3.66E-06	0.59	-1.14E-08
0.09	-3.77E-06	0.59	-1.47E-08
0.09	-3.77E-06	0.48	-1.01E-08
0.14	-3.45E-06	0.66	-1.49E-08
0.14	-3.45E-06	0.77	-1.60E-08
0.14	-3.45E-06	0.63	-1.65E-08
0.14	-4.08E-06	0.56	-1.72E-08
0.14	-4.08E-06	0.59	-1.07E-08
0.14	-4.44E-06	0.67	-1.50E-08
0.14	-4.44E-06	0.56	-1.29E-08
0.18	-4.27E-06	1	-1.90E-08
0.18	-4.27E-06	0.83	-2.09E-08
0.18	-4.27E-06	1	-2.41E-08
0.18	-4.27E-06	0.77	-1.99E-08

Case (c): 2t1mr Γ Probe and 710-850 μm PE

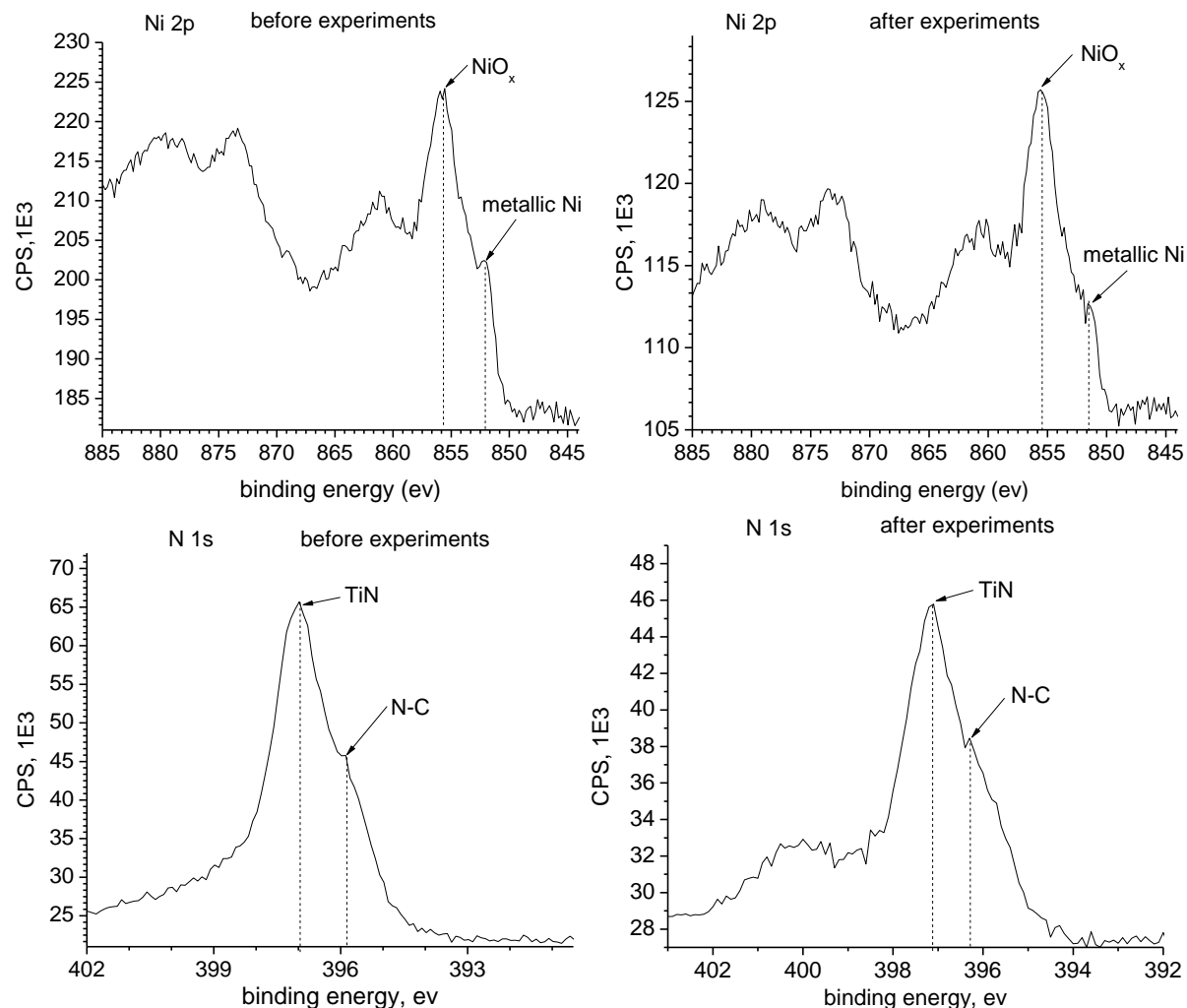
$U_g - U_{mf}$ (m/s)	q_m (C/kg)	U_B (m/s)	I_{peak} (A)
0.04	-7.32E-6	0.59	-2.15E-8
0.04	-7.32E-6	0.40	-2.70E-8
0.04	-7.32E-6	0.54	-1.88E-8
0.04	-7.19E-6	0.45	-2.13E-8
0.04	-6.85E-6	0.53	-2.06E-8
0.04	-7.03E-6	0.42	-1.57E-8
0.04	-6.58E-6	0.48	-1.74E-8
0.06	-8.31E-6	0.50	-4.42E-8
0.06	-8.48E-6	0.71	-3.30E-8
0.06	-8.67E-6	0.45	-2.78E-8
0.09	-9.08E-6	0.71	-4.21E-8
0.09	-9.58E-6	0.67	-4.38E-8
0.09	-8.94E-6	0.63	-4.36E-8
0.09	-8.94E-6	0.67	-4.70E-8
0.09	-9.20E-6	0.59	-3.49E-8
0.13	-1.25E-5	0.77	-6.35E-8
0.13	-1.19E-5	0.77	-6.20E-8
0.13	-1.09E-5	0.63	-6.15E-8
0.13	-1.23E-5	0.71	-6.50E-8

Case (d): 2t1mr Γ Probe and 100-1500 μm PE

$U_g - U_{mf}$ (m/s)	q_m (C/kg)	U_B (m/s)	I_{peak} (A)
0.06	-5.21E-06	0.38	-1.38E-08
0.06	-5.21E-06	0.42	-9.48E-09
0.06	-4.85E-06	0.40	-1.19E-08
0.06	-4.85E-06	0.42	-1.42E-08
0.06	-5.35E-06	0.40	-2.24E-08
0.06	-5.35E-06	0.42	-1.68E-08
0.06	-5.35E-06	0.41	-1.20E-08
0.06	-5.43E-06	0.45	-2.53E-08
0.06	-5.43E-06	0.43	-1.70E-08
0.09	-5.67E-06	0.53	-2.98E-08
0.09	-5.67E-06	0.59	-2.40E-08
0.09	-5.24E-06	0.50	-2.26E-08
0.09	-5.24E-06	0.55	-2.42E-08
0.09	-5.60E-06	0.56	-2.58E-08
0.09	-5.60E-06	0.57	-2.68E-08
0.14	-5.72E-06	0.63	-4.57E-08
0.14	-5.72E-06	0.65	-3.72E-08
0.14	-6.05E-06	0.71	-4.98E-08
0.14	-6.05E-06	0.62	-3.67E-08
0.14	-5.89E-06	0.60	-4.19E-08
0.14	-5.89E-06	0.67	-3.65E-08

B.2 X-ray Photoelectron Spectrometers characterization of Ni and TiN tips

Results from a X-ray Photoelectron Spectrometer (XPS) tests, performed by an Omicron & Leybold MAX200, are shown in Figure B.1. This shows that the Ni and TiN tips before and after experiments were similar, with metallic nickel and TiN identified for both the Ni and TiN tips before and after the experiments. The measurement depth of XPS is 8-10 nm, meaning that any oxidation of the tip identified was within 8 nm in depth from the top surface, a very thin layer compared to the total thickness of 1 mm. For the Ni tips, Ni2p shows that binding energies at 855 ev and 852 ev are contributed to nickel oxide and metallic nickel. For the TiN tips, the binding energies for N1s at 397 ev and 396 ev correspond to TiN and N-C in the TiN coating. The binding energies for Ti2p at 458 ev, 456 ev and 455 ev are contributed to TiO_2 , Ti_2O_3 and TiN, respectively.



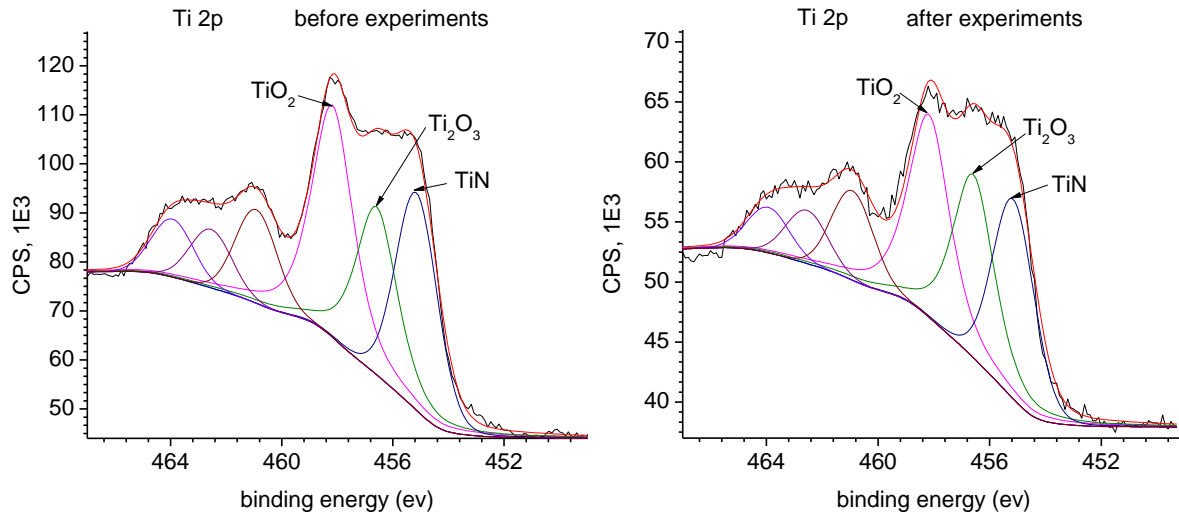


Figure B.1 XPS of Ni and TiN tips before and after experiments.

B.3 Probe response time

The response time of a dual-tip (two-material) probe was tested on a simple setup as shown in Figure B.2. The probe signals were synchronized with video image. The probe were moved downward into a bottle of particles, and then pulled back. By comparing the probe signals with recorded video images, a current peak was found to correspond to the moment when the probe tip contacted the particles. It could be estimated that the probe response time was less than 1 millisecond.

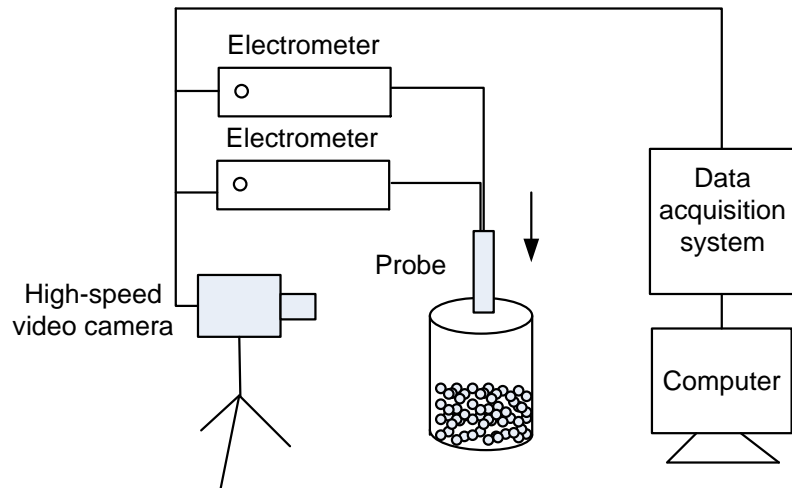


Figure B.2 Schematic of setup for testing probe response time.

B.4 Sensitivity test in 0.10 m ID three-dimensional fluidization column

The 0.10 m ID three-dimensional fluidization column (see Figure 3.1) was used. The column was made of Plexiglas with an inner diameter of 0.10 m and a height of 1.0 m. A 2t2ma probe (see Table 2.1) was inserted horizontally from the side, 0.10 m above the distributor. Details of the experimental facilities are provided in Section 3.2.2.

The fluidized bed with a static bed height of 0.20 m was operated at different U_g for extended time intervals (1 h, 3 min or 20-30 s). Then U_g was abruptly changed and the probe measurements took for certain sampling times (3 min or 20-30 s). It was expected that the in-bed charge density would change much more slowly than the hydrodynamics. The ratio of mean currents from Ni and TiN were calculated, and the results appear in Table B.3. A smaller ratio means a larger difference between the transferred currents from the two materials. For the effect of operating time, a short operating time (3 min, compared to 1 h) resulted in smaller ratios at different U_g , suggesting that the in-bed charge density decreased with time after changing U_g . The ratio first decreased with increasing U_g , then increased when U_g was decreased back to its previous value. Changing of hydrodynamic in a short period of time (20-30 s) may cause the local charge density level to change as well, especially in the small (0.10 m ID) column; so it was difficult to maintain the charge density level while changing U_g . This indicates that the probe has a short response time and is sensitive to changes in both hydrodynamic and charge density in the bed.

In another experiment, U_g was changed stepwise to several different values with about one hour between each shift. The current signals were measured by the probe every 20 min for a sampling time of 5 min. Figure B.3 shows mean currents, ratio and absolute difference of the mean currents from the two probe materials for changing U_g in 8 h. After U_g was abruptly changed each time, the mean currents from both tips first increased, and became stable as time increased, consistent with results in Table B.3. Both the mean currents and absolute difference between the mean currents from Ni and TiN, increased with increasing U_g .

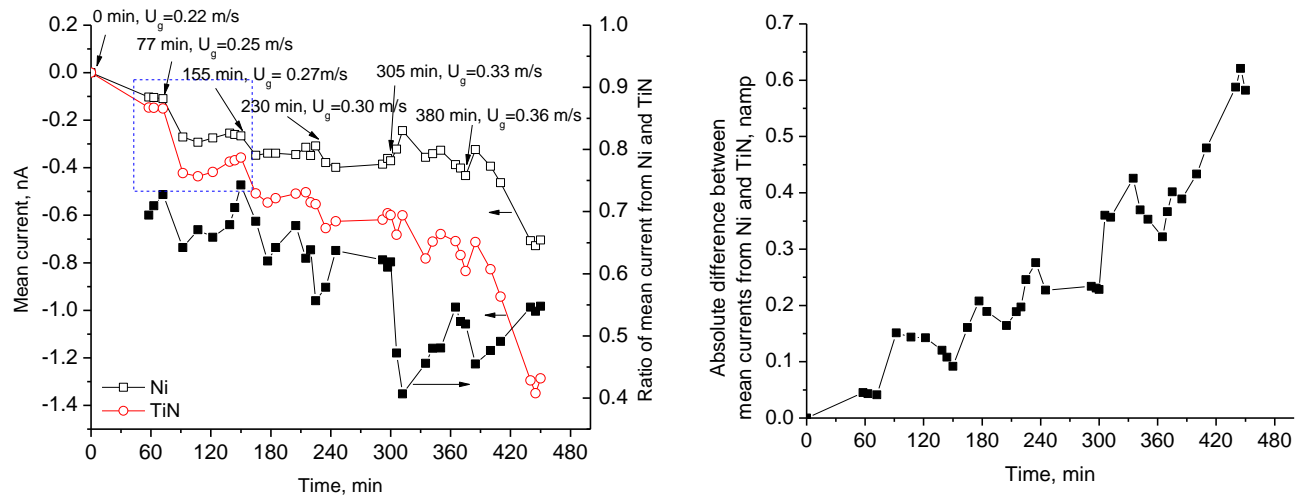


Figure B.3 Changes in mean currents, ratio and difference of mean currents from Ni and TiN of 2t2ma probe in 0.10 m ID freely bubbling fluidized bed when U_g changed continuously from 0.22 to 0.36 m/s. ($f_s = 100 \text{ Hz}$, $t_s = 5 \text{ min}$, Fluidizing gas air: $T=22\pm2^\circ\text{C}$, $RH=10\pm2\%$)

Table B.3 Ratio of mean currents from Ni and TiN of 2t2ma probe when U_g was changed in 0.10 m ID freely bubbling fluidized bed. ($f_s = 100$ Hz,
Fluidizing gas air: $T=22\pm2^\circ\text{C}$, $\text{RH}=10\pm2\%$.)

Exp	operating time	sampling time	U_g , superficial gas velocity					
			$\bar{I}_{Ni} / \bar{I}_{TiN}$, ratio of mean current from Ni and TiN					
Increase U_g in sequence	1 h	3 min	0.17 m/s	0.20 m/s	0.22 m/s	0.25 m/s	0.28 m/s	0.31 m/s
			0.73	0.74	0.56	0.62	0.52	0.55
Increase U_g in sequence	3 min	3 min	0.17 m/s		0.22 m/s		0.28 m/s	
			0.64		0.66		0.52	
Increase U_g in sequence	20-30 s	20-30 s	0.20 m/s		0.25 m/s		0.31 m/s	
			0.73		0.71		0.58	
Change U_g randomly	20-30 s	20-30 s	0.25 m/s		0.20 m/s		0.36 m/s	
			0.58		0.49		0.44	
First increase then decrease U_g	20-30 s	20-30 s	0.20 m/s	0.25 m/s	0.31 m/s	0.36 m/s	0.31 m/s	0.25 m/s
			0.68	0.71	0.52	0.40	0.49	0.53

B.5 Troubleshooting signal drift of custom-made probe

Challenge: The newly fabricated probe showed drift when there was nothing contacting the probe tip.

Diagnosis: a short circuit contact between the shield and the signal of the coaxial cable was found when the probe was disassembled. This was because of conductive epoxy gluing the metal tip to the cable. However, after isolating the shield from the signal of the coaxial cable, the probe signal still showed drift. 400 MOhms was measured between signal line and shield, whereas a proper working probe should provide infinite resistance. It was suspected that the connection of coaxial wire with metal was the reason. Tests of various wiring configurations of the probe were performed to track the origin of the probe signal drift. After eliminating possible causes, it was found that contamination between the signal lead and shield reduced impedance and resulted in signal drift. The contamination was by filling materials used in the 3D printing, left because of incomplete cleaning. Accumulation of debris on the probe surface may have caused the signal drift.

Solutions: Printed parts were completely cleaned and filling materials were removed as much as possible. Isolate the signal from the shield of coaxial cable. Clean the probe, reassemble and re-glue sensing tip to signal wires. After these measures were taken, the signal drift disappeared and noise was minimized.

B.6 Determination of minimum fluidization velocity

The minimum fluidization velocities were measured from pressure drop over bed height in different columns versus superficial gas velocity curves at the intersection of two straight-lines.

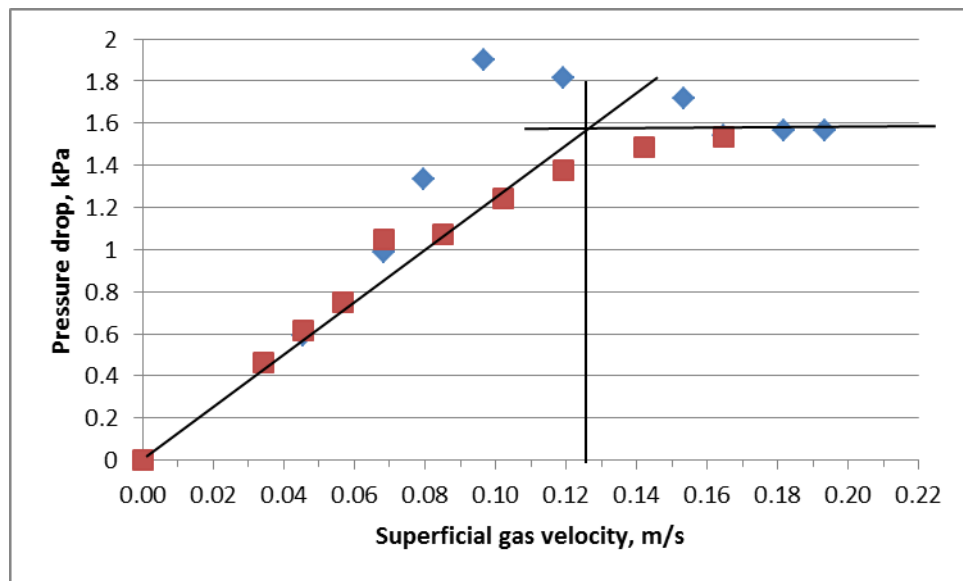


Figure B.4 Experimental minimum fluidization velocity (U_{mf}) curve for original PE-I (100-1500 μm) in two-dimensional fluidization column.

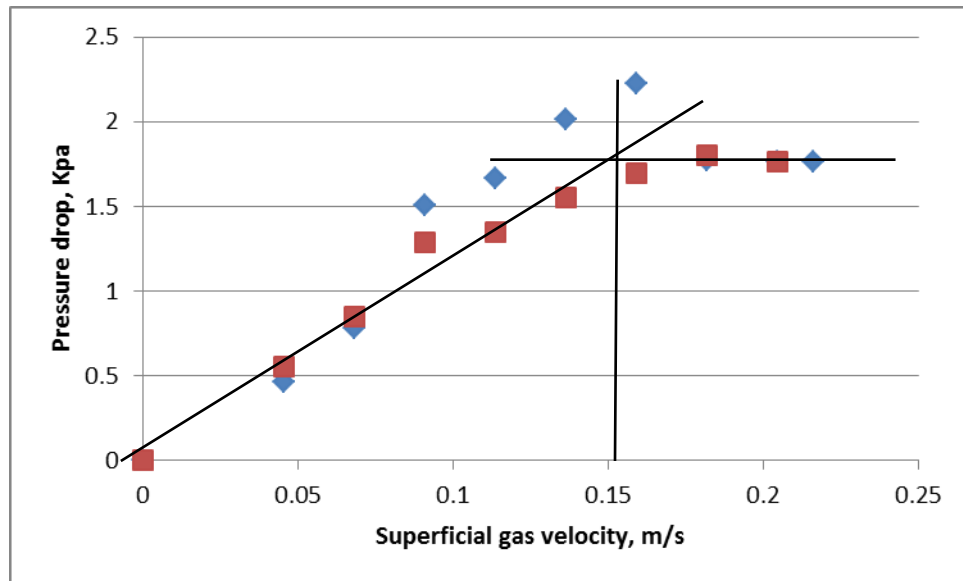


Figure B.5 Experimental minimum fluidization velocity (U_{mf}) curve for sieved PE (710-850 μm) in two-dimensional fluidization column.

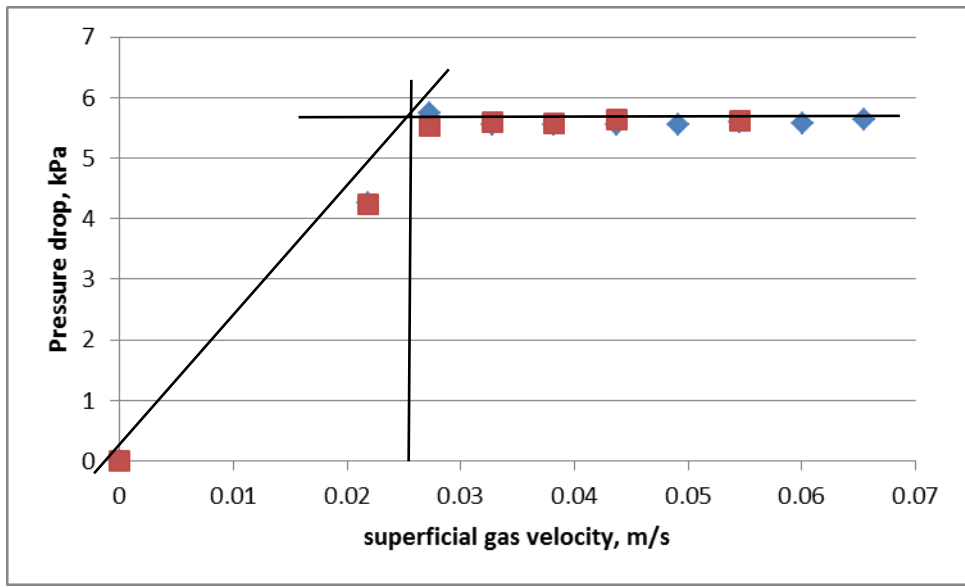


Figure B.6 Experimental minimum fluidization velocity (U_{mf}) curve for GB (106-212 μm) in two-dimensional fluidization column.

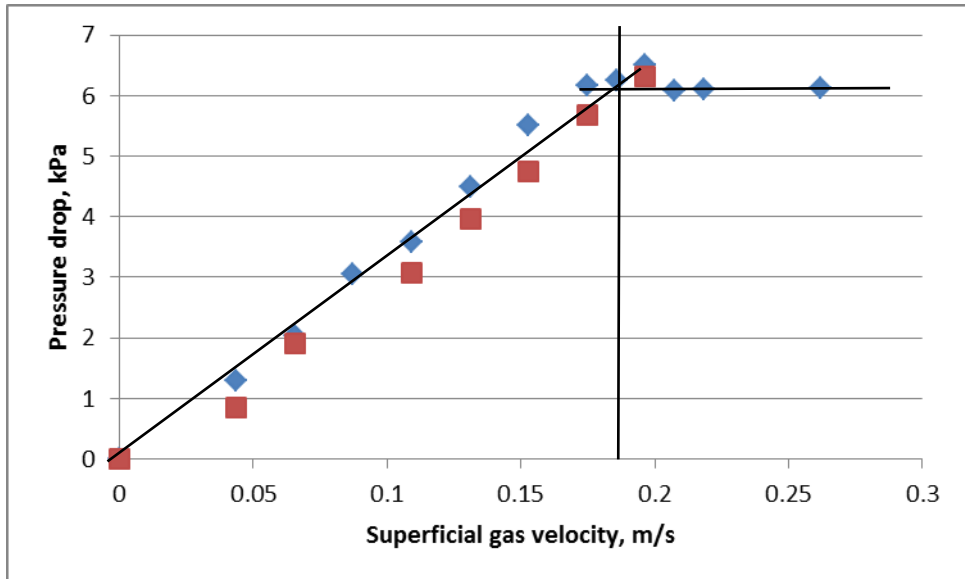


Figure B.7 Experimental minimum fluidization velocity (U_{mf}) curve for GB (500-600 μm) in two-dimensional fluidization column.

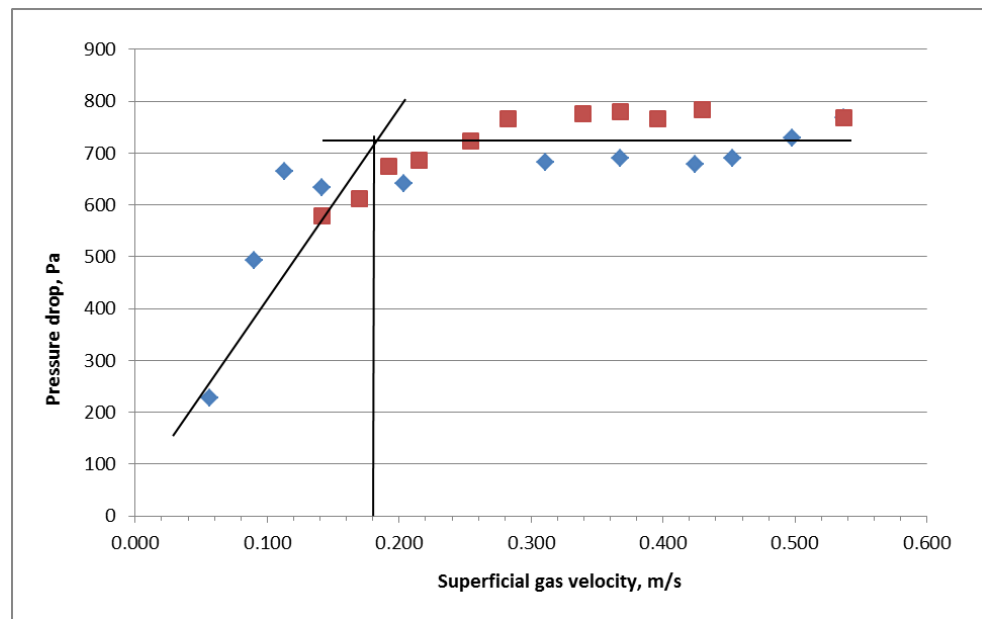


Figure B.8 Experimental minimum fluidization velocity (U_{mf}) curve for original PE-II (wide size distribution) in pressurized three-dimensional fluidization column. (absolute pressure in freeboard: 138 kPa)

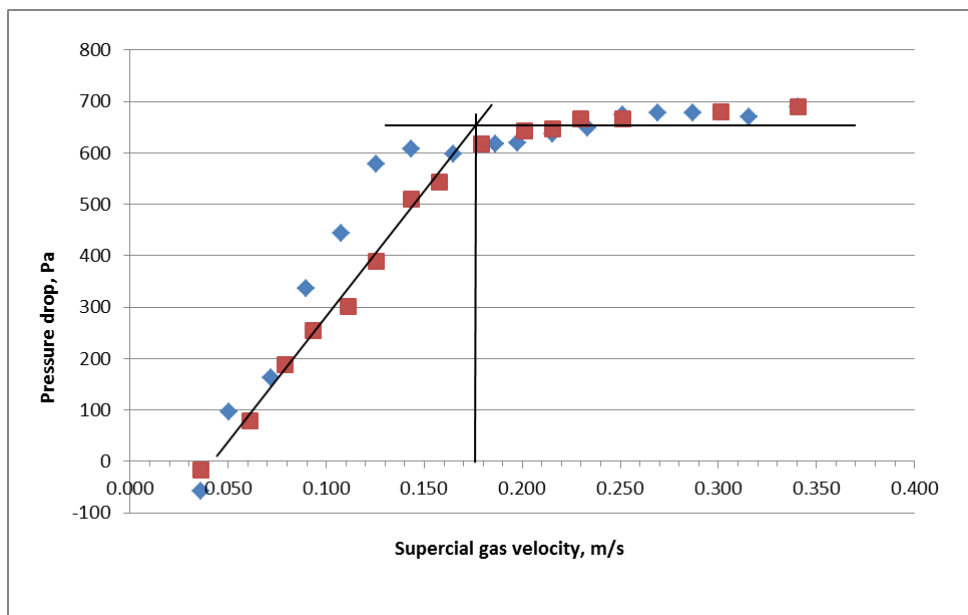


Figure B.9 Experimental minimum fluidization velocity (U_{mf}) curve for original PE-II (wide size distribution) in pressurized three-dimensional fluidization column. (absolute pressure in freeboard: 276 kPa)

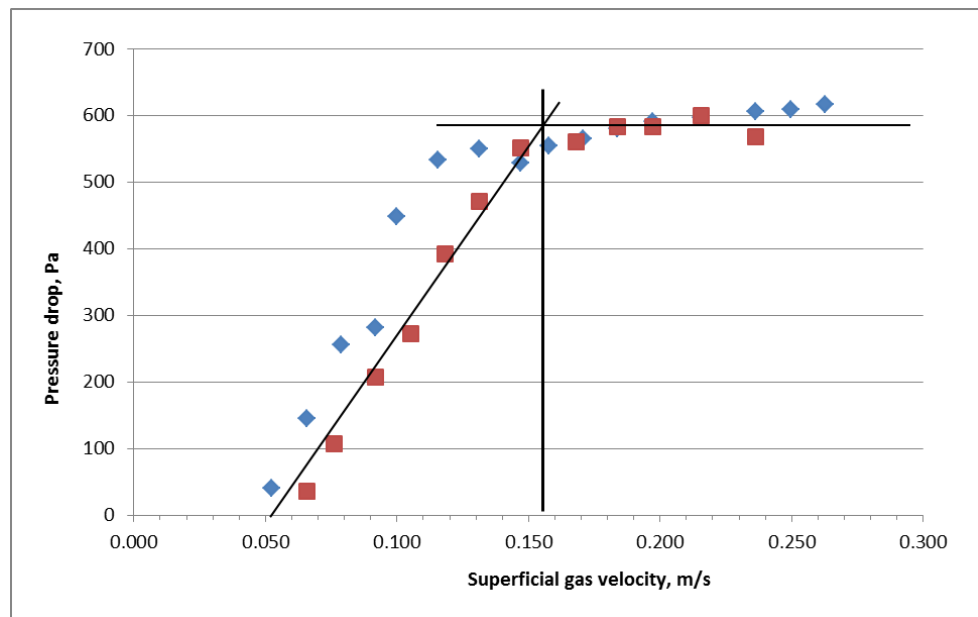


Figure B.10 Experimental minimum fluidization velocity (U_{mf}) curve for original PE-II (wide size distribution) in pressurized three-dimensional fluidization column. (absolute pressure in freeboard: 414 kPa)

B.7 Particle size distributions

The size distributions were determined using a Malvern Mastersizer 2000 equipped with a wet cell. This instrument uses laser diffraction to measure particle size distributions from 0.02 to 2000 μm . Glass bead samples were suspended in distilled water and polyethylene particles in ethanol for these measurements.

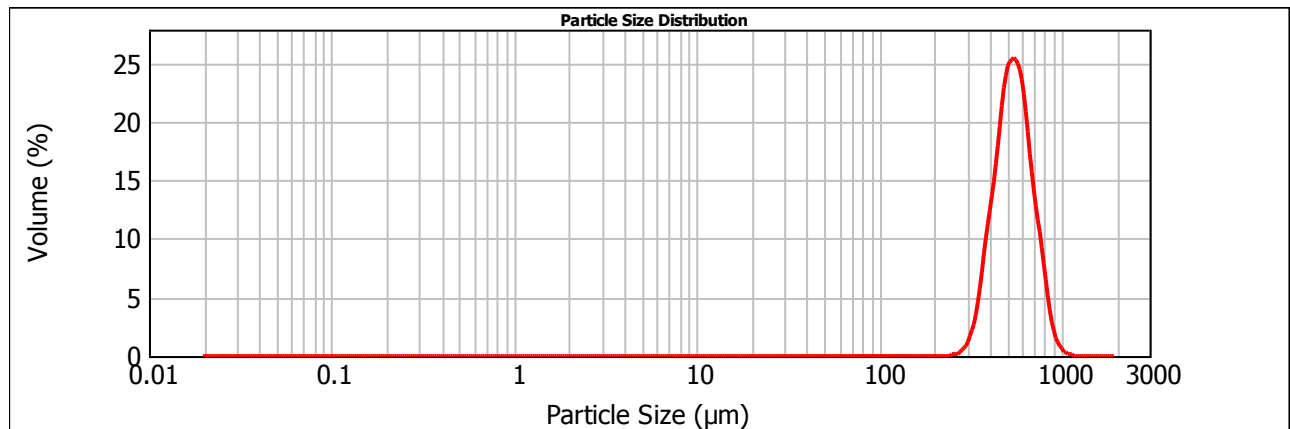
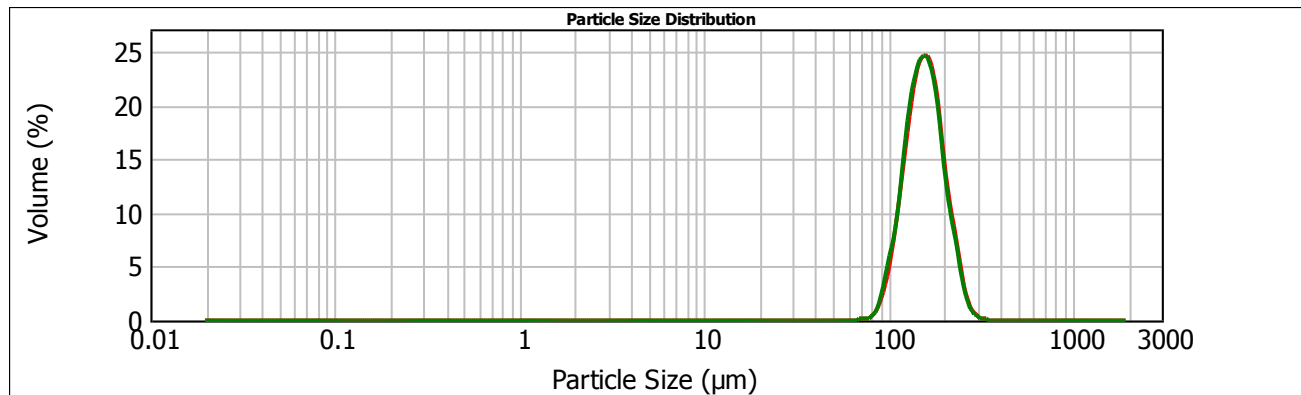


Figure B.11 Particle size distribution of GB (500-600 μm).



—: before experiments; —: after experiments

Figure B.12 Particle size distribution of GB (106-212 μm).

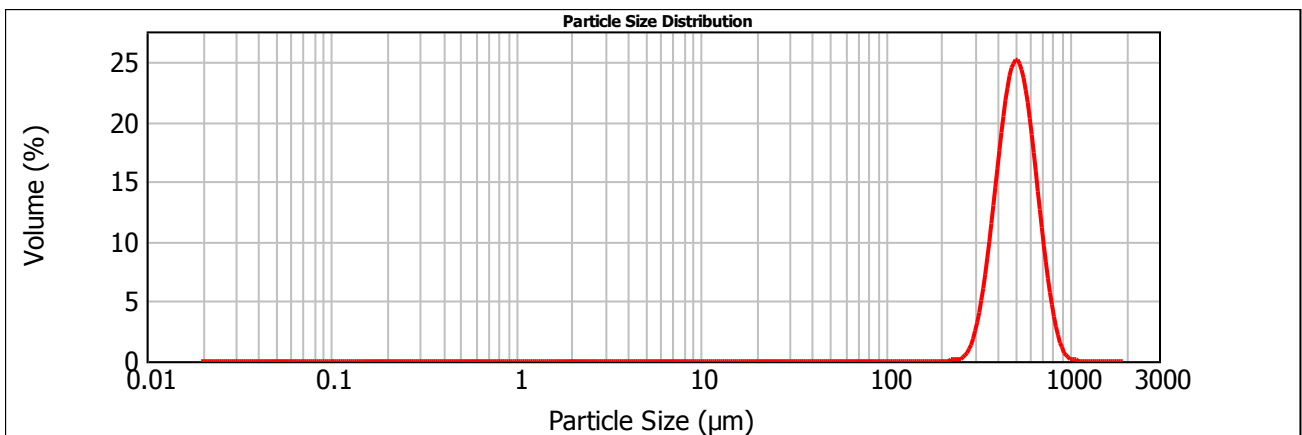


Figure B.13 Particle size distribution of GB (420-590 μm).

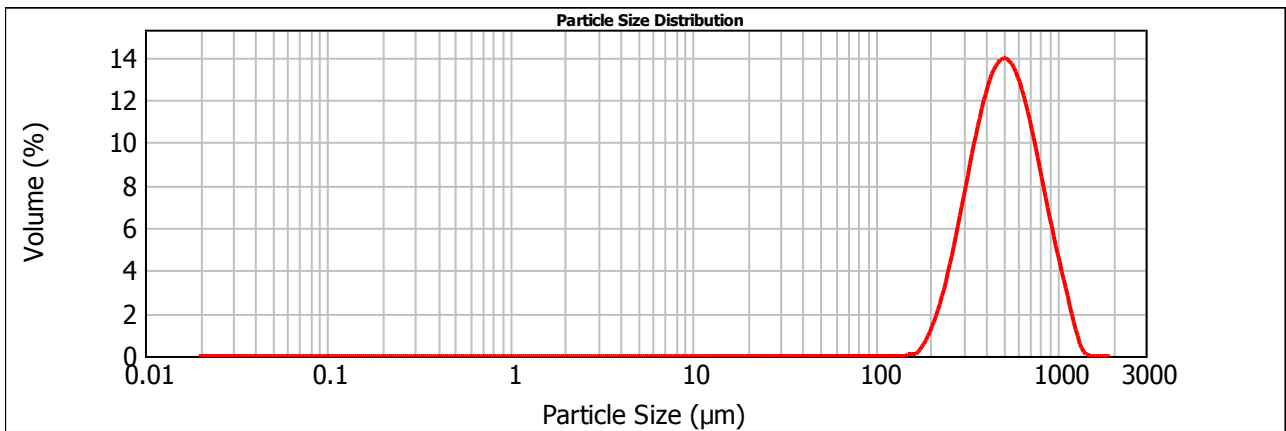
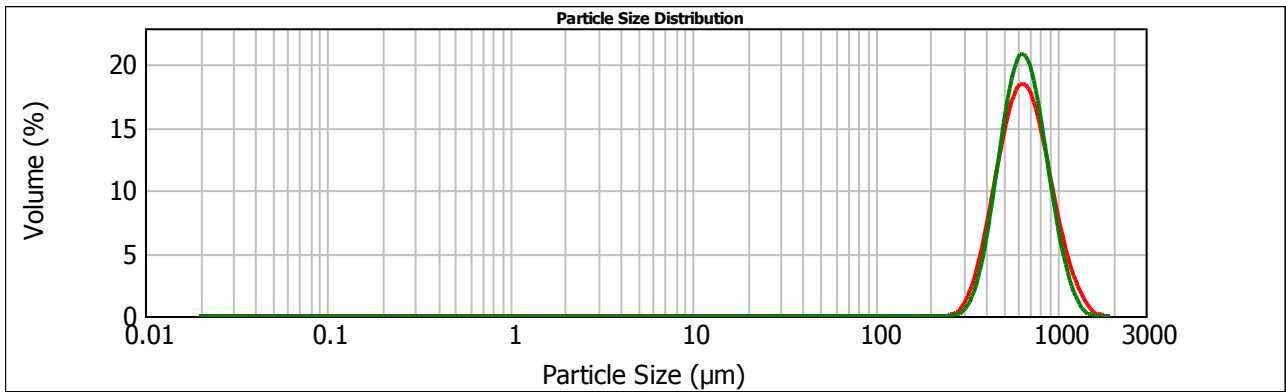


Figure B.14 Particle size distribution of original PE-I (100-1500 μm).



—: before experiments; —: after experiments

Figure B.15 Particle size distribution of sieved PE (710-850 μm).

B.8 Synchronization of camera and probe

Recorded images from the camera (MS70K, Mega Speed) and electrostatic signals from the probe were synchronized through hardware triggering. The camera was put into the “Start and Stop by Trigger” mode and connected to the data acquisition card (PCIe-6321, National Instrument) through BNC cables. In this mode, the camera starts filming on the rising edge of the trigger input and stops capturing on the rising edge of the next trigger input. An analog output of 3.3 V DC was sent from the data acquisition card to trigger the camera, and the reaction time was a few microseconds. Simultaneous analog voltage measurement and voltage generation were achieved by a Labview program, as shown in Figure B.17. First, an analog input and an analog output voltage channel were created. Then the rate for the sample clock was set and the sample mode was defined to be continuous. Called the Get Terminal Name with Device Prefix VI. Then the parameters for a Digital Edge Start Trigger were defined and set the Analog output to trigger off the AI Start Trigger. The Basic Function Generator VI was then used to create the signal to be generated, called the Start VI to arm the two functions. Make sure the analog output is armed before the analog input. This will ensure both will start at the same time. Lastly, called the Clear VI to Clear the Task and used the popup dialog box to display an error if any. Figure B.16 shows a synchronized frame with probe signal. A resolution of 1 millisecond was achieved. Minimum peaks correspond to the moment when the bubble wake reached the probe.

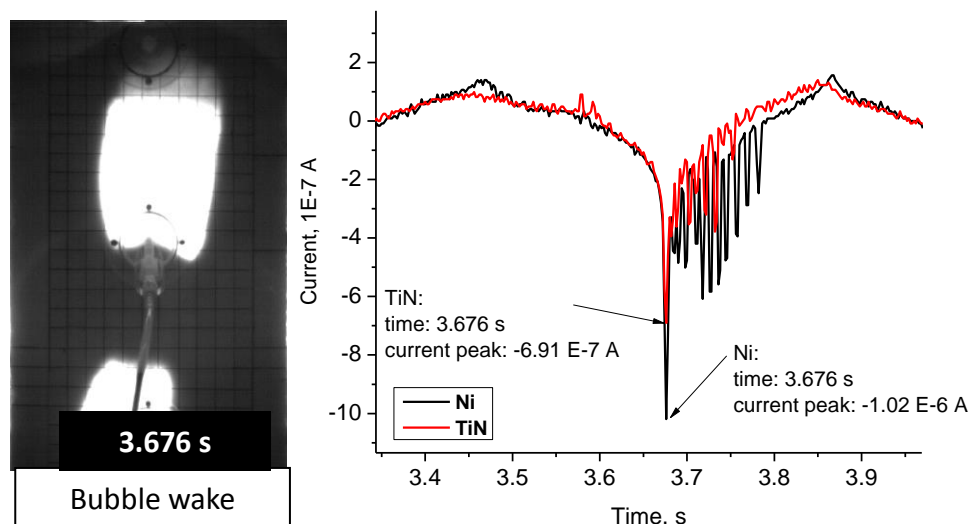


Figure B.16 Example of synchronized frame with 2t2mb probe signal from freely bubbling two-dimensional fluidized column at $U_g=0.39$ m/s.

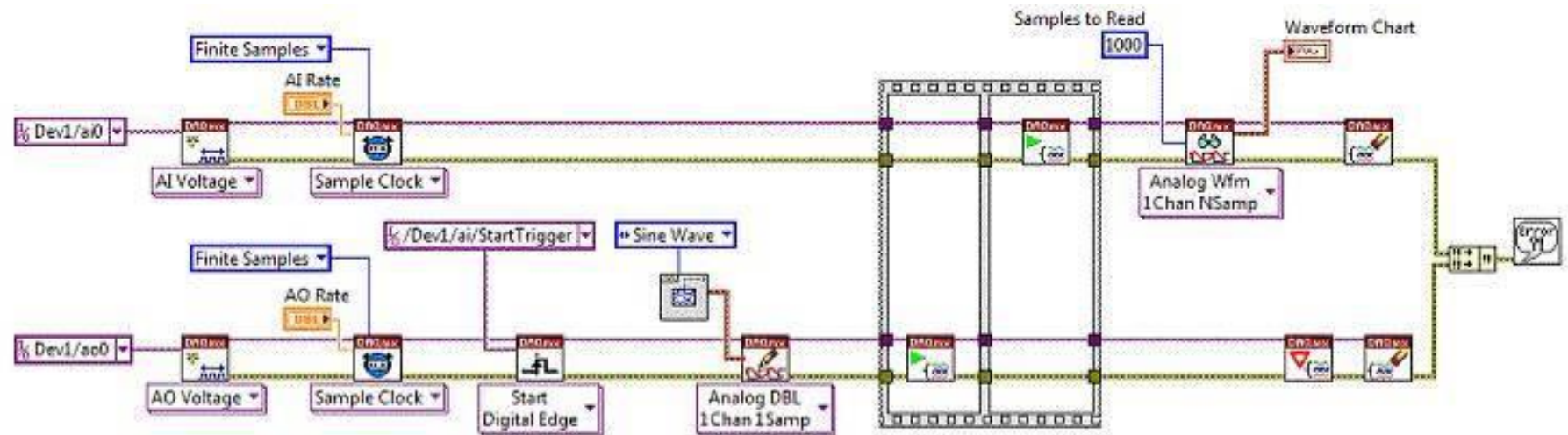


Figure B.17 Labview VI for simultaneous start of analog input and output.

B.9 Polarity of cumulative charge signals from probe

Phenomena: Cumulative charge signals from the fabricated dual-tip (two-material) probes showed different polarity, compared with the particle charge density measured by the Faraday cup. The polarity of cumulative charge signals from the probe changed when the operating conditions were changed.

Diagnose by experiments: tests of probe inside the two-dimensional fluidized bed with different conditions were performed. The following factors were considered.

- Electrometer: different meters were used to test the probe.
- Relative humidity of fluidizing gas: compressed air (RH: 8–15%) and Nitrogen from tank (RH: ~0%) were used as fluidizing gases.
- Probe responses to charged objects: the probe showed negative cumulative charge after contacting with a negatively charged object (e.g. plastic ruler after rubbing with hair), and responded with positive cumulative charge after contacting by a positively charged object (e.g. glass rod after rubbing with cotton).
- Dust on column wall: The column was washed, dried and then tested again. The probe still showed positive cumulative charge, and the charge density measured by a Faraday cup was negative (-2.37 $\mu\text{C}/\text{kg}$).
- Vibration tray test: Particles were passed through the vibrated tray, contacted with the probe and collected by a Faraday cup. The polarity on the charged particles was altered by covering the tray with Scotch tape, then uncovering. When the tray was covered by the tape, the charge density from the Faraday cup measurement was negative (-0.22 $\mu\text{C}/\text{kg}$), while the probe showed negative cumulative charge signal; when the tape was removed, the charge density from the Faraday cup measurement was positive (2.52 $\mu\text{C}/\text{kg}$) and the probe showed a negative cumulative charge.
- Charge density of in-bed particles: The in-bed particle charge density was measured by the Faraday cup method. Particles were either scooped out of the bed or discharged through the sampling port on the column wall during the fluidization. Table B.4 shows that the in-bed particles were charged negatively. The charge densities of scooped particles were less than for those directly discharged through the sampling port, likely because of charge migration

during scooping. As shown in Table B.5, charge densities at 6 s and 25 s were negative, and results from the former were smaller than from the latter, indicating that 6 s may not be enough time to establish equilibrium inside the sampling port and tube.

Table B.4 Faraday cup measurements by scooping particles (static bed height: 0.30 m, $U_g = 0.30 \text{ m/s}$).

Charge on particles, μC	Mass, g	Charge density, $\mu\text{C/kg}$
-6.8E-03	46.65	-0.146
-7.1E-03	47.08	-0.151
-7.4E-03	42.16	-0.176
-6.6E-03	46.96	-0.141
average		-0.154±0.016

Table B.5 Faraday cup measurements of particles discharged through sampling port within 6 s and 25 s (static bed height: 0.30 m, sampling port: 0.22 m above distributor, $U_g = 0.30 \text{ m/s}$).

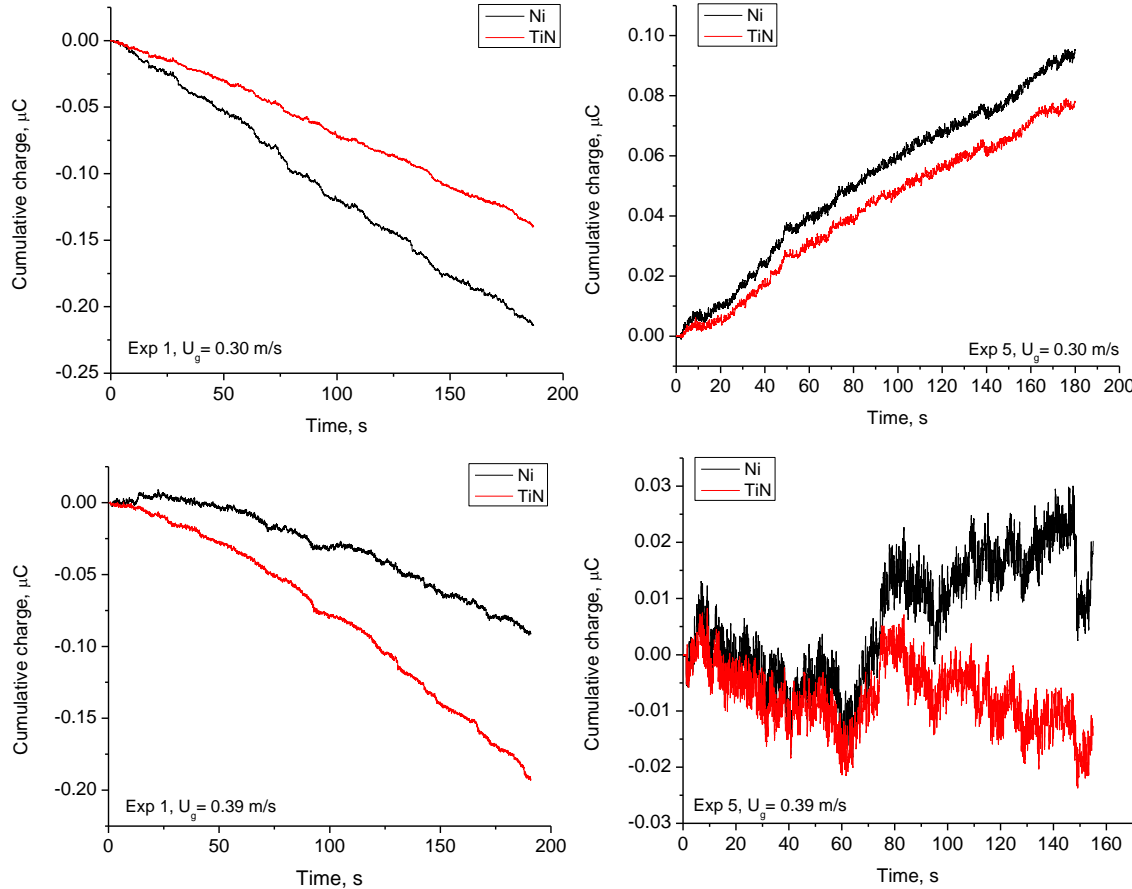
Discharge time	Charge on particles, μC	Mass, g	Charge density, $\mu\text{C/kg}$
6 s	-9.74E-03	6.73	-1.45
	-1.30E-02	6.01	-2.16
	-7.00E-03	5.26	-1.33
average			-1.65±0.62
25 s	-1.84E-01	82.67	-2.23
	-2.14E-01	84.84	-2.52
	-2.20E-01	86.78	-2.54
average			-2.43±0.24

Free bubbling experiments were performed in the two-dimensional fluidization column with glass beads. The 2t2mb probe (see Table 2.1), located 0.22 m above the distributor, was used to measure electrostatics inside the bed with the static bed height maintained at 0.30 m. The charge density on the particles was measured by discharging particles into the Faraday cup through the sampling port located on the opposite face of the column at the same height as the probe. The charge density results are given in Table B.6. Both values were negative. Higher charge densities were obtained when the fluidizing gas was nitrogen with almost zero moisture content. Cumulative charge signals from the probe corresponding to the experiments in Table B.6 are plotted in Figure B.18. Some results show positive cumulative charge signals, while the charge densities were negative.

Table B.6 Results from Faraday cup measurements of particles discharged through sampling port
(Static bed height: 0.30 m, sampling port: 0.22 m above distributor).

	U_g , m/s	Exp 1	Exp 2	Exp 3	Exp 4	Exp 5
Charge density,	0.30	-1.29 ± 0.17	-2.83 ± 0.08	-2.75 ± 0.20	-2.40 ± 0.02	-3.08 ± 0.07
$\mu\text{C}/\text{kg}$	0.39	-2.42 ± 0.09	-4.55 ± 0.39	-3.95 ± 0.16	-4.84 ± 0.18	-5.21 ± 0.20
$\mu\text{C}/\text{kg}$	0.49	-4.18 ± 0.02	-5.03 ± 0.21	-5.64 ± 0.35	-7.44 ± 0.60	-7.00 ± 0.27
Fluidizing gas	Compressed air (RH: 8–15%, T: 21±2°C)				Nitrogen (RH: ~0%, T: 20±2°C)	
Environmental relative humidity and temperature	15%, 21°C		31%, 22°C	33%, 23°C	39%, 21°C (rain)	38%, 23°C

(Note that Exps 1–5 were conducted on different days.)



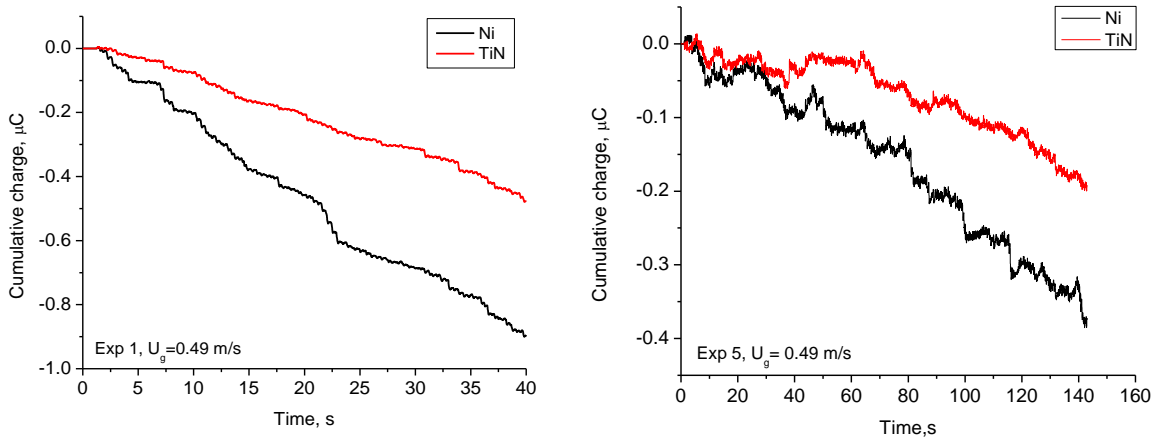


Figure B.18 Cumulative charge signals from 2t2mb probe in freely bubbling two-dimensional fluidized column with glass beads at different U_g (Static bed height: 0.30 m, probe: 0.22 m above distributor, Exps 1 and 5 correspond to Table B.6).

Conclusion: The probe signal polarity is not necessarily the same as the polarity of the particles. The polarity of probe signal depends on charge transfer mechanisms and operating conditions. Therefore, the probe signal should not be used to determine the charge polarity on particles. Instead, it is necessary to extract the particle charge density from probe signals.

B.10 Further results from pressurized three-dimensional fluidization column

This appendix presents more experimental results from the pressurized fluidization column. Both the column and the charge measurement system were the same as described by Moughrabiah et al. [42] and Liu et al. [94]. In brief, the stainless steel column has an inner diameter of 0.15 m, and the height of its straight section is 2.0 m. The gas distributor consists of two stainless steel perforated-plates (top and bottom), each containing 50 aligned holes with diameters of 4.0 and 5.6 mm, respectively. The top perforated plate had an open area ratio of 3.8%. Air was supplied by a KS 19 compressor into a buffer tank and then into the bed.

All experiments were carried out at room temperatures and at three operating pressures (138, 276 and 414 kPa, absolute pressure in freeboard) and three superficial gas velocities ($U_{mf}+0.5$ m/s, $U_{mf}+0.1$ m/s and $U_{mf}+0.15$ m/s). The minimum fluidization velocities, U_{mf} , at these three pressures for PE, determined by measuring the pressure drop across the bed while varying the superficial velocity, are listed in Table B.7. Experimental data are provided in Appendix B.6.

Table B.7 Minimum fluidization velocities of polyethylene particles (PE-II) at different pressures in pressurized three-dimensional column.

Absolute pressure in freeboard, kPa	138	276	414
U_{mf} , m/s	0.19	0.17	0.16

Seven 1t1m probes (see Table 2.1) made by Moughrabiah et al. [42] were located at different axial and radial positions in the column as shown in Figure B.19. Probes A, A', B, B' were located below the static bed height, while C and C' were just above the static bed height, and D was located in the freeboard. Probes A, B, C and D were on the column central axis, while A', B', and C' were 25 mm from the inner wall.

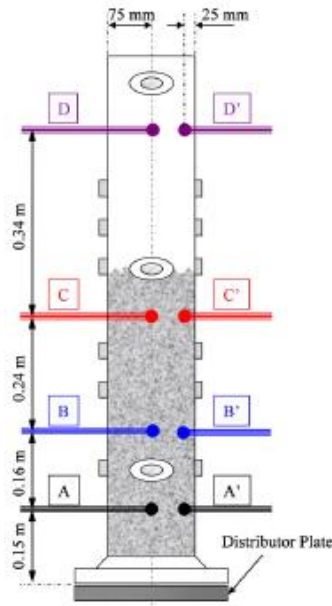


Figure B.19 Locations of 1t1m probes in pressurized three-dimensional fluidization column.

The pressure drop across the bed was measured by a differential pressure transducer (Omega PX-750). The cumulative charges received by the probe at the seven locations inside the bed were measured by Kistler 5010 Dual Mode Amplifiers attached to custom-made contact ball probes. All electrostatic charge and pressure signals were collected by a computer through an A/D converter. Both charge and pressure signals were recorded over time after steady state was reached (usually after one hour of fluidization) at different sampling frequencies (25, 100, 200 and 300 Hz). Sampling frequencies and time periods are listed in Table B.8.

Table B.8 Sampling parameters for each run in pressurized three-dimensional column.

Sampling frequency, f_s , Hz	25	100	200	300
Sampling time, t_s , s	600	150	75	50

B.10.1 Sampling parameters and signal conditioning

Some sampling conditions and denoising methods for electrostatic signal are listed in Table B.9. Some of these papers did not reveal their sampling frequency, an important factor in data sampling processes. A variety range of sampling frequencies and little denoising have been applied to obtain electrostatic signals. The Nyquist–Shannon sampling theorem states that perfect reconstruction of a signal is possible only when the sampling frequency is greater

than twice the maximum frequency of the signal being sampled. Hence, if the sampling frequency is less than twice the characteristic frequency of the charge signals, the signal cannot fully represent the information, losing high-frequency components, so that results from signal analysis tend to be inaccurate. Clearly, the sampling time and measurement frequency need to be chosen with care.

Table B.9 Summary of literature on sampling conditions and denoising of fluidized bed electrostatic signals.

	Sampling frequency and time	Denoising	Charge measurement environment
Yao et al. [16]	50 Hz for 100 s	N/A	Collision probe, 3D fluidized bed
Chen et al. [23]	300 Hz	N/A	Induction probe, 2D fluidized bed
Wang et al. [44]	100 Hz for 300 s	N/A	Collision probe, 3D fluidized bed
Demirbas et al. [99]	200 Hz	Kistler type 5011 or 5015 incorporated a high-pass filter with a cut-off frequency of 0.016 Hz; then a 5th order Butterworth high-pass filter with a cut-off frequency of 0.1 Hz	Induction probe, 2D fluidized bed
Xu et al. [78])	2000 Hz for 3 s	N/A	Electrostatic sensor, dense-phase pneumatic transport line

The collision probes measured the electrostatic charges transferred or induced from collisions with charged particles. Figure B.20(a) shows that the cumulative charges, calculated from the measured voltages, increased with time. Varying the sampling frequency over the range of 25 to 300 Hz did not significantly change the trend. Even when the base line was filtered by a high-pass filter (60 Hz), the cumulative charge signals were essentially the same for different sampling frequencies. The current signals, based on the increase of cumulative charge per unit time interval, appear in Figure B.20(b). These current signals show many local fluctuations around the base line. The amplitudes of fluctuations were less near the wall (detected by probes A', B' and C') than in the center (detected by probes A, B and C).

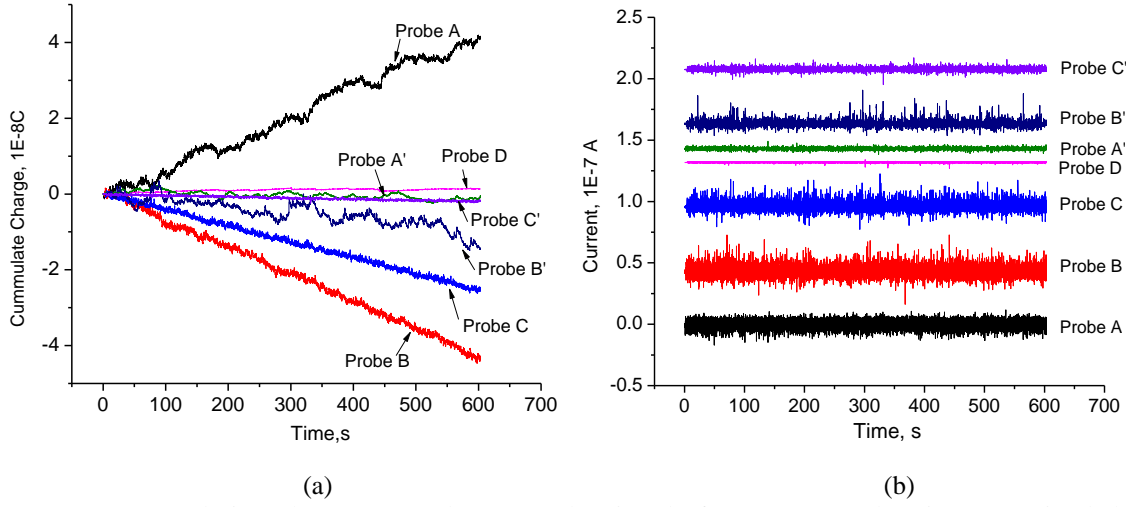


Figure B.20 Cumulative charge (a) and current (b) signals from 1t1m probes in pressurized three-dimensional column ($U_g=U_{mf}+0.1$ m/s, absolute pressure in freeboard region: 276 kPa, $f_s=25$ Hz, $t_s=600$ s).

B.10.1.1 Sampling time

Sampling time is an important factor in data sampling. Insufficient sampling time leads to loss of information. In this work, the total number of data points was maintained the same by making the sampling time inversely proportional to the sampling frequency. Three runs were conducted at high sampling frequencies (200 and 300 Hz). The F-test of data from each runs showed that the data could be considered to be from the same population, so we added the three separate runs together to increase the total sampling time. In Figure B.21, mean current signals from both probes A and B stabilized after ~ 120 s, suggesting that a minimum sampling time of 120 s is required in this study. It should be also noted that longer sampling time may be needed for large scale industrial reactors depending on the reactor size/volume.

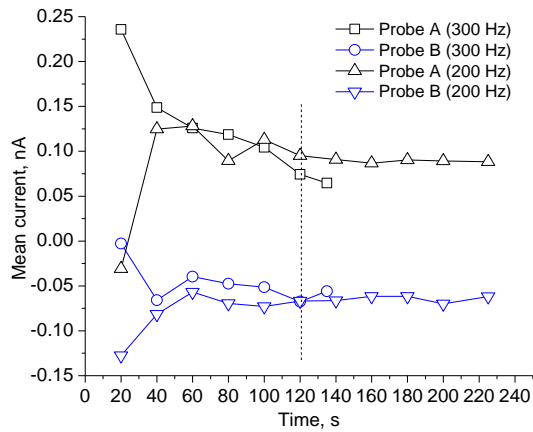


Figure B.21 Mean current signals from 1t1m probes in pressurized three-dimensional column ($f_s=200$ and 300 Hz, $U_g=U_{mf}+0.1$ m/s).

B.10.1.2 De-noising

There is inevitable noise in sampled signals when electrostatic signals of low intensities are to be acquired. Figure B.22 shows the power spectra of raw current signals and noise analyzed by FFT for different operating conditions. FFT result shows that the amplitude of original signals gradually decreased. The noise was estimated from static (no air flow) experiments. The current signals show some frequencies around 60 and 150 Hz. Comparison of the noise and raw signals indicates that high-frequency (>60 Hz) components are likely caused by noise, originating from electrical circuits and measurement tools. Low-pass filtration sharply erases signals above the cut-off frequency, possibly removing signals corresponding to micro-scale phenomena (small particles) as well.

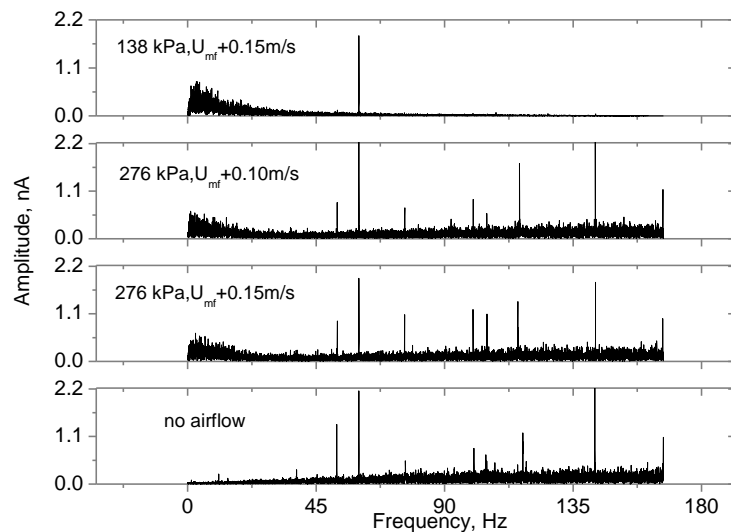
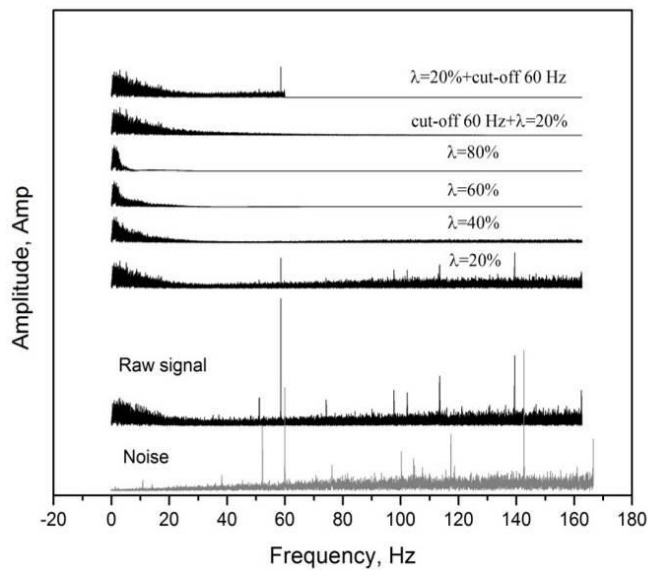


Figure B.22 FFT power spectra of raw current signals and noise from 1t1m probe (probe B) in pressurized three-dimensional column for different operating conditions ($f_s = 300$ Hz).

Although the wavelet de-noising method has excellent time-frequency localization and multi-resolution analysis, parts of low frequency signals may be removed when eliminating noise. So, we adopted a combined de-noising procedure: low-pass FFT filtration followed by wavelet de-noising. The Daubechies 5 wavelet was chosen as the analyzing wavelet having a sufficient number of vanishing moments and for its smoothness [97]. Six levels of decomposition were applied in the wavelet de-noising. For the FFT and wavelet analysis, Origin Pro[®] software was utilized. Figure B.23 shows the result for original current signals

after different de-noising methods. The raw current signal from probe B was adopted for analysis because this probe was located in the middle of the bed, see Figure B.19. It shows that with increasing threshold value, the amplitude decreases, meaning that some information is lost. Wavelet de-noising followed by FFT filtration also did not work well. During these tests, combined de-noising: first low-pass filtration at a cut-off frequency of 60 Hz, then wave-let de-noising at a threshold value of 20%, showed the best potential to remove noise from the electrostatic signals while maintaining the integrity of the signal. Hence this combined de-noising method was chosen to treat the raw signals in the following analyses.



$\lambda=x\%$: wavelet de-noising at threshold value of $x\%$,

$\lambda=20\%+\text{cut-off } 60 \text{ Hz}$: first wave-let de-noising at threshold value of 20%, then low-pass filtration at cut-off frequency of 60 Hz,

$\text{cut-off } 60 \text{ Hz}+\lambda=20\%$: first low-pass filtration at cut-off frequency of 60 Hz, then wave-let de-noising at threshold value of 20%.

Figure B.23 FFT power spectra of raw signal, noise and denoised signals by different methods from 1t1m probe (Probe B) in pressurized three-dimensional column ($U_g=U_{mf}+0.1 \text{ m/s}$, absolute pressure in freeboard: 276 kPa and $f_s=300 \text{ Hz}$).

B.10.1.3 Comparison of pressure and current signals

Synchronized pressure signals from the pressure transducers and current signals from probe A sampled at different frequencies are shown in Figure B.24. Pressure signals obtained at different sampling frequencies show a characteristic frequency of ~0.5-1 Hz, and the intensity distribution did not change significantly with the sampling frequency for the range covered. The current signals at different sampling frequencies indicate that high-frequency

components start to appear at high sampling frequencies. For the same time scale, there were more fluctuations when the sampling frequency was increased from 25 to 300 Hz. It could be seen that the characteristic frequency range of raw current signals was from 0 to \sim 50 Hz. According to Shannon theory, the sampling frequency of the raw current signal should be at least 100 Hz.

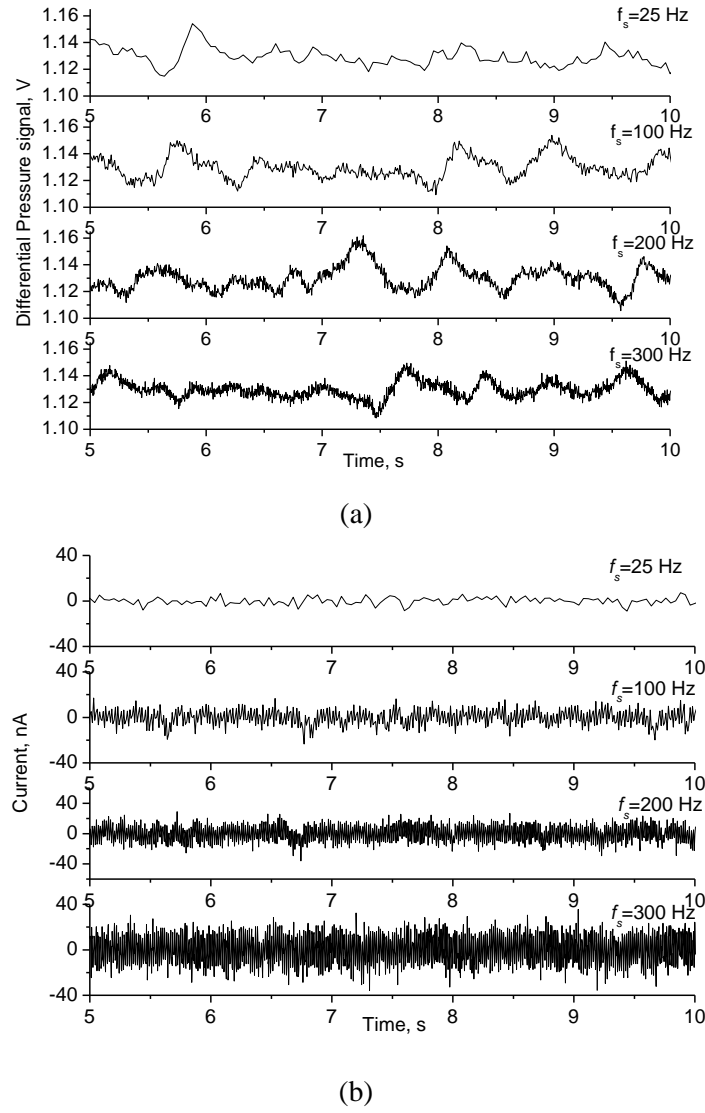


Figure B.24 Synchronized pressure (a) and current signal (1t1m probe, Probe A) (b) of 5 s period for different sampling frequencies at $U_g=U_{mr}+0.1$ m/s and absolute freeboard pressure of 276 kPa.

Figure B.25 compares the pressure signals and current signals on the same plots. One again sees that current signals from different probes differ markedly. Signals from Probes A, B and C (on the axis of the dense bed) fluctuated more strongly than those detected by A' B' and C' (near the wall). The signal from probe D (in the freeboard region) showed negligible

variation. With increasing sampling frequency, signals from both pressure transducers and collision probes display more high-frequency components, but there were still marked differences in the strength of fluctuations for different probes.

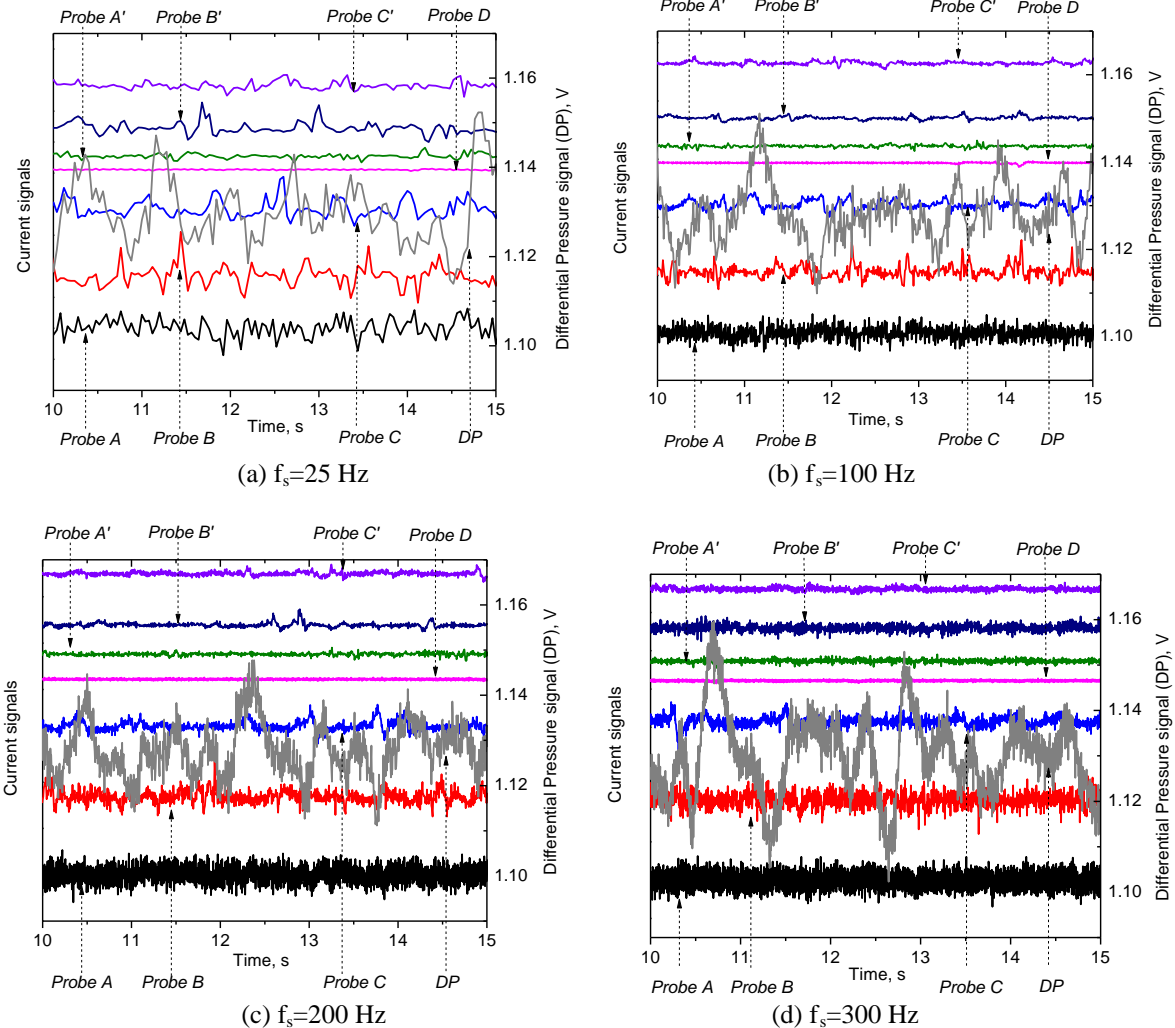


Figure B.25 Pressure and current signals from different 1t1m probes for different sampling frequencies at $U_g = U_{mf} + 0.1$ m/s and absolute freeboard pressure of 276 kPa.

B.10.2 Statistical and time-frequency analysis

B.10.2.1 Mean and standard deviations of current signals

From the above, there are two preliminary conditions for further analysis of current signals: first, the sampling time must be sufficient; second, the raw signal should be de-noised. Because the noise frequency varies for different sampling frequencies and is affected by the

probe position as well, the cut-off frequency and threshold used in de-noising were selected each time by comparing the FFT of raw, noise and denoised signals. Table B.10 lists the values applied in the de-noising method for different probes and sampling frequencies. Typically, a cut-off frequency of 60 Hz and a threshold value of 20% were applied. For a sampling frequency of 25 Hz, only wavelet de-noising was applied. Probe A showed a noise peak at \sim 40 Hz for a sampling frequency of 100 Hz; a band block filtration (cut-off frequency: 39.96-40.04 Hz) was added after normal de-noising.

Table B.10 Values used in de-noising for different 1t1m probes and sampling frequencies.

	Cut-off frequency, Hz			
Sampling frequency, Hz	25	100	200	300
Probe A	N/A	60	59	58
Probe B	N/A	60	60	60
Probe C	N/A	60	60	60
Probe D	N/A	60	60	58
Probe A'	N/A	60	60	60
Probe B'	N/A	60	60	60
Probe C'	N/A	60	60	60
	Threshold value, %			
Probe A	20	20	20	20
Probe B	20	20	20	20
Probe C	20	20	20	20
Probe D	20	20	20	20
Probe A'	20	20	20	20
Probe B'	20	20	20	20
Probe C'	20	20	20	20

The cut-off frequency influences the standard deviation, whereas the threshold influences the mean. Figure B.26 shows the mean and SD of current from different probes for different sampling frequencies. The SD of current signals increases a little from 25 Hz to 100 Hz, and remains the same for sampling frequencies of 100, 200 and 300 Hz for each of the probes. The mean currents are probably the same with little fluctuation for different sampling frequencies. This indicates that the mean and SD of current signals are the same if the current is measured over a sufficient sampling time and denoised appropriately. The cut-off frequency and threshold varied for different probes and sampling frequencies, so these should be chosen each time by comparing the FFT of raw and denoised signals.

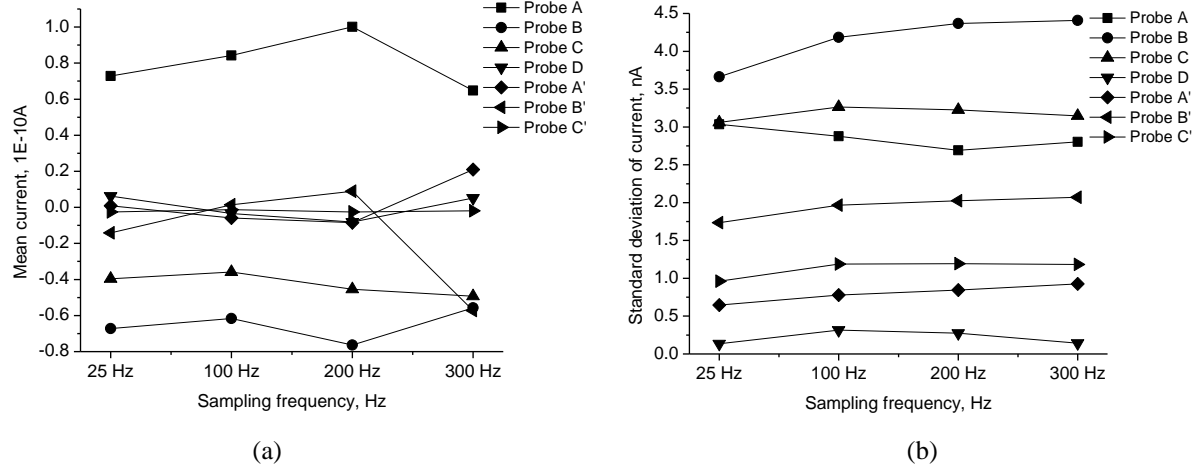


Figure B.26 (a) Mean and (b) standard deviation of denoised current signals from different 1t1m probes and sampling frequencies at $U_g=U_{mf}+0.1$ m/s and absolute freeboard pressure of 276 kPa.

B.10.2.2 FFT

Liu et al. [94] and Boland and Geldart [92] found that the hydrodynamics of fluidized beds and electrostatic charges are closely related. To illustrate this relationship, the pressure drop signals from pressure transducers and current signals from collision probes were analyzed by FFT to obtain their power spectral distributions. As shown in Figure B.27, pressure signals contain a characteristic frequency of around 1 Hz, seen more clearly at high superficial gas velocities. From the FFT spectral distribution of current signals, probe C contains a noticeable characteristic frequency from 1 to 2 Hz, similar to the pressure signals. As the gas velocity increased, the characteristic frequencies of both current signals and the pressure signal increased. Liu et al. [94] proposed that the hydrodynamic fluctuations are mainly caused by bubble rise, coalescence, and breakage. Pressure drop fluctuates more strongly with increasing gas velocity because of coalescence and eruption of large bubbles at the bed surface. Hence the characteristic frequency of pressure fluctuations was dominated at higher gas velocities by large bubbles near the bed surface, where Probe C was located. Particles around large bubbles collide with probes more energetically at higher gas velocities, leading to greater charge density. Hence the fluctuations of current also reflect large bubbles properties. Therefore the characteristic frequency of the current signal from probe C is more consistent with that of pressure signals.

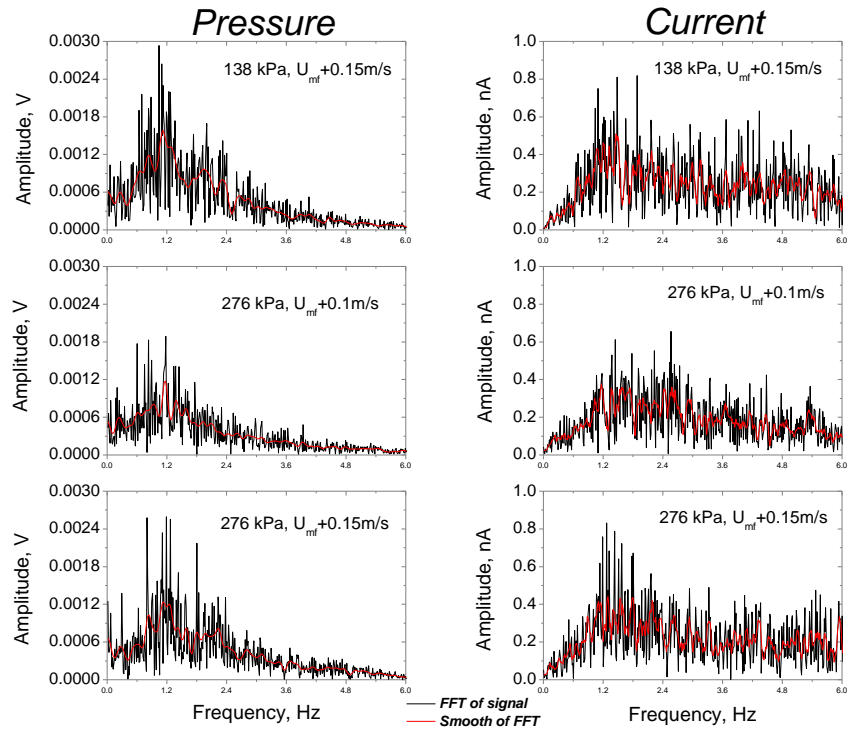


Figure B.27 FFT spectra of bed pressure (ΔP) (left) and current (1t1m probe, Probe C) (right) signals under different operating conditions for sampling frequency of 200 Hz.

B.10.3 Conclusions

Electrostatic charges of polyethylene particles in a pressurized fluidized bed were measured by 1t1m probes for different operating conditions. The characteristic frequency range of raw current signals was from 0 to ~ 50 Hz, so that from Shannon theory, the sampling frequency of the raw current signal should be at least 100 Hz.

A combined FFT low pass filtration and wavelet de-noising method successfully removed noise from the electrostatic signals, while maintaining their integrity. A cut-off frequency of 60 Hz and a threshold value of 20% were selected for combined de-noising by comparing the FFT of raw, noise and denoised signals. A minimum sampling time of 120 s was required for the case under study. After de-noising, the mean and SD of current signals appear to be the same for different sampling frequencies for all probes. Low sampling frequency may cause incomplete data recording, while high sampling frequency may require complex de-noising. Suitable sampling frequency and de-noising are necessary pre-conditions for analysis of electrostatic charge signals from gas-solid fluidized beds.

Appendix C Details of modeling and signal processing

C.1 Simulation results from a charge transfer and induction model

Induced charge and current signals, by the passage of a single bubble in a fluidized bed filled with charged particles, are simulated following an approach similar to Chen et al. [21]. It aims to prove that the relative magnitudes of induced currents when bubble noses and weaks contact the probe tip are almost the same. Exact absolute values for induced currents were not required, and the relatively simple model is considered sufficient to provide a first approximation. The probe tip in this work (6×6 mm) and in the literature (a few millimetres, as shown in Table 1.2) is usually very small compared with the size of injected bubbles so that it is reasonable to consider the probe tip as a field point. The bubble wake and drift are first ignored. Assume that the bubble rises at constant velocity, U_B , with the centre of the probe tip lying on the axis of the rising bubble. Each bubble is assumed to have a spherical shape. Its radius (R_B) and shape are assumed to remain constant. Particle holdup inside the bubble is neglected, and we assume that there are no charges inside the bubble. The charge distribution in the fluidized bed can be obtained by superposition of two simple contributions: (a) a uniformly charged bed with a specific charge of q_{m0} ; (b) charged spherical ball with a uniform charge density of $-q_{m0}$, as shown in Figure C.1.

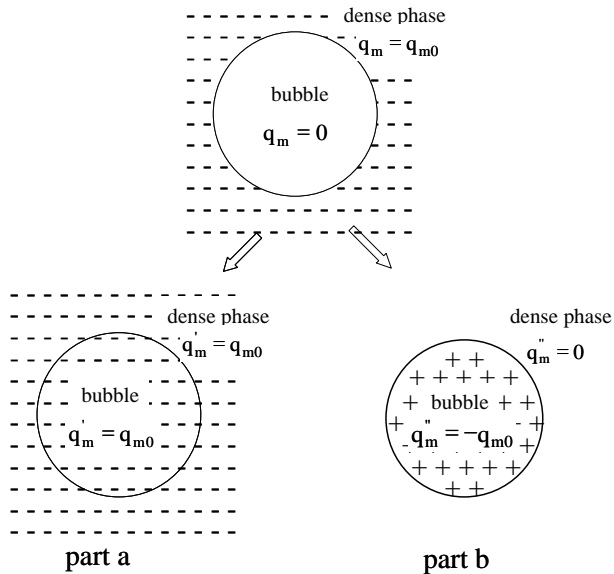


Figure C.1 Representation of specific charge distribution due to two additive components.

For part (a), the induced charge is taken as zero because of the uniform distribution of volume charge density throughout the whole bed and only dynamic changes of induced charge are important.

$$\dot{Q}_{ind} = 0 \quad (C.1)$$

For part (b), there is no charge outside the hypothetical particle-filled bubble. The induced charge is only generated from the charge inside the bubble.

$$\ddot{Q}_{ind} = \frac{-q_{m0}(1-\varepsilon)\rho_s R_p^2}{4\pi\Pi_r} \int_0^{R_B} \int_0^{2\pi} \int_{-\pi/2}^{\pi/2} \int_0^{2\pi} \int_{-\beta_0}^{\beta_0} r_B^{-2} \cos\theta \cos\beta \left(\frac{1}{r_1^2} \frac{\partial r_1}{\partial r} + \frac{c}{r_2^2} \frac{\partial r_2}{\partial r} - \frac{1}{r_2 d} \right) d\beta d\gamma d\theta d\phi dr_B \quad (C.2)$$

The total induced charge is the sum of the two terms.

$$Q_{ind} = \dot{Q}_{ind} + \ddot{Q}_{ind} \quad (C.3)$$

The induced current can then be calculated from

$$I_{ind} = -\frac{dQ_{ind}}{dt} \quad (C.4)$$

Table C.1 gives the parameters used in the simulation. Figures C.2 and C.3 show the simulated induced charges and currents with varying q_{m0} and D_B . By fitting I_{ind} with q_{m0} and D_B , a form of Eq. (2.12) could be obtained.

Table C.2 lists the minimum and maximum induction peak values and their relative differences. The results show that the magnitudes of the simulated induced currents when the bubble nose and wake contact the probe surface are almost the same, with the relative difference less than 0.3% for the cases investigated, these small differences likely being caused by the relatively coarse grid used in the calculation.

Table C.1 Input parameters used in simulation.

Particle diameter, $d_s, \mu\text{m}$	Particle density, $\rho_p, \text{kg/m}^3$	Probe tip diameter, D_p, mm	Voidage, ε_{mf}	Distance between probe tip and bubble injector, L, m	Time step, s
550	2500	6	0.45	0.5	0.01

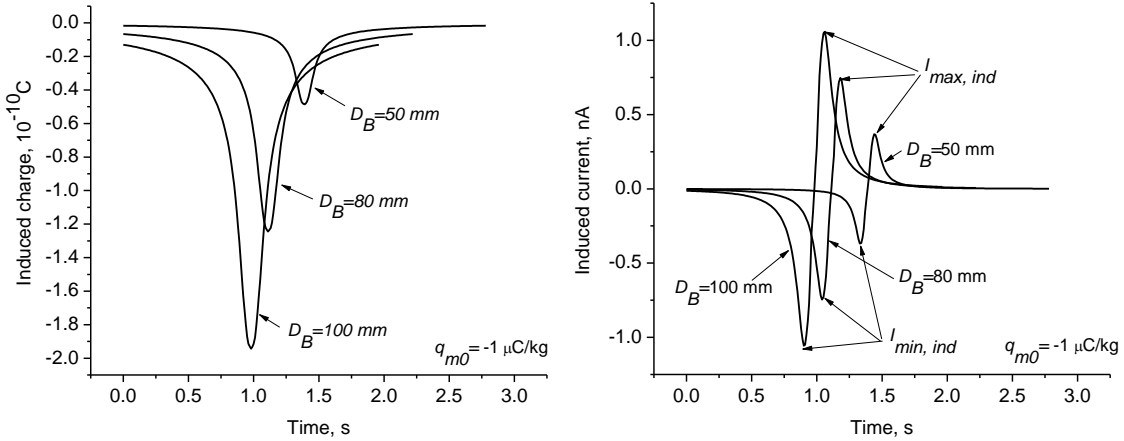


Figure C.2 Simulated induced charges and currents for different D_B (50, 80 and 100 mm) when $q_{m0} = -1 \mu\text{C}/\text{kg}$.

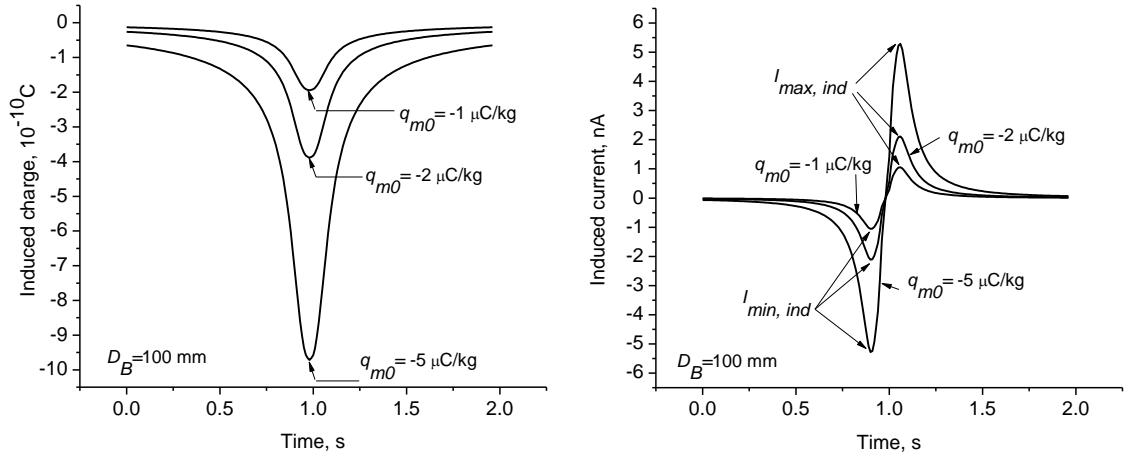


Figure C.3 Simulated induced charges and currents with different q_{m0} (-1, -2 and $-5 \mu\text{C}/\text{kg}$) when $D_B = 100 \text{ mm}$.

Table C.2 Simulated minimum and maximum peaks and their relative differences in Figures C.2 and C.3.

		Minimum induction peak ($I_{\min, \text{ind}}$), nA	Maximum induction peak ($I_{\max, \text{ind}}$), nA	Relative difference, %
$D_B = 100 \text{ mm}$	$q_{m0} = -1 \mu\text{C}/\text{kg}$	-1.056	1.057	0.09
	$q_{m0} = -2 \mu\text{C}/\text{kg}$	-2.112	2.115	0.14
	$q_{m0} = -5 \mu\text{C}/\text{kg}$	-5.280	5.287	0.13
$q_{m0} = -1 \mu\text{C}/\text{kg}$	$D_B = 50 \text{ mm}$	-0.368	0.369	0.27
	$D_B = 80 \text{ mm}$	-0.746	0.747	0.13
	$D_B = 100 \text{ mm}$	-1.056	1.057	0.09

Transfer current signals from two different probe materials (Ni and TiN) when single bubbles passed are also simulated. Figure C.4 shows that the transfer currents increased as the bubble

approached the probe; two minima appeared when the bubble nose and wake reached the probe.

By solving two simulated signals from the two materials, charge density and average particle velocity were calculated. As shown in Figure C.4, the calculated particle charge density (q_m) consists with the initial input charge density (q_{m0}) with zero value when the probe is inside the bubble, consistent with the assumption that no particles inside the bubble. The calculated average particle velocities around the probe display two maxima (equal to the input bubble rise velocity) when the bubble nose and wake reach the probe and also become zero when the probe is enclosed in the bubble.

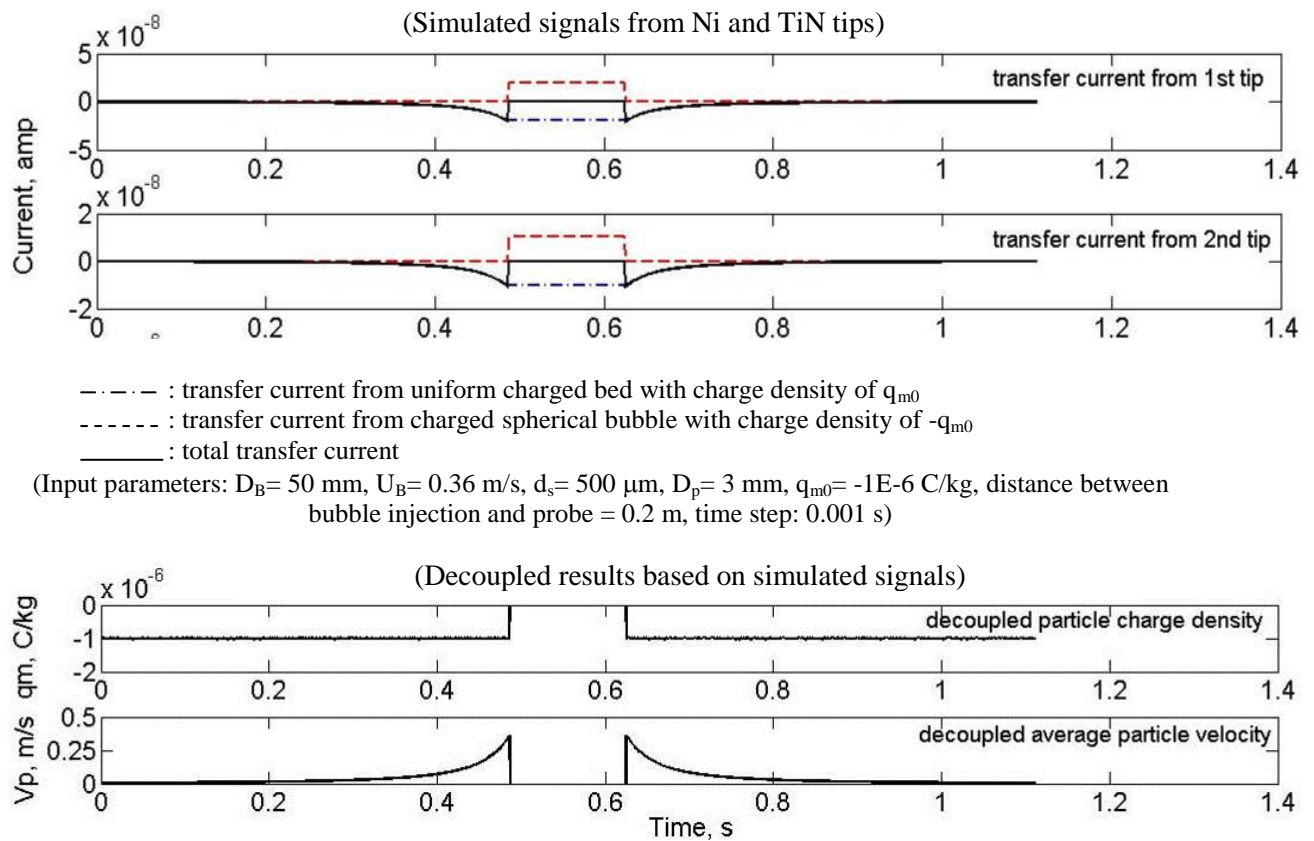


Figure C.4 Simulated transfer currents from Ni and TiN tips of 2t2m probe caused by bubble passing and decoupled charge density and average particle velocity.

C.2 Improvement of charge transfer model

The model of Park et al. [20] and Chen et al. [21] on charge transfer between charged particles surrounding bubble and a ball probe is modified to take into account the particle charging theory of Matsusaka et al. [60, 61] and Cole et al. [59]. In the previous model, the charge transfer was calculated by analogy to heat transfer and based on the potential difference between two contact surfaces [58, 149]. In the revised model, the total transfer current is re-calculated based on the total potential difference between the probe and particles. The transfer current is not only a function of charge density and hydrodynamics (bubble size), but also the surface work function difference of the particles and probe materials. The revised and previous models are compared in Figure C.5.

The total charge difference (or charge acquired after impact) is treated as a continuous quantity dq / dn , (where n is the number of collisions). The net transfer charge is the sum of charge accumulation plus charge relaxation.

$$\frac{dq}{dn} = \frac{dq_c}{dn} + \frac{dq_r}{dn} \quad (C.5)$$

Applying the condenser model to the charge accumulation part gives:

$$\frac{dq_c}{dn} = k_c CV \quad (C.6)$$

where k_c is the electrification efficiency, C is the capacitance between the contact bodies (probe and particles). The total potential difference between probe and particle is:

$$V = V_c - V_e - V_b \quad (C.7)$$

V_c is based on the surface work functions, with the work function defined as the work required to remove an electron from a metal at the top of the energy distribution. ϕ_p is effective work function of particles and ϕ_M is work function of metal. V_e is caused by the image charging effect, and V_b by the space charging effect. k_e and k_b are coefficients related to the probe and particle properties, permittivity of the medium, dimensions of the fluidized bed and bubble rise velocity.

$$V_c = -\frac{(\phi_p - \phi_M)}{e} \quad (C.8)$$

$$V_e = k_e q \quad (C.9)$$

$$V_b = k_b q \quad (C.10)$$

From Gauss's law

$$\int \mathbf{E} \cdot d\mathbf{s} = \sum q / \Pi_0 \Pi_r \quad (C.11)$$

$\sum q$ is the total charge enclosed by the surface, and Π_r is the relative permittivity or dielectric constant of the medium outside the surface. If the surface density of charges is Q_s

$$E = Q_s / \Pi_0 \Pi_r \quad (C.12)$$

The electrical field between parallel plates, with a total charge q , separated by a distance z_0 , is given by:

$$q / A = \Pi_0 \Pi_r E \quad (C.13)$$

so that:

$$C = q / V = \Pi_0 \Pi_r A / z_0 \quad (C.14)$$

We treat the contact area as a hard sphere: collisions are then assumed to be instantaneous and only one is possible at a time. In this case, the contact area A_p between the probe metal surface and particle does not change during the time interval, and the contact area is approximated by the surface area of the probe. The charge relaxation is approximated [150] by

$$\frac{dq_r}{dt} = -k_r q \quad (C.15)$$

where k_r is a constant. When the sphere is struck at regular intervals, and the particle collision frequency is defined as f , the above equation can be written as:

$$\frac{dq_r}{dn} = -\frac{k_r}{f} q \quad (C.16)$$

so that the net charge becomes:

$$\frac{dq}{dn} = \frac{k_c \Pi_0 \Pi_r A_p V_c}{z_0} - \left[\frac{(k_e + k_b) k_c \Pi_0 \Pi_r A_p}{z_0} + \frac{k_r}{f} \right] q \quad (\text{C.17})$$

Solving the equation with initial conditions: $n=0$, $q=q_i$, leads to

$$q = q_i \exp\left(-\frac{n}{n_0}\right) + q_\infty [1 - \exp\left(-\frac{n}{n_0}\right)] \quad (\text{C.18})$$

$$n_0 = \frac{1}{(k_e + k_b) k_c \Pi_0 \Pi_r A_p / z_0 + (k_r / f)} \quad (\text{C.19})$$

$$q_\infty = \frac{V_c}{(k_e + k_b) + (k_r z_0 / k_c \Pi_0 \Pi_r A_p f)} \quad (\text{C.20})$$

By analogy to the charge transfer model in pneumatic transport in a pipeline, $n(\Delta x)$.is the numbers of collision during the particles moving a distance of Δx . In the fluidized bed, at time interval Δt , the charge transferred by the bubble movement is Δq , and the number of collisions, $n(\Delta x)$, denotes how many particles collide with the probe during time interval Δt .

$$\Delta q = q(t + \Delta t) - q(t) = (q_\infty - q_i) [1 - \exp\left(-\frac{n(\Delta t)}{n_0}\right)] \quad (\text{C.21})$$

$$q_i = q_{m0} \rho_p \frac{\pi}{6} d_s^3 \quad (\text{C.22})$$

The current is represented by:

$$I_{tran} = -\frac{\Delta q}{\Delta t} \quad (\text{C.23})$$

From Taylor expansion, the above equation can be rewritten:

$$I_{tran} = -\frac{1}{\Delta t} (q_\infty - q_{m0} \rho_p \frac{\pi}{6} d_s^3) \frac{n(\Delta t)}{n_0} \quad (\text{C.24})$$

where $n(\Delta t)$ is the number of collisions during time interval Δt .

$$n(\Delta t) = \frac{6V_p (1-\varepsilon) A_p \Delta t}{\pi d_s^3} \quad (\text{C.25})$$

When the charge relaxation is sufficiently small compared to particle charging, $k_r=0$, the charging efficiency $k_c=1$,

$$n_0 = \frac{z_0}{(k_e + k_b) \Pi_0 \Pi_r A_p} \quad (C.26)$$

$$q_\infty = \frac{V_c}{(k_e + k_b)} \quad (C.27)$$

From Eqs. (C.19-23), the current is written as:

$$I_{tran} = \frac{(k_e + k_b) \Pi_0 \Pi_r \rho_p V_p (1 - \varepsilon) A_p^2}{z_0} q_{m0} + \frac{6 \Pi_0 \Pi_r V_p (1 - \varepsilon) A_p^2}{\pi z_0 d_s^3} \frac{(\phi_p - \phi_M)}{e} \quad (C.28)$$

Eq. (C.28) shows physical meanings of the properties of the probe materials and particles. This equation was tried to fit experimental data, however better coefficient of determination was obtained by fitting the data with a form of Eq. (2.5).

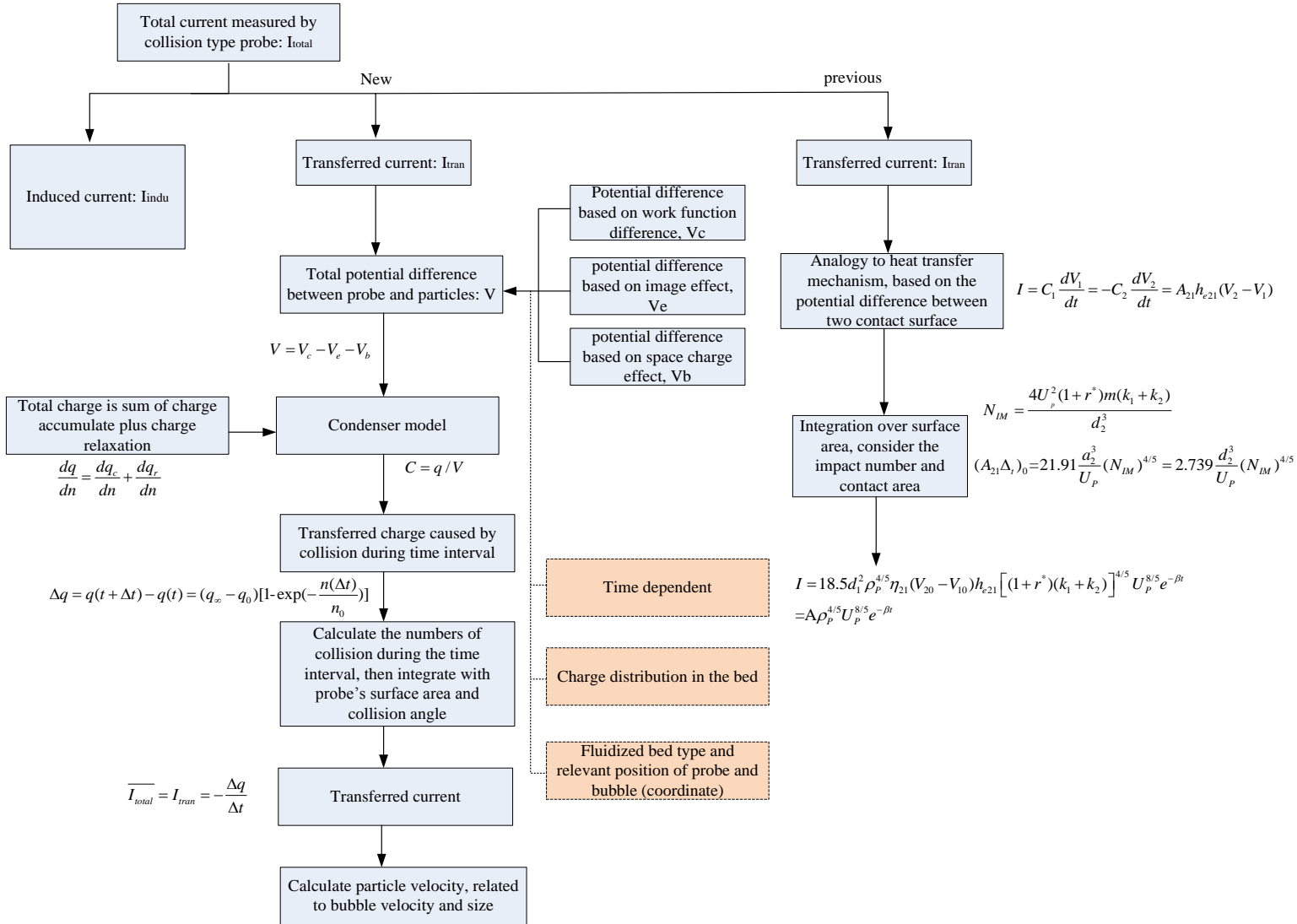


Figure C.5 Schematic of model improvement.

C.3 MATLAB codes for charge transfer and induction model as well as signal processing and decoupling

Available upon request.